Reactivity of Surfaces with F Centers

Dissertation
zur
Erlangung des Doktorgrades (Dr. rer. nat.)
der
Mathematisch-Naturwissenschaftlichen Fakultät
der
Rheinischen Friedrich-Wilhelms-Universität Bonn

von
Michael Francesco Häfner
aus
Buchen

Bonn, März 2023

This dissertation is dedicated to my grandmother Gertrud Einig, who inspired and supported me throughout my life, but who unfortunately did not live to see my graduation.

Ömchen, diese Zeilen sind für dich.

* 18.05.1932
† 26.12.2022

Acknowledgements

Abstract

This thesis presents a comprehensive theoretical investigation of the alkali halide F center. It explores how density functional theory (DFT) and statistical mechanics can be applied to obtain the defective system's electronic properties, its dynamic properties, its interaction with small gas phase molecules, and its effect on various hydrogenation reactions.

In the first two chapters of this thesis, the topic of catalysis and alkali halide F centers are introduced, and the theoretical fundamentals required to describe the defective alkali halides are elaborated.

The third chapter investigates how DFT describes the electronic properties of the alkali halides NaCl, KCl, NaBr, and KBr, employing a multi-level approach with the generalized-gradient approximation (GGA) functional PBE and the dispersion correction D3(BJ) for optimization and the self-consistent dielectric-dependent global hybrid (sc-DDGH) functional sc-PBE0 for the calculation of all electronic properties. In a comparison with experimental measurements, the method is found to reproduce the dielectric constants, electronic band gaps, ionization energies, and electron affinities of the investigated alkali halides within experimental errors, greatly surpassing the results of GGA-level theory and the standard global hybrid functional PBE0. After substantiating the accuracy of this methodology, it is employed to calculate the electronic properties and the defect orbitals of the alkali halide F center. The results for the defect level energy of the F centers are consistent with previous research and show that the defects are predominantly affected by Coulomb interaction, exhibiting an anti-proportional relationship between the lattice parameter and the defect level energy. Furthermore, the KCl M center is calculated and characterized as a system of two largely uncoupled F centers in an antiferromagnetic ground state, which is in accordance with the results from magnetic resonance experiments.

Chapter four investigates the migration of the F center across the bulk lattice and the (100) surface of NaCl, KCl, NaBr, and KBr with the same multi-level approach, vibrational thermodynamic corrections, and thermal corrections to make the theoretical model comparable with the experimental high-temperature measurements. The obtained migration enthalpies are in close agreement with the experimental results for NaCl, KCl, and KBr, and the barrier for NaBr is predicted. Furthermore, the barriers are found to correlate with the single vibrational mode of the primitive unit cells of the respective alkali halides. The migration across the (100) surface is simulated and the barrier heights are found to be lower than for the bulk migration because of symmetry reduction. The electronic structure and geometry of the transition states are evaluated, and the delocalized nature of the defect electron in the transition state is identified to cause a self-interaction error in the order of $0.2 - 0.4\,\mathrm{eV}$, necessitating a description by hybrid-level DFT.

Chapter five deals with the activation and reactivity of nitrogen on the NaCl and KCl F center on the (100) surface. The simulated defect reduces the nitrogen molecule and activates its triple bond for a reaction with hydrogen, significantly diminishing the reaction barrier of the reaction compared to the gas phase. The transfer of the defect electron into the lowest unoccupied molecular orbital (LUMO) of gaseous nitrogen is found to be the driving force behind the enhanced reactivity, while the surface

provides additional stabilization to the transition states and intermediate structures.

Chapter six investigates the activation and hydrogenation of carbon monoxide and carbon dioxide on the KCl F center. The defect reduces all carbon-containing reagents and intermediates by occupying their LUMOs, and it weakens their bonds for reaction with hydrogen. The thermodynamic and kinetic properties of all reaction steps are calculated, and the barriers for the hydrogenation are found to be significantly lower than the barriers for the gas phase reaction. The computed reaction rate is comparable to the rate measured for the conventional copper-based catalyst. The homolytic dissociation of the intermediates formic acid, water, and methanol are explored and found to inhibit the synthesis of methanol on the F center.

Chapter seven examines the effects of doping the KCl F center with a copper atom. The metal atom is found to strongly interact with the defect, changing its electronic structure from an open-shell into a closed-shell state. The doped defect still stabilizes the adsorbates CO, H_2CO, and CH_3OH, but it does not dissociate methanol to methane. The reaction of the adsorbates with hydrogen is investigated, and bi-hydrogenated copper, HCuH, is identified as a more thermodynamically stable state than a single copper atom in the defect. Moreover, it catalyzes the synthesis of methanol in a step-wise, copper-mediated hydrogen addition. The kinetic properties of the reaction are analyzed with a kinetic Monte Carlo simulation, yielding a reaction rate that surpasses the rate on the empty defect and on the conventional catalyst by several orders of magnitude.

In the summary and outlook, all findings are summarized and evaluated on how they provide a foundation for future research into the physical, chemical, and catalytic properties of defective alkali halides and electronically similar systems, as the copper-doped F center in particular presents a promising candidate for catalytic hydrogenation.

Kurzzusammenfassung

In dieser Arbeit wird eine umfassende theoretische Untersuchung des Alkalihalogenid-F-Zentrums vorgestellt. Es wird untersucht, in welcher Weise Dichtefunktionaltheorie (DFT) und statistische Mechanik angewendet werden können, um die elektronischen und dynamischen Eigenschaften des defekten Systems sowie dessen Wechselwirkung mit kleinen Gasphasenmolekülen und den Einfluss auf verschiedene Hydrierungsreaktionen zu beschreiben.

In den ersten zwei Kapiteln dieser Arbeit werden das Thema Katalyse und die Alkalihalogenid-F-Zentren vorgestellt und die theoretischen Grundlagen zur Beschreibung der Defekte erarbeitet.

In Kapitel drei wird untersucht, wie DFT die elektronischen Eigenschaften der Alkalihalogenide NaCl, KCl, NaBr und KBr beschreibt. Hierzu wird ein Mehrebenenansatz eingesetzt, welcher aus dem verallgemeinerten Gradientennäherungsfunktional PBE und der Dispersionskorrektur D3(BJ) zur Optimierung und dem selbstkonsistenten, dielektrizitätsabhängigen globalen Hybridfunktional sc-PBE0 zur Berechnung aller elektronischer Eigenschaften besteht. In einem Vergleich mit experimentellen Messungen reproduziert diese Methode die dielektrischen Konstanten, elektronischen Bandlücken, Ionisationsenergien und Elektronenaffinitäten der untersuchten Alkalihalide im Rahmen des experimentellen Messfehlers, womit es die Ergebnisse von PBE und dem globalen Hybridfunktional PBE0 deutlich übertrifft. Nachdem die Genauigkeit dieser Methode nachgewiesen wurde, wird sie dazu eingesetzt, um die elektronischen Eigenschaften und die Defektorbitale des Alkalihalogenid-F-Zentrums zu berechnen. Die berechneten Ergebnisse für die Defektniveauenergie des F-Zentrums stimmen mit den Ergebnissen der bisherigen Forschung überein und zeigen, dass der Defekt hauptsächlich von der Coulombwechselwirkung bestimmt wird, welches durch eine antiproportionale Abhängigkeit zwischen der Gitterkonstante und der Defektniveauenergie untermauert wird. Darüber hinaus wird das M-Zentrum auf KCl berechet, welches ein System aus zwei größtenteils entkoppelten F-Zentren in einem antiferromagnetischen Grundzustand darstellt, wie es bereits in Magnetresonanzexperimenten gemessen wurde.

In Kapitel vier wird die Wanderung des F-Zentrums durch den Festkörper und über die (100)-Oberflächen von NaCl, KCl, NaBr und KBr mit dem zuvor etablierten Mehrebenenansatz, thermodynamischen Schwingungskorrekturen und thermischen Korrekturen untersucht, um das Modell mit den experimentellen Hochtemperaturmessungen vergleichbar zu machen. Die berechneten Migrationsenthalpien stimmen gut mit den experimentellen Ergebnissen für NaCl, KCl und KBr überein, und die Barriere für NaBr wird vorhergesagt. Zudem korrelieren die Barrieren mit der fundamentalen Schwingungsmode der primitiven Einheitszellen der jeweiligen Alkalihalogenide. Die Wanderung entlang der (100)-Oberfläche wird simuliert, und es wird festgestellt, dass die Wanderungsbarriere aufgrund der erniedrigten Symmetrie geringer ist als für die Wanderung durch den Festkörper. Die elektronische Struktur und die Geometrie der Übergangszustände werden ermittelt, und es wird festgestellt, dass die Delokalisierung des Defektelektrons im Übergangszustand zu einem Selbstwechselwirkungsfehler in der Größenordnung $0.2 - 0.4\,\mathrm{eV}$ führt, welcher eine Beschreibung durch DFT

auf Hybridniveau erforderlich macht.

Kapitel fünf beschäftigt sich mit der Aktivierung und der Reaktivität von molekularem Stickstoff im F-Zentrum auf der (100)-Oberfläche von NaCl und KCl. Der Defekt reduziert das Stickstoffmolekül und aktiviert dessen Dreifachbindung für eine Reaktion mit Wasserstoff. Die dafür erforderliche Reaktionsbarriere ist auf dem Defekt deutlich geringer als in der Gasphasenreaktion. Der Transfer des Defektelektrons vom F-Zentrum in das niedrigste unbesetzte Molekülorbital (LUMO) des Stickstoffs stellt die treibende Kraft hinter der gesteigerten Reaktivität dar, während die Oberfläche eine zusätzliche Stabilisierung der Übergangszustände und Zwischenzustände bewirkt.

In Kapitel sechs wird die Aktivierung und Hydrierung von Kohlenmonoxid und Kohlendioxid auf dem F-Zentrum von KCl untersucht. Der Defekt reduziert alle kohlenstoffhaltigen Edukte, Produkte und Zwischenprodukte der Hydrierung, indem er ihre LUMOs besetzt, und er schwächt ihre Bindungen für die Reaktion mit Wasserstoff. Die thermodynamischen und kinetischen Eigenschaften aller Reaktionsschritte werden berechnet, wobei sich herausstellt, dass die Barrieren für die Hydrierung auf dem Defekt deutlich niedriger sind als in der Gasphasenreaktion. Die berechnete Reaktionsgeschwindigkeit ist vergleichbar mit der Reaktionsgeschwindigkeit, die für den herkömmlichen Kupferkatalysator gemessen wurde. Die homolytische Spaltung der Zwischenprodukte Ameisensäure, Wasser und Methanol werden untersucht und es wird festgestellt, dass sie die Methanolsynthese auf dem F-Zentrum hemmen.

In Kapitel sieben werden die Auswirkungen einer Kupferdotierung des F-Zentrums auf der KCl-(100)-Oberfläche untersucht. Es zeigt sich, dass das Metallatom stark mit dem Defekt wechselwirkt und dessen elektronische Struktur von einem offenschaligen Zustand in einen geschlossenschaligen Zustand umwandelt. Der dotierte Defekt stabilisiert immer noch die Adsorbate CO, H_2CO, und CH_3OH, jedoch dissoziiert er Methanol nicht zu Methan. Anschließend wird die Reaktion der Adsorbate mit Wasserstoff untersucht, und zweifach hydriertes Kupfer, HCuH, wird als ein thermodynamisch stabilerer Zustand identifiziert als ein einzelnes Kupferatom im Defekt. Diese Zwischenstruktur katalysiert die Synthese von Methanol in einer schrittweisen, kupfervermittelten Wasserstoffaddition. Die kinetischen Eigenschaften dieser Reaktion werden mit einer kinetischen Monte Carlo Simulation analysiert. Das Ergebnis ist eine Reaktionsgeschwindigkeit, die die Reaktionsgeschwindigkeit im leeren Defekt und auf dem herkömmlichen Katalysator um mehrere Größenordnungen übertrifft.

In der Zusammenfassung und dem Ausblick werden die Ergebnisse dieser Arbeit zusammengefasst und bewertet, in welcher Weise sie die Grundlage für die zukünftige Forschung zu den physikalischen, chemischen und katalytischen Eigenschaften defekter Alkalihalogenide und elektronisch ähnlicher Systeme bilden. Insbesondere das kupferdotierte F-Zentrum stellt einen vielversprechenden Kandidaten für katalytische Hydrierungen dar.

Contents

Introduction

Catalysis is one of the most important fields of contemporary chemistry, as it is an indispensable asset for the efficient large-scale production of substances like methanol, ammonia, and their derivatives, which is in the order of several hundred million tons per year as it enables and facilitates kinetically hindered reactions.[1, 2] The topic is divided into homogenous catalysis, in which the catalyst is in the same phase as the reactants, and heterogeneous catalysis, which takes place at the phase boundary between catalyst and reactants and is the focus of this work.[3, 4]

Catalysts come in all shapes and forms, and even the same reaction can be catalyzed in different ways. This is notably the case for the first reaction examined in this work, the hydrogenation of nitrogen. Thanks to its apolarity, stable triple bond, and low boiling point, the nitrogen molecule has become the most abundant component in the Earth's atmosphere, comprising about 70% of it. Yet, the element nitrogen is also an essential component of amino acids and nucleobases, which are the fundamental building blocks of life, meaning that any reaction from the gaseous to its bound form has to overcome the second-strongest covalent bond in chemisty.[5] This results in reaction barriers in the range of $4-6\,\text{eV}$,[6, 7] so the assistance of a catalyst is required to make the reaction thermodynamically feasible. In nature, this task is taken over by a class of enzymes called nitrogenases,[8–10] which carry out the reaction in alternating steps of protonation and single-electron reduction in aqueous solution at room temperature. In the industry, the Haber–Bosch process is the method of choice to react molecular hydrogen and nitrogen via homolytic cleavage of the molecules on iron.[6, 11–13] Developed at the beginning of the 20th century,[11, 12] this process is indispensible for the production of nitrogen-based fertilizers, but it suffers from a huge energy usage of 1-2% of the worldwide annual energy production due to the high temperatures of $700-800\,\text{K}$ and pressures of $50-200\,\text{bar}$ required for the reaction. The reaction also consumes 3-5% of the annual natural gas production to generate the required amounts of hydrogen,[14] but it remains without a reasonable alternative to date. Hence, there is plenty of research for alternative catalysts to reduce the energy requirements, with the most promising candidate currently being an electride-assisted reductive ruthenium catalyst.[15, 16]

The other reaction investigated in this work is the hydrogenation of carbon monoxide and carbon dioxide. In this case, the choice of catalyst determines the final product based on the same reagents. Copper-based catalysts lead to the synthesis of methanol, as employed in the industrial methanol synthesis with CO/CO_2,[17] but nickel-based catalysts yield a complete reduction to methane, as utilized in the Sabatier process with CO_2.[18] The former is an industrially crucial process with an annual production of above 100 million tons of methanol,[2] which is the focus in this work, while

the latter is a crucial reaction in the methaniation of the greenhouse gas carbon dioxide to synthetic natural gas for the generation of carbon neutral fuels.[19]

The current catalysts used for the synthesis of methanol are still based on the original copper/zinc oxide catalyst first developed in 1966.[17] Although they feature additional oxides such as MgO, Al_2O_3, or SiO_2 to improve stability during synthesis, the general chemistry and overall reaction rates for modern catalysts have remained the same, requiring high temperatures of ~ 500 K and high pressures of ~ 50 bar to operate, which has led to extensive research into optimizing and improving the catalyst.[17, 20–29]

Since the use of catalysis is so widespread and crucial for modern life, the search for cheaper, more efficient, more stable, and less toxic catalysts is just as important as understanding already established catalysts, as many reactions still rely on expensive nobel metals like platinum, ruthenium, or iridium or on toxic compounds like osmium-(VIII)-oxide and numerous organometallic molecules. For most of the 20th century, this research was limited to experimental investigations, but thanks to the increasing computational power of computers and the development of efficient quantum chemical methods such as density functional theory (DFT) or domain based local pair-natural orbital singles and doubles coupled cluster theory with perturbative triples (DLNPO-CCSD(T)),[30] the field of theoretical chemistry has become a powerful tool to predict the properties of prospective catalytic materials and analyze reaction mechanisms to further facilitate research.[31–37]

In the wake of this development, this work shines a light on a group of crystalline substances that are generally not known for their heterogeneous catalytic activity, namely the alkali halides, e.g., halite (NaCl, rock salt) and sylvite (KCl, potash salt). These compounds are readily accessible in large underground deposits or in ocean water and are largely non-hazardous to human and environmental health, making them cheap and sustainable reagents, but they are also almost completely inert in their pristine solid state due to their wide band gap.[38] However, the introduction of defects into their lattice significantly changes their electronic structure, potentially activating their surface and turning them into catalytically active materials.

Generally, there exists a wide range of crystallographic defects.[39] There are two-dimensional planar defects like grain boundaries, which occur at the interface between crystals, or stacking faults, where repeating atom layers are stacked in the wrong order, and one-dimensional line defects like edge dislocations and screw dislocations, where a plane of atoms in the lattice terminates within the bulk. The simplest defects are zero-dimensional point defects, which are centered around a single lattice point, e.g., vacancy defects such as Schottky defects, where some lattice sites are left unoccupied, substitutions with atoms of other elements, and interstitial defects such as Frenkel defects, where an atom leaves its lattice site and moves to a site between the regularly occupied lattice positions.

Of those, the F center is a particularly promising candidate for chemical activity, because it is composed of a single electron that replaces a halide ion in the alkali halide lattice,[40] which is much more mobile than the ion. Named after its ability to tint the otherwise transparent crystals (F stands for "Farbe", engl. color), it occurs naturally or can be introduced via heating, irradiation, additive coloring, or electrolysis. The physical properties of the defect have been investigated experimentally in extensive detail, from their formation process [41–48] and their response to pressure [49, 50] to their interaction with electromagnetic radiation [51–64] and their diffusion behavior.[65–72]

On the other hand, the chemical potential of the F centers has only been studied in a few experimental works about the dissociation of water [73, 74] and the reduction of adsorbed salicylic acid.[75, 76] And although there exists ample of theoretical work on the alkali halides F centers in the bulk of LiF and NaCl [77–84] and other systems,[85, 86], only a handful investigated the defect on the surface and

its interaction with adsorbates,[84, 87–89] corroborating the findings for salicylic acid and indicating that the defect acts as a strong local reducing agent.

In continuation of these studies, this work seeks to deepen the theoretical understanding of the physical properties of the F center and explore its chemical properties in closer detail, investigating the influence of the defect on reactions of small adsorbed molecules.

First, the electronic properties of the alkali halides NaCl, KCl, NaBr, and KBr and their F centers are assessed in chapter 3. Employing the theoretical multi-level approach introduced in [89], an optimization with the GGA-functional PBE [90] followed by a single-point calculation with a self-consistent dielectric-dependent global hybrid, the dielectric constant, the band gap, the conduction band minimum, and the valence band maximum of the pristine alkali halides are evaluated and compared to experimental references. Next, the band structures of the defective alkali halides are calculated and the electronic properties of the F center are characterized and examined for similarities, trends, and differences between the different structures. In the final section, the simplest defect agglomeration, the M center, is explored. Composed of two directly adjacent F centers, it is a natural side product of their generation and a potential candidate for optical information storage systems [91, 92] that was extensively investigated in experiments.[93–102].

Chapter 4 is about the mobility of the F center in the bulk and across the (100) surface of the same set of alkali halides, which is relevant for understanding the dynamic properties of the defect and its potential ramifications for its interaction with adsorbed molecules and its catalytic activity. Moreover, the results are evaluated in a comparison with experimental data on the F center migration in alkali halides,[65–72] and the relevance of electronic and thermal effects is investigated.

After establishing the theoretical framework and basic understanding of the properties of the F center, the methodology is employed to investigate the hydrogenation of nitrogen on the defective KCl (100) surface in chapter 5. This reaction is not only of great significance for contemporary chemistry, as mentioned above, but it is also a perfect model system for studying the catalytic capabilites of the alkali halide F center, because it consists of small molecules that can react only in a limited range of reactions. First, the interaction of N_2 with the F center is evaluated, before the reaction with H_2 toward hydrazine is modeled and calculated based on the two reaction paths found in the gas-phase reaction to examine the strength and nature of a catalytic effect. In addition, parts of these calculations are repeated on NaCl to check the similarities and differences between the KCl and NaCl F centers with respect to their chemical capabilities.

Chapter 6 is about the hydrogenation of the gaseous carbon oxides on the defective KCl (100) surface, which is another set of reactions chosen for their model simplicity, relevance in contemporary chemistry, and the fact that neither of them takes place without a catalyst. The interaction of the various reagents, intermediates, and products with the F center is evaluated, and the reactions from CO and CO_2 to methanol are calculated and evaluated regarding their thermodynamic and kinetic properties. Finally, interfering side reactions are investigated and the results are compared to the gas-phase reaction and the performance of conventional copper catalysts.

In chapter 7, the KCl F center is doped with a copper atom to examine the effect of doping on the reductive behavior and catalytic effect regarding the hydrogenation of carbon monoxide to methanol. The interaction with all relevant reactants is examined, and the reaction diagram of the hydrogenation is investigated until complete reduction to methane. The theoretical performance of the copper-doped F center as catalyst is then simulated and compared to the empty F center and industrial catalysts.

Finally, the results of this thesis are summarized in chapter 8, based on which the future chemical and catalytic potential of the alkali halide F centers is evaluated.

Theoretical Background

In this chapter, the theoretical foundations for this thesis are explained on the base of literature and lectures on quantum chemistry,[103–105], ranging from the quantum mechanical description of many-particle systems to solid-state theory and statistical mechanics.

2.1 Many-Body Wave Function

The most fundamental problem quantum chemistry seeks to solve is the Schrödinger equation of a system composed of M nuclei and N electrons, which in its time-independent, non-relativistic form is described by

$$\hat{\mathbf{H}}\Psi(\vec{r}, \vec{R}) = E\Psi(\vec{r}, \vec{R}) \tag{2.1}$$

where the Hamilton operator $\hat{\mathbf{H}}$ is applied to the wave function Ψ of the system to yield its total energy E. $\hat{\mathbf{H}}$ for a system of M nuclei A and B at the positions $\vec{R}$ and N electrons i and j at the positions $\vec{r}$ can be written as

$$\hat{\mathbf{H}} = -\sum_{i=1}^{N} \frac{\nabla_i^2}{2} - \sum_{A=1}^{M} \frac{\nabla_A^2}{2M_A} - \sum_{i=1}^{N}\sum_{A=1}^{M} \frac{Z_A}{r_{iA}} + \sum_{i=1}^{N}\sum_{j>i}^{N} \frac{1}{r_{ij}} + \sum_{A=1}^{M}\sum_{B>A}^{M} \frac{Z_A Z_B}{R_{AB}} \tag{2.2}$$

$$= \hat{\mathbf{T}}_{\mathrm{N}} + \hat{\mathbf{T}}_{\mathrm{e}} + \hat{\mathbf{V}}_{\mathrm{NN}} + \hat{\mathbf{V}}_{\mathrm{eN}} + \hat{\mathbf{V}}_{\mathrm{ee}}$$

where $\hat{\mathbf{T}}$ are the kinetic operators and $\hat{\mathbf{V}}$ the potential operators of the nuclei and electrons. Their mass is considered by the mass ratio M_A between the nucleus A and the electron mass m_{e} and the charge of A is reflected by Z_A.

Equation 2.2 can be further simplified via the application of the Born–Oppenheimer approximation [106]. Since the mass of the nuclei is at least three orders of magnitude greater than that of the electrons, their motion can be separated as the movement of the nuclei is effectively frozen compared to the movement of the electrons. Consequently, the kinetic energy of the nuclei can be neglected, their interaction treated as a Coulomb repulsion between point charges at fixed positions, and the Coulomb attraction to the electrons is simplified.

$$\hat{\mathbf{H}}_{\mathrm{BO}} = -\sum_{i=1}^{N} \frac{\nabla_i^2}{2} - \sum_{i=1}^{N}\sum_{A=1}^{M} \frac{Z_A}{r_{iA}} + \sum_{i=1}^{N}\sum_{j>i}^{N} \frac{1}{r_{ij}} + \sum_{A=1}^{M}\sum_{B>A}^{M} \frac{Z_A Z_B}{R_{AB}} \tag{2.3}$$

The many-body wave function Ψ can be approximated as a Slater determinant of N orthonormal single-electron spin orbitals $\chi_i(q_i)$ as

$$\Psi(1, 2, \ldots, N) = \frac{1}{\sqrt{N!}} \begin{vmatrix} \chi_1(q_1) & \chi_2(q_1) & \cdots & \chi_N(q_1) \\ \chi_1(q_2) & \chi_2(q_2) & \cdots & \chi_N(q_2) \\ \vdots & \vdots & \ddots & \vdots \\ \chi_1(q_N) & \chi_2(q_N) & \cdots & \chi_N(q_N) \end{vmatrix} \tag{2.4}$$

with $q_i(i = 1, \ldots, N)$ being the spatial and spin coordinates of electron i. This ansatz inherently fulfills the basic requirements of a fermionic wave function, which consist of its anti-symmetry and the Pauli principle.

2.2 Density Functional Theory

One way to numerically approximate the solution of the many-body Schrödinger equation is the density functional theory (DFT). According to the equations by Hohenberg and Kohn,[107] it links the electron density ρ of a quantum mechanical system to its ground state energy E_0 via a functional F. This formulation replaces the many-body problem by an effective one-electron density, which only depends on the spatial coordinates and the number N of electrons in the system.

2.2.1 Hohenberg–Kohn Theorems

The relationship of ρ and E_0 is specified by the two theorems by Hohenberg and Kohn. The first theorem shows that it is possible to calculate the exact ground state energy from the electron density with the exact functional F_{exact},

$$E_0 = F_{\text{exact}}\left[\rho_0\right] \tag{2.5}$$

The second theorem applies the variational principle by Rayleigh and Ritz [108, 109] to the first theorem, stating that any valid test density yields an energy larger or equal to the ground state energy, according to

$$E_0 \leq F_{\text{exact}}[\rho_{\text{test}}(\vec{r})] \tag{2.6}$$

This circumstance makes numerical convergence to the true density possible. The exact functional F_{exact} is not yet known, but there are various approximations to it.

2.2.2 Kohn–Sham Equations

The energy functional E_{KS} can be composed of terms similar to the Hamilton operator in equation 2.2 as

$$E_{KS}[\rho(\vec{r})] = T_{\text{e}}[\rho(\vec{r})] + V_{\text{NN}} + V_{\text{eN}}[\rho(\vec{r})] + J[\rho(\vec{r})] + E_{xc}[\rho(\vec{r})] \tag{2.7}$$

where J is the classical Coulomb interaction of the electrons and E_{xc} an expression containing all non-classical exchange and correlation interactions.

DFT does not require orbitals to calculate the energy from the electron density, but it can only approximate the kinetic energy T_{e} and the exchange correlation term E_{xc}. Unfortunately, T_{e} represents a large part of the total energy, and purely density-based functionals struggle to describe it with sufficient

accuracy. To address this, Kohn and Sham introduced orbitals to DFT, which is denoted as Kohn–Sham density functional theory (KS-DFT). This allows the exact calculation of the non-interacting part of the kinetic energy T_{KS}, which accounts for the largest share of T_e. The remainder T_c, which is based on the correlation of the electrons, is consequently merged into the exchange correlation term E_{xc}.

The density ρ is obtained as the integral of the squared all-electron KS wave function Φ_e as

$$\rho(\vec{r}) = N \int |\Phi_e(\vec{r}_2, \cdots, \vec{r}_N)|^2 d\vec{r}_2 \cdots d\vec{r}_N \tag{2.8}$$

Analogous to equation 2.4, Φ_e is composed as a Slater determinant of the KS orbitals $\phi_i(\vec{r})$.

Similarly, the one-electron Schrödinger equation for KS-DFT is based on the Kohn–Sham orbitals instead of the electron density, yielding the Kohn–Sham equation

$$\left\{ -\frac{1}{2}\nabla_i^2 - \sum_A^M \frac{Z_A}{|\vec{r} - \vec{R}_A|} + \int \frac{\rho(\vec{r}\prime)}{|\vec{r} - \vec{r}\prime|} + V_{xc}(\vec{r}) \right\} \phi_i(\vec{r}) = \varepsilon_i \phi_i(\vec{r}). \tag{2.9}$$

where V_{xc} is the exchange correlation potential containing all approximations, and ε_i is the energy of orbital ϕ_i.

2.2.3 Exchange-Correlation Functionals

Whereas the exact exchange-correlation functional remains unknown, many approximations to it have been developed over the course of time. The quality of the various functionals usually correlates with computational effort, but unlike methods from wave function theory, they cannot be systematically improved. Yet, they can be divided into different classes depending on their complexity. The most common subdivision is called Jacob's ladder after Perdew and Schmidt,[110], and in the following, its rungs are depicted in ascending order of complexity. The simplest functionals are based on LSDA (**L**ocal **S**pin **D**ensity **A**pproximation) for open-shell calculations and LDA for closed-shell calculations. These functionals assume that the gradient of the electron density is sufficiently small that the exchange and correlation at each point of the system can be approximated by the homogeneous electron gas. In this case, the electron exchange energy E_x for a given density ρ is analytically known as

$$E_x^{\text{LDA}}[\rho] = \int \rho(\vec{r})\epsilon_x(\rho(\vec{r}))d\vec{r} \tag{2.10}$$

with the exchange term ϵ_x amounting to

$$\epsilon_x = -\frac{3}{4}\left(\frac{3}{\pi}\right)^{\frac{1}{3}} [\rho(\vec{r})]^{\frac{1}{3}}. \tag{2.11}$$

The correlation energy E_c is obtained as a numerical fit of a quantum Monte Carlo simulation of the homogeneous electron gas.

By their nature, LD(S)A functionals are a sufficient approximation for homogeneous systems like metals, but they exhibit shortcomings in describing the geometry and electronic structure of more complex systems. The local inhomogeneity of their electron density can be taken into account by considering the gradient of the density, and the type of approximation utilizing this approach is called

generalized gradient approximation (GGA). The corresponding functionals scale the exchange of the homogeneous electron gas with a factor $F(s)$ according to

$$\epsilon_x^{\mathrm{GGA}}[\rho] = \epsilon_x^{\mathrm{LDA}} F(s) \tag{2.12}$$

where the scaling factor depends on the dimensionless density gradient s,

$$s = \frac{|\nabla \rho|}{2(3\pi^2)^{\frac{1}{3}} \rho^{\frac{4}{3}}} \tag{2.13}$$

In the case of the GGA-functional PBE [90], which is applied extensively in this thesis, $F(s)$ depends on two parameters κ and μ according to

$$F^{\mathrm{PBE}}(s) = 1 + \kappa - \frac{\kappa}{1 + \mu s^2 / \kappa}. \tag{2.14}$$

Both parameters are derived from physical considerations based on model systems.

The next rung on the Jacob's ladder consists of the meta-GGA functionals, which also take the second derivative of the electron density into consideration. Apart from a generally more accurate calculation of the exchange energy, it also allows the kinetic energy density

$$\tau_\sigma(\vec{r}) = \sum_i^{occ} \frac{1}{2} \left| \nabla \Phi_e(\vec{r}) \right|^2 \tag{2.15}$$

of the occupied Kohn–Sham orbitals Φ_e to be fully considered. Two prominent representatives of this rung are TPSS [111] and SCAN [112].

All functionals up to this point are impeded by the fact that KS-DFT reduces the information contained in the many-electron wave function as it maps it to the electron density. This approximation breaks down the moment the interaction of an electron with itself is considered, because the electron density makes it impossible to distinguish electrons and a functional consequently yields Coulomb repulsion where it should be zero. Hence, this error is called self-interaction error (SIE). One way to address this inadequacy is to replace a fraction α of a functional's exchange with exact Fock exchange E_x^{F}, obtained as two-electron integral based on the KS orbitals ϕ_i according to

$$E_x^{\mathrm{F}} = -\frac{1}{2} \sum_{i,j} \iint \phi_i^*(\vec{r}_1) \phi_j^*(\vec{r}_2) \frac{1}{r_{12}} \phi_j(\vec{r}_1) \phi_i(\vec{r}_2) d\vec{r}_1 d\vec{r}_2. \tag{2.16}$$

The resulting functional is called hybrid functional, which in its most basic shape is defined as

$$E_{xc}^{\mathrm{hyb}} = E_c^{\mathrm{GGA}} + (1 - \alpha) E_x^{\mathrm{GGA}} + \alpha E_x^{\mathrm{F}}. \tag{2.17}$$

A particular hybrid functional employed in this thesis is PBE0,[113] which is based on the GGA functional PBE, with 25 % exact exchange. For solid state insulators, there exists a physical relationship between the exact exchange fraction α and the static dielectric constant ϵ_∞ of the system, described by Skone et al. [114] as

$$\alpha = \frac{1}{\epsilon_\infty}. \tag{2.18}$$

α can be calculated from experimental data for ϵ_∞, or alternatively be obtained from first principles based on density functional second-order perturbation theory [115, 116]. In this work, this was done in a self-consistent manner until a convergence of $\Delta\alpha < 0.1\%$ was reached. The resulting hybrid functional is a self-consistent dielectric-dependent global hybrid (sc-DDGH), and the one used in this thesis is denoted as sc-PBE0, since it is based on PBE0.

2.2.4 Dispersion Correction

In addition to the self-interaction error, the London dispersion forces are another significant non-local interaction which are insufficiently described by density functional theory. As a consequence of the fluctuating electron distribution in a system, they pertain to the correlated interactions and can be described by post-Hartree–Fock methods or approximated by a correction scheme like the D3(BJ)-correction by Grimme et al. [117, 118]

This method is based on the pairwise interaction of a system's M nuclei A, B according to

$$E_{\text{disp}}^{D3(BJ)} = -\frac{1}{2} \sum_{A,B}^{M} \sum_{n=6,8} s_n \frac{C_n^{AB}}{r_{AB}^n + \left[f(r_{AB}^0) \right]^n} \tag{2.19}$$

where R_{AB} is the distance between the nuclei, C_n represents the average dispersion coefficient of the nth order, and s_n is the functional-dependent scaling factor. The dispersion coefficient of the sixth order C_6 is obtained from the Casimir–Polder equation

$$C_6^{AB} = \frac{3}{\pi} \int_0^\infty \alpha^A(i\omega)\alpha^B(i\omega)d\omega \tag{2.20}$$

in which α and β are the averaged dipole polarizabilities at frequency ω. In practice, the coefficient is computed with TD-DFT calculations for model hydrides of all elements. C_6 of the real system is then calculated by mapping the geometric coordination number of the nuclei to the model system values and interpolating or extrapolating the coefficient accordingly.

C_8 is computed from C_6 according to

$$C_8^{AB} = 3C_6^{AB}\sqrt{Q^A Q^B} \tag{2.21}$$

with Q depending on the multipole-type expectation values the nuclear charge of their respective nuclei.

For small distances, D3 shows an unphysical singularity. This is counteracted by the additional damping term $f(r_{AB}^0)$, whose function was proposed by Becke and Johnson [118] as

$$f(r_{AB}^0) = a_1 R_{AB}^0 + a_2 \tag{2.22}$$

with

$$R_{AB}^0 = \sqrt{\frac{C_8^{AB}}{C_6^{AB}}} \tag{2.23}$$

and the empirically fitted parameters a_1 and a_2.

2.3 Solid State Quantum Chemistry

In its ideal configuration, a crystalline solid can be described as a three-dimensional, infinite arrangement of atoms composed of repeating lattice points. These points are indistinguishable from each other and are related by lattice vectors $\vec{T}$. Accordingly, neighboring lattice points are linked through basis vectors $\vec{a}$ as

$$\vec{T} = \sum_{i=1}^{3} n_i \vec{a}_i, n_i \in \mathbb{Z}, \tag{2.24}$$

generating a network of the smallest periodically repeating parallelepipeds, called primitive unit cells (PUC). However, in crystallographic terms, the conventional unit cell (CUC) is usually of greater interest, since it contains the entire symmetry of the crystal. The CUC is composed of one to four lattice points and belongs to one of 230 space groups.

Positions inside the unit cell are represented by $\vec{f}$, which are constructed from the basis vectors $\vec{a}$ and fractional coordinates u as

$$\vec{f} = \sum_{i=1}^{3} u_i \vec{a}_i, u_i \in \mathbb{R} \tag{2.25}$$

Unlike a notation in Cartesian coordinates, these are independent of the size and shape of the unit cell.

For the quantum-chemical description of a periodic solid, it is often necessary to use a reciprocal lattice with the basis vectors b. These are related to a via

$$\vec{b}_i \cdot \vec{a}_j = 2\pi \delta_{ij},$$
$$\vec{b}_k = 2\pi \frac{\vec{a}_j \times \vec{a}_i}{V}, i, j, k \in 1, 2, 3 \tag{2.26}$$

where V is the volume of the PUC and δ_{ij} the Kronecker delta. Analogous to the real basis vectors, the reciprocal lattice vectors $\vec{b}$ produce a reciprocal lattice vector $\vec{G}$ via

$$\vec{G} = \sum_{i=1}^{3} m_i \vec{b}_i, m_i \in \mathbb{Z}. \tag{2.27}$$

Similarly, a general position in reciprocal space is given by the vector $\vec{k}$,

$$\vec{k} = \sum_{i=1}^{3} k_i \vec{b}_i, k_i \in \mathbb{R}. \tag{2.28}$$

Instead of a parallelepiped, the reciprocal unit cell consists of the first or irreducible Brillouin zone (IBZ). It is constructed as a Voronoi cell around the origin of the reciprocal lattice, which terminates halfway to the adjacent lattice points. Its real-space counterpart is called the Wigner–Seitz cell.

2.3.1 Bloch's theorem

Due to the periodicity of the infinite crystal, the electrons experience a similarly periodic nuclear attraction V, which repeats with $\vec{T}$ as

$$V(\vec{r}) = V(\vec{r} + \vec{T}). \tag{2.29}$$

Because of the translational symmetry of the system, the translational operator $\hat{T}$ commutes with the Hamilton operator, yielding a common eigenbasis. Consequently, every periodically repeated section of the wave function $\phi(\vec{r} + \vec{T})$ can be separated into a phase factor and the wave function in the origin cell as follows

$$\phi(\vec{r} + \vec{T}) = e^{i\vec{k}\cdot\vec{T}} \phi(\vec{r}). \tag{2.30}$$

Equation 2.30 is the fundamental result of Bloch's theorem.

On this basis, the eigenfunctions of the Hamilton operator can be constructed as the product of a plane wave $e^{i\vec{k}\cdot\vec{r}}$ and a lattice-periodic function u_k,

$$\phi^{\vec{k}}(\vec{r}) = e^{i\vec{k}\cdot\vec{r}} u_k(\vec{r}) \tag{2.31}$$

to obtain the so-called Bloch functions.

The crystal wave function consists of crystal orbitals $\varphi_a^{\vec{k}}$, which are obtained as a linear combination of Bloch functions $\phi_a^{\vec{k}}$ according to

$$\varphi_a^{\vec{k}}(\vec{r}) = \sum_\mu c_{\mu a}^{\vec{k}} \phi^{\vec{k}}(\vec{r}). \tag{2.32}$$

The nature of the lattice-periodic function u_k (equation 2.31) is dependent on the choice of basis set. It can consist of atom-centered atomic orbitals like in the solid-state program package CRYSTAL [119], or of atom-independent plane waves of the general shape

$$u_{\vec{G}}(\vec{r}) = e^{i\vec{G}\cdot\vec{r}} \tag{2.33}$$

determined by the reciprocal lattice vector $\vec{G}$, as defined in equation 2.27.

The basis set is truncated through E_{cut}, which limits $\vec{G}$ according to

$$E_{\text{cut}} \geq \frac{1}{2} \left| \vec{G} \right|^2. \tag{2.34}$$

The choice of E_{cut} is usually tied to convergence criteria related to the total energy, geometry, or electronic structure of the system.

2.3.2 Born–von Kármán Boundary Conditons

So far, the crystal was assumed to be perfect and infinitely extended. However, the description of such a system is not possible in practice, and a truncation has to be made in a way that maintains the translational invariance of the crystal. This condition is fulfilled by the boundary conditions proposed by Born and von Kármán for a large part of the crystal, the *main region*,

$$\phi(\vec{r}) = \phi(\vec{r} + N_i \vec{a}_i), i \in 1, 2, 3, N_i \in \mathbb{N}. \tag{2.35}$$

containing N unit cells in all three dimensions of the lattice N_i being

$$N = \prod_{i=1}^{3} N_i. \tag{2.36}$$

Applying these periodic boundary conditions to the Bloch functions yields

$$\phi(\vec{r} + N_i \vec{a}_i, \vec{k}) = e^{i\vec{k}\cdot N_i \vec{a}_i} \phi(\vec{r}, \vec{k}) \tag{2.37}$$

on the condition that $e^{i\vec{k}\cdot N_i \vec{a}_i} = 1$. This is given by

$$e^{i\vec{k}\cdot N_i \vec{a}_i} = e^{i\Sigma_{j=1}^{3} k_j \vec{b}_j \cdot N_i \vec{a}_i} = e^{i\Sigma_{j=1}^{3} k_j 2\pi \delta_{ij} N_i} = e^{i2\pi k_i N_i} = 1. \tag{2.38}$$

This restricts the set of all wave vectors $\vec{G}$ (equation 2.27) to a subset of allowed wave vectors $\vec{\kappa}$, which are limited as follows

$$\vec{\kappa} = \sum_{i=1}^{3} \frac{2\pi m_i}{N_i} \vec{b}_i, m_i \in \mathbb{Z}. \tag{2.39}$$

The overall number of $\vec{\kappa}$ is still infinite, but the phase vectors in equation 2.38 are 2π-periodic, which makes it possible to limit the choice of m_i to the interval $[0, 1]$ or $[-\frac{1}{2}, \frac{1}{2}]$ corresponding to the irreducible Brillouin zone (IBZ).

2.3.3 Monkhorst–Pack Grid

One way to implement the Born–von Kármán boundary conditions in practice is the Monkhorst–Pack grid [120, 121]. It subdivides the reciprocal lattice vectors $\vec{b}_i$ with the shrinking factors s_i into even sections

$$\frac{\vec{b}_1}{s_1}, \frac{\vec{b}_2}{s_2}, \frac{\vec{b}_3}{s_3}. \tag{2.40}$$

This truncates the amount of allowed wave vectors, determining the number of κ-points considered within the IBZ. Symmetry equivalent points on the boundaries of the IBZ are weighted accordingly.

2.4 Thermodynamics and Kinetics

The electronic energies E_0 obtained from a quantum chemical calculation cannot directly be correlated with experimental results. They need to be augmented with thermodynamic contributions to obtain the system's enthalpy H, entropy S, and Gibbs free energy G, which can be compared to measurements. The Gibbs free energy G, which is the most relevant quantity for reaction kinetics, is computed from the enthalpy H and the entropy S at a given temperature T according to

$$G(T) = H(T) - TS(T). \tag{2.41}$$

The enthalpy H herein is calculated as

$$H(T) = U(T) + pV \tag{2.42}$$

where U is the inner energy, p is the pressure, and V the volume assumed by the system. Approximately, the latter term for pV is close to 0 for the solid state and derived from the ideal gas law for the gas phase

$$pV = nRT \tag{2.43}$$

where n is the molar amount of substance and R the ideal gas constant. The inner energy U is finally obtained from the electronic energy E_0, the zero-point vibrational energy E_{ZPVE}, and the various thermal contributions E_T:

$$U(T) = E_0 + E_{ZPVE} + E_T(T) \tag{2.44}$$

For gas-phase molecules, E_{ZPVE} and $E_T(T)$ are calculated in the RRHO-approximation with a frequency calculation as implemented in the ORCA program package [122–124]. For the solid state and the adsorbed molecules, the thermal contributions are obtained in a similar fashion with a frequency calculation with VASP. Using the method of finite differences [125], the frequencies ω are obtained in the harmonic approximation via the diagonalized, mass-weighted Hesse matrix. The results of the frequency calculation help to distinguish not fully converged structures from local minima, which contain no imaginary frequencies, and transitions states, which contain one imaginary frequency. Furthermore, the frequencies can be used to calculate the thermal corrections and the entropy S according to eqns. 2.45 and 2.46 from statistical mechanics, respectively.

$$E_{ZPVE} + E_T(T) = h\omega_i \sum_{i=1}^{N} \left(\frac{1}{2} + \frac{1}{e^{\frac{h\omega_i}{k_B T}} - 1} \right) \tag{2.45}$$

$$S(T) = k_B \sum_{i=1}^{N} \left(\frac{h\omega_i}{k_B T e^{\frac{h\omega_i}{k_B T}} - 1} - \ln\left(1 - e^{\frac{h\omega_i}{k_B T}}\right) \right) \tag{2.46}$$

Due to the singularity of the harmonic entropy for low frequencies, an approximation proposed by Ribeiro et al. [126] was introduced in which all frequencies smaller than $100\,\mathrm{cm}^{-1}$ were shifted to $100\,\mathrm{cm}^{-1}$.

For the adsorption of gas-phase molecules, the change of the Gibbs free energy also includes a contribution of the molecular partial pressure p according to

$$E_p(p,T) = k_\mathrm{B} T \ln\left(\frac{p}{p^0}\right) \tag{2.47}$$

where the reference pressure p^0 is set to 1 bar.

With the Gibbs energy of the ground states and transition states, the kinetic properties of the corresponding reactions can be computed. The most fundamental quantity of kinetics, the rate constant k, is obtained as

$$k = \frac{k_\mathrm{B} T}{h} e^{\frac{-\Delta G^{\ddagger}}{k_\mathrm{B} T}} \tag{2.48}$$

where $\Delta G^{\ddagger}$ is the energetic difference of the ground state and the transition state. The second fundamental quantity, the equilibrium constant K_eq, quantifies the concentration ratio of two states obtained from their energy difference ΔG as

$$K_\mathrm{eq} = e^{\frac{-\Delta G}{k_\mathrm{B} T}}. \tag{2.49}$$

Alternatively, it is related to the rate constants k and k' for the reaction and corresponding back reaction via

$$K_\mathrm{eq} = \frac{k}{k'}. \tag{2.50}$$

Combined with equation 2.47, they furthermore result in the Langmuir adsorption equation, which yields the relative coverage of a surface θ as

$$\theta = \frac{K_\mathrm{eq} p}{1 + K_\mathrm{eq} p} \tag{2.51}$$

These equations are the foundation for all kinetic calculations in this thesis.

2.4.1 Kinetic Monte Carlo Simulation

The kinetic Monte Carlo (kMC) method is an established method in solid state physics to simulate diffusion and migration processes in the bulk or on the surface. [127–132] In this work, the same method was implemented according to the equations by Voter [133] and employed to simulate a system as it moves from a reagent to a product across a network of reactions, as the fundamental kinetic principles are the same as for a diffusion or migration process. In principle, the Gibbs free activation energy $\Delta G^{\ddagger}_{ij}$ at temperature T is the only property required for the kMC simulation, yielding the corresponding rate constant k_{ij} for a reaction from state i to j as

$$k_{ij} = \frac{k_\mathrm{B} T}{h} e^{-\frac{\Delta G^{\ddagger}_{ij}}{k_\mathrm{B} T}} \tag{2.52}$$

At any ground state i, the total reaction rate $k_{\mathrm{tot},i}$ to all attainable states j is obtained via the sum of all individual reaction rates,

$$k_{\text{tot},i} = \sum_j k_{ij} \tag{2.53}$$

In combination with a uniformly distributed random number r from the interval $(0,1)$, $k_{\text{tot},i}$ determines how long the system remains in state i before it moves to another state according to

$$t_{\text{step}} = -\frac{1}{k_{\text{tot},i}} \ln(r) \tag{2.54}$$

After the time t_{step} elapses, the subsequent state is determined via an evaluation of the normalized reaction rates of all available reaction paths with a probability of

$$p_{\text{ij}} = \frac{k_{ij}}{k_{\text{tot},i}} \tag{2.55}$$

each. This process is either repeated to obtain and quantify the equilibrium of all states involved in the reaction, or it is interrupted once a certain state J is reached and returned to another state I to simulate the turnover frequency from state I to J.

Electronic Properties of the Alkali Halide F and M Center

Michael Häfner[*] and Thomas Bredow[*]

Own manuscript contributions   I wrote the manuscript and performed all calculations and interpretations of the models presented in it. Many ideas and hypotheses featured in this work emerged from discussions with Thomas Bredow, who also contributed corrections to the manuscript for the final publication.

---

[*] Mulliken Center for Theoretical Chemistry, Universität Bonn, Beringstr. 4, 53115 Bonn, Germany
[†] Any request for the permisson to reuse material from this chapter should be directed to the American Physical Society.

To explore the chemical behavior of the alkali halide *F* center, a theoretical methodology is established that accurately describes the electronic properties of the alkali halides and the defects. Based on previous studies,[88, 89] this work employs a multi-level approach with the generalized-gradient approximation (GGA) functional PBE [90] and the dispersion correction D3(BJ) [117, 118] for optimization and the PBE-based dielectric-dependent self-consistent hybrid functional sc-PBE0 for the electronic properties,[114, 134] in combination with a plane-wave method as implemented in the program package VASP.[135–138]

Due to the lack of experimental references for the electronic structure of the alkali halide *F* centers, the methodology is evaluated on the properties of the pristine bulk and (100) surface of NaCl, KCl, NaBr, and KBr. The calculated dielectric constants ϵ_∞ for NaCl, KCl, NaBr, and KBr reproduce the experimental dielectric constants [139] within a 1% error. To enhance the comparability of the calculated band structure with the experiments, the electron-phonon coupling is computed on GGA-level, yielding a result for NaCl that is in line with a previous calculation.[140] For NaCl, the calculated electronic band gap (BG), conduction band minimum (CBM), and valence band maximum (VBM) are within 0.3 eV of the experimental values (literature review [141]), and for KCl, they are within 0.2 eV of the experiments (literature review [89]). For KBr, the results are within 0.2 eV of the averaged experimental results,[142–160] and for NaBr, the results for BG and VBM are within 0.3 eV of the averaged experimental results [144, 148, 151, 154, 157, 158, 160–163], but the CBM deviates by ∼ 0.6 eV. This divergence is likely based on the inconsistencies in the setup of the experimental references and the low amount of data. It is found that the surface band gap undercuts the bulk band gap by 0.1 − 0.6 eV, which is explained with the existence of additional surface states. In summary, the methodology accurately reproduces the electronic properties of all four alkali halides, surpassing the performance of the standard global hybrid PBE0 [113] by 1 − 2 eV.

Calculating the *F* center in bulk, it is found that the electronic structure is qualitatively identical among the four investigated alkali halides. Their defect bands lie 4 − 5 eV above the valence band maximum and 3 − 4 eV below the conduction band minimum. In the case of the α-ladder, the band gap between VBM and CBM is enlarged compared to the pristine bulk because the defect electron destabilizes the unoccupied bands, and in the case of the β-ladder, the band gap between VBM and CBM is diminished because of a favorable interaction between the unoccupied defect band and the conduction band. A strong correlation is found between the inverse lattice parameter and the absolute defect band levels of the surface *F* centers, which is in accordance with the theoretical calculations by Krumhansl and Schwartz and indicates that the defect band level is mostly determined by Coulomb interaction.[164] The strongly localized $1s$-type character of the occupied defect band and the $2p$-type character of the unoccupied excited states of the *F* center are obtained both at GGA-level and scDDGH-level, matching the results of magnetic resonance experiments [40, 52–56, 64] and previous theoretical investigations.[78] The excited states are found to be degenerate in the bulk and split on the surface, according to the lowered symmetry of the defect site, potentially offering a way to measure the *F* center surface concentration.

For KCl, the electronic structure of the *M* center barely differs from the electronic structure of the *F* center. In accordance with experimental observations, the defect electrons of the neighboring cavities have an antiferromagnetic ground state, allowing for excitations that are forbidden in the *F* center. The stability of the *M* center is calculated as −0.3 eV/*M*-center (exp.: −0.2 eV/*M*-center [95]).

In conclusion, the combination of PBE and sc-PBE0 reproduces the electronic properties of the investigated alkali halides within experimental accuracy and qualitatively reproduces the experimental findings for the *F* and *M* center, validating it as a method for the modeling of the defective system.

Mobility of F Centes in Alkali Halides

Michael Häfner[*] and Thomas Bredow[*]

The content of this chapter was reprinted in Appendix B with permission[†] from
Michael Häfner and Thomas Bredow, *Mobility of F Centes in Alkali Halides*, J. Phys. Chem. C **125** (2021) 9085–9095, DOI:10.1021/acs.jpcc.1c00602
Copyright 2021 American Chemical Society.

Own manuscript contributions   I wrote the manuscript and performed all calculations and interpretations of the models presented in it. Many ideas and hypotheses featured in this work emerged from discussions with Thomas Bredow, who also contributed corrections to the manuscript for the final publication.

[*] Mulliken Center for Theoretical Chemistry, Universität Bonn, Beringstr. 4, 53115 Bonn, Germany
[†] Any request for the permisson to reuse material from this chapter should be directed to the American Chemical Society.

To explore the migration behavior of the *F* center, a DFT-based simulation is carried out for NaCl, KCl, NaBr, and KBr, employing the same methodology as in chapter 3. The ground and transition states are computed on GGA and meta-GGA level with the plane-wave program VASP and the nudged elatic band (NEB) method as implemented by Henkelman et al.[165–170] The energy and electronic properties of the states are additionally evaluated with the self-consistent dielectric-dependent hybrid functional sc-PBE0.

First, the migration through the bulk is simulated with PBE,[90] PBE-D3(BJ),[117, 118] PBE-D4,[171, 172] revPBE,[173] SCAN,[174] and SCAN-rVV10.[175] The direct path via the ⟨110⟩ direction with the least amount of symmetry-reduction is identified as the most favorable path for all investigated alkali halides and methods, which is in line with previous calculations [176–178] and indicates that the bulk is too rigid to allow for deviations from the direct path. All functionals yield the same transition state and the same energetic ordering of the migration barrier, NaCl > KCl ≥ NaBr > KBr, matching the ordering of the vibrational frequencies of their respective bulk modes with a high correlation $R^2 > 0.98$. The barrier is predominantly determined by the energy required to locally displace the ions, while the ionic radii, the cohesive energy of the crystal, and the defect formation energies do not have a strong influence on the barrier, indicating that the alkali halides provide an electronically and geometrically very similar environment for the *F* center. The dispersion correction has a negligible influence on the migration barrier, but a comparison between the various functionals shows that the migration process is insufficiently described on GGA and meta-GGA level, as they overstabilize the transition state by $0.2 - 0.4$ eV compared to sc-PBE0. This is in line with theoretical investigations of the similar polaronic migration of V_K centers,[179] and indicates that hybrid functionals are required to describe the *F* center migration. The thermal expansion of the crystals is investigated regarding its influence on the migration barriers to further improve comparability with the experimental diffusion measurements.[65–72] The expansion is approximated via the intrinsic overestimation of the lattice parameter by PBE, PBE-D3(BJ), and revPBE. An effective temperature T_{eff} is assigned to each functional based on a regression with experimental measurements of the thermal expansion,[180–182] and the functional with T_{eff} closest to the temperatures in the diffusion measurements is chosen. Based on this, PBE is selected for KCl and KBr and revPBE is selected for NaCl and NaBr, whereas PBE-D3(BJ) most closely represents the low-temperature structure. The final migration energy is calculated with sc-PBE0, yielding a barrier for the high-temperature model that undercuts the low-temperature model by $0.1 - 0.4$ eV, confirming the relevance of considering the thermal expansion. A local frequency calculation of the ground and transition states is carried out to confirm the validity of the transition states and to obtain the vibrational contributions to the electronic energy, which reduces the migration barriers by another 0.1 eV. The final migration enthalpies match the experimental results for NaCl, KCl, and KBr well within 0.1 eV. For NaBr, where no experimental reference was found, a migration enthalpy of 0.93 eV is predicted. On the (100) surface, the migration energies are smaller than in the bulk by $0.1 - 0.3$ eV, in part due to the lowered symmetry. During the migration, the anion jumps above the neighboring surface cations to switch places with the *F* center. For KCl and KBr, another energetically favorable pathway is found with a descending anion, facilitated by the larger size of the potassium ions compared to the sodium ions. The same findings hold for the descent of the *F* center into the bulk, as calculated for KCl. Thermal expansion simulated for KCl is found to further reduce the migration energies.

In summary, thermal corrections and hybrid functionals are required to describe the *F* center migration due to thermal expansion and the self-interaction error, yielding results that agree well with the experiments, and migration across the surface is more facile than migration through the bulk.

Nitrogen Activation on Defective Potassium Chloride and Sodium Chloride

Michael Häfner[*] and Thomas Bredow[*]

Own manuscript contributions   I wrote the manuscript and performed all calculations and interpretations of the models presented in it. Many ideas and hypotheses featured in this work emerged from discussions with Thomas Bredow, who also contributed corrections to the manuscript for the final publication.

---

[*] Mulliken Center for Theoretical Chemistry, Universität Bonn, Beringstr. 4, 53115 Bonn, Germany

The hydrogenation of nitrogen on the F center is explored with the methodology introduced in chapter 3. The gas phase models are calculated with the LCAO-based program ORCA [122, 123] and the def2-QZVPPD basis set.[183] The energies of the systems are calculated with PBE-D3(BJ), and their electronic properties and orbital images are obtained via a single point calculation with sc-PBE0.

First, the interaction of the nitrogen molecule with the defective (100) KCl surface is calculated and evaluated. Two minimum geometries are found, one parallel and one orthogonal to the surface plane. A reduction is identified both on GGA-level and sc-DDGH-level based on the shape of the defect orbital, which resembles the canonical LUMO of N_2, and the following findings: a DDEC6 charge analysis [184–186] yields a negative charge of $-0.8\,e$ on the nitrogen molecule, the bond length is increased from 1.11 Å to 1.19 Å, and the vibrational frequency is lowered from 2425 cm^{-1} to 1908 cm^{-1}, indicating a weakening of the bond from a bond order of 3 to 2.5. This matches a calculation of the anion in the gas phase. Furthermore, the molecule shows a strong interaction with the defective surface, as indicated by an electronic adsorption energy of -0.8 eV for the most stable configuration and a lowering of the defect band from -3.0 eV to -4.4 eV. Nitrogen is only weakly bound to the pristine KCl (100) surface by about -0.1 eV, predominantly on the account of dispersion interactions, and it is highly mobile with low migration barriers (< 0.03 eV), suggesting that the molecules will swiftly occupy all surface defects.

The hydrogenation of nitrogen to hydrazine is modeled on the basis of the gas-phase reaction via the two intermediates *iso*-diimide and *cis*-diimide. Both diimides are instable in the gas phase,[187] but their anions are strongly stabilized on the F center by about -2.2 eV, indicating a significant thermodynamic benefit of the F center on the reaction intermediates. As for the reaction itself, the 1,1-addition of hydrogen to the molecule is favored over the 1,2-addition both in the gas phase and on the defect. For this addition, the barrier is reduced from 4.53 eV in the neutral gas phase to 2.21 eV on the F center. This effect is largely attributed to the reduction of nitrogen, as an anionic gas phase reaction yields a comparable reduction of the reaction barrier to 2.23 eV. A similar reduction of barrier height is obtained for the 1,2-addition. However, the stabilizing effect is not sufficient to make either reaction step thermodynamically feasible, because at the temperatures required for reasonable reaction rates ($k = 0.37\,\mathrm{s}^{-1}$ at 1000 K, close to the melting point of KCl), entropic effects prevent the adsorption of nitrogen and hydrogen on the surface and force the thermodynamic equilibrium onto the side of the reagents. As for the subsequent reactions, the hydrogenation of *iso*-diimide to hydrazine does not benefit from the reduction, since it is so unstable that it readily reacts with hydrogen on its own. On the other hand, the barrier for the hydrogenation of *cis*-diimide on the F center is lower than for the neutral and anionic gas phase analoga, because the surface provides additional stabilization that enables a reaction via an alternative transition state. In all cases, the anti-bonding π^* orbitals of N_2 and the intermediates are identified as the crucial factor for the enhanced reactivity. Since all transition state orbitals are found to contain significant contributions of anti-bonding orbitals, less physical strain is required to move the reduced system with a partially occupied π^* orbital from its ground state to its transition state than a neutral system with an empty π^* orbital. The adsorption of nitrogen and the 1,1-addition of hydrogen is also modeled on the defective NaCl (100) surface, which yields an almost identical adsorption energy and reaction barrier.

In conclusion, the employed methodology successfully models the hydrogenation of nitrogen of the F center and identifies that the powerful catalytic effect of the defect is linked to its reductive behavior, which is most pronounced on reactions that involve molecules with a stable, low-lying HOMO like N_2 and CO_2. Moreover, the surface cations adjacent to the defect stabilize certain transition states, further augmenting the catalytic effect.

Hydrogenation of CO and CO$_2$ Catalyzed by Potassium Chloride F Centers

Michael Häfner[*] and Thomas Bredow[*]

Own manuscript contributions I wrote the manuscript and performed all calculations and interpretations of the models presented in it. Many ideas and hypotheses featured in this work emerged from discussions with Thomas Bredow, who also contributed corrections to the manuscript for the final publication.

---

[*] Mulliken Center for Theoretical Chemistry, Universität Bonn, Beringstr. 4, 53115 Bonn, Germany

The hydrogenation of CO and CO_2 is modeled according to the methodology outlined in chapter 3, and the general approach matches the one described for the hydrogenation of nitrogen in chapter 5. To ensure comparability with the experiments, all thermal corrections are calculated for a temperature of 500 K. Accordingly, the first section focuses on the interaction of the carbon oxides and hydrogen with the F center on the KCl (100) surface. CO and CO_2 exhibit the same reduction and bond weakening as N_2 on the defect. Their antibonding canonical π^*-orbitals are singly occupied by the defect electron and a Bader charge analysis [188–190] locates a negative charge of $-0.81\,e$ on CO and $-0.88\,e$ on CO_2. Additionally, their bond lengths are increased, CO_2 is bent on the defect, and their vibrational modes are lowered from $2127\,cm^{-1}$ to $1670\,cm^{-1}$ for CO and from $2368\,cm^{-1}$ to $1734\,cm^{-1}$ for the asymmetric stretching mode of CO_2. Both molecules also show a strong interaction with the F center, as CO is bound by $-0.88\,eV$ and CO_2 by $-1.52\,eV$ at 0 K. Because of entropic effects, the Gibbs free adsorption energy is reduced to $-0.13\,eV$ for CO and $-0.73\,eV$ for CO_2 at 500 K, but this is still sufficient to occupy all defect sites at pressures greater than 1 bar. Meanwhile, hydrogen does not show any significant interaction with the F center. It is not reduced and does not adsorb with a positive Gibbs free adsorption energy of $\Delta G_{ads} = +0.16\,eV$ at 0 K.

The hydrogenation of CO to methanol is modeled using the NEB method and found to take place via two steps, $CO + H_2 \longrightarrow H_2CO$ and $H_2CO + H_2 \longrightarrow CH_3OH$, each occurring via a homolytic dissociation of H_2 and a transition state stabilized by the surface cations. The reduction and additional stabilization greatly decrease the energy barriers of both steps compared to the gas phase reaction. At 500 K and 1 bar, the barrier for the initial hydrogenation decreases from 3.38 eV to 1.20 eV, and the barrier for the second hydrogenation drops from 3.51 eV to 1.71 eV, raising the reaction rates from below $10^{-20}\,s^{-1}$ to $4 \times 10^{-3}\,s^{-1}$ and $1 \times 10^{-4}\,s^{-1}$, respectively. By adjusting the pressure in the thermodynamic equations to 50 bar and taking both steps into consideration, a turnover frequency (TOF, reaction rate for the entire reaction from CO to CH_3OH) is obtained that is in the same order of magnitude as the performance of the established industrial copper catalysts. The TOF per active site on the F center exceeds the TOF on the conventional copper catalysts by a factor of 10.[17, 20–29] However, the TOF per area is about a factor 3000 smaller than on the copper catalysts, because the F center concentration is based on a conservative estimation from the diffusion measurements by Kuczynski and Byun at 800 K.[72] Larger concentrations of up to 1 % are technically possible at lower temperatures,[47, 48] but there are no dedicated concentration measurements for the relevant temperature region around 500 K. The hydrogenation of CO_2 to methanol takes place via four steps, a two-step reaction to formic acid, $CO_2 + H_2 \longrightarrow HCOOH$, $HCOOH + H_2 \longrightarrow H_2CO + H_2O$, and $H_2CO + H_2 \longrightarrow CH_3OH$, each of which resembling the hydrogenation of CO while water as obtained as a side product. A similarly significant reduction of barrier heights is found for all new reaction steps, but the reaction to formic acid also demonstrates the shortcoming of the F center-assisted catalysis, as the defect readily catalyzes the homolytic dissociation of formic acid to a radical hydrogen atom and a formate anion, $HCOOH^{\bullet-} \longrightarrow HCOO^- + H^\bullet$. The dissociation of methanol, according to $CH_3OH^{\bullet-} \longrightarrow OH^- + CH_3{}^\bullet$, and water, according to $H_2O^{\bullet-} \longrightarrow OH^- + H^\bullet$, is facilitated on the F center as well with barriers below the rate limiting barrier for the synthesis, subsequently deactivating the F center as the anion substitutes the missing chlorine anion.

In summary, the F center activates CO and CO_2 as much as N_2, and it facilitates the hydrogenation to the extent that it shows similar performance as the industrial catalyst. The reaction is hindered by the low concentration of active sites and the facile dissociation of certain molecules like the reaction intermediate formic acid, the product methanol, and the side product water, but the investigation further substantiates the strong reactivity and catalytic capabilities of the defective KCl (100) surface.

Methanol Synthesis on Copper-Doped F Centers

Michael Häfner[*] and Thomas Bredow[*]

Own manuscript contributions   I wrote the manuscript and performed all calculations and interpretations of the models presented in it. Many ideas and hypotheses featured in this work emerged from discussions with Thomas Bredow, who also contributed corrections to the manuscript for the final publication.

[*] Mulliken Center for Theoretical Chemistry, Universität Bonn, Beringstr. 4, 53115 Bonn, Germany

The previous investigations show that the KCl *F* center has a significant catalytic effect on the hydrogenation of N_2, CO, and CO_2, but this reactivity is associated with a major drawback, since the same defect catalyzes the homolytic dissociation of the intermediates formic acid and water, and the end product methanol. To circumvent these side reactions, a copper atom is added to the model of the *F* center. The effect of this alteration is investigated for the hydrogenation of CO to methanol. The theoretical methodology is identical to the one described in chapter 6 and all thermodynamic and kinetic parameters are calculated at a temperature of 500 K to maintain comparability with experimental measurements.[17, 20–29]

On the defective KCl (100) surface, the copper atom preferably occupies the chlorine vacancy with an adsorption energy of −2.35 eV and is not expected to vacate the defect cavity and agglomerate at low concentrations. The copper atom is reduced by the defect electron, as indicated by a Bader charge of $q_{Cu} = -0.7\,e$, the shape of the highest occupied crystal orbital (HOCO), and simple geometric considerations based on the ionic radii and distances of the ions around the defect. Electronically, the process pairs the unpaired 1*s*-type defect electron with the unpaired 4*s* electron of copper, combining the two open-shell components into a closed-shell system while maintaining the strong localization of the defect orbital.

In the case of carbon monoxide, copper-doping diminishes the reductive strength of the doped *F* center by approximately 50%, yielding a longer C–O bond, a higher stretching frequency, and a lower negative charge on the molecule than in the empty *F* center, as the molecule shares the excess defect electron with the copper. This finding is corroborated by the shape of the highest occupied crystal orbital, which is in between the 1*s*-type defect orbital and the antibonding π^* orbital of CO, and can be explained by the similar electron affinity of Cu and CO.[191, 192] Accordingly, the adsorption energy of CO rises from −0.88 eV to −0.48 eV, which reduces the defect coverage under experimental conditions from > 90 % to 0.2 % and slow the reaction with hydrogen. The same weakened interaction with the doped defect is obtained for formaldehyde and methanol, as the adsorption energy of each is approximately halved compared to the empty defect, favoring the desorption of methanol as product. The hydrogenation from CO to CH_3OH is modeled as in chapter 6. In the first step of the reaction to formaldehyde, the barrier matches the barrier on the empty defect, indicating that the Cu-doped defect is similarly reactive as the empty defect. An alternative two-step process via an intermediate leads to even lower barriers than the direct reaction, as it is mediated by the copper atom and facilitated by its hydrogen affinity, but the same hydrogen affinity also stabilizes the intermediate and effectively prevents the synthesis of formaldehyde. This alternate reaction shows conceptual similarities to the reactive behavior of copper hydride complexes in solution [193–199] and observations for [HCuH]⁻ in the gas phase.[200] The methanol formation from formaldehyde on the Cu-doped defect is sterically hindered, but the homolytic dissociation of methanol, one of the shortcomings of the empty *F* center, is not a problem on the doped defect. An alternative dissociation of methanol to methane is significantly slower and poses no relevant side reaction, but a third side reaction with a low barrier is identified to isomerize methanol to a thermodynamically favorable intermediate.

Bi-hydrogenated copper (HCuH) is obtained as a stable intermediate in the *F* center. The direct formation from copper and hydrogen is kinetically hindered, but it is facilitated by the presence of CO. CO and CH_3OH bind slightly stronger to the HCuH-doped defect than to the Cu-doped defect, and it hinders all dissociation reactions of CH_3OH. The hydrogen atoms bound to the copper are highly mobile, resulting in negligible barriers for the intramolecular addition and removal of single hydrogen atoms to the adsorbed carbon-containing molecule, and lower barriers for the dissociation of H_2 than on the Cu-doped defect. The resulting thermodynamic and kinetic properties are evaluated with a

kinetic Monte Carlo simulation, yielding a TOF from CO to CH_3OH three orders of magnitude larger than on the empty defect and four orders of magnitude larger than on the conventional copper catalysts.

In conclusion, the copper-doping addresses the shortcomings of the empty F center, as it changes the electronic state of the defect and hinders the homolytic dissociation of intermediates. Furthermore, it improves the catalytic performance of the F center by combining its reductive strength with the versatility and hydrogen affinity of copper to significantly outperform the industrially established catalysts for the synthesis of methanol, making it a promising candidate for hydrogenation reactions.

Summary and Outlook

A framework for calculating the alkali halide *F* center was established in chapter 3 based on the self-consistent dielectric-dependent global hybrid (sc-DDGH) sc-PBE0. The theoretical results match the experimental measurements of the dielectric constant within 1% and of the band gap, the conduction band minimum, and the valence band maximum for NaCl, KCl, and KBr within 0.3 eV with additional zero-point renormalization, surpassing the accuracy of standard hybrid functionals and further validating the performance of sc-DDGH functionals for the alkali halide bulk and surface. The results of previous experiments and theoretical calculations of the alkali halide *F* centers were confirmed, corroborating the findings for the localized $1s$-type shape of the occupied defect orbitals and $2p$-type shape of the unoccupied defect orbitals. A simple antiproportional relationship between the lattice parameter and the absolute surface defect band level was obtained, and it was found that the *F* centers of the investigated alkali halides do not differ significantly. Furthermore, the alkali halide *M* center was first investigated on DFT level, confirming the findings from experimental studies for its magnetic configuration, electronic properties, and formation enthalpy, which further corroborates the established methodology.

The methodology was further evaluated with respect to the diffusion of the alkali halide *F* center in chapter 4. The simulated bulk migration is in good agreement with previous theoretical investigations, and it was revealed that a hybrid functional is necessary to correct for the self-interaction error. The migration barrier correlates to the vibrational frequency of the single vibrational mode in the primitive alkali halide unit cell, indicating that the process is dominated by the elastic deformation of the lattice and allowing for a simple estimation of the barrier energies for the remaining cubic alkali halides. Moreover, the effects of thermal corrections and thermal expansion were found to be necessary to obtain a final migration enthalpy that agrees with the experimental measurements for the right reasons. The tendency of different GGA functionals to overestimate the lattice parameters of the alkali halides was exploited as a simple but effective method of approximating their thermal expansion. It was observed that defect migration across the (100) surface is more favorable than migration through the bulk, suggesting future experimental research into the diffusion behavior of defective alkali halides.

The hydrogenation of nitrogen in chapter 5 was the first reaction in this work where DFT and the NEB method were successfully employed to demonstrate the catalytic effect of the *F* center on the KCl and NaCl (100) surfaces. It was shown that the defect is reactive enough to reduce N_2 and activate its strong nitrogen-nitrogen bond, which poses the biggest obstacle in this reaction, and it reduces the highest reaction barriers by up to 50%. The mechanism is the same as in the gas-phase

reaction, showing a homolytic split of the hydrogen molecule, which is in contrast to the mechanisms for the hydrogenation via the Haber–Bosch process and in the nitrogenase. The reduction of nitrogen through the defect electron of the F center was identified as the main driving force behind its catalytic effect, as it occupies the lowest unoccupied molecular orbital of the adsorbate, while the electrostatic environment of the defect cavity only influences the reaction by restricting access and stabilizing the transition state. This process was identified both for NaCl and KCl, yielding no significant energetic differences for adsorption and activation barriers. Furthermore, the investigation indicates that reactions on the F center can be modeled with an anionic gas-phase reaction, providing a fast way to check whether the defect will have a significant effect on a given reaction. These results also suggest that the catalytic effect is the strongest in molecules with a low-lying highest occupied molecular orbital, indicating that reactions featuring molecules like carbon monoxide, carbon dioxide, ethyl acetate, or ammonia are enhanced by the F center.

In chapter 6, the catalytic effect was further corroborated for the hydrogenation of carbon monoxide and carbon dioxide on defective KCl. The F center was found to reduce CO and CO_2 and weaken their bonds, occupying their lowest unoccupied molecular orbital as observed for nitrogen and in previous research, and it halves all hydrogenation energies compared to the gas-phase reaction. Based on the activation barriers, the methanol synthesis on the defect exceeds the performance of the industrial copper catalyst by an order of magnitude per active site The theoretical performance per active area is hampered by a low F center concentration in KCl, and the reaction is further inhibited by dissociative side reactions as the F center facilitates the homolytic dissociation of formic acid, water, and methanol, leading to self-deactivation. This agrees with experimental findings for water, but indicates that the empty F center is not suited as a catalyst for hydrogenation reactions.

In chapter 7, it was shown that doping the KCl F center with a copper atom suppresses these dissociative side reactions, as it changes the fundamental electronic structure from an open-shell system into a closed-shell system. A copper atom preferentially occupies the defect site rather than adsorbing to the pristine (100) surface or agglomerating. The doping halves the interaction strength with adsorbates, such as CO, H_2CO, CH_3OH, or H_2, but it does not diminish the overall reactivity of the defect. The reduction of the adsorbed copper complex through the defect electron still constitutes the main driving force behind the reactivity of the system, but the reaction also benefits from the hydrogen affinity of copper, which promotes the dissociation of H_2 and distribution of hydrogen atoms to other adsorbates, emulating the reactive behavior of organometallic copper hydride complexes as a heterogeneous catalyst. Bihydrogenated copper (HCuH) was shown to be generated in-situ on the F center during the hydrogenation of CO and constitutes a more stable dopant than copper. A kinetic Monte Carlo simulation was employed to calculate the turnover frequency for the methanol synthesis on the HCuH-doped defect, and it was found to exceed the performance of the empty defect by three orders of magnitude while not suffering from the same side reactions. This also makes the HCuH-doped F center competitive to the macroscopic performance of the industrial copper catalyst while requiring only a fraction of copper as active material.

In summary, this thesis successfully employs density functional theory, the NEB method, and statistical mechanics to expand the initial research on the chemical properties of the alkali halide F center, laying the theoretical foundation for further investigations into their catalytic capabilities. The multi-level approach, combining an optimization on GGA-level with PBE-D3(BJ) and single-point calculation on hybrid-level with sc-PBE0 has proven to yield accurate results for the electronic properties of the defective systems, while PBE on its own has been demonstrated to sufficiently describe the reductive performance and qualitative band structure of the F center, obviating the use of

computationally demanding hybrid-level DFT for the modeling of the reactions. The alkali halide F centers themselves were identified as electronically fairly simple and qualitatively interchangable. The reactivity of the F center was demonstrated for the hydrogenation of N_2, CO, and CO_2. Several side reactions were identified as obstacles for the applicability of the defect for catalysis, but copper was found to be a perfect dopant to remedy these side reactions and improve the reactivity regarding hydrogenation reactions. Furthermore, this work represents an example for an extensive theoretical characterization of the physical and chemical properties of a prospective catalytic material, and it demonstrates a way in which kinetic Monte Carlo theory can be employed to describe a complicated reaction network.

However, since the main focus of this work is on the catalytic activity of potassium chloride, the reactivity for the other alkali halides, F centers in other materials, and electrides, and to what extent the results and findings of this work remain applicable, require further study and comparison. Another field of interest are F centers located on surface features like step edges or on the (110) and (111) surface, as the different electrostatic and geometric environment is expected to alter the reactivity. Moreover, this work reveals potential targets for further research into the surface of pristine and defective alkali halides, such as the change of electronic properties from surface to bulk and the surface-bound migration of F centers. Due to their simple structure, they represent ideal model systems for such investigations.

Concerning the chemical potential of the F center, this works indicates that the copper-doped defect is a potent hydrogenation catalyst. This raises the question to what extent and for which other molecules it is applicable, and how much different metal atoms as dopants, such as silver, gold, rhodium, iridium, or cobalt, amplify and alter the reactivity. Furthermore, the enhanced reactivity potentially applies to other reactions like carbon-carbon-coupling reactions, because the reductive environment of the defect turns the adsorbate into a nucleophile. Concerning the empty alkali halide F center, the results of this work for the homolytic dissociation of methanol, formic acid, and water suggest that it can serve as a radical initiators in a radical chain reaction, corroborating the findings of previous studies. The major drawback of this method remains its irreversibility, as the defects are healed during the radical formation. However, based on the findings for copper-doping, which successfully hindered all homolytic dissociations, the use of a metal with an even number of electrons, like palladium or platinum, as dopants may alter the energy balance to the point where the defect facilitates certain types of homolytic dissociation and acts as a reusable radical initiator.

Finally, the predictions and insights from this work on the properties and reactivity of the F center form the basis for further experimental studies of its chemical behavior and support the process of exploring its applications in catalysis.

Bibliography

[1] L. E. Apodaca, *Nitrogen (fixed)—Ammonia*,
    https://pubs.usgs.gov/periodicals/mcs2021/mcs2021-nitrogen.pdf, accessed March 17, 2022,
    2018.

[2] I. R. E. A. (IRENA), *Innovation Outlook: Renewable Methanol*,
    International Renewable Energy Agency (IRENA), 2021.

[3] W. P. Jencks, *Catalysis in chemistry and enzymology*, Courier Corporation, 1987.

[4] Z. Ma and F. Zaera, "Heterogeneous Catalysis by Metals,"
    Encyclopedia of Inorganic Chemistry, American Cancer Society, 2006,
    ISBN: 9780470862100, DOI: `10.1002/0470862106.ia084`.

[5] D. R. Lide, ed., *CRC Handbook of Chemistry and Physics*, vol. 85, CRC press, 2004.

[6] A. Hellman, E. J. Baerends, M. Biczysko, T. Bligaard, C. H. Christensen, D. C. Clary, S. Dahl,
    R. van Harrevelt, K. Honkala, H. Jonsson, G. J. Kroes, M. Luppi, U. Manthe, J. K. Nørskov,
    R. A. Olsen, J. Rossmeisl, E. Skúlason, C. S. Tautermann, A. J. C. Varandas, and J. K. Vincent,
    Predicting Catalysis: Understanding Ammonia Synthesis from First-Principles Calculations,
    J. Phys. Chem. B **110** (2006) 17719, DOI: `10.1021/jp056982h`.

[7] D.-Y. Hwang and A. M. Mebel,
    Reaction Mechanism of N2/H2 Conversion to NH3: A Theoretical Study,
    J. Phys. Chem. A **107** (2003) 2865, DOI: `10.1021/jp0270349`.

[8] J. W. Peters and R. K. Szilagyi,
    Exploring New Frontiers of Nitrogenase Structure and Mechanism, Curr. Opin. Chem. Biol.
    10 (2006), Bioinorganic chemistry / Biocatalysis and biotransformation 101, ISSN: 1367-5931,
    DOI: `https://doi.org/10.1016/j.cbpa.2006.02.019`.

[9] B. K. Burgess and D. J. Lowe, *Mechanism of Molybdenum Nitrogenase*,
    Chem. Rev. **96** (1996) 2983, DOI: `10.1021/cr950055x`.

[10] L. E. Mortenson and R. N. F. Thorneley, *Structure and Function of Nitrogenase*,
     Annu. Rev. Biochem. **48** (1979) 387, DOI: `10.1146/annurev.bi.48.070179.002131`.

[11] M. Appl, "Ammonia," *Ullmann's Encyclopedia of Industrial Chemistry*,
     Weinheim: Wiley-VCH Verlag GmbH & Co. KGaA, 2006, ISBN: 9783527306732,
     DOI: `https://doi.org/10.1002/14356007.a02_143.pub2`.

[12] G. Ertl, *Elementary Steps in Heterogeneous Catalysis*,
     Angew. Chem. Int. Ed. Engl. **29** (1990) 1219,
     DOI: `https://doi.org/10.1002/anie.199012191`.

[13] K. Honkala, A. Hellman, I. N. Remediakis, A. Logadottir, A. Carlsson, S. Dahl, C. H. Christensen, and J. K. Nørskov, *Ammonia Synthesis from First-Principles Calculations*, Science **307** (2005) 555, ISSN: 0036-8075, DOI: `10.1126/science.1106435`.

[14] M. Appl, "Ammonia," *Ullmann's Encyclopedia of Industrial Chemistry*, John Wiley & Sons, Ltd, 2006, ISBN: 9783527306732, DOI: `https://doi.org/10.1002/14356007.a02_143.pub2`.

[15] M. Kitano, Y. Inoue, Y. Yamazaki, F. Hayashi, S. Kanbara, S. Matsuishi, T. Yokoyama, S.-W. Kim, M. Hara, and H. Hosono, *Ammonia Synthesis Using a Stable Electride as an Electron Donor and Reversible Hydrogen Store*, Nat. Chem. **4** (2012) 934, DOI: `https://doi.org/10.1038/nchem.1476`.

[16] M. Kitano, S. Kanbara, Y. Inoue, N. Kuganathan, P. V. Sushko, T. Yokoyama, M. Hara, and H. Hosono, *Electride Support Boosts Nitrogen Dissociation over Ruthenium Catalyst and Shifts the Bottleneck in Ammonia Synthesis*, Nat. Comm. **6** (2015) 1, DOI: `https://doi.org/10.1038/ncomms7731`.

[17] K. Klier, "Methanol Synthesis," ed. by D. Eley, H. Pines, and P. B. Weisz, vol. 31, Advances in Catalysis, Academic Press, 1982 243, DOI: `https://doi.org/10.1016/S0360-0564(08)60455-1`.

[18] S. Rönsch, J. Schneider, S. Matthischke, M. Schlüter, M. Götz, J. Lefebvre, P. Prabhakaran, and S. Bajohr, *Review on methanation – From fundamentals to current projects*, Fuel **166** (2016) 276, ISSN: 0016-2361, DOI: `https://doi.org/10.1016/j.fuel.2015.10.111`.

[19] J. Kopyscinski, T. J. Schildhauer, and S. M. Biollaz, *Production of synthetic natural gas (SNG) from coal and dry biomass – A technology review from 1950 to 2009*, Fuel **89** (2010) 1763, ISSN: 0016-2361, DOI: `https://doi.org/10.1016/j.fuel.2010.01.027`.

[20] R. Burch, S. Golunski, and M. Spencer, *The Role of Hydrogen in Methanol Synthesis over Copper Catalysts*, Catal. Letters **5** (1990) 55, DOI: `https://doi.org/10.1007/BF00772093`.

[21] J. L. Robbins, E. Iglesia, C. Kelkar, and B. DeRites, *Methanol Synthesis over Cu/SiO 2 Catalysts*, Catal. Letters **10** (1991) 1, DOI: `https://doi.org/10.1007/BF00764730`.

[22] R. Dalebout, L. Barberis, G. Totarella, S. J. Turner, C. La Fontaine, F. M. F. de Groot, X. Carrier, A. M. J. van der Eerden, F. Meirer, and P. E. de Jongh, *Insight into the Nature of the ZnOx Promoter during Methanol Synthesis*, ACS Catal. **12** (2022) 6628, DOI: `10.1021/acscatal.1c05101`.

[23] R. Van Den Berg, G. Prieto, G. Korpershoek, L. I. Van Der Wal, A. J. Van Bunningen, S. Lægsgaard-Jørgensen, P. E. De Jongh, and K. P. De Jong, *Structure Sensitivity of Cu and CuZn Catalysts Relevant to Industrial Methanol Synthesis*, Nat. Commun. **7** (2016) 1, DOI: `https://doi.org/10.1038/ncomms13057`.

[24] R. Höppener, E. Doesburg, and J. Scholten, *Preparation and Characterization of Stable Copper/zinc oxide/alumina Catalysts for Methanol Systhesis*, Appl. Catal. **25** (1986) 109, DOI: `https://doi.org/10.1016/S0166-9834(00)81227-0`.

[25] F. Studt, M. Behrens, E. L. Kunkes, N. Thomas, S. Zander, A. Tarasov, J. Schumann, E. Frei, J. B. Varley, F. Abild-Pedersen, J. K. Nørskov, and R. Schlögl, *The Mechanism of CO and CO2 Hydrogenation to Methanol over Cu-Based Catalysts*, ChemCatChem **7** (2015) 1105, DOI: https://doi.org/10.1002/cctc.201500123.

[26] J. Yoshihara and C. T. Campbell, *Methanol Synthesis and Reverse Water–Gas Shift Kinetics over Cu(110) Model Catalysts: Structural Sensitivity*, J. Catal. **161** (1996) 776, ISSN: 0021-9517, DOI: https://doi.org/10.1006/jcat.1996.0240.

[27] J. Friedrich, D. Young, and M. Wainwright, *Methanol Synthesis over Raney copper-zinc Catalysts: II. Activities and Surface Properties of a Partially Leached Alloy*, J. Catal. **80** (1983) 14, ISSN: 0021-9517, DOI: https://doi.org/10.1016/0021-9517(83)90224-5.

[28] A. Bridgewater, M. Wainwright, D. Young, and J. Orchard, *Methanol Synthesis over Raney Copper-zinc Catalysts. III. Optimization of Alloy Composition and Catalyst Preparation*, Appl. Catal. **7** (1983) 369, ISSN: 0166-9834, DOI: https://doi.org/10.1016/0166-9834(83)80036-0.

[29] W. Pan, R. Cao, D. Roberts, and G. Griffin, *Methanol Synthesis Activity of CuZnO Catalysts*, J. Catal. **114** (1988) 440, ISSN: 0021-9517, DOI: https://doi.org/10.1016/0021-9517(88)90047-4.

[30] Y. Guo, C. Riplinger, U. Becker, D. G. Liakos, Y. Minenkov, L. Cavallo, and F. Neese, *Communication: An improved linear scaling perturbative triples correction for the domain based local pair-natural orbital based singles and doubles coupled cluster method [DLPNO-CCSD(T)]*, J. Chem. Phys. **148** (2018) 011101, DOI: 10.1063/1.5011798.

[31] K. Lv and X. Bao, *Mechanistic insights into nickel- and gold-catalyzed diastereoselective [4 + 2 + 1] cycloadditions between dienynes and diazo compounds: a DFT study*, Org. Chem. Front. **9** (2022) 693, DOI: 10.1039/D1QO01468D.

[32] M. S. S. Adam, M. Makhlouf, A. Alharbi, and N. M. El-Metwaly, *Novel isatin-based complexes of Mn(II) and Cu(II) ions: Characterization, homogeneous catalysts for sulfides oxidation, bioactivity screening and theoretical implementations via DFT and pharmacokinetic studies*, J. Mol. Liq. **351** (2022) 118620, ISSN: 0167-7322, DOI: https://doi.org/10.1016/j.molliq.2022.118620.

[33] N. R. Khafizov, T. I. Madzhidov, C. Yuan, M. A. Varfolomeev, and O. N. Kadkin, *Theoretical insight into the catalytic effect of transition metal ions on the aquathermal degradation of heavy oil: A DFT study of cyclohexyl phenyl amine cleavage*, Fuel **312** (2022) 123002, ISSN: 0016-2361, DOI: https://doi.org/10.1016/j.fuel.2021.123002.

[34] Y. Yang, J. Wang, Y. Shu, Y. Ji, H. Dong, and Y. Li, *Significance of density functional theory (DFT) calculations for electrocatalysis of N2 and CO2 reduction reactions*, Phys. Chem. Chem. Phys. **24** (2022) 8591, DOI: 10.1039/D1CP05442B.

[35] L. F. Rasteiro, R. A. De Sousa, L. H. Vieira, V. K. Ocampo-Restrepo, L. G. Verga, J. M. Assaf, J. L. Da Silva, and E. M. Assaf, *Insights into the alloy-support synergistic effects for the CO2 hydrogenation towards methanol on oxide-supported Ni5Ga3 catalysts: An experimental and DFT study*, Appl. Cat. B **302** (2022) 120842, ISSN: 0926-3373, DOI: https://doi.org/10.1016/j.apcatb.2021.120842.

[36] V. Korpelin, T. Kiljunen, M. M. Melander, M. A. Caro, H. H. Kristoffersen, N. Mammen, V. Apaja, and K. Honkala, *Addressing Dynamics at Catalytic Heterogeneous Interfaces with DFT-MD: Anomalous Temperature Distributions from Commonly Used Thermostats*, J. Phys. Chem. Lett. **13** (2022) 2644, DOI: 10.1021/acs.jpclett.2c00230.

[37] X. Liao, R. Lu, L. Xia, Q. Liu, H. Wang, K. Zhao, Z. Wang, and Y. Zhao, *Density Functional Theory for Electrocatalysis*, ENERGY & ENVIRONMENTAL MATERIALS **5** (2022) 157, DOI: https://doi.org/10.1002/eem2.12204.

[38] E. Riedel and C. Janiak, *Anorganische Chemie*, Berlin, Boston: De Gruyter, 2022, ISBN: 9783110694444, DOI: doi:10.1515/9783110694444.

[39] A. Kelly and K. M. Knowles, *Crystallography and crystal defects*, John Wiley & Sons, 2020.

[40] F. Seitz, *Color Centers in Alkali Halide Crystals. II*, Rev. Mod. Phys. **26** (1954) 7, DOI: 10.1103/RevModPhys.26.7.

[41] J. Dickinson, S. Orlando, S. Avanesyan, and S. Langford, *Color center formation in soda lime glass and NaCl single crystals with femtosecond laser pulses*, Appl. Phys. A **79** (2004) 859, DOI: https://doi.org/10.1007/s00339-004-2571-8.

[42] R. T. Williams, B. B. Craig, and W. L. Faust, *F-Center Formation in NaCl: Picosecond Spectroscopic Evidence for Halogen Diffusion on the Lowest Excitonic Potential Surface*, Phys. Rev. Lett. **52** (1984) 1709, DOI: 10.1103/PhysRevLett.52.1709.

[43] H. Rabin and C. C. Klick, *Formation of F Centers at Low and Room Temperatures*, Phys. Rev. **117** (1960) 1005, DOI: 10.1103/PhysRev.117.1005.

[44] A. B. Scott and W. A. Smith, *The Thermal Stability of F-centers in Alkali Halides*, Phys. Rev. **83** (1951) 982, DOI: 10.1103/PhysRev.83.982.

[45] C. L. H. Howard and P. F. Kerr, *Blue Halite*, Science **132** (1960) 1886, DOI: 10.1126/science.132.3443.1886.

[46] V. Zielasek, T. Hildebrandt, and M. Henzler, *Surface Color Centers on Epitaxial NaCl Films*, Phys. Rev. B **62** (2000) 2912, DOI: 10.1103/PhysRevB.62.2912.

[47] K. Przibram, *Verfärbung und Lumineszenz durch Becquerelstrahlen V nebst Verwandten Erscheinungen*, Z. Phys. **130** (1951) 269, DOI: https://doi.org/10.1007/BF01340165.

[48] R. Kaiser, *Störstellen Hoher Konzentration in Alkalihalogeniden*, Z. Phys. **132** (1952) 482, DOI: https://doi.org/10.1007/BF01333192.

[49] C. J. Buchenauer and D. B. Fitchen, *Pressure Shift of the F Band in Alkali Halides: Ion-Size Effects*, Phys. Rev. **167** (1968) 846, DOI: 10.1103/PhysRev.167.846.

[50] A. Perregaux and G. Ascarelli, *Piezo-optic study of the F center in alkali halides-Evidence for structure in the F band of KCl, KBr, and NaCl*, Phys. Rev. B **10** (1974) 1683, DOI: `10.1103/PhysRevB.10.1683`.

[51] J. M. Worlock and S. P. S. Porto, *Raman Scattering by F Centers*, Phys. Rev. Lett. **15** (1965) 697, DOI: `10.1103/PhysRevLett.15.697`.

[52] C. A. Hutchinson, *Paramagnetic Resonance Absorption in Crystals Colored by Irradiation*, Phys. Rev. **75** (1949) 1769, DOI: `10.1103/PhysRev.75.1769.2`.

[53] C. A. Hutchison and G. A. Noble, *Paramagnetic Resonance Absorption in Additively Colored Crystals of Alkali Halides*, Phys. Rev. **87** (1952) 1125, DOI: `10.1103/PhysRev.87.1125.2`.

[54] A. H. Kahn and C. Kittel, *F-Center Wave Functions and Electronic g-Values in KCl Crystals*, Phys. Rev. **89** (1953) 315, DOI: `10.1103/PhysRev.89.315`.

[55] A. F. Kip, C. Kittel, R. A. Levy, and A. M. Portis, *Electronic Structure of F Centers: Hyperfine Interactions in Electron Spin Resonance*, Phys. Rev. **91** (1953) 1066, DOI: `10.1103/PhysRev.91.1066`.

[56] A. M. Portis, *Electronic Structure of F Centers: Saturation of the Electron Spin Resonance*, Phys. Rev. **91** (1953) 1071, DOI: `10.1103/PhysRev.91.1071`.

[57] G. Benedek and G. F. Nardelli, *Raman Scattering by Color Centers*, Phys. Rev. **154** (1967) 872, DOI: `10.1103/PhysRev.154.872`.

[58] M. Ghomi, E. Rzepka, and L. Taurel, *Study of initial stages of F-centre aggregation in NaCl by Raman scattering*, Phys. Status Solidi B **92** (1979) 447, DOI: `10.1002/pssb.2220920213`.

[59] M. Ghomi and J. P. Buisson, *Study of Raman spectra of KBr doped with F-centres by excitation in the F and K bands*, J. Phys. Condens. Matter **12** (1979) 4631, DOI: `10.1088/0022-3719/12/21/027`.

[60] U. M. Grassano, G. Margaritondo, and R. Rosei, *Unrelaxed 2S State of the F Center in Alkali Halides Studied by the Stark Effect*, Phys. Rev. B **2** (1970) 3319, DOI: `10.1103/PhysRevB.2.3319`.

[61] L. D. Bogan and D. B. Fitchen, *Stark Effects in F-Center Emission*, Phys. Rev. B **1** (1970) 4122, DOI: `10.1103/PhysRevB.1.4122`.

[62] L. F. Stiles, M. P. Fontana, and D. B. Fitchen, *Effect of Electric Field and Temperature on the Radiative Lifetime of the F Center*, Phys. Rev. B **2** (1970) 2077, DOI: `10.1103/PhysRevB.2.2077`.

[63] T. Koyama, M. Nakajima, and T. Suemoto, *Femtosecond Depolarization of Hot Luminescence from the F Center in KCl*, J. Physical Soc. Japan **78** (2009) 075002, DOI: `10.1143/jpsj.78.075002`.

[64] C. Kittel and E. Abrahams, *Dipolar Broadening of Magnetic Resonance Lines in Magnetically Diluted Crystals*, Phys. Rev. **90** (1953) 238, DOI: `10.1103/PhysRev.90.238`.

[65] J. C. Gravitt, G. E. Gross, D. K. Benson, and A. B. Scott, *Motion of F Centers in KCl and KI*, J. Chem. Phys. **37** (1962) 2783, DOI: 10.1063/1.1733105.

[66] R. C. Tyagi, R. Singh, and A. K. Gupta, *Kinetics of Electrolytic Coloration in Alkali Halide Crystals*, J. Phys. Condens. Matter **3** (1970) 769, DOI: 10.1088/0022-3719/3/4/004.

[67] M. Montojo, F. Jaque, and C. Sánchez, *Transient and Steady Electron Currents Limited by Ionic Space Charge in Electrolytically Coloured Potassium Halides*, J. Phys. Chem. Solids **38** (1977) 657, ISSN: 0022-3697, DOI: https://doi.org/10.1016/0022-3697(77)90234-7.

[68] M. L. Dalal, S. Sivaraman, and Y. V. G. S. Murti, *Thermal Dissociation Energy of F-Centers in Alkali Halides*, Phys. Status Solidi B **110** (1982) 349, DOI: 10.1002/pssb.2221100140.

[69] S. Kar, A. K. Maiti, M. Sengupta, and K. Goswami, *Ionic Transport in Alkali Halides with Doping-induced Defects and Colour Centre Migration by Thermal Bleaching*, FIZIKA A **9** (2000) 159.

[70] H. Mizuno and M. Inoue, *Diffusion of F Centers into Potassium Chloride Single Crystals*, Phys. Rev. **120** (1960) 1226, DOI: 10.1103/PhysRev.120.1226.

[71] E. L. Wolf, *Diffusion Effects in the Inhomogeneously Broadened Case: High-Temperature Saturation of the F-Center Electron Spin Resonance*, Phys. Rev. **142** (1966) 555, DOI: 10.1103/PhysRev.142.555.

[72] G. Kuczynski and J. Byun, *Diffusion of F-centers in Potassium Chloride Crystals*, Phys. Status Solidi B **50** (1972) 367, DOI: https://doi.org/10.1002/pssb.2220500143.

[73] S. Fölsch and M. Henzler, *Water Adsorption on the NaCl Surface*, Surf. Sci. **247** (1991) 269, ISSN: 0039-6028, DOI: 10.1016/0039-6028(91)90136-G.

[74] U. Malaske, H. Pfnür, M. Bässler, M. Weiss, and E. Umbach, *Adsorption Geometry of OH Adsorbed at F Centers on a NaCl(100) Surface*, Phys. Rev. B **53** (1996) 13115, DOI: 10.1103/PhysRevB.53.13115.

[75] C. Tegenkamp and H. Pfnür, *Adsorbate Induced Contact Charging: Pure and OH-substituted Benzoic Acids Adsorbed on Wide Band Gap Insulators*, Phys. Chem. Chem. Phys. **4** (2002) 2653, DOI: 10.1039/B110517E.

[76] U. Malaske, C. Tegenkamp, M. Henzler, and H. Pfnür, *Defect-induced Band Gap States and the Contact Charging Effect in Wide Band Gap Insulators*, Surf. Sci. **408** (1998) 237, ISSN: 0039-6028, DOI: https://doi.org/10.1016/S0039-6028(98)00247-7.

[77] M. R. Pederson and B. M. Klein, *Improved theoretical methods for studies of defects in insulators: Application to the F center in LiF*, Phys. Rev. B **37** (1988) 10319, DOI: 10.1103/PhysRevB.37.10319.

[78] F. Karsai, P. Tiwald, R. Laskowski, F. Tran, D. Koller, S. Gräfe, J. Burgdörfer, L. Wirtz, and P. Blaha, *F center in lithium fluoride revisited: Comparison of solid-state physics and quantum-chemistry approaches*, Phys. Rev. B **89** (2014) 125429, DOI: 10.1103/PhysRevB.89.125429.

[79] G. Mallia, R. Orlando, C. Roetti, P. Ugliengo, and R. Dovesi,
F center in LiF: A quantum mechanical ab initio investigation of the hyperfine interaction between the unpaired electron at the vacancy and its first seven neighbors,
Phys. Rev. B **63** (2001) 235102, DOI: `10.1103/PhysRevB.63.235102`.

[80] J.-i. Adachi and N. Kosugi, *An Ab Initio Molecular Orbital Approach to Electronic Structures of the F Center in NaCl. Effects of Basis Set and Cluster Size*,
Bull. Chem. Soc. Jpn. **66** (1993) 3314, DOI: `10.1246/bcsj.66.3314`.

[81] C. M. Fang and R. A. de Groot, *Wavefunction character of the F-center in table salt*,
J. Phys. Condens. Matter **20** (2008) 075219, DOI: `10.1088/0953-8984/20/7/075219`.

[82] H. A. Kassim and M. M. Uoda,
A Study of F-center in the Ionic Crystal by Using The Quantum Dot Model Potential,
Journal of University of Babylon for Pure and Applied Sciences **26** (2018) 173.

[83] A. Popov, E. Kotomin, and J. Maier,
Basic properties of the F-type centers in halides, oxides and perovskites,
Nucl. Instrum. Methods Phys. Res. B **268** (2010) 3084, ISSN: 0168-583X,
DOI: `https://doi.org/10.1016/j.nimb.2010.05.053`.

[84] W. Chen, C. Tegenkamp, H. Pfnür, and T. Bredow,
Color Centers in NaCl by Hybrid Functionals, Phys. Rev. B **82** (2010) 104106,
DOI: `10.1103/PhysRevB.82.104106`.

[85] R. D. Zwicker, *Pseudopotential calculation of F-center spin densities in KCl, NaCl, and NaF*,
Phys. Rev. B **18** (1978) 2004, DOI: `10.1103/PhysRevB.18.2004`.

[86] P. Tiwald, F. Karsai, R. Laskowski, S. Gräfe, P. Blaha, J. Burgdörfer, and L. Wirtz,
Ab initio perspective on the Mollwo-Ivey relation for F centers in alkali halides,
Phys. Rev. B **92** (2015) 144107, DOI: `10.1103/PhysRevB.92.144107`.

[87] W. Chen, C. Tegenkamp, H. Pfnür, and T. Bredow, *Tailoring Band Gaps of Insulators by Adsorption at Surface Defects: Benzoic Acids on NaCl Surfaces*,
Phys. Rev. B **79** (2009) 235419, DOI: `10.1103/PhysRevB.79.235419`.

[88] M. Hochheim and T. Bredow, *Adsorption of PTCDA on NaCl Surfaces with Color Centers: Charge Transfer and Formation of Radical Ions*, J. Phys. Chem. C **122** (2018) 29426,
DOI: `10.1021/acs.jpcc.8b10840`.

[89] M. Häfner, M. Hochheim, and T. Bredow, *Chemistry with F Centers: Reduction of Organic Molecules on the Defective Potassium Chloride(100) Surface*,
J. Phys. Chem. C **124** (2020) 12606, DOI: `10.1021/acs.jpcc.0c03511`.

[90] J. P. Perdew, K. Burke, and M. Ernzerhof, *Generalized Gradient Approximation Made Simple*,
Phys. Rev. Lett. **77** (1996) 3865, DOI: `10.1103/PhysRevLett.77.3865`.

[91] T. J. Turner, R. De Batist, and Y. Haven,
Photon-Induced Reorientation of M-Centers in Potassium Chloride,
Phys. Status Solidi B **11** (1965) 535, DOI: `10.1002/pssb.19650110205`.

[92] I. Schneider, M. Marrone, and M. N. Kabler,
Dichroic Absorption of M Centers as a Basis for Optical Information Storage,
Appl. Opt. **9** (1970) 1163, DOI: `10.1364/AO.9.001163`.

[93] W. D. Compton and H. Rabin, *F-Aggregate Centers in Alkali Halide Crystals*, ed. by F. Seitz and D. Turnbull, vol. 16, Solid State Physics, Academic, 1964 121, DOI: https://doi.org/10.1016/S0081-1947(08)60516-0.

[94] H. Seidel and H. C. Wolf, *Paramagnetische Resonanz (ESR- und ENDOR-Spektroskopie) von Farbzentren in Alkalihalogenid-Kristallen*, Phys. Status Solidi B **11** (1965) 3, DOI: 10.1002/pssb.19650110102.

[95] J. D. Zahrt, A. B. Scott, and E. H. Coker, *Thermodynamics of M-Center Formation*, J. Chem. Phys. **46** (1967) 791, DOI: 10.1063/1.1840741.

[96] J. Rolfe and S. R. Morrison, *Absorption spectra of F-aggregate centers in KCl crystals*, Phys. Rev. B **15** (1977) 3211, DOI: 10.1103/PhysRevB.15.3211.

[97] E. R. Hodgson, A. Delgado, and J. L. A. Rivas, *In-beam studies of M-centre production processes in NaCl*, J. Phys. Condens. Matter **12** (1979) 1239, DOI: 10.1088/0022-3719/12/7/014.

[98] S. Petroff, *Photochemische Beobachtungen an KCl-Kristallen*, Z. Phys. **127** (1950) 443, DOI: https://doi.org/10.1007/BF01329841.

[99] F. Okamoto, *Optical Absorption of M Centers in Potassium Chloride Crystals*, Phys. Rev. **124** (1961) 1090, DOI: 10.1103/PhysRev.124.1090.

[100] P. R. Moran, S. H. Christensen, and R. H. Silsbee, *Electron Spin Resonance and Optical Absorption of Electron Excess Centers in KCl*, Phys. Rev. **124** (1961) 442, DOI: 10.1103/PhysRev.124.442.

[101] H. Ohkura and K. Murase, *Electron Spin Resonance of the M center in Potassium Chloride*, J. Phys. Soc. Jpn. **16** (1961) 2076, DOI: 10.1143/JPSJ.16.2076.

[102] E. Sonder, *Magnetism of KCl*, Phys. Rev. **125** (1962) 1203, DOI: 10.1103/PhysRev.125.1203.

[103] W. Koch and M. C. Holthausen, *A chemist's guide to density functional theory*, Weinheim, John Wiley & Sons, 2015.

[104] J. Reinhold, *Quantentheorie der Moleküle: Eine Einführung*, Springer-Verlag, 2012.

[105] T. Bredow, *Quantum-chemical treatment of crystalline solids and their surfaces*, Vorlesungsskript, 2015.

[106] M. Born and R. Oppenheimer, *Zur Quantentheorie der Molekeln*, Ann. Phys. **389** (1927) 457, DOI: https://doi.org/10.1002/andp.19273892002.

[107] P. Hohenberg and W. Kohn, *Inhomogeneous Electron Gas*, Phys. Rev. **136** (1964) B864, DOI: 10.1103/PhysRev.136.B864.

[108] J. K. L. MacDonald, *Successive approximations by the Rayleigh-Ritz variation method*, Phys. Rev. **43** (1933) 830, DOI: https://doi.org/10.1103/PhysRev.43.830.

[109] W. Ritz, *Über eine neue Methode zur Lösung gewisser Variationsprobleme der mathematischen Physik.*, J. Reine Angew. Math. **135** (1909) 1, DOI: https://doi.org/10.1515/crll.1909.135.1.

[110] J. P. Perdew and K. Schmidt,
Jacob's ladder of density functional approximations for the exchange-correlation energy,
AIP Conference Proceedings **577** (2001) 1, DOI: `10.1063/1.1390175`.

[111] J. Tao, J. P. Perdew, V. N. Staroverov, and G. E. Scuseria,
*Climbing the Density Functional Ladder: Nonempirical Meta–Generalized Gradient
Approximation Designed for Molecules and Solids*, Phys. Rev. Lett. **91** (2003) 146401,
DOI: `10.1103/PhysRevLett.91.146401`.

[112] J. Sun, A. Ruzsinszky, and J. P. Perdew,
Strongly Constrained and Appropriately Normed Semilocal Density Functional,
Phys. Rev. Lett. **115** (2015) 036402, DOI: `10.1103/PhysRevLett.115.036402`.

[113] J. P. Perdew, M. Ernzerhof, and K. Burke,
Rationale for Mixing Exact Exchange With Density Functional Approximations,
J. Chem. Phys. **105** (1996) 9982, DOI: `10.1063/1.472933`.

[114] J. H. Skone, M. Govoni, and G. Galli, *Self-consistent hybrid functional for condensed systems*,
Phys. Rev. B **89** (2014) 195112, DOI: `10.1103/PhysRevB.89.195112`.

[115] S. Baroni and R. Resta, *Ab initio calculation of the macroscopic dielectric constant in silicon*,
Phys. Rev. B **33** (1986) 7017, DOI: `10.1103/PhysRevB.33.7017`.

[116] M. Gajdoš, K. Hummer, G. Kresse, J. Furthmüller, and F. Bechstedt,
Linear optical properties in the projector-augmented wave methodology,
Phys. Rev. B **73** (2006) 045112, DOI: `10.1103/PhysRevB.73.045112`.

[117] S. Grimme, S. Ehrlich, and L. Goerigk,
Effect of the Damping Function in Dispersion Corrected Density Functional Theory,
J. Comput. Chem. **32** (2011) 1456, DOI: `10.1002/jcc.21759`.

[118] S. Grimme, J. Antony, S. Ehrlich, and H. Krieg,
*A Consistent and Accurate ab Initio Parametrization of Density Functional Dispersion
Correction (DFT-D) for the 94 Elements H-Pu*, J. Chem. Phys. **132** (2010) 154104,
DOI: `10.1063/1.3382344`.

[119] R. Dovesi, A. Erba, R. Orlando, C. M. Zicovich-Wilson, B. Civalleri, L. Maschio, M. Rérat,
S. Casassa, J. Baima, S. Salustro, and B. Kirtman,
Quantum-mechanical condensed matter simulations with CRYSTAL,
Wiley Interdisciplinary Reviews: Computat. Mol. Sci. **8** (2018) e1360,
DOI: `10.1002/wcms.1360`.

[120] H. J. Monkhorst and J. D. Pack, *Special points for Brillouin-zone integrations*,
Phys. Rev. B **13** (1976) 5188, DOI: `10.1103/PhysRevB.13.5188`.

[121] J. D. Pack and H. J. Monkhorst, *"Special points for Brillouin-zone integrations"—a reply*,
Phys. Rev. B **16** (1977) 1748, DOI: `10.1103/PhysRevB.16.1748`.

[122] F. Neese, *The ORCA Program System*, Wiley Interdiscip. Rev. Comput. Mol. Sci. **2** (2012) 73,
DOI: `https://doi.org/10.1002/wcms.81`.

[123] F. Neese, *Software Update: the ORCA Program System, Version 4.0*,
Wiley Interdiscip. Rev. Comput. Mol. Sci. **8** (2018) e1327,
DOI: `https://doi.org/10.1002/wcms.1327`.

[124]   S. Grimme, *Supramolecular Binding Thermodynamics by Dispersion-Corrected Density Functional Theory*, Chem. Eur. J. **18** (2012) 9955, DOI: https://doi.org/10.1002/chem.201200497.

[125]   J. Hafner, *FD*, Journal of Molecular Structure **651-653** (2003), Molecular Spectroscopy and Molecular Structure 2002. Proceedings of the XXVIth European Congress on Molecular Spectroscopy, Villeneuve d'Ascq, France, September 1-6, 2002. 3, ISSN: 0022-2860, DOI: https://doi.org/10.1016/S0022-2860(02)00624-5.

[126]   R. F. Ribeiro, A. V. Marenich, C. J. Cramer, and D. G. Truhlar, *Use of Solution-Phase Vibrational Frequencies in Continuum Models for the Free Energy of Solvation*, J. Phys. Chem. B **115** (2011) 14556, DOI: 10.1021/jp205508z.

[127]   W. Cai, V. V. Bulatov, J. F. Justo, A. S. Argon, and S. Yip, *Intrinsic Mobility of a Dissociated Dislocation in Silicon*, Phys. Rev. Lett. **84** (2000) 3346, DOI: 10.1103/PhysRevLett.84.3346.

[128]   W. Janke, L. Höltkemeier, A. Kühnle, and T. Speck, *Structure Formation of C60 on Insulating CaF2 Substrates: Matching Experiments with Simulations*, Advanced Materials Interfaces (2022) 2201510.

[129]   W. Cai, V. V. Bulatov, J. F. Justo, A. S. Argon, and S. Yip, *Kinetic Monte Carlo approach to modeling dislocation mobility*, Computational Materials Science **23** (2002) 124, ISSN: 0927-0256, DOI: https://doi.org/10.1016/S0927-0256(01)00223-3.

[130]   B. Meng and W. Weinberg, *Dynamical Monte Carlo studies of molecular beam epitaxial growth models: interfacial scaling and morphology*, Surface Science **364** (1996) 151, ISSN: 0039-6028, DOI: https://doi.org/10.1016/0039-6028(96)00597-3.

[131]   W. M. Young and E. W. Elcock, *Monte Carlo studies of vacancy migration in binary ordered alloys: I*, Proceedings of the Physical Society **89** (1966) 735, DOI: 10.1088/0370-1328/89/3/329.

[132]   S. A. Baeurle, T. Usami, and A. A. Gusev, *A new multiscale modeling approach for the prediction of mechanical properties of polymer-based nanomaterials*, Polymer **47** (2006) 8604, ISSN: 0032-3861, DOI: https://doi.org/10.1016/j.polymer.2006.10.017.

[133]   A. F. Voter, "Introduction to the Kinetic Monte Carlo Method," *Radiation Effects in Solids*, ed. by K. E. Sickafus, E. A. Kotomin, and B. P. Uberuaga, Dordrecht: Springer Netherlands, 2007, chap. 1 1, ISBN: 978-1-4020-5295-8.

[134]   J. H. Skone, M. Govoni, and G. Galli, *Nonempirical range-separated hybrid functionals for solids and molecules*, Phys. Rev. B **93** (2016) 235106, DOI: 10.1103/PhysRevB.93.235106.

[135]   G. Kresse and J. Hafner, *Ab Initio Molecular Dynamics for Liquid Metals*, Phys. Rev. B **47** (1993) 558, DOI: 10.1103/PhysRevB.47.558.

[136]   G. Kresse and J. Furthmüller, *Efficiency of Ab-initio Total Energy Calculations for Metals and Semiconductors Using a Plane-wave Basis Set*, Comput. Mater. Sci. **6** (1996) 15.

[137] G. Kresse and J. Furthmüller, *Efficient Iterative Schemes for Ab Initio Total-energy Calculations Using a Plane-wave Basis Set*, Phys. Rev. B **54** (1996) 11169.

[138] G. Kresse and D. Joubert,
From Ultrasoft Pseudopotentials to the Projector Augmented-wave Method,
Phys. Rev. B **59** (1999) 1758.

[139] R. P. Lowndes, D. H. Martin, and L. F. Bates,
Dielectric dispersion and the structures of ionic lattices,
Proc. R. Soc. Lond. A Math. Phys. Sci. **308** (1969) 473, DOI: `10.1098/rspa.1969.0021`.

[140] W. R. L. Lambrecht, C. Bhandari, and M. van Schilfgaarde, *Lattice Polarization Effects on the Screened Coulomb Interaction W of the GW Approximation*,
Phys. Rev. Mater. **1** (2017) 043802, DOI: `10.1103/PhysRevMaterials.1.043802`.

[141] M. Hochheim and T. Bredow, *Band-edge levels of the NaCl(100) surface: Self-consistent hybrid density functional theory compared to many-body perturbation theory*,
Phys. Rev. B **97** (2018) 235447, DOI: `10.1103/PhysRevB.97.235447`.

[142] N. F. Mott, *Conduction in polar crystals. II. The conduction band and ultra-violet absorption of alkali-halide crystals*, Trans. Faraday Soc. **34** (1938) 500, DOI: `10.1039/TF9383400500`.

[143] G. Baldini and B. Bosacchi, *Optical Properties of Alkali-Halide Crystals*,
Phys. Rev. **166** (1968) 863, DOI: `10.1103/PhysRev.166.863`.

[144] C. Gout and F. Pradal, *Pertes caracteristiques d'energie des electrons dans quelques halogenures alcalins: Structure de bande et plasmons*, J. Phys. Chem. Solids **29** (1968) 581,
ISSN: 0022-3697, DOI: `https://doi.org/10.1016/0022-3697(68)90025-5`.

[145] D. Blechschmidt, M. Skibowski, and W. Steinmann,
Photoemission from the Potassium Halides in the Photon Energy Range 7 to 30 eV,
Phys. Status Solidi B **42** (1970) 61, DOI: `10.1002/pssb.19700420106`.

[146] D. Blechschmidt, M. Skibowski, and W. Steinmann,
Photoelectric Yield of the Potassium Halides in the Photon Energy Range 10 to 35 eV,
Opt. Commun. **1** (1970) 275, ISSN: 0030-4018,
DOI: `https://doi.org/10.1016/0030-4018(70)90109-4`.

[147] T. Sasaki, Y. Iguchi, H. Sugawara, S. Sato, T. Nasu, A. Fjiri, S. Onari, K. Kojima, and T. Oya,
Photoelectric Emission of Potassium Halides in the Extreme Ultraviolet,
J. Phys. Soc. Jpn. **30** (1971) 580, DOI: `10.1143/JPSJ.30.580`.

[148] R. T. Poole, J. G. Jenkin, J. Liesegang, and R. C. G. Leckey,
Electronic Band Structure of the Alkali Halides. I. Experimental Parameters,
Phys. Rev. B **11** (1975) 5179, DOI: `10.1103/PhysRevB.11.5179`.

[149] I. Maruyama and R. Onaka, *Low Energy Electron Scattering by Alkali Halides*,
J. Phys. Soc. Jpn. **44** (1978) 196, DOI: `10.1143/JPSJ.44.196`.

[150] B. L. Henke, J. Liesegang, and S. D. Smith, *Soft-x-ray-induced Secondary-electron Emission from Semiconductors and Insulators: Models and Measurements*,
Phys. Rev. B **19** (1979) 3004, DOI: `10.1103/PhysRevB.19.3004`.

[151] G. Roy, G. Singh, and T. Gallon,
The Electron Energy Loss Spectra of Some Alkali Halides in the Band Gap Region,
Surf. Sci. **152–153** (1985) 1042, ISSN: 0039-6028,
DOI: https://doi.org/10.1016/0039-6028(85)90519-9.

[152] P. A. Rodnyi,
Problems and perspectives in the investigation of the electron conductivity of ionic crystals,
Sov. Phys. J. **32** (1989) 476.

[153] E. Taft and H. Philipp, *Photoelectric Emission from the Valence Band of Some Alkali Halides*,
J. Phys. Chem. Solids **3** (1957) 1, ISSN: 0022-3697,
DOI: https://doi.org/10.1016/0022-3697(57)90041-0.

[154] J. E. Eby, K. J. Teegarden, and D. B. Dutton, *Ultraviolet Absorption of Alkali Halides*,
Phys. Rev. **116** (1959) 1099, DOI: 10.1103/PhysRev.116.1099.

[155] T. Timusk, *Room temperature luminescence in pure alkali halides*,
J. Phys. Chem. Solids **18** (1961) 265, ISSN: 0022-3697,
DOI: https://doi.org/10.1016/0022-3697(61)90176-7.

[156] T. Timusk and W. Martienssen, *Recombination Luminescence in Alkali Halides*,
Phys. Rev. **128** (1962) 1656, DOI: 10.1103/PhysRev.128.1656.

[157] J. C. Phillips, *Ultraviolet Absorption of Insulators. III. fcc Alkali Halides*,
Phys. Rev. **136** (1964) A1705, DOI: 10.1103/PhysRev.136.A1705.

[158] P. H. Metzger, *On the Quantum Efficiencies of Twenty Alkali Halides in the 12-21 eV Region*,
J. Phys. Chem. Solids **26** (1965) 1879, ISSN: 0022-3697,
DOI: https://doi.org/10.1016/0022-3697(65)90221-0.

[159] G. R. Huggett and K. Teegarden, *Intrinsic Photoconductivity in the Alkali Halides*,
Phys. Rev. **141** (1966) 797, DOI: 10.1103/PhysRev.141.797.

[160] D. Fröhlich and B. Staginnus,
New Assignment of the Band Gap in the Alkali Bromides by Two-Photon Spectroscopy,
Phys. Rev. Lett. **19** (1967) 496, DOI: 10.1103/PhysRevLett.19.496.

[161] S. W. Duckett and P. H. Metzger, *Intrinsic Photoemission of Alkali Halides*,
Phys. Rev. **137** (1965) A953, DOI: 10.1103/PhysRev.137.A953.

[162] P. E. Best, *The Characteristic Electron Energy Loss Spectra of Some Alkali Halides*,
Proc. Phys. Soc. **79** (1962) 133, DOI: 10.1088/0370-1328/79/1/318.

[163] W. Pong and J. A. Smith, *Photoemission Studies of NaBr*, Phys. Rev. B **7** (1973) 5410,
DOI: 10.1103/PhysRevB.7.5410.

[164] J. A. Krumhansl and N. Schwartz, *The Calculation of F Center Energy Levels*,
Phys. Rev. **89** (1953) 1154, DOI: 10.1103/PhysRev.89.1154.2.

[165] D. Sheppard, P. Xiao, W. Chemelewski, D. D. Johnson, and G. Henkelman,
A Generalized Solid-state Nudged Elastic Band Method, J. Chem. Phys. **136** (2012) 074103.

[166] D. Sheppard and G. Henkelman, *Paths to Which the Nudged Elastic Band Converges*,
J. Comput. Chem. **32** (2011) 1769.

[167] D. Sheppard, R. Terrell, and G. Henkelman,
Optimization Methods for Finding Minimum Energy Paths,
J. Chem. Phys. **128** (2008) 134106.

[168] G. Henkelman, B. P. Uberuaga, and H. Jónsson, *A Climbing Image Nudged Elastic Band
Method for Finding Saddle Points and Minimum Energy Paths*,
J. Chem. Phys. **113** (2000) 9901.

[169] G. Henkelman and H. Jónsson, *Improved Tangent Estimate in the Nudged Elastic Band
Method for Finding Minimum Energy Paths and Saddle Points*,
J. Chem. Phys. **113** (2000) 9978.

[170] H. Jónsson, G. Mills, and K. W. Jacobsen,
"Nudged Elastic Band Method for Finding Minimum Energy Paths of Transitions,"
Classical and Quantum Dynamics in Condensed Phase Simulations,
ed. by B. J. Berne, G. Ciccotti, and D. F. Coker, World Scientific, 1998, chap. 16 385.

[171] E. Caldeweyher, C. Bannwarth, and S. Grimme,
Extension of the D3 Dispersion Coefficient Model, J. Chem. Phys. **147** (2017) 034112,
DOI: 10.1063/1.4993215.

[172] E. Caldeweyher, S. Ehlert, A. Hansen, H. Neugebauer, S. Spicher, C. Bannwarth, and
S. Grimme,
A Generally Applicable Atomic-charge Dependent London Dispersion Correction,
J. Chem. Phys. **150** (2019) 154122, DOI: 10.1063/1.5090222.

[173] Y. Zhang and W. Yang, *Comment on "Generalized Gradient Approximation Made Simple"*,
Phys. Rev. Lett. **80** (1998) 890, DOI: 10.1103/PhysRevLett.80.890.

[174] J. Sun, A. Ruzsinszky, and J. P. Perdew,
Strongly Constrained and Appropriately Normed Semilocal Density Functional,
Phys. Rev. Lett. **115** (2015) 036402, DOI: 10.1103/PhysRevLett.115.036402.

[175] H. Peng, Z.-H. Yang, J. P. Perdew, and J. Sun, *Versatile van der Waals Density Functional
Based on a Meta-Generalized Gradient Approximation*, Phys. Rev. X **6** (2016) 041005,
DOI: 10.1103/PhysRevX.6.041005.

[176] R. J. Brown and J. M. Vail,
Saddle-Point Configuration of the F-Centre in NaCl-Type Alkali Halides,
Phys. Status Solidi B **40** (1970) 737, DOI: 10.1002/pssb.19700400234.

[177] R. J. Brown and J. M. Vail,
Saddle-point F–centre: Role of the Excess Electron in Step Diffusion,
Phys. Status Solidi B **49** (1972) K33, DOI: 10.1002/pssb.2220490144.

[178] M. Kuklja, E. Kotomin, and A. Popov,
Semi-empirical Simulations of F-center Diffusion in KCl Crystals,
J. Phys. Chem. Solids **58** (1997) 103, ISSN: 0022-3697,
DOI: https://doi.org/10.1016/S0022-3697(96)00096-0.

[179] B. Sadigh, P. Erhart, and D. Åberg, *Variational Polaron Self-interaction-corrected
Total-energy Functional for Charge Excitations in Insulators*, Phys. Rev. B **92** (2015) 075202,
DOI: 10.1103/PhysRevB.92.075202.

[180] D. Walker, P. K. Verma, L. M. Cranswick, R. L. Jones, S. M. Clark, and S. Buhre,
Halite-sylvite Thermoelasticity, Am. Mineral. **89** (2004) 204.

[181] V. T. Deshpande, *Thermal Expansion of Sodium Fluoride and Sodium Bromide*,
Acta Crystallogr. **14** (1961) 794, DOI: `10.1107/S0365110X61002357`.

[182] Y. Venudhar, L. Iyengar, and K. K. Rao,
Thermal Expansion and Debye Temperatures of KCl-KBr Mixed Crystals by an X-ray Method,
J. Mater. Sci. **21** (1986) 110.

[183] D. Rappoport and F. Furche,
Property-optimized Gaussian Basis Sets for Molecular Response Calculations,
J. Chem. Phys. **133** (2010) 134105, DOI: `10.1063/1.3484283`.

[184] T. A. Manz and N. G. Limas, *Introducing DDEC6 Atomic Population Analysis: Part 1.
Charge Partitioning Theory and Methodology*, RSC Adv. **6** (2016) 47771,
DOI: `10.1039/C6RA04656H`.

[185] N. G. Limas and T. A. Manz, *Introducing DDEC6 Atomic Population Analysis: Part 2.
Computed Results for a Wide Range of Periodic and Nonperiodic Materials*,
RSC Adv. **6** (2016) 45727, DOI: `10.1039/C6RA05507A`.

[186] T. A. Manz, *Introducing DDEC6 Atomic Population Analysis: Part 3. Comprehensive Method
to Compute Bond Orders*, RSC Adv. **7** (2017) 45552, DOI: `10.1039/C7RA07400J`.

[187] C. E. Miller, *Hydrogenation with diimide*, J. Chem. Educ. **42** (1965) 254.

[188] G. Henkelman, A. Arnaldsson, and H. Jónsson,
A Fast and Robust Algorithm for Bader Decomposition of Charge Density,
Computat. Mater. Sci. **36** (2006) 354, ISSN: 0927-0256,
DOI: `https://doi.org/10.1016/j.commatsci.2005.04.010`.

[189] E. Sanville, S. D. Kenny, R. Smith, and G. Henkelman,
Improved Grid-based Algorithm for Bader Charge Allocation,
J. Comput. Chem. **28** (2007) 899, DOI: `https://doi.org/10.1002/jcc.20575`.

[190] W. Tang, E. Sanville, and G. Henkelman,
A Grid-based Bader Analysis Algorithm without Lattice Bias,
J. Phys. Condens. Matter **21** (2009) 084204, DOI: `10.1088/0953-8984/21/8/084204`.

[191] X. Wu, Z. Qin, H. Xie, R. Cong, X. Wu, Z. Tang, and H. Fan,
Photoelectron Imaging and Theoretical Studies of Group 11 Cyanides MCN (M = Cu, Ag, Au),
J. Phys. Chem. A **114** (2010) 12839, DOI: `10.1021/jp1013708`.

[192] *Endoergic Ion–molecule-collision Processes of Negative Ions. III. Collisions of I− on O2, CO,
and CO2*, Int. J. Mass Spectrom. Ion Phys. **20** (1976) 19, ISSN: 0020-7381,
DOI: `https://doi.org/10.1016/0020-7381(76)80029-0`.

[193] C. M. Zall, J. C. Linehan, and A. M. Appel,
A Molecular Copper Catalyst for Hydrogenation of CO2 to Formate,
ACS Catal. **5** (2015) 5301, DOI: `10.1021/acscatal.5b01646`.

[194] N. O. Thiel, F. Pape, and J. F. Teichert,
       "Homogeneous Hydrogenation with Copper Catalysts,"
       Homogeneous Hydrogenation with Non-Precious Catalysts, ed. by J. F. Teichert,
       John Wiley & Sons, Ltd, 2019, chap. 4 87, ISBN: 9783527814237,
       DOI: https://doi.org/10.1002/9783527814237.ch4.

[195] C. M. Zall, J. C. Linehan, and A. M. Appel, *Triphosphine-Ligated Copper Hydrides for CO2
       Hydrogenation: Structure, Reactivity, and Thermodynamic Studies*,
       J. Am. Chem. Soc. **138** (2016) 9968, DOI: 10.1021/jacs.6b05349.

[196] L. Zhang, J. Cheng, and Z. Hou, *Highly Efficient Catalytic Hydrosilylation of Carbon Dioxide
       by an N-heterocyclic Carbene Copper Catalyst*, Chem. Commun. **49** (2013) 4782,
       DOI: 10.1039/C3CC41838C.

[197] K. Nakamae, B. Kure, T. Nakajima, Y. Ura, and T. Tanase, *Facile Insertion of Carbon Dioxide
       into Cu2(μ-H) Dinuclear Units Supported by Tetraphosphine Ligands*,
       Chem. Asian J. **9** (2014) 3106, DOI: https://doi.org/10.1002/asia.201402900.

[198] K. Motokura, D. Kashiwame, N. Takahashi, A. Miyaji, and T. Baba,
       *Highly Active and Selective Catalysis of Copper Diphosphine Complexes for the
       Transformation of Carbon Dioxide into Silyl Formate*, Chem. Eur. J. **19** (2013) 10030,
       DOI: https://doi.org/10.1002/chem.201300935.

[199] R. Watari, Y. Kayaki, S.-i. Hirano, N. Matsumoto, and T. Ikariya, *Hydrogenation of Carbon
       Dioxide to Formate Catalyzed by a Copper/1,8-Diazabicyclo[5.4.0]undec-7-ene System*,
       Adv. Synth. Catal. **357** (2015) 1369, DOI: https://doi.org/10.1002/adsc.201500043.

[200] A. Zavras, H. Ghari, A. Ariafard, A. J. Canty, and R. A. J. O'Hair,
       Gas-Phase Ion-Molecule Reactions of Copper Hydride Anions [CuH2]− and [Cu2H3]−,
       Inorg. Chem. **56** (2017) 2387, DOI: 10.1021/acs.inorgchem.6b02145.

Appendix

Electronic Properties of the Alkali Halide F and M Center

Michael Häfner[*] and Thomas Bredow[*]

[*] Mulliken Center for Theoretical Chemistry, Universität Bonn, Beringstr. 4, 53115 Bonn, Germany

F and M centers in alkali halides: A theoretical study applying self-consistent dielectric-dependent hybrid density functional theory

Michael Häfner ⬤ and Thomas Bredow[*]

Mulliken Center for Theoretical Chemistry, Institut für Physikalische und Theoretische Chemie, Universität Bonn,
Beringstraße 4, 53115 Bonn, Germany

Point defects significantly change electronic properties of alkali halides and thereby enhance their reactivity. However, both the experimental and theoretical description of defects such as the *F* center and the *M* center are still far from complete, in particular for the less common bromides. A self-consistent dielectric-dependent global hybrid and plane-wave approach is employed for a comparative theoretical study of the electronic properties of NaCl, KCl, NaBr, and KBr bulk and (100) surface, both perfect and defective. For these systems, a zero-point renormalization was calculated to account for electron-phonon interaction and enhance comparability with the experiment. We focus on anion vacancy defects, the so-called *F* and *M* centers. The methodology employed is capable of reproducing measured defect level energies, electronic band gaps, ionization energies, and electron affinities within experimental errors. A general trend of the *F* center defect level energy with respect to the lattice parameter is found. The results for both the *F* and the *M* center of KCl agree with findings from magnetic resonance experiments. The defect orbitals are analyzed and virtual states of the defect electron are identified.

I. INTRODUCTION

The presence of defects can lead to drastic changes of the electronic structure of insulating compounds. Even unreactive substances, e.g., table salt NaCl, become reactive when point defects such as *F* centers are introduced. For NaCl and KCl, the reductive power of the trapped electron in surface *F* centers has been explored both experimentally [1–4] and theoretically [5–8]. The defect electron is transferred to adsorbed water [3,4] and salicylic acid molecules [1,2]. There exists a plethora of experimental works for the electronic structure of the pristine alkali halides. Available experimental results for pristine NaCl and KCl were summarized recently by our group [8,9]. For the bromides, there are also many experimental results for KBr [10–28] but significantly less for NaBr [12,15,16,18,20,24,27,29,30]. There are also theoretical works [9,31–40] that calculated the electronic structure of bulk and surfaces, usually employing the GW approximation. However, these studies are limited to the chlorides; no first-principles calculations of the alkali bromides were found.

F centers in alkali halides were investigated experimentally [41–54]. Most theoretical work on *F* centers is limited to LiF and NaCl [6,55–61], but there also exists an analysis of NaF and KCl by Zwicker [62] and an extensive analysis of the *F* center absorption energies for the fluorides, chlorides, and bromides of Li, Na, and K by Tiwald *et al.* [63]. Aside from Refs. [5,7,8] there are no investigations of defective surfaces available.

In recent studies of defective NaCl and KCl, we employed self-consistent dielectric-dependent global hybrid (sc-DDGH)

functionals [35,64] and were able to reproduce measured electronic properties [7,8] with an accuracy comparable to GW methods. These sc-DDGH calculations were performed with wave functions based on a linear combination of atomic orbitals (LCAO). However, a drawback of this approach is the choice of a sufficiently diffuse basis set to correctly describe the unoccupied states, because pseudolinear dependencies occur that severely affect SCF convergence and need to be addressed, in particular in slab models. In this study, we circumvented this issue by switching to a plane-wave basis.

The sc-DDGH functionals obtained with LCAO and plane waves are compared for the alkali halides NaCl, KCl, NaBr, and KBr, and it is shown that the latter provide better agreement with experimental dielectric constants. The plane-wave sc-DDGH functionals were then employed to investigate *F* centers in the bulk and on the (100) surface of the four alkali halides, in particular the defect level and the valence band and conduction band edge levels.

A new aspect in this study are *M* centers, which have been extensively investigated experimentally [65–74] and which, due to their optical properties, may serve as information carriers of optical information storage systems [75,76]. To the best of our knowledge, *M* centers in alkali halides, consisting of two adjacent halogen vacancies, have so far only been described once using DFT methods. Eid [77] explored the diffusion of atoms in the KBr(100) surface with *M* centers. We decided to study the *M* center in the bulk and on the (100) surface of KCl because there are experimental reference data available for this substance. We investigate the closed-shell state with two paired electrons localized in one vacancy site and two open-shell states where the defect electrons are localized in both defect sites.

---

[*]bredow@thch.uni-bonn.de

In the following section we provide details of our computational setup. We then compare dielectric constants obtained with LCAO and plane-wave wave functions. Plane-wave sc-DDGH is applied to defective NaCl, KCl, NaBr, and KBr.

II. COMPUTATIONAL DETAILS

We performed all calculations with the CRYSTAL17 crystalline orbital program package (version 1.0.2) [78] and the VASP 6.1.1 plane-wave program package [79–81]. For the bulk calculations with CRYSTAL we have used tight integral tolerances (7 7 7 14 42), a $8 \times 8 \times 8$ $\vec{k}$-point Monkhorst-Pack (MP) grid, and the adjusted def2-QZVPP [82] basis set from Ref. [8]. For the bulk calculations with VASP, we used the precision mode Accurate, a cutoff energy of 500 eV, and the standard pseudopotentials for the PAW method [83]. Here, the $4 \times 4 \times 4$ $\vec{k}$-point MP grid was sufficiently converged (see Supplemental Material [84]). All primitive-cell surface calculations were carried out with a $4 \times 4 \times 1$ $\vec{k}$-point MP grid, 10 layers, and 20 Å of vacuum between the repeating slabs. The defect models were calculated with a 4×4 supercell of the primitive cell for the surface and a $2 \times 2 \times 2$ supercell of the crystallographic cell for the bulk, a Γ-$\vec{k}$-point MP grid, and 20 Å vacuum distance for the surface. For the defect calculations the accuracy parameter was lowered to Normal. Both the surface F center and the M center were calculated using five-layer models. It was tested that this slab thickness is large enough to reduce defect-defect interaction to less than a tenth of an eV.

We optimized the atom positions of surface and defective models with PBE [85] and D3(BJ)-dispersion correction [86,87] using fixed lattice constants from the bulk optimizations. A structure was considered converged when all forces were <0.001 eV/Å. On average, the experimental 0 K lattice constants are overestimated by around 1%. Electronic properties were calculated using a sc-DDGH functional based on PBE that will be called sc-PBE0 in this work, following the naming convention by Fritsch *et al.* [88]. For the CRYSTAL calculations, the Fock-exchange fraction x was self-consistently calculated from the inverse of the dielectric constant ε_∞ [89–91]. With VASP, ε_∞ is calculated from the self-consistent response of the solid to a finite electric field. PBE0 with $x = 0.25$ was taken as a starting point for all self-consistent iterations of x. It has to be noted that, according to our experience, the final result for x is essentially independent from the starting point. In all cases, the Fock-exchange fraction x is used for the bulk as well as the surface models which is considered a valid strategy according to Ref. [64]. The defective surface models contain two vacancies in the top and bottom layer in order to increase symmetry and to avoid artificial dipole moments. Whenever PBE is used, the SCF calculation is carried out with the default Kosugi algorithm. For any hybrid functional calculation, a preconditioned conjugate gradient algorithm is used in the SCF procedure. Gaussian smearing is applied with a $\sigma = 0.05$ eV. Mixing of the density matrix is performed with the Kerker scheme [92] with BMIX = 0.01 to enhance electronic convergence. A zero-point renormalization (ZPR) of the orbital energies was calculated with PBE using the $5 \times 5 \times 5$ crystallographic

TABLE I. Comparison of the static dielectric constant ε_∞ calculated with sc-PBE0 for RT lattice parameters and experiment.

System	ε_∞			deviation (%)	
	CRYSTAL	VASP	exp.[a]	CRYSTAL	VASP
NaCl	2.262	2.308	2.329	-2.9	-0.9
KCl	2.105	2.149	2.173	-3.1	-1.1
NaBr	2.52	2.62	2.60	-3.0	0.5
KBr	2.280	2.344	2.358	-3.3	-0.6

[a]Reflectivity experiment at 290 K [98].

supercell of the bulk and a one-shot method by Zacharias and Giustino [93,94] as implemented in VASP. Convergence details can be found in the Supplemental Material [84]. The electron-phonon interaction is evaluated statistically with a Monte-Carlo sampling.

III. RESULTS AND DISCUSSION

A. Bulk properties

In the first step the Fock-exchange fraction x was self-consistently calculated as the inverse of the dielectric constant ε_∞ [35] for NaCl, KCl, NaBr, and KBr, using both room temperature (RT) and 0 K lattice parameters. The literature values of RT lattice parameters are 5.640 Å for NaCl [95], 6.288 Å for KCl [95], 5.974 Å for NaBr [96], and 6.599 Å for KBr [97]. The static dielectric constants ε_∞ obtained with VASP and CRYSTAL are compared to experimental data measured at 290 K [98] in Table I.

The plane-wave results are significantly closer (mean deviation ∼−0.5%) to the experimental references than the LCAO results (mean deviation ∼−3.0%). The main reason for the larger error of the LCAO results is probably the insufficient description of the polarizability of the systems with the finite-size basis. The inclusion of more diffuse functions would improve the results but leads to SCF instabilities due to pseudolinear dependencies, which are a nontrivial issue to solve. For this reason, we only used VASP for all further calculations.

In the next step we evaluated the influence of the temperature on the dielectric constant. We compared the dielectric constant calculated with the 0 K lattice constant to the measurement at 4 K [98] in Table II. The experimental lattice constants we used are 5.595 Å for NaCl [99], 6.161 Å for KCl [100], and 6.511 Å for KBr [101]. For NaBr no experimental low-temperature lattice constant was found.

TABLE II. Comparison of the static dielectric constant ε_∞ calculated with sc-PBE0 for low-temperature lattice parameters and experiment.

System	VASP	Experiment[a]	Deviation (%)
NaCl	2.330	2.351	0.9
KCl	2.211	2.204	-0.3
KBr	2.392	2.390	-0.1

[a]Reflectivity experiment at 4K [98].

TABLE III. Electronic bulk band gap E_g with RT lattice parameters.

System	NaCl (eV)	KCl (eV)	NaBr (eV)	KBr (eV)
E_g	8.80	9.07	7.13	7.70

The deviations from the experiment are smaller than 1% and the average deviation is 0.2%, well within the experimental errors. We conclude that the plane-wave sc-PBE0 method correctly describes the increase of the dielectric constant with decreasing temperature.

With the same theoretical setup we calculated the fundamental band gap E_g for all four halides. The results are given in Table III.

A comparison with experimental data is not made, since measurements that specifically measure the bulk band gap were not found for any of the halides. In contrast, alkali halides bulk band gaps were studied at various theoretical levels including GW methods [9,31–34,36–38,40,102]. Most of these first-principles studies focused on NaCl. GW methods are more sophisticated than sc-DDGH functionals and are thus expected to yield higher accuracy for electronic properties. However, due to their large computational effort, approximations have to be introduced, e.g., in the degree of self-consistency of the GW cycle or the number of bands. For these reasons, the results from the GW methods differ considerably among each other and from sc-PBE0 (see Supplemental Material [84]).

For KCl there are only two works [38,40]. The bromides were not studied using GW at all up to now.

For the surface calculations described below, we recalculated the optimal Fock exchange fraction x after optimizing the bulk lattice parameters with PBE-D3(BJ). A comparison of the optimized values of a to experimental data can be found in the Supplemental Material [84]. We obtained $x = 42.8\%$ for NaCl, $x = 46.3\%$ for KCl, $x = 37.7\%$ for NaBr, and $x = 42.4\%$ for KBr.

B. Electronic properties of the alkali halide(100) surfaces

Due to an arbitrary shift of one-electron levels in three-dimensional periodic calculations, absolute band energies are only meaningful for two-dimensional slab models. For the bulk, only the electronic band gap is physically meaningful. For the slab models, conduction band minimum (CBM) and valence band maximum (VBM) are calculated relative to the vacuum level. Convergence of the electronic properties of our models within 0.1 eV was achieved with a five-layer slab model and 20 Å of vacuum. For comparison with other theoretical studies [103], we however calculated the surfaces with ten-layer slab models. For NaBr and KBr there is no comprehensive collection of measured electronic properties in the literature, aside from a relatively small and dated analysis by Poole *et al.* [24]. As experimental references for NaCl and KCl we used our recent summaries [8,9].

To ensure a correct comparison of the experiments with the calculation, electron-phonon coupling must be considered. Unfortunately, we could not find data for any other system

than NaCl. Lambrecht *et al.* [36] calculated a ZPR of 0.167 eV for NaCl, which has to be applied to the KS-DFT band gap. We calculated the same parameter based on a one-shot Monte-Carlo sampling method [93,94] and obtained a converged ZPR correction of 0.181 eV for NaCl bulk. The deviation from the earlier result is lower than the standard deviation of the experimental measurements. The CBM and VBM energies of all halides are adjusted according to the results of the present bulk ZPR calculations. It was attempted to calculate the ZPR directly for the (100) slab models. However, the calculated ZPR did not converge with increasing surface supercell size, showing erratic behavior indicating further yet unresolved issues with the one-shot approach applied to slabs.

1. The KBr(100) surface

A considerable number of experimental studies of the electronic properties of KBr are available in the literature. In Table IV we list values obtained from an extensive literature search [10–28]. The experimental results for the electronic band gap E_g range from 7.3 to 8.05 eV with a relatively even distribution of values above and below the average value, 7.6 eV. Most of the electronic band gaps obtained more recently with modern methods such as electron energy loss spectroscopy (EELS) [27], energy distribution curves (EDC) [26], and electronic conductivity [28] are below this value. Two experiments [16,17] yield rather high band gaps of around 8 eV and may be considered as outliers. Only four values were found for the ionization potential (*IP*), ranging from 7.5 eV to 8.2 eV. Three of them lie at 8 eV or above; only Poole *et al.* found a much lower value of 7.5 eV [24]. This group generally underestimates the ionization potentials of all halides discussed in this work, therefore the corresponding values were regarded as outliers.

Most results for the electron affinity (*EA*) are obtained as the difference of *IP* and E_g. The value derived by Blechschmidt *et al.* [22] was excluded because their methodology generally overestimated *EA* for all considered systems. Only the two EDC measurements obtained *EA* directly through a data fit [25,26]. Most results for *EA* obtained as $IP - E_g$ are either about 1 eV or about 0.3 eV, while the direct results are ~0.5 eV.

The averages of the selected experimental results are 7.61 ± 0.25 eV for E_g, 7.95 ± 0.31 eV for *IP*, and 0.63 ± 0.29 eV for *EA* (Table IV). After applying a ZPR correction of 0.10 eV (0.08 eV to the VBM and 0.02 eV to the CBM) the reference values are $E_g = 7.71 \pm 0.25$, $IP = 8.03 \pm 0.31$, and $EA = 0.61 \pm 0.29$. These values are not fully consistent as the relationship $E_g = IP - EA$ is not fulfilled. This error amounts to 0.28 eV, a clear indication of a fundamental discrepancy between the various methods of determining the different electronic properties.

The sc-PBE0 results for E_g, *IP*, and *EA* of KBr(100) are 7.60 eV, 8.05 eV, and 0.45 eV, respectively. They are within the error bars of the experimental average, also after accounting for ZPR. The calculated surface band gap is 0.1 eV lower than the bulk band gap (cf. Table III). This indicates that there are no pronounced surface states in this system. It is thus expected that differences between the experimental studies are not due to the surface sensitivity of the measurement.

TABLE IV. Measured electronic properties of KBr (electronic band gap E_g, ionization potential IP, and electron affinity EA). UPS is ultraviolet-photoelectron spectrometry, EELS is electron energy loss spectroscopy, EDC is the energy distribution curve of secondary electrons emitted after irradiation with soft x rays.

Reference	Method	System	E_g (eV)	IP (eV)	EA (eV)
Mott (1985)[a]	UV absorption	Literature data			*0.7* [u]
Taft (1957)[b]	UPS	Film on LiF, 300 K		8.1	
Eby (1959)[c]	UV absorption	Film on LiF, 80 ± 2 K	7.8		*0.3*[u]
Timusk (1961)[d]	Luminescence	Single crystal, RT			*1.0*[u]
Timusk (1962)[e]	Luminescence	Single crystal, RT	7.3	8.2	*0.9*[u]
Phillips (1964)[f]	Evaluation of literature[c]	Film on LiF, 80 ± 2 K	7.8		
Metzger (1965)[g]	UPS	Films on 450Å, Al_2O_3[h]	8.05		*0.25*[u]
Huggett (1966)[i]	UV absorption/photocond.	Thin film, single crystalline, 10 K	8.0		
Fröhlich (1967)[j]	Two-photon spectroscopy	Single crystal, 20 K	7.4		
Baldini (1968)[k]	Reflectivity	Single crystal, 55 K	7.45		
Gout (1968)[l]	EELS	1000 Å films	7.6		
Blechschmidt (1970)[m]	UPS	2000–5000 Å films on Al		8.0	
Blechschmidt (1970)[n]	UPS	Thin films			*1.5–1.9*[u]
Sasaki (1971)[o]	UPS	Film on stainless steel			*0.9*[u]
Poole (1975)[p]	UPS	Single crystal		7.5	
Maruyama (1978)[q]	2nd elec. EDC (fit)	500 Å, coated with gold	7.8		0.4
Henke (1979)[r]	2nd elec. EDC (fit)	3000 Å, coated with gold	7.4		0.55
Roy (1985)[s]	EELS	Thin film on stainless steel	7.4		
Rodnyi (1989)[t]	Electronic conductivity	Literature data	7.5		
Averaged values			7.61 ± 0.25	7.95 ± 0.31	0.63 ± 0.29
ZPR corrected			7.71 ± 0.25	8.03 ± 0.31	0.61 ± 0.29
This study	sc-PBE0		7.60	8.05	0.45

[a]Reference [10].
[b]Reference [11].
[c]Reference [12].
[d]Reference [13].
[e]Reference [14].
[f]Reference [15].
[g]Reference [16].
[h]Reference [104].
[i]Reference [17].
[j]Reference [18].
[k]Reference [19].
[l]Reference [20].
[m]Reference [21].
[n]Reference [22].
[o]Reference [23].
[p]Reference [24].
[q]Reference [25].
[r]Reference [26].
[s]Reference [27].
[t]Reference [28].
[u]*EA* not measured directly, but calculated from the difference $IP - E_g$.

For comparison, the corresponding VASP-PBE0 ($x = 0.25$) values are $E_g = 6.31$ eV, IP $= 7.18$ eV, and EA $= 0.88$ eV. They deviate significantly from the sc-DDGH result and from experiment. This underlines the importance of self-consistent optimization of the Fock-exchange fraction x for the calculation of electronic properties.

2. The NaBr(100) surface

There are comparably few experimental data available on electronic properties of NaBr [12,15,16,18,20,24,27,29,30],

see Table V. For the ionization potential, only three values, 7.6 eV, 8.0 eV, and 7.3 eV, were found. The latter result obtained by Poole *et al.* [24] is most likely an outlier for the same reason as discussed for KBr. The electron affinity was only determined once (as $IP - E_g$); we did not find any direct measurements. Averages of the experimental results are 7.35 ± 0.30 eV for E_g and 7.63 ± 0.35 eV for IP. The reference value for EA is obtained by subtracting the averages of E_g and IP. A ZPR of 0.12 eV (0.10 eV to the VBM and 0.02 eV to the CBM) was calculated, giving experimental references 7.47 ± 0.33 eV for E_g, 7.73 ± 0.35 eV for IP, and 0.26 eV for EA.

TABLE V. Measured electronic properties of NaBr (electronic band gap E_g, ionization potential IP, and electron affinity EA) in eV. UPS is ultraviolet-photoelectron spectrometry; EELS is the electron energy loss spectrum.

Reference	Method	System	E_g (eV)	IP (eV)	EA (eV)
Eby (1959)[a]	UV absorption	Film on LiF, 80 ± 2 K	7.7		
Best (1962)[b]	EELS	Films on tungsten		7.6	
Phillips (1964)[c]	Evaluation of literature	Film on LiF, 80 ± 2 K	7.5		
Metzger (1965)[d]	UPS	Films on 450 Å Al_2O_3[j]	8.1		*0.4*[k]
Fröhlich (1967)[e]	Two-photon spectroscopy	Single crystal, 20 K	7.1		
Gout (1968)[f]	EELS	1000 Å films	7.7		
Pong (1973)[g]	UPS	Evaporated films		8.0	
Poole (1975)[h]	UPS	Single crystal		7.3	
Roy (1985)[i]	EELS	Thin film on stainless steel	7.1		
Averaged values			7.35 ± 0.30	7.63 ± 0.35	0.28[k]
ZPR corrected			7.47 ± 0.30	7.73 ± 0.35	0.26[k]
This study	sc-PBE0		7.16	8.15	0.99

[a]Reference [12].
[b]Reference [29].
[c]Reference [15].
[d]Reference [16].
[e]Reference [18].
[f]Reference [20].
[g]Reference [30].
[h]Reference [24].
[i]Reference [27].
[j]Reference [104].
[k]*EA* not measured directly but calculated from the difference $IP - E_g$.

The sc-PBE0 values for E_g, IP, and EA of NaBr(100) are 7.16 eV, 8.15 eV, and 0.99 eV, respectively. As observed for KBr(100), the surface band gap is almost the same as for the bulk (cf. Table III). For comparison, PBE0 yields $E_g = 6.18$ eV, IP = 7.53 eV, and EA = 1.35 eV. Similar differences between the standard and the self-consistent hybrid method are observed as for KBr.

The band gap resulting from sc-PBE0 is still within the error of the experimental reference. However, there is a clear discrepancy between our result and the average of the IP and several of the experimental measurements. The functional overestimates the average experimental IP by about 0.5 eV. The comparison is, however, difficult due to the small number of measurements and their large scatter. According to Fröhlich and Bernd [18], the electronic properties of NaBr are

more difficult to measure than for other alkali halides, and a clear determination from single-photon absorption (as, e.g., in UPS) is not easily possible. They circumvented this by using two-electron spectroscopy and obtained a band gap of 7.1 eV which is close to the theoretical result. Unfortunately, they did not measure the IP in that study. Considering the performance of sc-PBE0 with the other systems and the good agreement of the dielectric constant with experiment, we suggest to use the sc-PBE0 result and not the experimental average as reference for further theoretical works. Similar considerations hold for the EA.

3. The NaCl and KCl(100) surfaces

The electronic properties calculated with sc-PBE0 for the NaCl(100) surface are $E_g = 8.60$ eV, IP = 8.99 eV, and

TABLE VI. Electronic properties of NaCl and KCl(100) surfaces (electronic band gap E_g, ionization potential IP, and electron affinity EA). The zero-point correction for NaCl is calculated as 0.18 eV (0.14 eV to the VBM and 0.04 eV to the CBM); the zero-point correction for KCl is calculated as 0.18 eV (0.15 eV to the VBM and 0.03 eV to the CBM).

Reference	Method	E_g (eV)	IP (eV)	EA (eV)
NaCl				
Hochheim (2018)[a]	Literature review	8.88 ± 0.2	9.14	0.54
Hochheim (2018)[l]	LCAO-sc-PBE0	8.75	9.10	0.34
This study	VASP-sc-PBE0	8.60	8.99	0.39
KCl				
Häfner (2020)[b]	Literature review	8.72 ± 0.18	8.68 ± 0.30	0.39 ± 0.21
Häfner (2020)[c]	LCAO-sc-PBE0	8.81	8.93	0.12
This study	VASP-sc-PBE0	8.53	8.69	0.16

[a]Literature review [9].
[b]Literature review [8].

TABLE VII. Spin-up and spin-down band gaps E_g, E^*, and $E^\dagger$ of the alkali halide solids with F centers.

	NaCl (eV)	KCl (eV)	NaBr (eV)	KBr (eV)
spin-up				
E_g	9.23	9.34	7.55	7.98
E^*	4.02	3.70	3.22	3.11
spin-down				
E_g	9.45	9.52	7.85	8.20
$E^\dagger$	8.19	8.51	6.73	7.30

EA = 0.39 eV (Table VI). The surface band gap is about 0.2 eV smaller than the bulk band gap. This difference is slightly larger than for the bromides. For the KCl(100) surface we obtained $E_g = 8.53$ eV, IP = 8.69 eV, and EA = 0.16 eV. In this case, the band gap of the surface is about 0.55 eV smaller than the band gap of the bulk. KCl is the only system where such a large discrepancy was observed. For this system we expect larger effects in measurements of electronic properties depending on their surface sensitivity. However, this was not observed in the experiments described in Ref. [8]. This indicates that none of the experiments is able to clearly distinguish between bulk and surface results.

We compared the sc-PBE0 results to average experimental values obtained in Refs. [9] and [8]. For both systems, the calculated values are within the error bars of the experimental averages. There are small deviations (0.04–0.28 eV) from our previous calculations obtained with LCAO-sc-PBE0. Due to the use of plane waves, the results of the present study are closer to the basis set limit of the sc-PBE0 method.

C. The F center

1. Bulk F center

We examined the bulk F center (F_B) of all four halides using sc-PBE0. The calculations were performed in the doublet state. The resulting band gaps are given in Table VII. E^* is the energy difference between the defect level and the CBM. For the unoccupied (spin-down) defect levels, E^* is about 1 eV.

FIG. 2. Defect orbital of the KCl bulk F center. Isosurface cutoff = 3.

E_g is the energy difference between VBM and CBM. These parameters are also explained in Fig. 1.

It is found that E_g is generally larger than in the pristine bulk and smaller for the spin-up than for the spin-down ladder. We conclude that this shift is due to two counteracting effects. The first results from the Coulomb repulsion introduced by the defect electron leading to a destabilization of all low-lying unoccupied bands. The second results from the stabilizing exchange interaction of the defect electron with the lowest-lying unoccupied band because it shares its s-type character with the defect. This exchange interaction also lowers other defect bands containing s-type or p-type contribution in the defect center. For the lowest-lying unoccupied band, the effects decrease with increasing supercell size, i.e., lower defect concentration. On the other hand, for orbitals which are localized in the defect site, the effect remains significant also for larger supercells. The effect is observed both for PBE and for sc-PBE0 and is significantly larger for sc-PBE0.

E^* decreases from 4.02 eV to 3.11 eV in the series NaCl to KBr. The values are however not quantitatively related to the lattice parameters of the dielectric constants.

A graphical representation of the defect orbital is given in Fig. 2, exemplarily for KCl. For the other alkali halides the
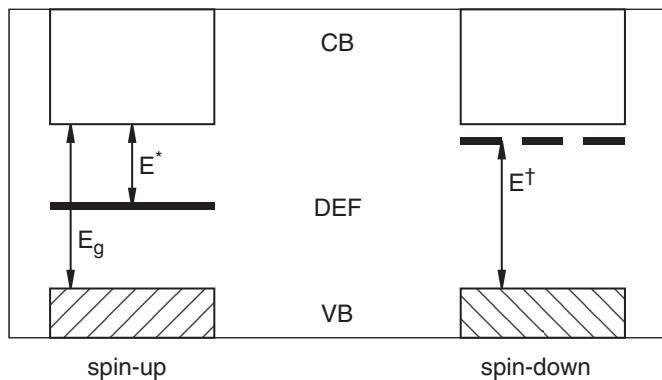

FIG. 1. Band scheme of the F center in the alkali halide bulk. The hatched bar and the solid line are occupied bands; the empty bar and the dashed line are unoccupied bands.
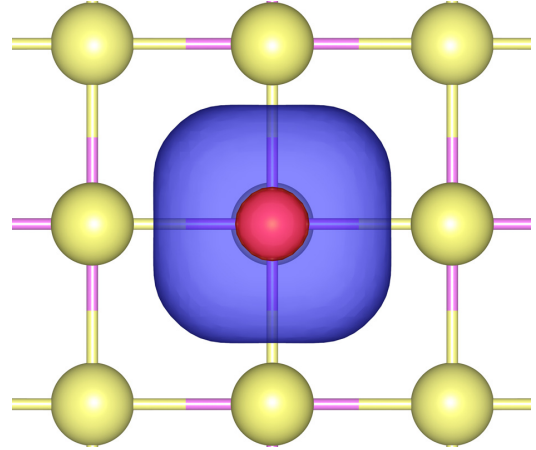
TABLE VIII. Band levels E_{def}, CBM, and VBM of the alkali halide (100) surfaces with F centers.

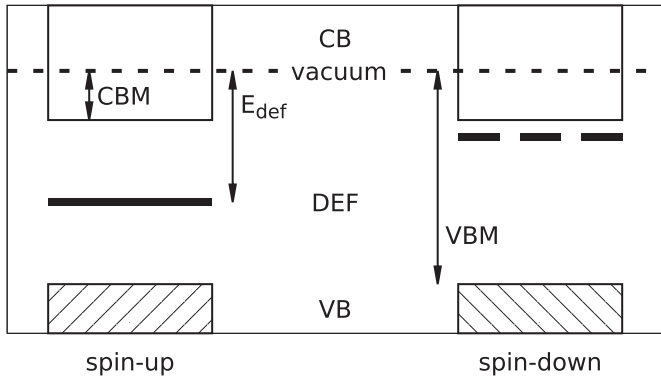|	NaCl (eV)	KCl (eV)	NaBr (eV)	KBr (eV)
spin-up				
VBM	−9.08	−8.82	−8.22	−8.12
E_{def}	−3.61	−3.12	−3.54	−3.08
CBM	−0.36	−0.19	−0.87	−0.42
spin-down				
VBM	−9.08	−8.82	−8.22	−8.12
E_{def}	−0.92	−0.48	−1.36	−0.79
CBM	−0.21	−0.05	−0.64	−0.27
pristine				
VBM	−8.99	−8.69	−8.15	−8.05
CBM	−0.39	−0.16	−0.99	−0.45

FIG. 3. Band scheme of the *F* center on the alkali halide(100) surface. The hatched bar and the solid line are occupied bands; the empty bar and the dashed line are unoccupied bands. The narrow dotted line indicates the vacuum reference.

FIG. 4. E_{def} as a function of $1/a$ for NaCl(100), KCl(100), NaBr(100), and KBr(100).

defect orbitals have similar shape. It is basically a diffuse *s*-type function but with some *p*-type contributions due to the interaction with the neighboring ions. This in line with magnetic spin resonance experiments conducted on the NaCl *F* center [105–110].

We also identified three degenerate virtual defect orbitals with a strong *p*-type contribution. They are similar to the orbitals calculated for LiF in Ref. [56]. The *p*-type orbitals are responsible for the first optical transition observed in measurements of the F_{B} center [52]. A depiction of those orbitals can be found in the Supplemental Material [84].

2. (100) surface F center

The electronic properties of the (100) surface *F* center (F_{S}) obtained with sc-PBE0 are given in Table VIII. The defective slab models are calculated as singlet or triplet states, since they contain two defects. The energies of both occupied and unoccupied defect levels relative to the vacuum level are denoted as E_{def}. The VBM are almost identical for spin-up and spin-down bands, also the CBM are similar. Here, the variation comes again from the diffuse, delocalized character of the conduction band and the interaction with the unoccupied defect level. All parameters are also explained in Fig. 3. The unoccupied spin-down defect levels are 0.43–0.72 eV below the CBM.

To the best of the authors' knowledge, no experiment has been conducted to measure these electronic properties. In a previous theoretical study Krumhansl and Schwartz [111] calculated the energy of the 1*s* defect level, which corresponds to our E_{def}. For NaCl (KCl) they obtained −3.85 (−3.18) eV, quite close to our results, −3.61 and −3.12 eV, respectively. They based their calculations on a $1/r$ Coulomb-like term for the ground state energy, where *r* is the radius of the defect cavity. We tested this hypothesis by plotting E_{def} vs $1/a$ (Fig. 4), assuming proportionality of *a* and *r*.

The correlation of data to the linear fit is reasonable ($R^2 = 0.898$). This confirms that the absolute defect level generally adheres to this relationship. Linear extrapolation of E_{def} to $1/a \rightarrow 0$ (corresponding to a free electron) is indeed close to 0 eV.
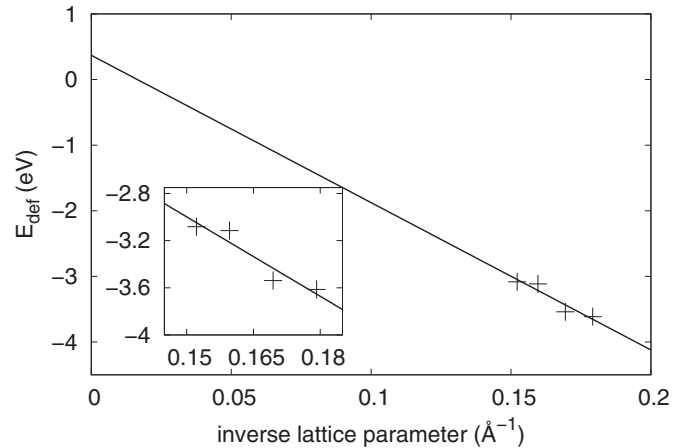
The surface defect orbital is not as symmetric as the bulk defect orbital [Fig. 5(a)]. It significantly extends into the vacuum region above the surface. Since the defect orbitals of all alkali halide surfaces have similar shape, we only show graphs for KCl(100).

Similar excited *p*-type states as observed for the bulk defect are found on the defective (100) surface. Due to site-symmetry lowering ($O_h \rightarrow C_{4v}$) the three formerly degenerate states split into a lower A_1 state [Fig. 5(b)] and two *E* states with
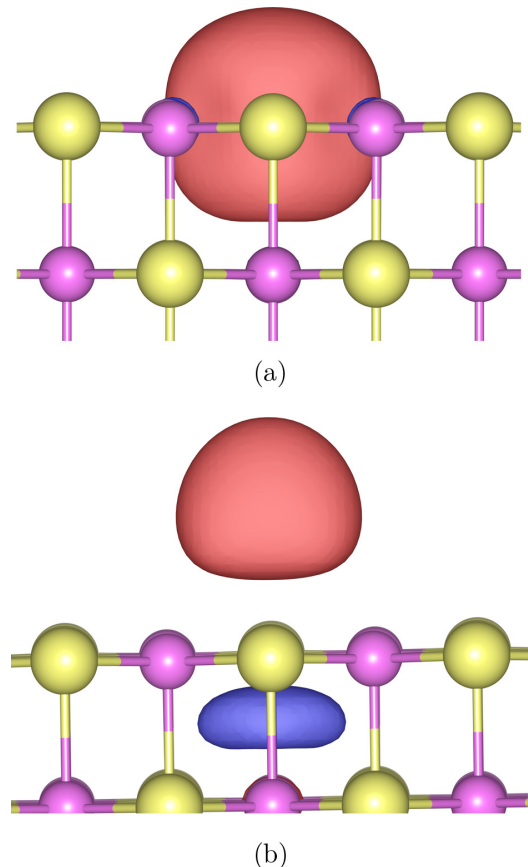

(a)

(b)

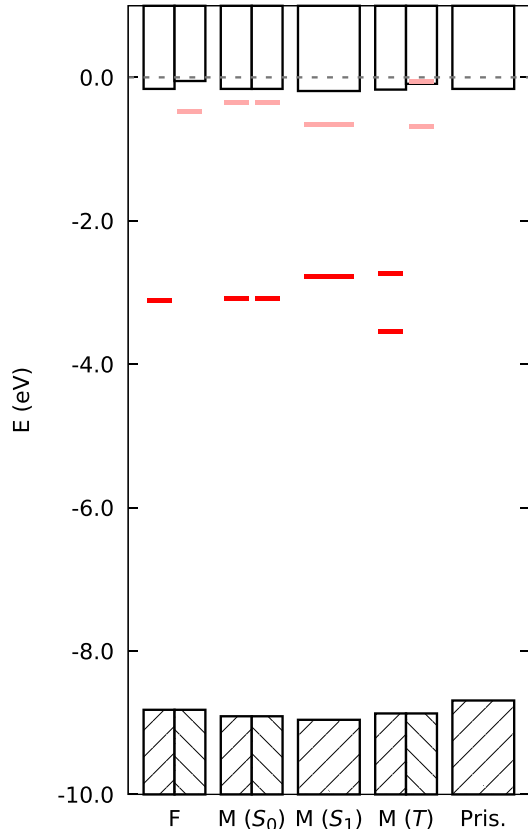FIG. 5. *F* center on the KCl(100) surface.

FIG. 6. Energy diagram of the pristine and defective KCl(100) surface. Red levels are occupied defect bands; pink levels are unoccupied defect bands.

higher energy. The lowering of the A_1 state is probably caused by a reduced Coulomb repulsion. A depiction of the E states is given in the Supplemental Material [84].

The spin-down band edges of defective and pristine surfaces do not differ significantly (Table VIII). Coupling of the valence and conduction bands with the localized spin-up defect states is small.

D. *M* centers

The M center (initially denoted as R$_2$ center by Seitz [52]) consists of two adjacent F centers. We calculated its properties for both the KCl bulk and the KCl(100) surface. To the best of the authors' knowledge, there has not been such a theoretical investigation of this defect type in the alkali halides yet.

The two defect electrons may be localized in separate defect sites in a triplet (T) or open-shell singlet state (S_0) or occupy the same defect orbital in a closed-shell singlet state (S_1). At sc-PBE0 level the open-shell singlet state is the ground state. The open-shell singlet is 0.24 eV lower than the closed-shell singlet and 0.78 eV lower than the triplet state. Previous experiments [70–74] concluded that the M center is not paramagnetic, which is consistent with our results. A distinction between S_0 or S_1 was not made in the experiments.

The electronic properties of all M center states, the F center, and the pristine (100) surface of KCl are shown in
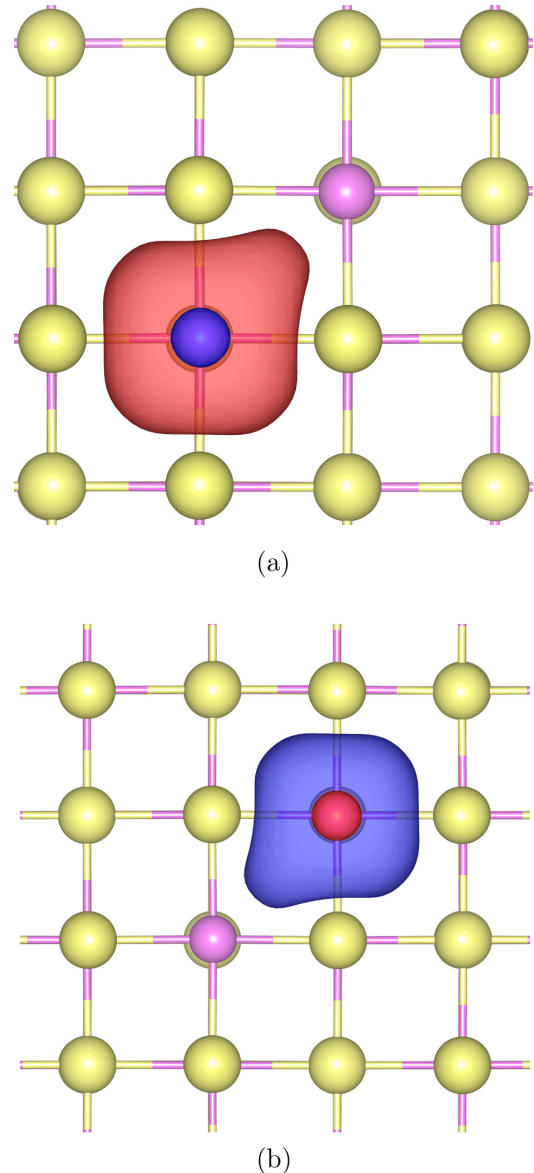

FIG. 7. M center in KCl bulk (S_0).

Fig. 6. Detailed results for the different M center states can be found in the Supplemental Material [84].

The occupied defect orbitals of the S_0 state are shown in Fig. 7. They have almost identical shapes but are confined in neighboring defect sites.

Compton and Rabin concluded that the M center is responsible for the so-called M band [65] which is the most prominent defect band aside from the F band. The S_0 state of the M center has two low-lying unoccupied defect orbitals (at -0.37 eV, shown in Fig. 6). They are located in the respective other cavity compared to their occupied counterparts. The M center excitation from the occupied to the unoccupied defect state is lower than the F center $1s \rightarrow 2p$ excitation, which is in agreement with the experimental observation by Petroff [69]. Okamoto [70] as well as Rolfe and Morrison [67] further analyzed the M band and found a second band overlapping with the F band. This was interpreted by Rolfe and Morrison [67] as transition from the occupied M center orbitals to

$2p$-type orbitals (shown in the Supplemental Material [84]). Our results are in good agreement with this explanation. Due to symmetry lowering and electron-electron interaction, the $2p$-type states are split compared to the F center $2p$-type state.

The occupied defect level energies of F and M centers (S_0 state) are quite similar, -3.05 eV compared to $-3.09/-3.08$ eV. This indicates that the coupling between the electrons in the M center is small. Reduction of adsorbed molecules should be quite similar on both defect types. However, a two-electron reduction may take place on the M center.

As a concluding remark, Zahrt *et al.* [66] measured the thermodynamic properties of the M center in KCl and determined that the enthalpy of the M center formation from two separate F centers is -0.18 eV/M center. With sc-PBE0 we obtained an energy difference of -0.29 eV/M center which is quite similar.

IV. CONCLUSIONS

The electronic properties of the four alkali halides NaCl, KCl, NaBr, and KBr were calculated using a self-consistent hybrid functional based on the PBE exchange-correlation functional. Using a plane-wave approach we were able to reproduce experimental measurements for both the solid and the surface within the experimental error range. The zero-point renormalization was calculated for all systems. The F centers in the bulk and on the (100) surface of all four halides were investigated with sc-PBE0. For the bulk, the defect levels are 4–5 eV above the VBM and 3–4 eV below the CBM. There is no quantitative correlation between the defect level position and the lattice parameters or the dielectric constants. Therefore local interactions with neighboring ions must be responsible for the observed changes. On the other hand, the binding energy of the surface defect level is in good approximation proportional to the inverse lattice constant. Both bulk and surface defect orbitals are highly localized at the vacancy sites. The interaction of the defect electrons with the delocalized electrons in the valence and conduction bands is small. The shape of the occupied ($1s$-type) and unoccupied ($2p$-type) defect orbitals is in line with experimental measurements and other theoretical investigations. The M center was investigated at DFT level. The results for the nature of the ground state are in agreement with experimental observations. It was also possible to identify the defect orbitals associated with the different M center excitations.

[1] C. Tegenkamp and H. Pfnür, Phys. Chem. Chem. Phys. **4**, 2653 (2002).

[2] U. Malaske, C. Tegenkamp, M. Henzler, and H. Pfnür, Surf. Sci. **408**, 237 (1998).

[3] S. Fölsch and M. Henzler, Surf. Sci. **247**, 269 (1991).

[4] U. Malaske, H. Pfnür, M. Bässler, M. Weiss, and E. Umbach, Phys. Rev. B **53**, 13115 (1996).

[5] W. Chen, C. Tegenkamp, H. Pfnür, and T. Bredow, Phys. Rev. B **79**, 235419 (2009).

[6] W. Chen, C. Tegenkamp, H. Pfnür, and T. Bredow, Phys. Rev. B **82**, 104106 (2010).

[7] M. Hochheim and T. Bredow, J. Phys. Chem. C **122**, 29426 (2018).

[8] M. Häfner, M. Hochheim, and T. Bredow, J. Phys. Chem. C **124**, 12606 (2020).

[9] M. Hochheim and T. Bredow, Phys. Rev. B **97**, 235447 (2018).

[10] N. F. Mott, Trans. Faraday Soc. **34**, 500 (1938).

[11] E. Taft and H. Philipp, J. Phys. Chem. Solids **3**, 1 (1957).

[12] J. E. Eby, K. J. Teegarden, and D. B. Dutton, Phys. Rev. **116**, 1099 (1959).

[13] T. Timusk, J. Phys. Chem. Solids **18**, 265 (1961).

[14] T. Timusk and W. Martienssen, Phys. Rev. **128**, 1656 (1962).

[15] J. C. Phillips, Phys. Rev. **136**, A1705 (1964).

[16] P. H. Metzger, J. Phys. Chem. Solids **26**, 1879 (1965).

[17] G. R. Huggett and K. Teegarden, Phys. Rev. **141**, 797 (1966).

[18] D. Fröhlich and B. Staginnus, Phys. Rev. Lett. **19**, 496 (1967).

[19] G. Baldini and B. Bosacchi, Phys. Rev. **166**, 863 (1968).

[20] C. Gout and F. Pradal, J. Phys. Chem. Solids **29**, 581 (1968).

[21] D. Blechschmidt, M. Skibowski, and W. Steinmann, Phys. Status Solidi B **42**, 61 (1970).

[22] D. Blechschmidt, M. Skibowski, and W. Steinmann, Opt. Commun. **1**, 275 (1970).

[23] T. Sasaki, Y. Iguchi, H. Sugawara, S. Sato, T. Nasu, A. Fjiri, S. Onari, K. Kojima, and T. Oya, J. Phys. Soc. Jpn. **30**, 580 (1971).

[24] R. T. Poole, J. G. Jenkin, J. Liesegang, and R. C. G. Leckey, Phys. Rev. B **11**, 5179 (1975).

[25] I. Maruyama and R. Onaka, J. Phys. Soc. Jpn. **44**, 196 (1978).

[26] B. L. Henke, J. Liesegang, and S. D. Smith, Phys. Rev. B **19**, 3004 (1979).

[27] G. Roy, G. Singh, and T. Gallon, Surf. Sci. **152–153**, 1042 (1985).

[28] P. A. Rodnyi, Sov. Phys. J. **32**, 476 (1989).

[29] P. E. Best, Proc. Phys. Soc. **79**, 133 (1962).

[30] W. Pong and J. A. Smith, Phys. Rev. B **7**, 5410 (1973).

[31] S. Botti and M. A. L. Marques, Phys. Rev. Lett. **110**, 226404 (2013).

[32] W. Chen and A. Pasquarello, Phys. Rev. B **86**, 035134 (2012).

[33] I.-H. Chu, J. P. Trinastic, Y.-P. Wang, A. G. Eguiluz, A. Kozhevnikov, T. C. Schulthess, and H.-P. Cheng, Phys. Rev. B **93**, 125210 (2016).

[34] A. L. Kutepov, Phys. Rev. B **95**, 195120 (2017).

[35] J. H. Skone, M. Govoni, and G. Galli, Phys. Rev. B **89**, 195112 (2014).

[36] W. R. L. Lambrecht, C. Bhandari, and M. van Schilfgaarde, Phys. Rev. Mater. **1**, 043802 (2017).

[37] E. L. Shirley, Phys. Rev. B **58**, 9579 (1998).

[38] M. J. van Setten, M. Giantomassi, X. Gonze, G.-M. Rignanese, and G. Hautier, Phys. Rev. B **96**, 155207 (2017).

[39] A. Dittmer, R. Izsák, F. Neese, and D. Maganas, Inorg. Chem. **58**, 9303 (2019).

[40] L. Hedin, Jo. Phys. Condens. Matter **11**, R489 (1999).

[41] H. Rabin and C. C. Klick, Phys. Rev. **117**, 1005 (1960).

[42] J. M. Worlock and S. P. S. Porto, Phys. Rev. Lett. **15**, 697 (1965).

[43] G. Benedek and G. F. Nardelli, Phys. Rev. **154**, 872 (1967).

[44] C. J. Buchenauer and D. B. Fitchen, Phys. Rev. **167**, 846 (1968).

[45] L. F. Stiles, M. P. Fontana, and D. B. Fitchen, Phys. Rev. B **2**, 2077 (1970).

[46] M. Ghomi, E. Rzepka, and L. Taurel, Phys. Status Solidi B **92**, 447 (1979).

[47] M. Ghomi and J. P. Buisson, J. Phys. Condens. Matter **12**, 4631 (1979).

[48] R. T. Williams, B. B. Craig, and W. L. Faust, Phys. Rev. Lett. **52**, 1709 (1984).

[49] J. Dickinson, S. Orlando, S. Avanesyan, and S. Langford, Appl. Phys. A **79**, 859 (2004).

[50] T. Koyama, M. Nakajima, and T. Suemoto, J. Phys. Soc. Jpn. **78**, 075002 (2009).

[51] A. Perregaux and G. Ascarelli, Phys. Rev. B **10**, 1683 (1974).

[52] F. Seitz, Rev. Mod. Phys. **26**, 7 (1954).

[53] U. M. Grassano, G. Margaritondo, and R. Rosei, Phys. Rev. B **2**, 3319 (1970).

[54] L. D. Bogan and D. B. Fitchen, Phys. Rev. B **1**, 4122 (1970).

[55] M. R. Pederson and B. M. Klein, Phys. Rev. B **37**, 10319 (1988).

[56] F. Karsai, P. Tiwald, R. Laskowski, F. Tran, D. Koller, S. Gräfe, J. Burgdörfer, L. Wirtz, and P. Blaha, Phys. Rev. B **89**, 125429 (2014).

[57] G. Mallia, R. Orlando, C. Roetti, P. Ugliengo, and R. Dovesi, Phys. Rev. B **63**, 235102 (2001).

[58] J.-i. Adachi and N. Kosugi, Bull. Chem. Soc. Jpn. **66**, 3314 (1993).

[59] C. M. Fang and R. A. de Groot, J. Phys. Condens. Matter **20**, 075219 (2008).

[60] H. A. Kassim and M. M. Uoda, J. Univ. Babylon Pure Appl. Sci. **26**, 173 (2018).

[61] A. Popov, E. Kotomin, and J. Maier, Nucl. Instrum. Methods Phys. Res. B **268**, 3084 (2010).

[62] R. D. Zwicker, Phys. Rev. B **18**, 2004 (1978).

[63] P. Tiwald, F. Karsai, R. Laskowski, S. Gräfe, P. Blaha, J. Burgdörfer, and L. Wirtz, Phys. Rev. B **92**, 144107 (2015).

[64] J. H. Skone, M. Govoni, and G. Galli, Phys. Rev. B **93**, 235106 (2016).

[65] W. D. Compton and H. Rabin, *F-Aggregate Centers in Alkali Halide Crystals*, edited by F. Seitz and D. Turnbull, Solid State Physics, Vol. 16 (Academic, New York, 1964), pp. 121–226.

[66] J. D. Zahrt, A. B. Scott, and E. H. Coker, J. Chem. Phys. **46**, 791 (1967).

[67] J. Rolfe and S. R. Morrison, Phys. Rev. B **15**, 3211 (1977).

[68] E. R. Hodgson, A. Delgado, and J. L. A. Rivas, J. Phys. Condens. Matter **12**, 1239 (1979).

[69] S. Petroff, Z. Phys. **127**, 443 (1950).

[70] F. Okamoto, Phys. Rev. **124**, 1090 (1961).

[71] P. R. Moran, S. H. Christensen, and R. H. Silsbee, Phys. Rev. **124**, 442 (1961).

[72] H. Ohkura and K. Murase, J. Phys. Soc. Japan **16**, 2076 (1961).

[73] E. Sonder, Phys. Rev. **125**, 1203 (1962).

[74] H. Seidel and H. C. Wolf, Phys. Status Solidi B **11**, 3 (1965).

[75] T. J. Turner, R. De Batist, and Y. Haven, Phys. Status Solidi B **11**, 535 (1965).

[76] I. Schneider, M. Marrone, and M. N. Kabler, Appl. Opt. **9**, 1163 (1970).

[77] K. M. Eid, Egypt. J. Sol. **23**, 189 (2000).

[78] R. Dovesi, A. Erba, R. Orlando, C. M. Zicovich-Wilson, B. Civalleri, L. Maschio, M. Rérat, S. Casassa, J. Baima, S. Salustro, and B. Kirtman, Wiley Interdiscip. Rev.: Comput. Mol. Sci. **8**, e1360 (2018).

[79] G. Kresse and J. Hafner, Phys. Rev. B **47**, 558 (1993).

[80] G. Kresse and J. Furthmüller, Comput. Mater. Sci. **6**, 15 (1996).

[81] G. Kresse and J. Furthmüller, Phys. Rev. B **54**, 11169 (1996).

[82] F. Weigend, F. Furche, and R. Ahlrichs, J. Chem. Phys. **119**, 12753 (2003).

[83] G. Kresse and D. Joubert, Phys. Rev. B **59**, 1758 (1999).

[84] See supplemental material at http://link.aps.org/supplemental/10.1103/PhysRevB.102.184108 for convergence tests and further orbital depictions.

[85] J. P. Perdew, K. Burke, and M. Ernzerhof, Phys. Rev. Lett. **77**, 3865 (1996).

[86] S. Grimme, S. Ehrlich, and L. Goerigk, J. Comput. Chem. **32**, 1456 (2011).

[87] S. Grimme, J. Antony, S. Ehrlich, and H. Krieg, J. Chem. Phys. **132**, 154104 (2010).

[88] D. Fritsch, B. J. Morgan, and A. Walsh, Nanoscale Res. Lett. **12**, 19 (2017).

[89] M. Ferrero, M. Rérat, B. Kirtman, and R. Dovesi, J. Chem. Phys. **129**, 244110 (2008).

[90] M. Ferrero, M. Rérat, R. Orlando, and R. Dovesi, J. Comput. Chem. **29**, 1450 (2008).

[91] M. Ferrero, M. Rérat, R. Orlando, and R. Dovesi, J. Chem. Phys. **128**, 014110 (2008).

[92] G. P. Kerker, Phys. Rev. B **23**, 3082 (1981).

[93] M. Zacharias, C. E. Patrick, and F. Giustino, Phys. Rev. Lett. **115**, 177401 (2015).

[94] M. Zacharias and F. Giustino, Phys. Rev. B **94**, 075125 (2016).

[95] D. Walker, P. K. Verma, L. M. Cranswick, R. L. Jones, S. M. Clark, and S. Buhre, Am. Mineral. **89**, 204 (2004).

[96] V. T. Deshpande, Acta Crystallogr. **14**, 794 (1961).

[97] O. D. Slagle and H. A. McKinstry, Acta Crystallogr. **21**, 1013 (1966).

[98] R. P. Lowndes, D. H. Martin, and L. F. Bates, Proc. R. Soc. Lond. A Math. Phys. Sci. **308**, 473 (1969).

[99] V. N. Staroverov, G. E. Scuseria, J. Tao, and J. P. Perdew, Phys. Rev. B **78**, 239907(E) (2008).

[100] R. Rodriguez, M. M. Barboza-Flores, R. Perez, and A. B. Clark, Eur. J. Phys. **13**, 189 (1992).

[101] W. T. Berg, J. A. Morrison, and E. W. R. Steacie, Proc. R. Soc. Lond. A Math. Phys. Sci. **242**, 467 (1957).

[102] A. L. Kutepov, Phys. Rev. B **94**, 155101 (2016).

[103] A. Grüneis, G. Kresse, Y. Hinuma, and F. Oba, Phys. Rev. Lett. **112**, 096401 (2014).

[104] S. W. Duckett and P. H. Metzger, Phys. Rev. **137**, A953 (1965).

[105] C. Kittel and E. Abrahams, Phys. Rev. **90**, 238 (1953).

[106] C. A. Hutchinson, Phys. Rev. **75**, 1769 (1949).

[107] C. A. Hutchison and G. A. Noble, Phys. Rev. **87**, 1125 (1952).

[108] A. H. Kahn and C. Kittel, Phys. Rev. **89**, 315 (1953).

[109] A. F. Kip, C. Kittel, R. A. Levy, and A. M. Portis, Phys. Rev. **91**, 1066 (1953).

[110] A. M. Portis, Phys. Rev. **91**, 1071 (1953).

[111] J. A. Krumhansl and N. Schwartz, Phys. Rev. **89**, 1154 (1953).

Mobility of F Centes in Alkali Halides

Michael Häfner[*] and Thomas Bredow[*]

[*] Mulliken Center for Theoretical Chemistry, Universität Bonn, Beringstr. 4, 53115 Bonn, Germany
[†] Any request for the permisson to reuse material from this chapter should be directed to the American Chemical Society.

Article

Mobility of *F* Centers in Alkali Halides

Michael Häfner and Thomas Bredow*

Read Online

ACCESS | Metrics & More | Article Recommendations | Supporting Information

ABSTRACT: The migration of *F* centers in alkali halides is important both for characterizing their chemical reactivity and as a benchmark for theoretical methods. In order to provide a solid basis for the assessment of theoretical methods, we reviewed the available experimental literature on the migration of *F* centers in NaCl, KCl, NaBr, and KBr. The migration of the *F* center through the bulk, across the (100) surface, and from the surface into the bulk was modeled. The activation enthalpy for the migration of an *F* center was calculated using dispersion-corrected generalized gradient approximation (GGA) functionals and a self-consistent dielectric-dependent global hybrid method based on plane-wave functions for the bulk and the (100) surface. The geometries of the transition states were characterized, and the position of the defect electron was determined. The influence of the theoretical methodology and the temperature dependence of the lattice parameter on the migration barrier was investigated. For the description of the bulk, thermal corrections were considered to enhance comparability with the experiment. The calculated migration enthalpies of 1.31, 1.46, and 1.32 eV for NaCl, KCl, and KBr, respectively, agree well with experimental measurements. For NaBr, a migration enthalpy of 0.93 eV is predicted. While only a direct hopping process between neighboring anion sites is found for the bulk, there are two possible pathways for some surfaces. The migration barrier on the surface and from the surface into the bulk is predicted to be lower than that in the bulk in all cases.
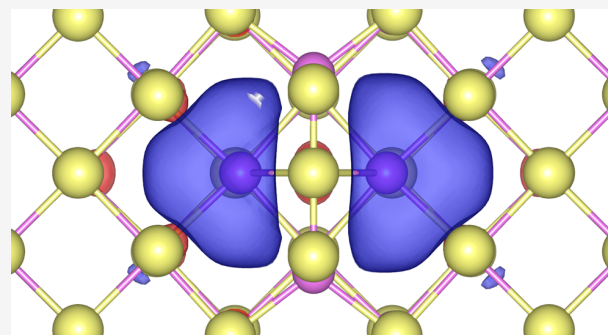
■ INTRODUCTION

Most of modern industrial-scale chemistry is based on catalyzed reactions.[1] Usually, those catalysts are metals, semiconductors, or molecular components. Insulating solid crystals, e.g., the alkali halides, are accessible in much higher quantities but are not suitable as catalysts as they have a large band gap, and thus, are hardly able to facilitate electron transfer or enhance reactivity through adsorption. However, they can be modified by means of electrolysis,[2–6] irradiation,[7,8] heating,[9] or additive reduction[10–12] to create defects in their lattice structure. One of the simplest defects is the *F* center, a single anion vacancy filled with an unpaired electron. The *F* center has been classified as a quasiparticle, the small polaron, and can be described by the polaron model.[13]

The electronic properties of the *F* center are well studied with a plethora of theoretical methods.[14–24] Its reactivity was explored for NaCl and KCl both in experiments[25–28] and theoretically using density functional theory (DFT) studies.[23,24,29–31] It acts as a strong, local reduction site, and readily transfers the defect electron to a wide range of organic molecules. This makes it an interesting candidate for catalytic reactions.

However, understanding the *F* center mobility is similarly important with regard to its possible role in catalysis. On the one hand, its migration rivals other reactions taking place on the surface, possibly impairing its usefulness as a catalyst. On the other hand, the migration could also enable the in situ generation of surface *F* centers via the migration of *F* centers from the bulk. Experimentally, direct methods were applied to measure the mobility of *F* centers in alkali halides.[2–6,10–12] Theoretically, *F* center migration has been explored for several insulators with semiempirical methods and the density functional theory (DFT). There are a few works on MgO[32,33] and the earth-alkaline fluorides.[34–37] To the best of the authors' knowledge, KCl is the only alkali halide explored in a similar fashion, in a one-electron approximation[38,39] and with a semiempirical method (intermediate neglect of differential overlap, INDO).[40] All aforementioned calculations only simulated the migration of the *F* center in the bulk, and no investigation into the transfer across a surface could be found. The migration of defects across a surface has been investigated for other systems, for example, for oxygen vacancies in TiO_2,[41,42] compounds with applications in catalysis, or $(La,Sr)MnO_3$, $(La,Sr)(Co,Fe)O_3$, and $(Ba,Sr)(Co,Fe)O_3$,[43–46] candidates for solid oxide fuel cells.
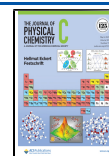
We used a plane-wave implementation of DFT to calculate the migration barrier for the migration of the F center in KCl as well as NaCl, NaBr, and KBr, both in the bulk and on the (100) surface. Geometrical optimizations were carried out at the generalized gradient approximation (GGA) level and meta-GGA level. Additional single-point calculations were performed with a self-consistent dielectric-dependent global hybrid method as in our previous study.[24] The aim of this work is to compare different rungs of DFT in terms of their applicability to F center migration in alkali halides.

First, we provide computational details and describe the construction of the calculated models. Then, we explore the differences between the four halides, the effects of different functionals and lattice constants on the migration barrier, and an assessment of thermal effects. Thereafter, we compare our bulk results to previous experiments and theoretical works. Next, the results for the migration across and into the (100) surface are discussed, and all findings are summarized in the Conclusions section.

■ COMPUTATIONAL DETAILS

All calculations were carried out with the plane-wave program package VASP version 6.1.1.[47−49] The standard PAW pseudo-potentials[50] and a cutoff energy of 500 eV were employed in the calculations if not noted otherwise. The calculation of the bulk was performed with a $4 \times 4 \times 4$ $\vec{k}$-point Monkhorst−Pack (MP) grid. The calculation of the (100) surface was performed with 5 layers for calculations simulating lateral migration and 7 layers for the vertical hopping processes. A vacuum distance of 20 Å was used to mitigate interactions between the repeating slabs. All supercells of the bulk or the surface were calculated with a Γ-$\vec{k}$-point MP grid. The model for the defective bulk is a $3 \times 3 \times 3$ supercell of the crystallographic unit cell and contains one anion defect. The model for the defective (100) surface is a 4×4 supercell of the primitive surface unit cell and contains two anion vacancies. The defects were mirrored to avoid artificial dipole moments, and it was confirmed that the interaction energy between the defects is below one-tenth of an eV. All calculations were performed with `normal` accuracy. Additional convergence tests are given in the Supporting Information (SI).

The optimizations of the bulk lattice constants of the stoichiometric halides and the atomic positions of the defective bulk and the (100) surface were carried out with Perdew−Burke−Ernzerhof (PBE)[51] and the D3(BJ)-dispersion correction.[52,53] This method was chosen due to its good geometric performance at a reasonable computational cost, as demonstrated in a review by Tran et al.[54]

Further optimizations of the stoichiometric and defective bulk were carried out with uncorrected PBE, with the D4-dispersion correction,[55,56] with the GGA functional revPBE,[57] and the meta-GGA functional SCAN,[58] additionally combined with the nonlocal correlation functional rVV10,[59] implemented in VASP by Klimeš et al.[60] In particular, the SCAN functional has demonstrated high accuracy for geometric and energetic properties of halides.[54] It is, however, computationally more demanding compared to the GGA functionals. The optimization was considered converged if the highest remaining force was below a threshold of 0.001 eV/Å. The 0 K lattice constants are overestimated by around 1%, whereas the room temperature lattice constants are always underestimated.

For the determination of the migration barriers, the migration process of the F center was modeled with the nudged elastic band (NEB) method,[61−66] as implemented in VASP by Henkelman et al. The force convergence constraint for the NEB was 0.03 eV/Å. The NEB calculation was carried out with three images between the optimized structures, using an LBFGS optimizer. The climbing image modification of the NEB method was used to obtain an improved approximation to the transition state (TS) by the energetically highest image.

Final energy calculations were performed with a self-consistent dielectric-dependent global hybrid functional (sc-DDGH)[67] based on PBE, denoted as sc-PBE0. In previous works,[24,31,68] we demonstrated that sc-PBE0 accurately describes the electronic properties of alkali halides. The exact Fock exchange fraction x is obtained by a self-consistent calculation based on the inverse of the dielectric constant ϵ_∞, which is obtained by the response of the solid to an external electrical field. According to ref 69, x resulting from the bulk can be applied on the surface as well. The optimized exchange fraction is $x = 42.8\%$ for NaCl, $x = 46.3\%$ for KCl, $x = 37.7\%$ for NaBr, and $x = 42.4\%$ for KBr.

In all GGA SCF calculations, the standard Kosugi algorithm is used. Hybrid and meta-GGA calculations are carried out with a preconditioned conjugate gradient algorithm. A Gaussian smearing of $\sigma = 0.05$ eV was applied, and `BMIX` was set to 0.01 in the standard Kerker scheme[70] used for density matrix mixing to enhance convergence.

Wannier90 (version 2.1.0)[71] was used to perform orbital projections, and VESTA (version 3.4.7)[72] was used to visualize defect orbitals and atomic structures.

■ RESULTS AND DISCUSSION

Bulk Migration. The migration path of the F center in the bulk obtained with the NEB method is essentially the same for all examined halides. It proceeds along the $\langle 110 \rangle$ axis and results in a D_{2h} symmetric TS (Figure 1). Asymmetric
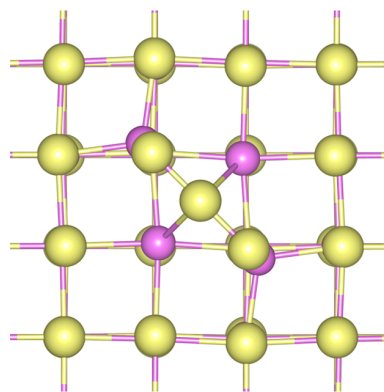

Figure 1. Transition state of the F center transfer in the KCl bulk representative for all bulk systems. Yellow spheres denote chlorine atoms, and purple spheres denote potassium atoms.

migration was explicitly investigated for KCl by manually changing the initial geometries to break the symmetry. The migrating anion was slightly shifted along the [100] axis and the [110] axis but no additional minima were found.

Influence of Functionals on the Migration Barrier. The migration barrier was calculated with a range of functionals in order to investigate the dependence from the theoretical approach. In particular, we tested various dispersion correction schemes, such as D3, D4, and rVV10. The geometries were

taken from the PBE-D3(BJ) optimizations. The calculated barriers are shown in Table 1.

Table 1. F Center Migration Barrier ΔE_M for NaCl, KCl, NaBr, and KBr Obtained with Selected Functionals as Single-Point Calculation at the PBE-D3(BJ) Optimized Geometry

system	PBE (eV)	PBE-D3(BJ) (eV)	PBE-D4 (eV)	revPBE	SCAN (eV)	SCAN-rVV10 (eV)	sc-PBE0 (eV)
NaCl	1.46	1.46	1.47	1.62	1.62	1.61	1.82
KCl	1.33	1.32	1.32	1.47	1.42	1.41	1.69
NaBr	1.18	1.20	1.21	1.41	1.43	1.43	1.61
KBr	1.09	1.09	1.09	1.24	1.28	1.27	1.47

With all methods, a similar trend is obtained: ΔE_M decreases in the order NaCl > KCl ≥ NaBr > KBr. The effect of dispersion correction is rather small, ≤0.03 eV. The PBE-based methods give smaller barriers than revPBE, SCAN, and, in particular, sc-PBE0.

The main reason for this systematic difference is the self-interaction error (SIE), which causes the GGA functional to artificially stabilize the defect orbital of the TS (Figure 2b) that is less localized than in the ground state (Figure 2a). However, this error only manifests in energies since the shape of the orbitals is virtually independent of the methodology used. The shape of the defect orbital in the transition state, furthermore, matches the shape assumed by Brown and Vail.[38]

The activation barrier is increased to a similar extent by the meta-GGA functional SCAN and the GGA revPBE. SCAN contains second derivatives of the electron density, which improve the overall description of the wavefunction. RevPBE is a version of PBE that has been reparameterized to yield superior atomization energies. Hence, we assume that the higher barrier is a consequence of a better description of the defect electron. However, both methods are still semilocal and suffer from SIE.

Hybrid methods are explicitly designed to reduce the SIE by the inclusion of exact Fock exchange. The Fock exchange contribution in sc-PBE0 was self-consistently optimized for each halide according to the scheme developed by Skone et al.,[67] and is expected to provide the most accurate electronic wavefunction. Accordingly, it yields the highest activation

barriers as it diminishes the stabilizing effect of the SIE on the transition state.

The influence of the polaron self-interaction error of the polaronic migration of V_K centers, self-trapped holes behaving similarly to the F center in the context of the polaron model, was investigated earlier.[73] It was shown that the use of local DFT functionals is not sufficient for the proper description of polarons, which is affirmed by our calculations.

However, irrespective of the theoretical approach, the migration barrier follows two trends. ΔE_M is larger in sodium halides compared to that in potassium halides and in chlorides compared to bromides. Possible reasons for this behavior are the ionic radii[74] relative to the lattice constants, changes of the local electrostatic environment during the migration, the cohesive energy of the crystal,[75] and the formation energy of the F center.

The size of the ions does not seem to significantly influence the barrier. Taking simple geometrical considerations into account, the migration of the anion in sodium halides should result in a smaller lattice distortion than in potassium halides (0.04 vs 0.14 Å). This would yield a smaller barrier but the opposite trend is observed. The distortion of the bulk structure in the TS is similar in both systems. In the transition state, the migrating Cl atom displaces the surrounding cations by 0.59 Å in KCl (0.52 Å in NaCl), which is significantly more than the displacement expected from the ionic model. This indicates that a simple ionic model is insufficient for the description of F center migration.

On the other hand, the vibrational frequencies of the fundamental bulk modes both show the same trends as found for the migration barriers.

The vibrational frequencies are linked to the energy required to distort the lattice to accommodate for the migrating anion and electron. The relationship of the frequencies to the barrier energy is shown in Figure 3. A high correlation of $R^2 > 0.98$ is obtained, indicating a possible strong link between these quantities. The cohesive energy of the crystal and the defect formation energy do not have a strong correlation with the migration barriers. Their differences within the four systems are only weakly reflected by the barriers. The migration barriers of bromides are slightly smaller (by 0.05 eV) than those of the chlorides. This is in line with the defect formation energies, which decrease from ~5.65 eV for chlorides to ~5.12 eV for bromides, but to a much smaller extent. Moreover, due
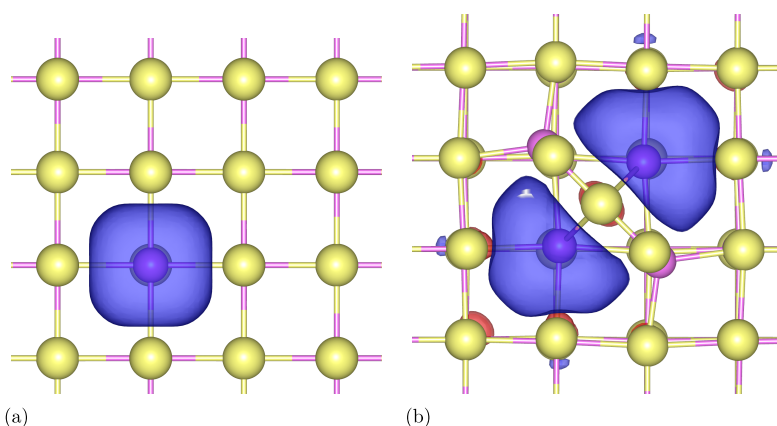

(a)   (b)

Figure 2. Singly occupied defect orbital of the F center transfer in the KCl bulk as calculated with PBE-D3(BJ). Singly occupied defect orbital of the (a) ground state, and (b) transition state. Isosurface cutoff = 3 Å$^{-3/2}$.
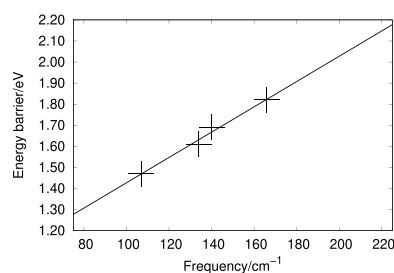
Figure 3. Correlation of the energy barrier obtained with sc-PBE0 on PBE-D3(BJ)-geometry, and the vibrational frequencies obtained with sc-PBE0.

Table 3. Theoretical results of the *F* Center Migration Barrier ΔE_M for NaCl, KCl, NaBr, and KBr obtained with Selected Functionals after Re-optimization

system	PBE (eV)	PBE-D3(BJ) (eV)	PBE-D4 (eV)	revPBE (eV)	SCAN (eV)	SCAN-rVV10 (eV)
NaCl	1.17	1.46	1.35	1.19	1.67	1.72
KCl	1.15	1.32	1.24	1.19	1.33	1.42
NaBr	0.83	1.20	1.04	0.80	1.43	1.38
KBr	0.97	1.09	1.10	1.00	1.30	1.44

to the geometric and electronic similarities between the halides, electrostatic effects influence the relative barrier height by only a small amount.

Lattice Parameter Dependence of the Migration Barrier. It is expected that the lattice parameter *a* significantly influences the migration barrier due to the different electrostatic interactions and Pauli repulsion in the TS. Due to thermal expansion, the bulk lattice parameters of the alkali halide increase by 1−2% from ∼0 K to room temperature, and by 2−3% from room temperature to the temperatures where the F center diffusion has been measured. The calculated migration barriers presented so far have been obtained with lattice parameters that correspond to low temperatures. Attempts to model the experimental lattice constants at higher temperatures by simple scaling would introduce artificial forces into the geometry optimization of the defect structures. We, therefore, followed a different strategy using optimized bulk lattice parameters *a* (from selected functionals) that are larger than those obtained with PBE-D3(BJ). The results for *a* are given in Table 2. The corresponding migration barriers obtained for the respective optimized lattice parameters are given in Table 3.

As expected, PBE without dispersion correction overestimates the room temperature lattice parameters by ≈1%. The inclusion of dispersion correction contracts the lattice parameters in all cases. With the D3(BJ) correction, the lattice parameters are in good agreement with the experimental values at 0 K, which is in line with the evaluation by Tran et al.[54] The D4 correction, which improves the description of dispersion over D3(BJ) by including electrostatic effects, leads to smaller reduction of the lattice parameters compared to D3(BJ). The obtained geometries rather correspond to room temperature values.

revPBE strongly overestimates the experimental lattice parameters,[54] which is exploited in the following. SCAN yields lattice parameters in good agreement with the low-temperature measurements. The use of the rVV10 dispersion correction decreases the lattice parameters and leads to an underestimation of the low-temperature values. sc-PBE0 gives a good

account of the room-temperature lattice parameters, yielding similar results as PBE-D4.

The migration barrier generally increases if the lattice parameter decreases compared to the initial PBE-D3(BJ) values used in Table 1 and vice versa. Whereas dispersion correction does not directly affect the barrier of a given system, it leads to smaller lattice parameters and therefore has an indirect effect. Due to the different geometry changes in the four systems, the relative values of the migration barriers also change.

These findings are relevant for the comparison with the experiments because all measurements were carried out between 673 and 923 K. Under those conditions, the thermal expansion significantly increases the lattice parameter of the halides, which is expected to decrease the migration barrier. We approximated the effect of thermal expansion by using PBE, PBE-D3(BJ), and revPBE optimized geometries, which span the largest range of lattice parameters and thus effective temperatures.

The optimized lattice parameters were compared with the temperature-dependent measurements for NaCl and KCl by Walker et al.,[77] for NaBr by Deshpande,[79] and for KBr by Venudhar et al.,[82] and the results are shown in Figure 4.

The temperatures corresponding to the lattice parameters obtained with the selected methods were determined by a linear fit of the experimental data ($R^2 > 0.99$) and are given in Table 4.

For KCl and KBr, the lattice parameters obtained with PBE are closest to the temperatures of the experimental measurements (673−923 K) and are expected to slightly overestimate the experimental temperature. The lattice parameters obtained with revPBE cannot be used because the salts are liquid at the extrapolated temperature.

For NaCl and NaBr, however, the lattice parameters obtained with revPBE closely correspond to the temperature range of the diffusion experiments and are expected to slightly underestimate the experimental temperature.

Accordingly, the lattice parameters optimized with PBE (revPBE) approximately reflect the geometries of the potassium (sodium) halides in the diffusion experiments.

Single-Point Calculations with sc-PBE0. As discussed before, sc-PBE0 yields the most accurate migration barriers

Table 2. Lattice Parameter *a* for NaCl, KCl, NaBr, and KBr Obtained with Selected Functionals

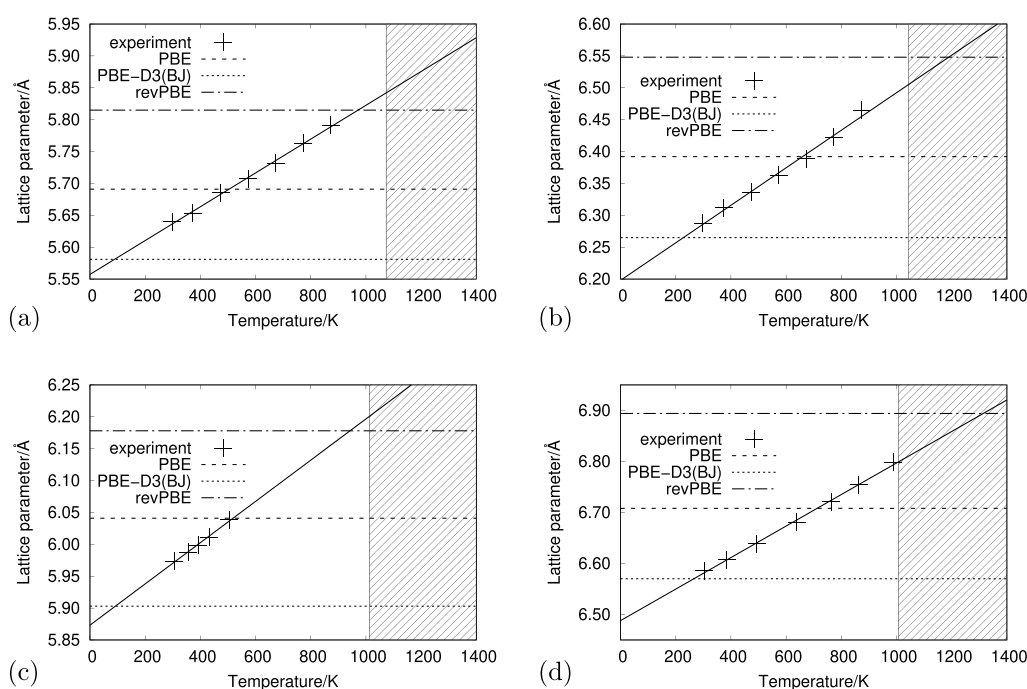| system	DFT							exp.	
	PBE (Å)	PBE-D3(BJ) (Å)	PBE-D4 (Å)	revPBE (Å)	SCAN (Å)	SCAN-rVV10 (Å)	sc-PBE0 (Å)	0 K (Å)	298 K (Å)
NaCl	5.691	5.581	5.636	5.815	5.548	5.516	5.613	5.595[76]	5.640[77]
KCl	6.382	6.265	6.316	6.548	6.258	6.186	6.302	6.161[78]	6.288[77]
NaBr	6.041	5.903	5.961	6.178	5.895	5.855	5.960		5.974[79]
KBr	6.709	6.570	6.620	6.894	6.566	6.497	6.626	6.511[80]	6.599[81]

Figure 4. Correlation of optimized lattice parameters obtained with selected functionals and temperatures. Temperature dependence of the lattice parameter of (a) NaCl, (b), KCl, (c) NaBr, and (d) KBr. Hatched area indicates the liquid phase.

Table 4. Effective Temperature Corresponding to the Optimized Lattice Parameter of Selected Methods for NaCl, KCl, NaBr, and KBr, as Obtained from a Linear Fit

system	PBE-D3(BJ) (K)	PBE (K)	revPBE (K)	melting point (K)
NaCl	89	504	972	1074[83]
KCl	227	626	1189	1043[83]
NaBr	92	518	942	1014[83]
KBr	266	712	1314	1007[84]

because it is least affected by the self-interaction error. This should result in migration barriers that are best compared to the experiments. The results of the single-point calculations based on the geometries obtained from the GGA functionals are given in Table 5.

If only the results for those methods are considered that give a good account of the high-temperature lattice parameters in the diffusion experiments (highlighted in Table 5), we obtain migration barriers of 1.40 eV for NaCl, 1.52 eV for KCl, 1.01 eV for NaBr, and 1.39 eV for KBr. This results in a change of the energetic order to KCl > NaCl ≈ KBr > NaBr.

Table 5. Theoretical Results of the *F* Center Migration Barrier ΔE_M for NaCl, KCl, NaBr, and KBr Obtained with a sc-PBE0 Single-Point Calculation for Different Optimized Geometries[a]

system	PBE-D3(BJ) (eV)	PBE (eV)	revPBE (eV)
NaCl	1.82	1.62	**1.40**
KCl	1.69	**1.52**	1.36*
NaBr	1.61	1.31	**1.01**
KBr	1.47	**1.39**	1.16*

[a]Activation energies obtained with lattice parameters that are larger than the highest experimental value are marked with an asterisk, and the results considered as most accurate are in boldface.

Thermal Corrections. Vibration corrections are expected to have a non-negligible effect on the calculated migration barriers. Therefore, frequency calculations were carried out to (i) confirm the validity of the TS and to (ii) calculate the thermal corrections for the bulk states, as shown in Table 6.

Table 6. Vibrational Energy Correction E_{tot}^{VIB} to the Migration Barrier Obtained with PBE-D3(BJ)[a]

system	E^{ZPVE} (eV)	E_{therm}^{VIB} (eV)	E_{tot}^{VIB}(eV)	T_{eff} (K)
NaCl	−0.09	0.00	−0.09	972
KCl	−0.12	0.06	−0.06	626
NaBr	0.00	−0.08	−0.08	942
KBr	−0.10	0.03	−0.07	712

[a]T_{eff} is the effective temperature of the PBE (revPBE) geometry.

Due to the size of the systems, only a subset of modes of the atoms surrounding the defect was considered in most calculations. For the 3 × 3 × 3 defective KCl supercell, full phonon spectra calculations were performed for ground and transition states. The inclusion of additional modes does not significantly change the vibrational energy correction, indicating that the chosen subset is sufficient. Details can be found in the SI.

The PBE-D3(BJ) method was employed for the optimization and frequency calculation. For bromides, ultrasoft pseudopotentials[85] had to be used because the PAW potentials lead to numerical instabilities. The calculations were carried out for a 3 × 3 × 3 supercell with a cutoff energy of 200 eV (convergence tests can be found in the SI). The vibrational zero-point energy of a harmonic oscillator is calculated with eq 1, and the thermal vibrational energy correction with eq 2

$$E^{ZPVE} = \frac{1}{2} \sum_{i=1}^{N} \nu_i \tag{1}$$

Table 7. Comparison of Experimental and Theoretical Results for the F Center Migration Barrier ΔH_M for Alkali Halides

experiment	F-center generation	measurement	temperature (K)	NaCl (eV)	KCl (eV)	NaBr (eV)	KBr (eV)
Mizuno[10]	additively	color drift	723		1.4		
Gravitt[2]	electrolytically	color drift	773–923		1.3		
Wolf[11]	additively	ESR	>773		1.6		
Tyagi[3]	electrolytically	color drift	723–923		0.86		
Kuczynski[12]	additively	color drift, bleaching	773–903		1.35 (1.65)		
Montojo[4]	electrolytically	current	772–816		1.8		1.5 (1.6)
Dalal[5]	electrolytically	color drift	673–873	1.17	1.59		1.41
Kar[6]	electrolytically	bleaching	793–833	1.33			
			Theory				
Brown[38,39]					2.23		
Kuklja[40]	224-atom cluster	INDO			1.64		
this study				1.31	1.46	0.93	1.32
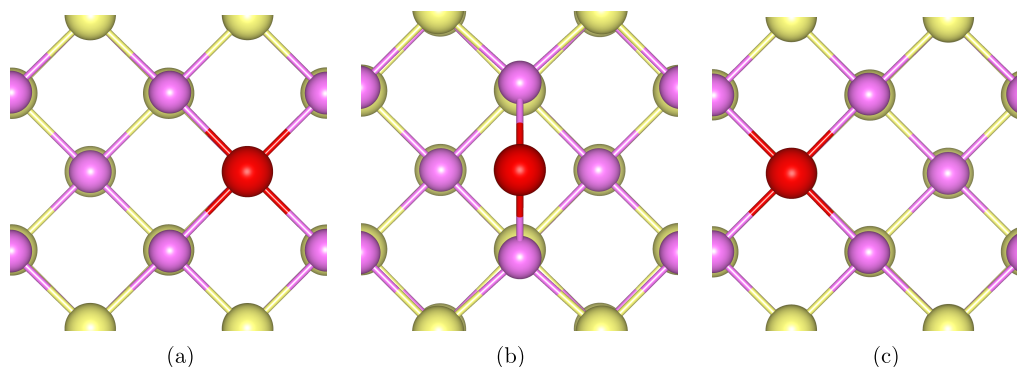
Figure 5. Transition state of the F center along [110] over the KCl (100) surface: (a) initial geometry, (b) transition geometry, and (c) final geometry. Top view, migrating atom marked in red.

$$E_{therm}^{VIB} = \sum_{i=1}^{N} \frac{\nu_i}{\exp\left(\frac{\nu_i}{k_B T_{eff}}\right) - 1} \tag{2}$$

where N is the total number of normal modes. As expected, the largest frequency change between the minima and TS occurs for modes that have large contributions from the migrating anions and neighboring cations, namely the mode with imaginary frequency and the mode with the highest frequency in the TS. The vibrational energy correction slightly lowers the calculated migration barrier by ∼0.1 eV for all four halides, which implies that the frequencies of modes including the ions surrounding the migrating anions are lowered.

Experimental Results. The combination of the sc-PBE0 single-point calculation on PBE (revPBE) geometry and the thermal corrections calculated with PBE-D3(BJ) yields the migration inner energy ΔU_M. However, the experiments measure the migration enthalpy ΔH_M.

$$\Delta H = \Delta U + pV \tag{3}$$

For solids, the term pV (eq 3) can be usually neglected, and thus, the internal energy approximately equals the enthalpy. We used this relation to obtain our final result, the migration enthalpy ΔH_M.

In Table 7, the calculated migration enthalpy ΔH_M is compared with the available results from available experiments measuring the F center migration barrier for alkali halides.

In the experiments, the F centers were created either additively by adding elemental alkali metal vapor or electrolytically by applying an electric field to the system. According to the given measurements, and discussions within the works,

this does not appear to influence the result. In all cases, the migration barrier is determined by measuring and interpreting the F center diffusion rate.

Most results fall into two categories. The first category includes measurements that attribute the obtained migration barrier solely to the migration of the F center via a hole-anion exchange along the ⟨110⟩ axis. For KCl, the measured migration enthalpies of this category are between 1.3 and 1.6 eV. These results correspond to the migration process modeled in this work. We obtained ΔH_M = 1.46 eV with our final method, which falls well into this range.

Two experiments yield a higher migration barrier. This discrepancy was explained by an additional electron transfer between neighboring anion vacancies (second category). This type of transport is assumed to take place at high defect concentrations and high temperatures.

The barriers measured by Tyagi et al.[3] are significantly lower than those of other experiments. They measured the drift of the colored defect cloud during their electrolytic generation. From their results, they concluded that for the given setup the migration of F centers is determined by the potassium ion self-diffusion. Thus, they measured a migration process different from the one we modeled and their barriers cannot be compared with our approach.

For NaCl, Dalal et al.[5] measured a migration barrier of 1.17 eV, smaller than that in our result (1.31 eV). However, Burshtein[86] later pointed out issues in their experimental method, suggesting that the migration of other defects affects the measured barriers. The barrier measured by Kar et al.[6] (1.33 eV) is very close to our result. However, the category of
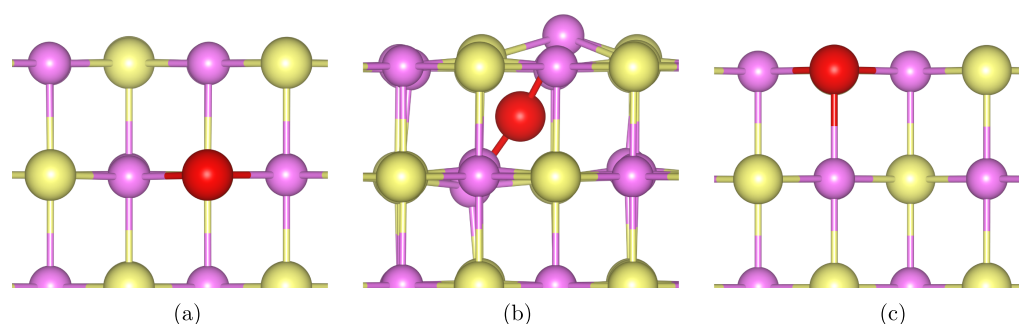
Figure 6. Transition of the F center along $[110]$ into the KCl(100) surface: (a) initial geometry, (b) transition geometry, and (c) final geometry. Side view, migrating atom marked in red.

migration responsible for the barrier was not discussed in either work.

For KBr, Dalal et al.[5] and Montojo et al.[4] measured migration barriers (1.41 and 1.5 eV) that are 0.1−0.2 eV larger than the calculated value (1.32 eV) and still within the experimental error. In both works, the diffusion of F centers was measured during their electrolytic generation. The results were criticized by Burshtein[86] for the same reason as given before.

The geometry of the TS for the KCl bulk obtained in this study (Figure 1) is similar to that found in previous theoretical studies by Brown and Vail[38,39] and Kuklja et al.[40] The former is based on a one-electron approximation and significantly overestimates all experimental migration barriers. The latter is a semiempirical calculation based on the intermediate neglect of differential overlap (INDO) approximation. Their result slightly overestimates the measured migration enthalpies. Neither study discussed thermal effects in their modeling.

(100) Surface Migration. For all surface optimizations, PBE-D3(BJ) was used, and the slab models were constructed from the corresponding optimized bulk structure. A quantitative analysis of the effects of temperature was not performed for the surface model because of the added complexity of the systems and the lack of experimental reference. For the (100) surface, there are two directions the defect can migrate along, either across the surface (Figure 5, along $\langle 011 \rangle$) or into the bulk (Figure 6, along $\langle 110 \rangle$). The surface migration processes differ from the bulk migration due to the symmetry lowering on the surface, allowing for additional degrees of freedom during the migration process. This lowers the migration barrier compared to the bulk, whereas the loss of stabilization due to fewer neighboring ions during the migration process increases the barrier. The first influence outweighs the latter in all halides, as can be seen from the barriers given in Table 8 compared to those in Table 1.

Table 8. Theoretical Results of the F Center Migration Barrier ΔE_M for All Halides Optimized with PBE-D3(BJ)[a]

system	PBE-D3(BJ)			sc-PBE0		
	S_{over} (eV)	S_{under} (eV)	S_{sink} (eV)	S_{over} (eV)	S_{under} (eV)	S_{sink} (eV)
NaCl	1.12		1.25	1.42		1.49
KCl	1.18	1.08	1.08	1.41	1.26	1.30
NaBr	0.92		1.15	1.19		1.38
KBr	1.09	1.03	1.01	1.25	1.16	1.08

[a]Reference in all cases is the defect on the (100) surface.

As observed for the migration in the bulk, single-point calculations performed with sc-PBE0 yield a larger migration barrier than PBE-D3(BJ).

The TSs of the migration pathways on the (100) surface are less symmetric than those in the bulk. In all systems, there is a migration path above the surface (Figure 7a). For potassium halides, an additional path below the surface (Figure 7b) has been observed, which is found to be energetically slightly favored over the above-surface migration.

The different pathways for the F center (100) surface migration in sodium and potassium halides are shown in Table 9. The vertical position of the halide atom above or below the average z-coordinate of the topmost layer in the TS is given there.

For sodium halides, the halide position in the TS is 0.33-0.49 Å above the surface. During the NEB calculation for the migration path below the surface, the halide ion moved upward, and TS_{over} was obtained. The sodium ions are small enough to let the halide ion pass through. The potassium cation,[74] however, is significantly larger than the sodium cation,[74] and thus, it creates a barrier for the movement of the halide ion between the two TSs. Therefore, two distinct pathways exist for potassium halides. The difference between TS_{over} and TS_{under} is most pronounced in KCl (Table 9 and Figure 7).

For KCl, an additional optimization with PBE was carried out in order to check the influence of the bulk lattice parameter on the migration. As found for the bulk, the migration barriers are lowered, whereas the vertical distance to the surface has not changed compared to the PBE-D3(BJ) optimization. For the pathway below the surface, the energy is lowered by 0.17 eV from 1.08 eV to 0.91 eV, which is exactly the same amount as observed in the bulk. For the pathway above the surface, the energy is lowered by 0.18 eV from 1.18 eV to 1.00 eV.

This suggests that measurements of the surface migration at higher temperatures will result in lower migration barriers compared to the sc-PBE0 results in Table 8.

Frequency calculations taking into account only atoms near the F center were carried out for the defective (100) surfaces of the alkali halides to confirm the validity of the TS and to obtain thermal corrections for the barriers, given in Table 10. For KCl, we consider an additional migration pathway of the F center from the first to the second layer (KCl_{sink}). For these calculations, we used the seven-layer model.

The results for KCl_{sink} are marked with an asterisk and should be considered with care because the calculation contains a few spurious imaginary modes.
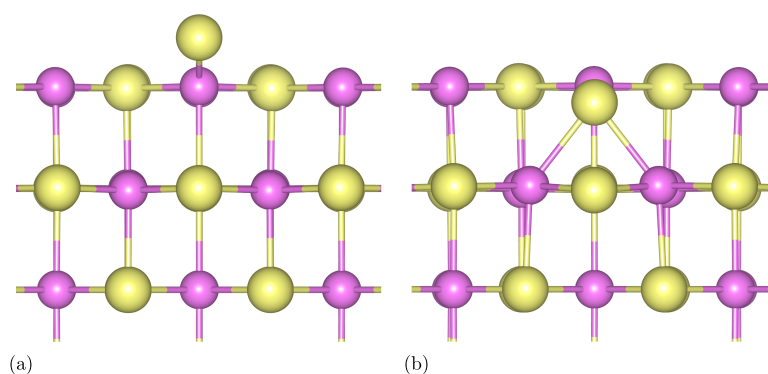
(a)   (b)

Figure 7. Transition state of the F center migration over the KCl (100) surface. Chlorine atom moves (a) above the surface plane (S_{over}), and (b) below the surface plane (S_{under}). Side view.

Table 9. Vertical Position of the Migrating Halide Atom in the Transition State for All Halides Relative to the Average z-coordinate of the Topmost Layer; PBE-D3(BJ) Results[a]

	TS_{over} (Å)	TS_{under} (Å)
NaCl	0.33	—
KCl	1.55	−0.48
NaBr	0.49	—
KBr	0.58	−0.35

[a]—, indicates that the corresponding minimum energy path was not found.

Table 10. Vibrational Energy Correction E_{tot}^{VIB} to the Migration Barrier Obtained with PBE-D3(BJ)[a]

system	E^{ZPVE} (eV)	E_{therm}^{VIB} (eV)	E_{tot}^{VIB} (eV)	T_{eff} (K)
NaCl	0.01	−0.01	0.00	89
KCl_{over}	0.01	−0.02	−0.02	227
KCl_{under}	0.03	−0.04	−0.01	227
KCl_{sink}*	−0.03	0.07	0.03	227
NaBr	−0.01	0.00	−0.01	92
KBr_{over}	−0.01	−0.02	−0.02	266
KBr_{under}	0.00	−0.02	−0.02	266

[a]T_{eff} is the effective temperature of the PBE-D3(BJ) lattice parameter obtained by a linear fit (see Table 4).

In general, the ZPVE correction is negligible for the surfaces. The corrections for the migration across the surface are of the same order of magnitude as for the bulk systems and slightly decrease the migration barriers. However, the correction for the exemplary migration into the surface slightly increases the migration barrier due to thermal contributions.

The sink migration from the surface into the bulk (Figure 6) along the ⟨110⟩ axis is geometrically more restricted than the transfer across the surface. For potassium halides, the migration barrier of the sink migration is comparable to under migration, and for sodium halides, this energetic barrier lies between the bulk and the surface results. This behavior was expected as the sink migration can exploit the symmetry reduction introduced by the surface cut, which can be seen in Figure 6b based on the dislocation of the potassium ion out of the surface.

CONCLUSIONS

F center migration was investigated theoretically for the four alkali halides NaCl, KCl, NaBr, and KBr at different levels of density functional theory and by considering the dispersion effects. For the bulk, a highly symmetric transition state was found and the location of the defect electron was visualized. Migration energies were calculated with sc-PBE0 based on geometries obtained with PBE and revPBE.

The activation barriers are sensitive to the change of the lattice parameter due to the change in temperature and vary by several tenths of eV at different temperatures. Thus, the functionals used for optimization were selected based on their lattice parameters and their agreement with the lattice parameters measured at elevated temperatures close to the conditions of the diffusion experiments. A hybrid functional is crucial to accurately calculate migration barriers since it mitigates the self-interaction error, which affects the electron density of the transition state. The self-consistent dielectric-dependent functional was chosen because it accurately reproduces the electronic properties of the alkali halides. At variance, dispersion corrections are of minor importance for the calculation of migration barriers. The energies were corrected by ZPE and vibrational contributions in order to be comparable with the experimental activation enthalpies. For these models, the calculated migration enthalpies are 1.31 eV for NaCl, 1.46 eV for KCl, 0.93 eV for NaBr, and 1.32 eV for KBr. For the alkali halides NaCl, KCl, and KBr, these results match the experimental results well, underlining the need for a hybrid DFT level description of the electronic structure and the need to account for thermal effects. The migration across and into the (100) surface was explored and different migration paths were identified for potassium halides. The existence of the different migration paths can qualitatively be explained with simple geometrical considerations. The ZPE and thermally corrected migration barriers for the (100) surface obtained with PBE-D3(BJ) are 1.42 eV (NaCl), 1.24 eV (KCl), 1.18 eV (NaBr), and 1.14 eV (KBr). They are slightly smaller than the respective barriers for bulk migration due to the additional degrees of freedom in the TS.

ASSOCIATED CONTENT

Ⓢ Supporting Information

The Supporting Information is available free of charge at https://pubs.acs.org/doi/10.1021/acs.jpcc.1c00602.

Convergence tests of $\vec{k}$-points and energetic cutoff for the ultrasoft pseudopotentials; and calculation of the vibrational corrections (PDF)

AUTHOR INFORMATION

Corresponding Author

Thomas Bredow − *Mulliken Center for Theoretical Chemistry, Institut für Physikalische und Theoretische Chemie, Universität Bonn, 53115 Bonn, Germany*; Phone: +49 (0) 228 733839; Email: bredow@thch.uni-bonn.de; Fax: +49 (0)228 739064

Author

Michael Häfner − *Mulliken Center for Theoretical Chemistry, Institut für Physikalische und Theoretische Chemie, Universität Bonn, 53115 Bonn, Germany;* ⊙ orcid.org/0000-0002-2765-6689

Complete contact information is available at:
https://pubs.acs.org/10.1021/acs.jpcc.1c00602

Notes

The authors declare no competing financial interest.

REFERENCES

(1) Ma, Z.; Zaera, F. Heterogeneous Catalysis by Metals. In *Encyclopedia of Inorganic Chemistry*; American Cancer Society, 2006.

(2) Gravitt, J. C.; Gross, G. E.; Benson, D. K.; Scott, A. B. Motion of F Centers in KCl and KI. *J. Chem. Phys.* **1962**, *37*, 2783−2784.

(3) Tyagi, R. C.; Singh, R.; Gupta, A. K. Kinetics of Electrolytic Coloration in Alkali Halide Crystals. *J. Phys. C: Solid State Phys.* **1970**, *3*, 769−772.

(4) Montojo, M.; Jaque, F.; Sánchez, C. Transient and Steady Electron Currents Limited by Ionic Space Charge in Electrolytically Coloured Potassium Halides. *J. Phys. Chem. Solids* **1977**, *38*, 657−663.

(5) Dalal, M. L.; Sivaraman, S.; Murti, Y. V. G. S. Thermal Dissociation Energy of F-Centers in Alkali Halides. *Phys. Status Solidi B* **1982**, *110*, 349−356.

(6) Kar, S.; Maiti, A. K.; Sengupta, M.; Goswami, K. Ionic Transport in Alkali Halides with Doping-induced Defects and Colour Centre Migration by Thermal Bleaching. *Fizika A* **2000**, *9*, 159−168.

(7) Howard, C. L. H.; Kerr, P. F. Blue Halite. *Science* **1960**, *132*, 1886−1887.

(8) Zielasek, V.; Hildebrandt, T.; Henzler, M. Surface Color Centers on Epitaxial NaCl Films. *Phys. Rev. B* **2000**, *62*, 2912−2919.

(9) Scott, A. B.; Smith, W. A. The Thermal Stability of *F*-centers in Alkali Halides. *Phys. Rev.* **1951**, *83*, 982−986.

(10) Mizuno, H.; Inoue, M. Diffusion of *F* Centers into Potassium Chloride Single Crystals. *Phys. Rev.* **1960**, *120*, 1226−1229.

(11) Wolf, E. L. Diffusion Effects in the Inhomogeneously Broadened Case: High-Temperature Saturation of the *F*-Center Electron Spin Resonance. *Phys. Rev.* **1966**, *142*, 555−569.

(12) Kuczynski, G.; Byun, J. Diffusion of F-centers in Potassium Chloride Crystals. *Phys. Status Solidi B* **1972**, *50*, 367−377.

(13) Devreese, J. T. Polarons. *Encycl. Appl. Phys.* **1996**, *14*, 383−409.

(14) Zwicker, R. D. Pseudopotential Calculation of *F*-center Spin Densities in KCl, NaCl, and NaF. *Phys. Rev. B* **1978**, *18*, 2004−2010.

(15) Pederson, M. R.; Klein, B. M. Improved Theoretical Methods for Studies of Defects in Insulators: Application to the F Center in LiF. *Phys. Rev. B* **1988**, *37*, 10319−10331.

(16) Karsai, F.; Tiwald, P.; Laskowski, R.; Tran, F.; Koller, D.; Gräfe, S.; Burgdörfer, J.; Blaha, P. F center in Lithium Fluoride Revisited: Comparison of Solid-state physics and Quantum-chemistry Approaches. *Phys. Rev. B* **2014**, *89*, No. 125429.

(17) Mallia, G.; Orlando, R.; Roetti, C.; Ugliengo, P.; Dovesi, R. F Center in LiF: A Quantum Mechanical Ab Initio Investigation of the Hyperfine Interaction Between the Unpaired Electron at the Vacancy and Its First Seven Neighbors. *Phys. Rev. B* **2001**, *63*, No. 235102.

(18) Adachi, J.-i.; Kosugi, N. An Ab Initio Molecular Orbital Approach to Electronic Structures of the F Center in NaCl. Effects of Basis Set and Cluster Size. *Bull. Chem. Soc. Jpn.* **1993**, *66*, 3314−3318.

(19) Tiwald, P.; Karsai, F.; Laskowski, R.; Gräfe, S.; Blaha, P.; Burgdörfer, J.; Wirtz, L. Ab Initio Perspective on the Mollwo-Ivey Relation for *F* Centers in Alkali Halides. *Phys. Rev. B* **2015**, *92*, No. 144107.

(20) Fang, C. M.; de Groot, R. A. Wavefunction Character of the F-center in Table Salt. *J. Phys.: Condens. Matter* **2008**, *20*, No. 075219.

(21) Kassim, H. A.; Uoda, M. M. A Study of F-center in the Ionic Crystal by Using The Quantum Dot Model Potential. *J. Univ. Babylon Pure Appl. Sci.* **2018**, *26*, 173−186.

(22) Popov, A.; Kotomin, E.; Maier, J. Basic Properties of the F-type Centers in Halides, Oxides and Perovskites. *Nucl. Instrum. Methods Phys. Res., Sect. B* **2010**, *268*, 3084−3089.

(23) Chen, W.; Tegenkamp, C.; Pfnür, H.; Bredow, T. Color Centers in NaCl by Hybrid Functionals. *Phys. Rev. B* **2010**, *82*, No. 104106.

(24) Häfner, M.; Bredow, T. *F* and *M* Centers in Alkali Halides: A Theoretical Study Applying Self-consistent Dielectric-dependent Hybrid Density Functional Theory. *Phys. Rev. B* **2020**, *102*, No. 184108.

(25) Tegenkamp, C.; Pfnür, H. Adsorbate Induced Contact Charging: Pure and OH-substituted Benzoic Acids Adsorbed on Wide Band Gap Insulators. *Phys. Chem. Chem. Phys.* **2002**, *4*, 2653−2659.

(26) Malaske, U.; Tegenkamp, C.; Henzler, M.; Pfnür, H. Defect-induced Band Gap States and the Contact Charging Effect in Wide Band Gap Insulators. *Surf. Sci.* **1998**, *408*, 237−251.

(27) Fölsch, S.; Henzler, M. Water Adsorption on the NaCl Surface. *Surf. Sci.* **1991**, *247*, 269−273.

(28) Malaske, U.; Pfnür, H.; Bässler, M.; Weiss, M.; Umbach, E. Adsorption Geometry of OH Adsorbed at F Centers on a NaCl(100) Surface. *Phys. Rev. B* **1996**, *53*, 13115−13120.

(29) Chen, W.; Tegenkamp, C.; Pfnür, H.; Bredow, T. Tailoring Band Gaps of Insulators by Adsorption at Surface Defects: Benzoic Acids on NaCl Surfaces. *Phys. Rev. B* **2009**, *79*, No. 235419.

(30) Hochheim, M.; Bredow, T. Adsorption of PTCDA on NaCl Surfaces with Color Centers: Charge Transfer and Formation of Radical Ions. *J. Phys. Chem. C* **2018**, *122*, 29426−29434.

(31) Häfner, M.; Hochheim, M.; Bredow, T. Chemistry with F Centers: Reduction of Organic Molecules on the Defective Potassium Chloride(100) Surface. *J. Phys. Chem. C* **2020**, *124*, 12606−12616.

(32) Popov, A. I.; Kotomin, E. A.; Kuklja, M. M. Quantum Chemical Calculations of the Electron Center Diffusion in MgO Crystals. *Phys. Status Solidi B* **1996**, *195*, 61−66.

(33) Reveles, J. U.; Köster, A. M.; Khanna, S. N.; Quintanar, C. Surface Oxygen Diffusion into Neutral, Cationic, and Dicationic Oxygen Vacancies on MgO(100) Surfaces. *J. Phys. Chem. C* **2010**, *114*, 12265−12270.

(34) Puchina, A.; Puchin, V.; Kotomin, E.; Reichling, M. Ab Initio Study of the F Centers in CaF2: Calculations of the Optical Absorption, Diffusion and Binding Energies. *Solid State Commun.* **1998**, *106*, 285−288.

(35) Shi, H.; Chang, L.; Jia, R.; Eglitis, R. I. Ab Initio Calculations of the Transfer and Aggregation of F Centers in CaF2. *J. Phys. Chem. C* **2012**, *116*, 4832−4839.

(36) Shi, H.; Chang, L.; Jia, R.; Eglitis, R. Ab Initio Calculations for the F-center Transfer and R Centers in SrF2. *Comput. Mater. Sci.* **2013**, *79*, 527−533.

(37) Shi, H.; Jia, R.; Eglitis, R. First-principles Simulations on the Aggregation of F Centers in BaF2: R Centers. *Solid State Ionics* **2011**, *187*, 1−7.

(38) Brown, R. J.; Vail, J. M. Saddle-Point Configuration of the F-Centre in NaCl-Type Alkali Halides. *Phys. Status Solidi B* **1970**, *40*, 737−747.

(39) Brown, R. J.; Vail, J. M. Saddle-point F-centre: Role of the Excess Electron in Step Diffusion. *Phys. Status Solidi B* **1972**, *49*, K33–K36.

(40) Kuklja, M.; Kotomin, E.; Popov, A. Semi-empirical Simulations of F-center Diffusion in KCl Crystals. *J. Phys. Chem. Solids* **1997**, *58*, 103–106.

(41) Cheng, H.; Selloni, A. Energetics and Diffusion of Intrinsic Surface and Subsurface Defects on Anatase TiO2(101). *J. Chem. Phys.* **2009**, *131*, No. 054703.

(42) Wang, Z.-W.; Shu, D.-J.; Wang, M.; Ming, N.-B. Strain Effect on Diffusion Properties of Oxygen Vacancies in Bulk and Subsurface of Rutile TiO2. *Surf. Sci.* **2012**, *606*, 186–191.

(43) Kuklja, M. M.; Kotomin, E. A.; Merkle, R.; Mastrikov, Y. A.; Maier, J. Combined Theoretical and Experimental Analysis of Processes Determining Cathode Performance in Solid Oxide Fuel Cells. *Phys. Chem. Chem. Phys.* **2013**, *15*, 5443–5471.

(44) Han, J. W.; Yildiz, B. Enhanced One Dimensional Mobility of Oxygen on Strained LaCoO3(001) Surface. *J. Mater. Chem.* **2011**, *21*, 18983–18990.

(45) Mastrikov, Y. A.; Merkle, R.; Kotomin, E. A.; Kuklja, M. M.; Maier, J. Surface Termination Effects on the Oxygen Reduction Reaction Rate at Fuel Cell Cathodes. *J. Mater. Chem. A* **2018**, *6*, 11929–11940.

(46) Kotomin, E. A.; Mastrikov, Y. A.; Heifets, E.; Maier, J. Adsorption of Atomic and Molecular Oxygen on the LaMnO3(001) Surface: Ab Initio Supercell Calculations and Thermodynamics. *Phys. Chem. Chem. Phys.* **2008**, *10*, 4644–4649.

(47) Kresse, G.; Hafner, J. Ab Initio Molecular Dynamics for Liquid Metals. *Phys. Rev. B* **1993**, *47*, 558–561.

(48) Kresse, G.; Furthmüller, J. Efficiency of Ab-initio Total Energy Calculations for Metals and Semiconductors Using a Plane-wave Basis Set. *Comput. Mater. Sci.* **1996**, *6*, 15–50.

(49) Kresse, G.; Furthmüller, J. Efficient Iterative Schemes for Ab Initio Total-energy Calculations Using a Plane-wave Basis Set. *Phys. Rev. B* **1996**, *54*, 11169–11186.

(50) Kresse, G.; Joubert, D. From Ultrasoft Pseudopotentials to the Projector Augmented-wave Method. *Phys. Rev. B* **1999**, *59*, 1758–1775.

(51) Perdew, J. P.; Burke, K.; Ernzerhof, M. Generalized Gradient Approximation Made Simple. *Phys. Rev. Lett.* **1996**, *77*, 3865–3868.

(52) Grimme, S.; Ehrlich, S.; Goerigk, L. Effect of the Damping Function in Dispersion Corrected Density Functional Theory. *J. Comput. Chem.* **2011**, *32*, 1456–1465.

(53) Grimme, S.; Antony, J.; Ehrlich, S.; Krieg, H. A Consistent and Accurate ab Initio Parametrization of Density Functional Dispersion Correction (DFT-D) for the 94 Elements H-Pu. *J. Chem. Phys.* **2010**, *132*, No. 154104.

(54) Tran, F.; Stelzl, J.; Blaha, P. Rungs 1 to 4 of DFT Jacob's Ladder: Extensive Test on the Lattice Constant, Bulk Modulus, and Cohesive Energy of Solids. *J. Chem. Phys.* **2016**, *144*, No. 204120.

(55) Caldeweyher, E.; Bannwarth, C.; Grimme, S. Extension of the D3 Dispersion Coefficient Model. *J. Chem. Phys.* **2017**, *147*, No. 034112.

(56) Caldeweyher, E.; Ehlert, S.; Hansen, A.; Neugebauer, H.; Spicher, S.; Bannwarth, C.; Grimme, S. A Generally Applicable Atomic-charge Dependent London Dispersion Correction. *J. Chem. Phys.* **2019**, *150*, No. 154122.

(57) Zhang, Y.; Yang, W. Comment on "Generalized Gradient Approximation Made Simple". *Phys. Rev. Lett.* **1998**, *80*, 890.

(58) Sun, J.; Ruzsinszky, A.; Perdew, J. P. Strongly Constrained and Appropriately Normed Semilocal Density Functional. *Phys. Rev. Lett.* **2015**, *115*, 036402.

(59) Peng, H.; Yang, Z.-H.; Perdew, J. P.; Sun, J. Versatile van der Waals Density Functional Based on a Meta-Generalized Gradient Approximation. *Phys. Rev. X* **2016**, *6*, No. 041005.

(60) Klimeš, J.; Bowler, D. R.; Michaelides, A. Van Der Waals Density Functionals Applied to Solids. *Phys. Rev. B* **2011**, *83*, No. 195131.

(61) Sheppard, D.; Xiao, P.; Chemelewski, W.; Johnson, D. D.; Henkelman, G. A Generalized Solid-state Nudged Elastic Band Method. *J. Chem. Phys.* **2012**, *136*, No. 074103.

(62) Sheppard, D.; Henkelman, G. Paths to Which the Nudged Elastic Band Converges. *J. Comput. Chem.* **2011**, *32*, 1769–1771.

(63) Sheppard, D.; Terrell, R.; Henkelman, G. Optimization Methods for Finding Minimum Energy Paths. *J. Chem. Phys.* **2008**, *128*, No. 134106.

(64) Henkelman, G.; Uberuaga, B. P.; Jónsson, H. A Climbing Image Nudged Elastic Band Method for Finding Saddle Points and Minimum Energy Paths. *J. Chem. Phys.* **2000**, *113*, 9901–9904.

(65) Henkelman, G.; Jónsson, H. Improved Tangent Estimate in the Nudged Elastic Band Method for Finding Minimum Energy Paths and Saddle Points. *J. Chem. Phys.* **2000**, *113*, 9978–9985.

(66) Jónsson, H.; Mills, G.; Jacobsen, K. W. *Classical and Quantum Dynamics in Condensed Phase Simulations*; Berne, B. J.; Ciccotti, G.; Coker, D. F., Eds.; World Scientific, 1998; Chapter 16, pp 385–404.

(67) Skone, J. H.; Govoni, M.; Galli, G. Self-consistent Hybrid Functional for Condensed Systems. *Phys. Rev. B* **2014**, *89*, No. 195112.

(68) Hochheim, M.; Bredow, T. Band-edge Levels of the NaCl(100) Surface: Self-consistent Hybrid Density Functional Theory Compared to Many-body Perturbation Theory. *Phys. Rev. B* **2018**, *97*, No. 235447.

(69) Skone, J. H.; Govoni, M.; Galli, G. Nonempirical Range-separated Hybrid Functionals for Solids and Molecules. *Phys. Rev. B* **2016**, *93*, No. 235106.

(70) Kerker, G. P. Efficient Iteration Scheme for Self-consistent Pseudopotential Calculations. *Phys. Rev. B* **1981**, *23*, 3082–3084.

(71) Mostofi, A. A.; Yates, J. R.; Pizzi, G.; Lee, Y.-S.; Souza, I.; Vanderbilt, D.; Marzari, N. An Updated Version of Wannier90: A Tool for Obtaining Maximally-localised Wannier Functions. *Comput. Phys. Commun.* **2014**, *185*, 2309–2310.

(72) Momma, K.; Izumi, F. VESTA3 for Three-dimensional Visualization of Crystal, Volumetric and Morphology Data. *J. Appl. Crystallogr.* **2011**, *44*, 1272–1276.

(73) Sadigh, B.; Erhart, P.; Åberg, D. Variational Polaron Self-interaction-corrected Total-energy Functional for Charge Excitations in Insulators. *Phys. Rev. B* **2015**, *92*, No. 075202.

(74) Shannon, R. D. Revised Effective Ionic Radii and Systematic Studies of Interatomic Distances in Halides and Chalcogenides. *Acta Crystallogr., Sect. A: Cryst. Phys., Diffr., Theor. Gen. Crystallogr.* **1976**, *32*, 751–767.

(75) Cubicciotti, D. Lattice Energies of the Alkali Halides and the Electron Affinities of the Halogens. *J. Chem. Phys.* **1959**, *31*, 1646–1651.

(76) *Landolt-Bornstein Numerical Data and Functional Relationships in Science and Technology: New Series. Crystal and Solid State Physics, Group III*; Hellwege, K.-H., Ed.; Springer: Berlin, 1966; Vol. 7.

(77) Walker, D.; Verma, P. K.; Cranswick, L. M.; Jones, R. L.; Clark, S. M.; Buhre, S. Halite-sylvite Thermoelasticity. *Am. Mineral.* **2004**, *89*, 204–210.

(78) Rodriguez, R.; Barboza-Flores, M. M.; Perez, R.; Clark, A. B. A Laboratory Project to Obtain the Low-temperature Lattice Constants of Ionic Crystals. *Eur. J. Phys.* **1992**, *13*, 189–192.

(79) Deshpande, V. T. Thermal Expansion of Sodium Fluoride and Sodium Bromide. *Acta Crystallogr.* **1961**, *14*, No. 794.

(80) Berg, W. T.; Morrison, J. A.; Steacie, E. W. R. The Thermal Properties of Alkali Halide Crystals. I. The Heat Capacity of Potassium Chloride, Potassium Bromide, Potassium Iodide and Sodium Iodide Between 2.8 and 270 K. *Proc. R. Soc. London, Ser. A* **1957**, *242*, 467–477.

(81) Slagle, O. D.; McKinstry, H. A. The Lattice Parameter in the Solid Solution KCl–KBr. *Acta Crystallogr.* **1966**, *21*, No. 1013.

(82) Venudhar, Y.; Iyengar, L.; Rao, K. K. Thermal Expansion and Debye Temperatures of KCl-KBr Mixed Crystals by an X-ray Method. *J. Mater. Sci.* **1986**, *21*, 110–116.

(83) Clark, S. P. Effect of Pressure on the Melting Points of Eight Alkali Halides. *J. Chem. Phys.* **1959**, *31*, 1526–1531.

(84) *CRC Handbook of Chemistry and Physics*; Lide, D. R., Ed.; CRC Press, 2004; Vol. *85*.

(85) Kresse, G.; Hafner, J. Norm-conserving and Ultrasoft Pseudopotentials for First-row and Transition Elements. *J. Phys.: Condens. Matter* **1994**, *6*, 8245−8257.

(86) Burshtein, Z. Comment on "Space Charge Limited Current (SCLC) in Alkali Halide Crystals During Electrolytic Coloration". *J. Phys. Chem. Solids* **1989**, *50*, No. 333.

Nitrogen Activation on Defective Potassium Chloride and Sodium Chloride

Michael Häfner[*] and Thomas Bredow[*]

---

[*] Mulliken Center for Theoretical Chemistry, Universität Bonn, Beringstr. 4, 53115 Bonn, Germany

Article

Nitrogen Activation on Defective Potassium Chloride and Sodium Chloride

Michael Häfner and Thomas Bredow*

Read Online

ACCESS | Metrics & More | Article Recommendations | Supporting Information

ABSTRACT: The *F* center on the KCl and NaCl (100) surfaces was investigated theoretically concerning its effect on adsorbed nitrogen. It was found that the defect on both halide surfaces reduces an adsorbed nitrogen molecule and weakens its triple bond. A strong reduction of the rate-determining barriers was found for reaction of adsorbed nitrogen with hydrogen toward hydrazine compared to the gas phase. The frontier orbitals were analyzed, and the singly occupied π^*-orbital of the reduced N_2 was identified as the driving force behind the enhanced reactivity. Surface cations further stabilize the transition structures by attractive interaction with dissociated H atoms. Gibbs free energy diagrams were calculated for all possible reaction pathways.
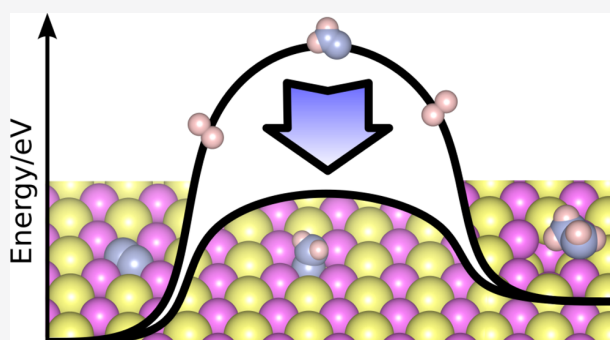
INTRODUCTION

Many technologically important reactions require efficient catalysts to make them economically feasible.[1,2] The choice of the catalyst depends on the type of reaction, toxicologic, and economical factors. Many reactions are catalyzed with expensive noble metals like platinum and palladium or toxic compounds like osmium-(VIII)-oxide. Therefore, the search for new catalysts that are both affordable and benign for human health and environment is an active field of research. One—unexpected—group of compounds that fulfill both these criteria are alkali halides. Although they are high band gap insulators and unreactive in their pristine state, their reactivity can be improved by introducing defects into the lattice. A simple but promising modification is the so-called color or *F* center, which occurs when a vacant anion site is occupied by a single electron. This can be achieved in various ways, for example, by adding gaseous alkaline metal,[3,4] heating the solid,[5] irradiation,[6,7] or through electrolysis.[8,9] The reactivity of the *F* center has been demonstrated experimentally. It is able to reduce different adsorbed molecules on the NaCl (100) surface[10,11] and split water.[12,13] Furthermore, several theoretical studies confirm the reductive power of the *F* center.[14−17]

In this work, we extend our previous theoretical work and investigate the effect of the KCl and NaCl *F* center on a surface reaction. We chose the reaction of nitrogen and hydrogen as a model reaction because it involves small molecules and few possible reaction paths. Furthermore, the efficient conversion of nitrogen to ammonia and related compounds is still one of the challenges of modern chemistry. Nitrogen derivatives, most prominently ammonia and hydrazine, play a crucial role in many fields of chemistry as they are required to produce

fertilizers or fuels.[18,19] The main obstacle is the breaking of the nitrogen−nitrogen triple bond. There are at least two viable pathways of generating ammonia from nitrogen. The method currently used on an industrial scale is an adsorptive cleavage of the molecule on a metal surface, as employed in the famous Haber−Bosch process.[20−23] For this pathway, there is already ongoing research in the effect of reductive solids on the cleavage of nitrogen on ruthenium, for example, by employing electrides.[24,25] In most natural processes, the fixation of nitrogen is done with the help of a class of enzymes called nitrogenases.[26−28] In that case, a reductive mechanism takes place in which single electrons and protons are added to an enzyme-bound nitrogen molecule.

We investigate an alternative mechanism which resembles the gas-phase reaction of nitrogen and hydrogen,[23,29] but on a defective alkali halide surface. We first analyze the general effect of the *F* center on the KCl and NaCl (100) surfaces on nitrogen by means of plane wave density functional theory (DFT), employing both the generalized gradient approximation (GGA) functional PBE and a self-consistent dielectric-dependent global hybrid functional to characterize the adsorption. Then, we explore the migration behavior of nitrogen on the perfect and defective (100) surfaces to assess the probability of side reactions. We discuss the results of the

23764
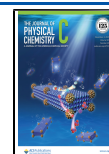
simulated reaction between hydrogen and nitrogen on the defective surface, following two possible pathways to hydrazine. Finally, we summarize our findings in a conclusion.

METHODS

Electronic Structure Calculations. The plane wave program package VASP (versions 6.0.8 and 6.1.1[30−32]) and the molecular orbital program package ORCA version 4.2.1[33,34] with libint[35] and libxc[36] were employed to carry out the DFT calculations. The molecular reference calculations with ORCA were carried out with standard settings except for a smaller SCF cutoff (10^{-8} E_h), a larger SCF damping factor invoked with SlowConv, and a tighter integration grid to guarantee convergence of the anionic systems. The def2-QZVPPD[37] basis set was employed in all calculations.

All surface supercell calculations with VASP were done with a cutoff energy of 500 eV, the precision mode Accurate, PAW pseudopotentials,[38] and a Γ-point Monkhorst Pack grid. Gaussian smearing with σ = 0.05 eV was employed. The standard Kosugi algorithm was used for GGA calculations, and a preconditioned conjugate gradient algorithm was used for hybrid calculations.

Unless denoted otherwise, the GGA functional PBE[39] with D3(BJ) dispersion correction[40,41] was employed for geometry optimizations, as in our previous studies of defective alkali halides.[17,42,43] This method overestimates the experimental 0 K lattice parameter of KCl by about 1.5% and reproduces the low-temperature value for NaCl.

Reaction paths were modeled with the nudged elastic band (NEB) method as implemented in VASP by Henkelman et al.[44−49] and in ORCA.[50] In both cases, the LBFGS optimizer was employed. The climbing image method was used to approximate the transition state (TS) of the reaction path.

A self-consistent dielectric-dependent global hybrid (sc-DDGH[51]) functional based on PBE was used to obtain accurate electronic properties. This functional is denoted as sc-PBE0. Its efficacy for alkali chlorides was shown in previous works.[17,42,52] The exchange functional contains a self-consistently optimized Fock exchange fraction x, which is determined via the bulk dielectric constant ε_∞. For KCl (NaCl), the optimized exchange fraction is x = 46.3% (42.8%).

DDEC6 charge and bond order analysis was performed with Chargemol (version 3.5).[53−56] Orbital projections were done with Wannier90 (version 2.1.0).[57] Orbitals and atomic structures were visualized with VESTA (version 3.4.7).[58]

Thermodynamic Properties. Unless denoted otherwise, all given adsorption and reaction energies are corrected by the zero-point vibrational energy obtained from frequency calculations with VASP. All systems were repeatedly optimized until their mass-weighted Hessian did not have any negative eigenvalues. For the reaction, only molecular vibrations were considered because the influence on the surface modes is negligible (<0.02 eV, see Supporting Information for tested systems).

For the reaction of nitrogen and hydrogen, all energies were additionally corrected for thermal vibrational energies, and the vibrational entropy to the Gibbs free energy at different temperatures from 0 − 1000 K. All thermodynamic properties were calculated in the harmonic approximation. Due to the breakdown of vibrational entropy for small frequencies in the model of the harmonic oscillator, all modes lower than 100 cm^{-1} were set to 100 cm^{-1} for the calculation of the entropy, similar to the approach by Ribeiro et al.[59] The zero-point

vibrational energy was obtained with eq 1. N is the total number of normal modes considered in the frequency calculation. In this and all subsequent equations, the energies and frequencies are used in the unit eV.

$$E_{vib}^{ZPVE} = \frac{1}{2}\sum_{i=1}^{N} \nu_i \tag{1}$$

The thermal vibrational energy was calculated with eq 2.

$$E_{vib}^{therm} = \sum_{i=1}^{N} \frac{\nu_i}{e^{(\nu_i/k_B T)} - 1} \tag{2}$$

the vibrational entropy was obtained with eq 3.

$$S_{vib} = k_B \sum_{i=1}^{N} \left(\frac{\nu_i}{k_B T e^{(\nu_i/k_B T)} - 1} - \ln(1 - e^{(\nu_i/k_B T)}) \right) \tag{3}$$

The thermodynamic data for the gas-phase molecules N_2, H_2, and N_2H_4, including translation and rotation entropy, were obtained from frequency calculations and thermodynamic analyses with ORCA and the methods implemented therein on the PBE-D3(BJ) level.

RESULTS AND DISCUSSION

Nitrogen Adsorption on the Defective Potassium and Sodium Chloride (100) Surface. In the first step, the effect of the F center on an adsorbed nitrogen molecule was investigated. The molecule was placed above the defect cavity and optimized, resulting in two different minimum geometries, both situated inside the cavity.

One of the minimum geometries of N_2 on the defective KCl (100) surface is orthogonal to the surface (Figure 1), and the
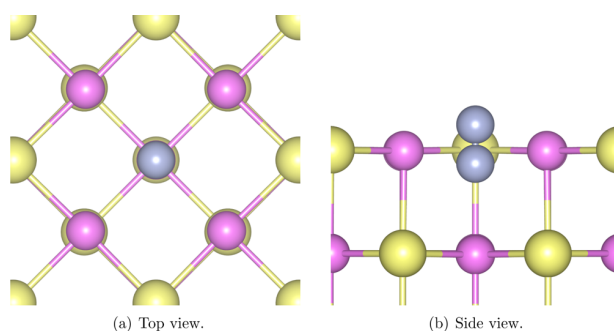

(a) Top view.   (b) Side view.

Figure 1. Optimized geometry of the nitrogen molecule located in the F center of KCl, perpendicular to the (100) surface plane. Yellow spheres denote chlorine atoms, purple spheres denote potassium atoms, and light blue spheres denote nitrogen atoms.

other one is parallel to it (Figure 2a). The parallel geometry is the energetically lowest structure of both and stabilized by −0.80 eV with respect to gas-phase N_2. The orthogonal geometry is slightly less stable, −0.69 eV.

On the defective NaCl (100) surface, parallel N_2 is rotated by 45°(Figure 2b), likely due to steric reasons to fit into the tighter cavity. It is stabilized by −0.83 eV, only slightly more than on KCl (100). No stable orthogonal geometry was found on NaCl (100).

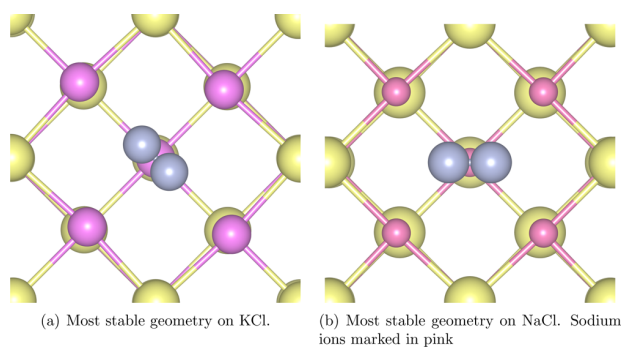In the following, only the most stable geometries were investigated.

(a) Most stable geometry on KCl.

(b) Most stable geometry on NaCl. Sodium ions marked in pink

Figure 2. Optimized geometries of the nitrogen molecule located in the F center parallel to the (100) surface plane.

A DDEC6 analysis was carried out, and the orbital of the defect electron was investigated (Figure 3a) for an analysis of the charge transfer.
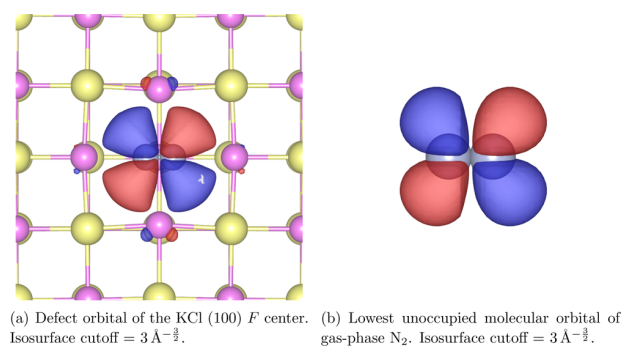

(a) Defect orbital of the KCl (100) F center. Isosurface cutoff = $3\,\text{Å}^{-\frac{3}{2}}$.

(b) Lowest unoccupied molecular orbital of gas-phase N_2. Isosurface cutoff = $3\,\text{Å}^{-\frac{3}{2}}$.

Figure 3. Comparison of the defect orbital of the KCl (100) F center with adsorbed N_2 and the lowest unoccupied molecular orbital (LUMO) of neutral gas-phase N_2.

According to the DDEC6 charge analysis, there is an excess charge of -0.79 e (-0.78 e) on the nitrogen molecule adsorbed on defective KCl (NaCl), indicating that the defect electron was essentially transferred to N_2. The defect electron is located in an orbital (Figure 3a) that closely resembles the LUMO of gas-phase N_2 (Figure 3b).

After adsorption, the N−N bond is elongated from 1.114 to 1.186 Å on KCl and to 1.190 Å on NaCl, which is halfway between the triple bond length and double bond length (1.246 Å for cis-N_2H_2).

The weakening of the bond also manifests in a decreased N−N stretching vibration frequency. At the PBE-D3(BJ) level, it is reduced by 21%, from 2425 cm^{-1} for the neutral molecule to 1908 cm^{-1} (1911 cm^{-1}) for the adsorbed molecule on KCl (NaCl). For comparison, the gas-phase molecule was calculated with ORCA and def2-QZVPPD basis sets. A similar reduction of the vibrational frequency of about 23% was obtained comparing the neutral molecule and the anion, further strengthening the above finding that the defective surface reduces the adsorbed nitrogen molecule.

The electronic properties were obtained with a sc-PBE0 single-point calculation based on the optimized geometries obtained with PBE-D3(BJ). The level of the defect band for the KCl (100) surface defect is lowered by 1.42 eV (from −3.02 to −4.44 eV) due to adsorption. For the NaCl (100) surface defect, the analogous band is lowered by 1.22 eV (from

−3.62 to −4.84 eV). In both cases, the shifts indicate a strong interaction of the molecule with the defect cavity.

In conclusion, the F center on the alkali halide (100) surfaces reduces the adsorbed nitrogen molecule to N_2^-. There is no significant difference between the adsorbate electronic structure of the two halide surfaces, even though the geometry of the molecule is changed to accommodate for the smaller lattice of NaCl.

Migration of Nitrogen on KCl. Prior to the investigation of surface reactions involving reduced N_2, we study other possible surface processes. Since the defect concentration is usually rather low (up to 1.5×10^{18} F centers/cm^3 or about 0.01%[60]), nitrogen will predominantly adsorb on defect-free parts of the surface. Knowledge of the diffusion barriers on the surface is important for an estimation of the F-center reactivity. Therefore, migration of adsorbed nitrogen was modeled for several paths across the pristine KCl (100) surface and from the terrace into the defect cavity. Additionally, the exchange with the neighboring chloride anion analogous to the mechanism of the F center diffusion[43,61] was studied.

The adsorption of N_2 on the pristine (100) surface of KCl is weak and dominated by dispersion interactions. Depending on the adsorption site, the adsorption energy calculated with PBE-D3(BJ)/500 eV ranges from 0.08−0.13 eV. Low-energy electron diffraction measurements determined an isosteric heat of adsorption for this combination of 0.114 ± 0.031 eV.[62] The favored adsorption structures of the molecule are a parallel geometry centered above neighboring potassium ions, and a tilted geometry [50° vs (100) surface] over a potassium ion pointing toward a chloride ion.

The minimum energy path (MEP) of the migration of nitrogen over the (100) surface calculated with NEB did not show a significant energetic barrier (<0.03 eV). Therefore, N_2 is highly mobile on the surface. For the migration into the defect cavity, two different migration pathways were investigated, starting from an adsorption site above a nearby cation or anion into the cavity with two different molecular orientations. In both cases, the migration is not hindered by an energetic barrier, but the energy surface is too shallow to immediately drive the molecule into the cavity. It is therefore concluded that nitrogen molecules are not actively attracted by the F centers, and adsorption at the defect site occurs randomly.

Possible reactions of the reduced nitrogen molecule are rivaled by desorption and subsequent deactivation or migration. The concerted migration of the nitrogen molecule in combination with the cavity was simulated with the nitrogen molecule migrating above and below the surface.

The barrier for N_2 migration above the surface (Figure 4a) is calculated as 1.70 eV. For N_2 migration below the surface (Figure 4b), the energy barrier is slightly larger, 1.87 eV. In both cases, the barrier is higher than for desorption or migration of the F center simulated on the same level of theory.[43] However, the same trend for the energy difference between the two available migration paths is observed with and without adsorbed nitrogen. In either case, the barrier is reduced if the chloride migrates below the surface, likely due to favorable electrostatic interaction of the chloride anion with the surrounding cations and additional degrees of freedom for the nitrogen molecule. In a direct comparison between the concerted migration and the alternative desorption, vacancy migration, and re-adsorption processes, the concerted migration is stabilized by about 0.1−0.2 eV. However, due to the
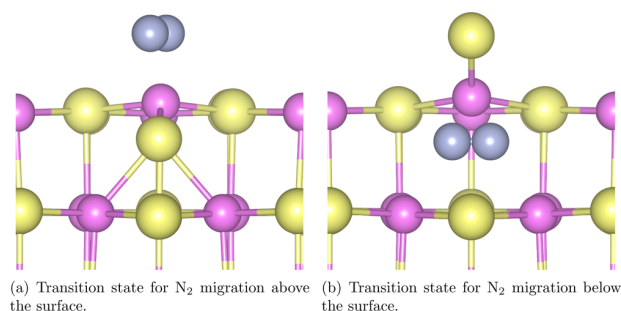
(a) Transition state for N_2 migration above the surface.

(b) Transition state for N_2 migration below the surface.

Figure 4. Migration of the nitrogen molecule in combination with the defect cavity across the KCl (100) surface.

relatively large barrier, it is very unlikely to occur. We therefore conclude that after adsorption on the pristine parts of the surface and diffusion into the F-center, N_2 is demobilized and can react with other molecules.

Finally, we studied if the nitrogen molecule can migrate toward a KCl bulk F center by placing it into the defect cavity in a bulk $3 \times 3 \times 3$ supercell (Figure 5). The absorbed
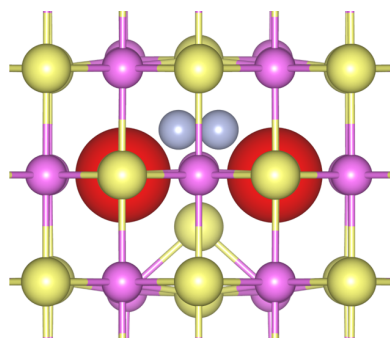
Figure 5. TS of the N_2 migration through the KCl bulk. The red spheres represent the position of the defect cavities. Viewed along $\langle 110 \rangle$.

nitrogen molecule is stabilized by -0.93 eV with respect to the gas phase. This is 0.13 eV lower than on the (100) surface F center, partially due to increased dispersion interaction, and partially to the enhanced electrostatic stabilization of N_2^- in the lattice.

Subsequently, the migration of the nitrogen molecule through the bulk was simulated to estimate the probability of this possible side reaction. The calculated migration enthalpy is 2.93 eV at 0 K, making bulk migration highly unlikely to occur compared to any of the other processes.

Reaction of Nitrogen with Hydrogen. As nitrogen is reduced by the defective surface, its bond is weakened and its reactivity is expected to increase. To test the change in reactivity, a reaction with hydrogen to hydrazine was modeled both on the defective surface (with VASP) and in the gas phase (with ORCA) for a neutral and a singly negative molecule for comparison. In the gas-phase calculations, we intentionally applied standard basis sets without Rydberg orbitals, in order to simulate the charge localization in N_2^- that was observed on the surface (see above).

The gas-phase models show that the reduction of gas-phase nitrogen strongly reduces the reaction barriers. For the 1,1-addition of hydrogen to nitrogen, the highest barrier is lowered from 4.53 eV (neutral) to 2.23 eV (anion), and for the same-

side 1,2-addition, the highest barrier is lowered from 5.71 to 2.27 eV. A similar decrease in barriers is expected for adsorbed N_2.

For the surface model, first, the adsorption of a hydrogen molecule was calculated on the pristine (100) surface and the defect cavity. On the pristine surface, the absorption energy is in the range -0.02 to -0.08 eV and the molecule is mainly bound by dispersion. The F center does not attract the hydrogen molecule and does not reduce it either. Therefore, it is safe to assume that the first step of the reaction is the adsorption and reduction of nitrogen in the defect cavity. Starting from this configuration, there are two possible pathways for the reaction of nitrogen and hydrogen to a diimide, similar to the gas-phase reaction. One pathway generates *cis*-diimide (Figure 6a, abbreviated as HNNH) via a 1,2-addition, and the other generates *iso*-diimide via a 1,1-addition (Figure 6b, abbreviated as NNH_2).
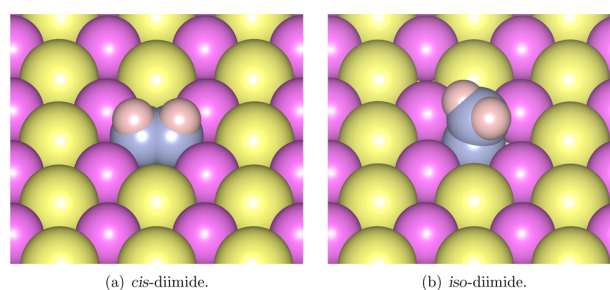

(a) *cis*-diimide.

(b) *iso*-diimide.

Figure 6. Geometry of the diimides in the KCl (100) defect cavity.

These diimides rapidly dissociate at high temperatures in the gas phase,[63] but are strongly bound to the F center. The additional stabilization amounts to -2.25 and -2.24 eV for *iso*-diimide and *cis*-diimide, respectively.

The isomerization of *iso*-N_2H_2 to *cis*-N_2H_2 in the KCl defect cavity was investigated as well. No one-step reaction path could be found, which is in line with theoretical findings for the gas-phase reaction.[23,29] The MEP indicates that the lowest reaction path occurs via dissociation of *iso*-N_2H_2 to N_2 and H_2. Therefore, the two pathways can be considered separately.

In the final step, a second H_2 molecule is added to the diimide to yield hydrazine (Figure 7), which is stabilized by -0.53 eV.

Thermodynamics of the H_2–N_2 Reaction. To assess the rate-limiting steps of the reactions, the Gibbs free energy was calculated for all minima and TSs. The diagram of the Gibbs free energy for the 1,1-addition pathway is given in Figure 8.
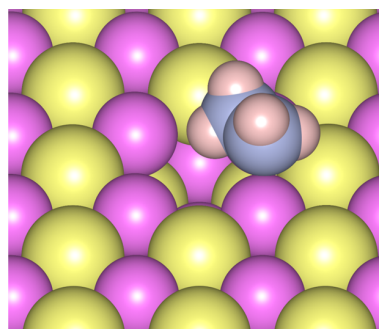

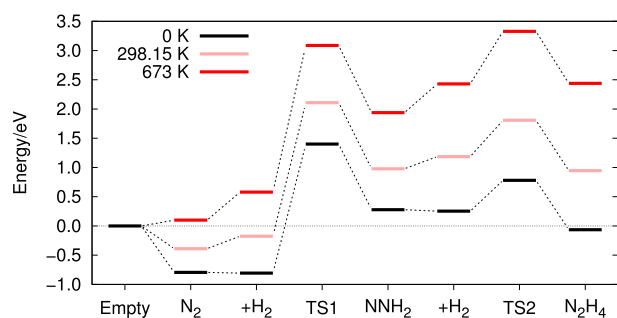**Figure 7.** Geometry of hydrazine in the KCl (100) defect cavity.

Figure 8. Calculated Gibbs free energy diagram for the two-step 1,1-addition of N_2 and H_2 to N_2H_4.

The rate-determining barrier is connected with the addition of hydrogen to the adsorbed nitrogen molecule. This can take place via an Eley−Rideal (ER) or a Langmuir−Hinshelwood (LH) mechanism. The LH mechanism, where the hydrogen molecule first adsorbs the nearby nitrogen molecule, yields a lower reaction barrier. However, hydrogen preadsorption is not likely to occur due to the low adsorption energy as mentioned above. At 0 K, the calculated barrier is 2.21 eV and rises with increasing temperature to 2.51 eV at 673 K (2.73 eV at 1000 K). The reaction rate k increases with growing temperature, but remains relatively small. At temperatures close to the melting point of KCl, 1000 K, $k = 0.37$ s^{-1}. An ER mechanism, in which the hydrogen molecule reacts from the gas phase, yields a similar barrier at 0 K, 2.19 eV. However, the Gibbs free energy barrier is increased to 2.50 eV at 673 K (3.42 eV at 1000 K) due to negative ΔS, reducing the reaction rate by a factor of 3000 with respect to the LH mechanism.

In both cases, increasing the hydrogen partial pressure facilitates the reaction. In the LH mechanism, this shifts the equilibrium toward hydrogen pre-adsorption, and in the ER mechanism, this lowers the barrier.

The diagram of the less favorable 1,2-addition pathway is given in Figure 9.
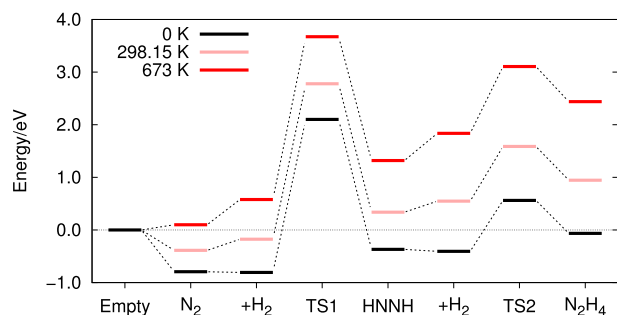

Figure 9. Calculated Gibbs free energy diagram for the two-step 1,2-addition of N_2 and H_2 to N_2H_4.

Again, the first hydrogen addition to N_2 has the highest barrier. Assuming a LH mechanism, the Gibbs free energy barrier is 2.91 eV at 0 K, which increases to 3.09 eV at 673 K. With an ER mechanism, it changes from 2.89 to 3.57 eV, respectively.

Since the initial step of both pathways has the highest barrier, the entire reaction has to take place under thermodynamic conditions. However, under such conditions, the reaction $N_2 + 2H_2 \rightarrow N_2H_4$ is entropically and

energetically disfavored. The reaction enthalpy ΔH amounts to 0.56 eV. At standard pressure, the Gibbs free energy ΔG rises monotonously with temperature and becomes 1.08 eV at room temperature.

We therefore decided not to continue and simulate the final formation of NH_3 because the initial addition already poses a major bottleneck. The barriers of the simulated reaction are higher than those found in the standard Haber−Bosch reaction pathways, in which the rate-determining barrier is only ≈1.2 eV.[64] However, the barriers calculated on the defective surface are significantly lower than the barriers found in the gas phase,[29] demonstrating a non-negligible catalytic effect of the F center.

In the following part, the single reaction steps are analyzed with respect to their gas-phase counterpart and their reactive orbitals are characterized. All following comparisons use the electronic energy because of convergence issues for the anionic systems in the gas-phase frequency calculations.

1,1-Addition to iso-N_2H_2. The 1,1-addition of hydrogen to nitrogen is simulated starting from a weakly bound initial geometry (Figure 10a). In the first step of the addition, the hydrogen molecule is split with one hydrogen atom (H1) bonding to the adjacent nitrogen atom and the other hydrogen atom (H2) being partially reduced ($q = -0.52$ e) and stabilized by the surface cations (Figure 10b). Then, H2 is transferred to NNH and *iso*-diimide is generated (Figure 10c).

Orbital Analysis. In the neutral gas-phase reaction to *iso*-diimide, the TS highest occupied molecular orbital (HOMO) consists of the $\pi_{N_2}^*$ orbital and the $\sigma_{H_2}^*$ orbital. Significant geometric distortion is required to lift the electrons from the bonding ground-state HOMOs into the anti-bonding transition state HOMO, which leads to a high barrier. The addition of an electron to the N_2 antibonding π^* orbital of nitrogen, as it occurs in the hypothetical anionic gas-phase reaction and on the defective surface (leading to a singly occupied molecular orbital), makes this unnecessary and consequently facilitates the reaction. The covalent interaction takes place between the $\pi_{N_2}^*$ orbital and the σ_{H_2} and $\sigma_{H_2}^*$ orbitals (Figure 11a,b, respectively), which mix to generate the two highest transition-state orbitals. The occupation of the $\sigma_{H_2}^*$ orbital breaks the H_2 single bond.

1,1-Addition to N_2H_4. The 1,1-addition of hydrogen to *iso*-diimide is analogous to the previous 1,1-addition. It begins with an essentially unbound starting geometry (Figure 12a). Unlike in the previous reaction, the diimide molecule moves upward in the cavity so that the hydrogen molecule can attack. After the hydrogen bond breaks, one hydrogen atom (H1) binds to the diimide and the other (H2) is partially reduced ($q = -0.68$ e) and is stabilized by the neighboring surface cations (Figure 12b). In the final step, H2 is transferred to the diimide to generate hydrazine (Figure 12c).

Orbital Analysis. For comparison, in the neutral gas-phase reaction $NNH_2 + H_2 \rightarrow N_2H_4$, an energy barrier of 0.69 eV is obtained. For the anionic radical reaction $NNH_2^- + H_2 \rightarrow N_2H_4^-$, the reaction barrier is lowered to 0.07 eV. In this case, the barrier calculated for the corresponding surface reaction, 0.53 eV, is closer to the neutral gas-phase reaction. This observation is supported by the orbitals involved in the transition-state HOMOs. In the neutral gas-phase reaction of *iso*-diimide to hydrazine, the $\pi_{N_2H_2}^*$, $\pi_{N_2H_2}$, $\sigma_{H_2}^*$, and σ_{H_2} orbitals are involved. Since the LUMO and HOMO of *iso*-diimide are energetically close, the reaction barrier is lower
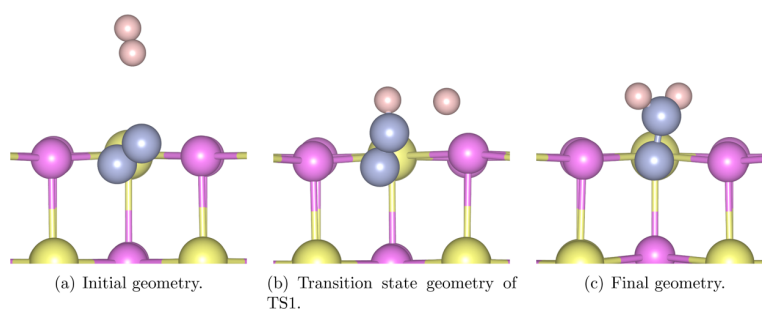
(a) Initial geometry.   (b) Transition state geometry of TS1.   (c) Final geometry.

Figure 10. Geometries of the 1,1-addition of hydrogen to nitrogen on the defective KCl (100) surface.

(a) Spin-up HOMO+1 of the transition state. Isosurface cutoff = $2.5\,\text{Å}^{-\frac{3}{2}}$.   (b) Spin-up HOMO of the transition state. Isosurface cutoff = $2.5\,\text{Å}^{-\frac{3}{2}}$.
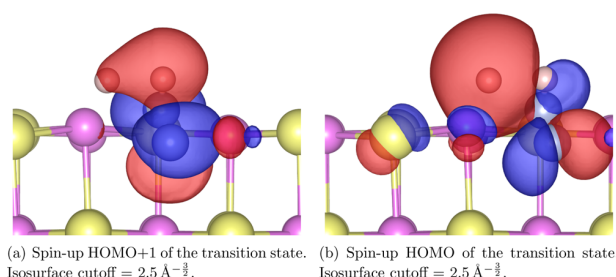
Figure 11. Orbitals of the transition state of the reaction $N_2 + H_2 \rightarrow NNH_2$.

(a) Spin-up HOMO+1 of the transition state. Isosurface cutoff = $2.5\,\text{Å}^{-\frac{3}{2}}$.   (b) Spin-up HOMO of the transition state. Isosurface cutoff = $2.5\,\text{Å}^{-\frac{3}{2}}$.
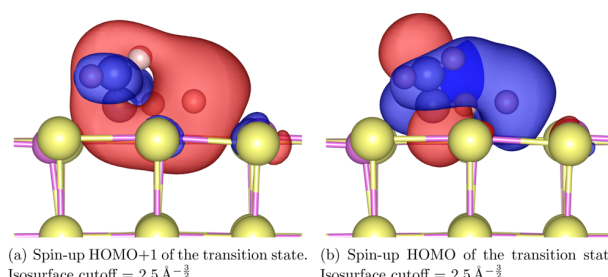
Figure 13. Orbitals of the transition state of the reaction $NNH_2 + H_2 \rightarrow N_2H_4$.

than for the reaction $N_2 + H_2$. In the case of the anionic gas-phase reaction, the additional electron is transferred to an extra orbital with a strong $\sigma_{H_2}^*$ character. Orbital analysis shows that the reaction on the defective surface resembles the neutral gas-phase reaction (Figure 13) and does not benefit from the reduction of the nitrogen molecule.

1,2-addition to cis-N$_2$H$_2$. In the 1,2-addition to *cis*-diimide, the bond between the hydrogen atoms is cleaved (From Figure 14a to Figure 14b), and one of the atoms (H1) binds to the closest nitrogen atom. Unlike in the previously discussed 1,1-additions, the free hydrogen atom (H2) does not interact with the neighboring cations before it binds to the other nitrogen atom (Figure 14c).

Orbital Analysis. In this case, atom H2 is a neutral radical after H_2 dissociation. The lack of electrostatic stabilization leads to a higher reaction barrier. In the gas phase, the reaction energy barriers for $N_2 + H_2 \rightarrow HNNH$ and $N_2^- + H_2 \rightarrow NNH_2^-$ are 5.71 and 2.27 eV, respectively. The barrier for the corresponding reaction on the defective surface amounts to 3.03 eV, and orbital analysis (Figure 15) shows that the $\pi_{N_2}^*$ orbital participates in all reactions. In the case of the neutral gas phase, a completely unbound hydrogen radical is generated.

A comparison between the previously discussed 1,1-addition to *iso*-diimide (Section) and this reaction shows that the surface ions do play a non-negligible role in stabilizing the transition state and lowering the reaction barrier.

1,2-Addition to N$_2$H$_4$. The 1,2-addition of hydrogen to *cis*-diimide occurs analogously to the 1,1-addition to *iso*-diimide. The hydrogen bond breaks and one hydrogen atom (H1) is bound to the upper nitrogen atom (Figure 16), whereas the other (H2) moves down and reacts with the lower nitrogen atom in a transition state that closely resembles the one in Figure 12b.

In this case, the reaction barrier on the defective surface, 0.84 eV, is much smaller than those of both gas-phase reactions. The calculated barriers for gas-phase reactions $HNNH + H_2 \rightarrow N_2H_4$ and $NNH_2^- + H_2 \rightarrow N_2H_4^-$ are 3.96 and 1.90 eV, respectively. In this case, the electrostatic effect of the surface seems to enable an alternative reaction path and facilitates the reaction even more than before.

Orbital Analysis. Since the reaction closely resembles the 1,1-addition, the same orbitals are involved in the reaction (Figure 17) and the free hydrogen atom H2 is partially reduced ($q = -0.68\ e$).
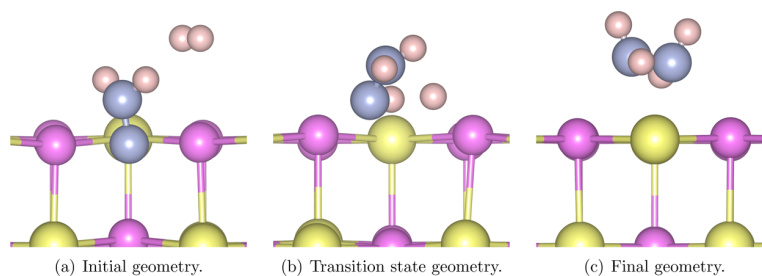

(a) Initial geometry.   (b) Transition state geometry.   (c) Final geometry.

Figure 12. Geometries of the 1,1-addition of hydrogen to iso $- N_2H_2$ on the defective KCl (100) surface.

(a) Initial geometry.   (b) Transition state geometry.   (c) Final geometry.
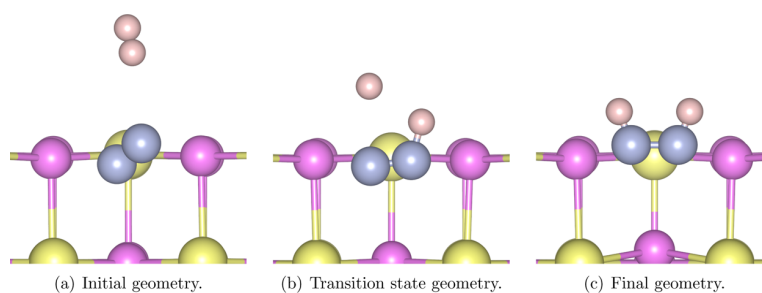
Figure 14. Geometries of the 1,2-addition of hydrogen to nitrogen on the defective KCl (100) surface.

(a) On the defective KCl (100) surface. Isosurface cutoff = $2.5\,\text{Å}^{-\frac{3}{2}}$.

(b) In the neutral gas phase. Isosurface cutoff = $2.5\,\text{Å}^{-\frac{3}{2}}$.

(c) In the hypothetical anionic gas phase. Isosurface cutoff = $2.5\,\text{Å}^{-\frac{3}{2}}$.
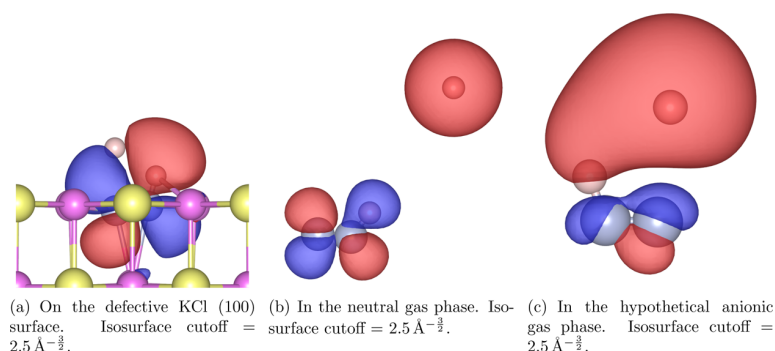
Figure 15. Highest occupied orbitals of the transition states of the reaction $N_2 + H_2 \rightarrow HNNH$.

(a) Initial geometry.   (b) Transition state geometry.   (c) Final geometry.
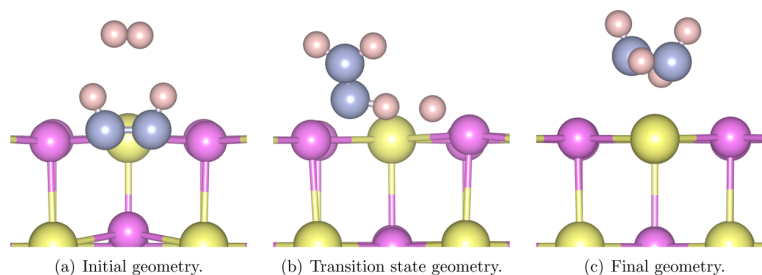
Figure 16. Geometries of the 1,1-addition of hydrogen to *cis*-N_2H_2 on the defective KCl (100) surface.

(a) Spin-up HOMO+1 of the transition state. Isosurface cutoff = $2.5\,\text{Å}^{-\frac{3}{2}}$.

(b) Spin-up HOMO of the transition state. Isosurface cutoff = $2.5\,\text{Å}^{-\frac{3}{2}}$.
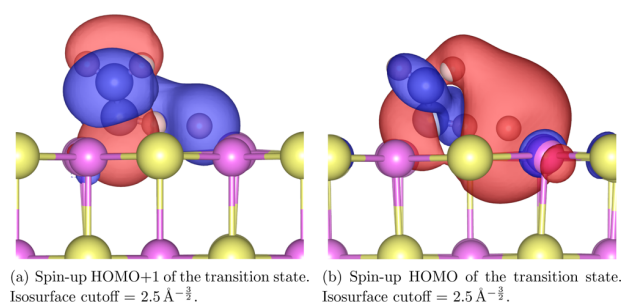
Figure 17. Orbitals of the transition state of the reaction $NNH_2 + H_2 \rightarrow N_2H_4$.

Due to the similarities of defective KCl (100) and NaCl (100) in terms of adsorption energies, geometries and electronic structure of N_2 and H_2, and also of the barrier of the 1,1-addition, we did not investigate the other reaction mechanisms for NaCl. We expect that the barriers and reaction energies are similar.

CONCLUSIONS

The reactivity of F centers on the KCl and NaCl (100) surfaces were investigated using a plane-wave approach and the generalized-gradient functional PBE. The defect was found to readily reduce adsorbed nitrogen in both investigated halides. No significant differences were found between the behavior of the F center on NaCl and KCl. The reaction of nitrogen and hydrogen to hydrazine was simulated on KCl (100), and two possible pathways were identified which bear similarities to the gas-phase reactions. In all cases, the rate-determining reaction barriers were significantly decreased on the KCl (100) surface due to the reduction of nitrogen. The first step of the 1,1-addition was also investigated on NaCl (100), and essentially, the same barrier was observed. A significant part of the catalytic activity was traced to the occupation of anti-bonding N_2 orbitals, which increases the reactivity of nitrogen. We therefore predict that for molecules with a high HOMO–LUMO gap, for example, N_2 and CO_2, reactions that are driven by the occupation of anti-bonding orbitals are facilitated by a reduction on the F center. The ionic surface provides an additional benefit by stabilizing the transition state, in the present case, a partially reduced hydrogen atom after H_2 bond cleavage. On the other hand, the catalytic effect on reactions of

molecules with small HOMO−LUMO gaps is expected to be less significant.

While the thermodynamic properties of the overall reaction disfavor the generation of hydrazine and the initial barrier is too high for practical applications, this model reaction demonstrates the catalytic capabilities of F centers on alkali halide surfaces.

■ ASSOCIATED CONTENT

Ⓢ Supporting Information

The Supporting Information is available free of charge at https://pubs.acs.org/doi/10.1021/acs.jpcc.1c07467.

> Evaluation of two different types of frequency calculation for selected systems (PDF)

■ AUTHOR INFORMATION

Corresponding Author

Thomas Bredow − *Mulliken Center for Theoretical Chemistry, Institut für Physikalische und Theoretische Chemie, Universität Bonn, 53115 Bonn, Germany*; Phone: +49 (0) 228 733839; Email: bredow@thch.uni-bonn.de; Fax: +49 (0)228 739064

Author

Michael Häfner − *Mulliken Center for Theoretical Chemistry, Institut für Physikalische und Theoretische Chemie, Universität Bonn, 53115 Bonn, Germany*; ⓞ orcid.org/0000-0002-2765-6689

Complete contact information is available at:
https://pubs.acs.org/10.1021/acs.jpcc.1c07467

Notes

The authors declare no competing financial interest.

■ ACKNOWLEDGMENTS

■ REFERENCES

(1) Jencks, W. P. *Catalysis in Chemistry and Enzymology*; Dover Publications: New York, 1969.

(2) Bond, G. C. *Heterogeneous Catalysis: Principles and Applications*; Oxford University Press, 1974.

(3) Mizuno, H.; Inoue, M. Diffusion of F Centers into Potassium Chloride Single Crystals. *Phys. Rev.* **1960**, *120*, 1226−1229.

(4) Wolf, E. L. Diffusion Effects in the Inhomogeneously Broadened Case: High-Temperature Saturation of the F-Center Electron Spin Resonance. *Phys. Rev.* **1966**, *142*, 555−569.

(5) Scott, A. B.; Smith, W. A. The Thermal Stability of F-centers in Alkali Halides. *Phys. Rev.* **1951**, *83*, 982−986.

(6) Howard, C. L. H.; Kerr, P. F. Blue Halite. *Science* **1960**, *132*, 1886−1887.

(7) Zielasek, V.; Hildebrandt, T.; Henzler, M. Surface Color Centers on Epitaxial NaCl Films. *Phys. Rev. B* **2000**, *62*, 2912−2919.

(8) Gravitt, J. C.; Gross, G. E.; Benson, D. K.; Scott, A. B. Motion of F Centers in KCl and KI. *J. Chem. Phys.* **1962**, *37*, 2783−2784.

(9) Tyagi, R. C.; Singh, R.; Gupta, A. K. Kinetics of Electrolytic Coloration in Alkali Halide Crystals. *J. Phys.: Condens. Matter* **1970**, *3*, 769−772.

(10) Tegenkamp, C.; Pfnür, H. Adsorbate Induced Contact Charging: Pure and OH-substituted Benzoic Acids Adsorbed on Wide Band Gap Insulators. *Phys. Chem. Chem. Phys.* **2002**, *4*, 2653−2659.

(11) Malaske, U.; Tegenkamp, C.; Henzler, M.; Pfnür, H. Defect-induced Band Gap States and the Contact Charging Effect in Wide Band Gap Insulators. *Surf. Sci.* **1998**, *408*, 237−251.

(12) Fölsch, S.; Henzler, M. Water Adsorption on the NaCl Surface. *Surf. Sci.* **1991**, *247*, 269−273.

(13) Malaske, U.; Pfnür, H.; Bässler, M.; Weiss, M.; Umbach, E. Adsorption geometry of OH adsorbed atFcenters on a NaCl(100) surface. *Phys. Rev. B* **1996**, *53*, 13115−13120.

(14) Chen, W.; Tegenkamp, C.; Pfnür, H.; Bredow, T. Tailoring Band Gaps of Insulators by Adsorption at Surface Defects: Benzoic Acids on NaCl Surfaces. *Phys. Rev. B* **2009**, *79*, 235419.

(15) Chen, W.; Tegenkamp, C.; Pfnür, H.; Bredow, T. Color Centers in NaCl by Hybrid Functionals. *Phys. Rev. B* **2010**, *82*, 104106.

(16) Hochheim, M.; Bredow, T. Adsorption of PTCDA on NaCl Surfaces with Color Centers: Charge Transfer and Formation of Radical Ions. *J. Phys. Chem. C* **2018**, *122*, 29426−29434.

(17) Häfner, M.; Hochheim, M.; Bredow, T. Chemistry with F Centers: Reduction of Organic Molecules on the Defective Potassium Chloride(100) Surface. *J. Phys. Chem. C* **2020**, *124*, 12606−12616.

(18) Erisman, J. W.; Sutton, M. A.; Galloway, J.; Klimont, Z.; Winiwarter, W. How a Century of Ammonia Synthesis Changed the World. *Nat. Geosci.* **2008**, *1*, 636−639.

(19) Smil, V. Nitrogen Cycle and World Food Production. *World Agric.* **2011**, *2*, 9−13.

(20) Appl, M. *Ullmann's Encyclopedia of Industrial Chemistry*; Wiley-VCH Verlag GmbH & Co. KGaA: Weinheim, 2006.

(21) Ertl, G. Elementary Steps in Heterogeneous Catalysis. *Angew. Chem., Int. Ed. Engl.* **1990**, *29*, 1219−1227.

(22) Honkala, K.; Hellman, A.; Remediakis, I. N.; Logadottir, A.; Carlsson, A.; Dahl, S.; Christensen, C. H.; Nørskov, J. K. Ammonia Synthesis from First-Principles Calculations. *Science* **2005**, *307*, 555−558.

(23) Hellman, A.; Baerends, E. J.; Biczysko, M.; Bligaard, T.; Christensen, C. H.; Clary, D. C.; Dahl, S.; van Harrevelt, R.; Honkala, K.; Jonsson, H.; et al. Predicting Catalysis: Understanding Ammonia Synthesis from First-Principles Calculations. *J. Phys. Chem. B* **2006**, *110*, 17719−17735.

(24) Kitano, M.; Inoue, Y.; Yamazaki, Y.; Hayashi, F.; Kanbara, S.; Matsuishi, S.; Yokoyama, T.; Kim, S.-W.; Hara, M.; Hosono, H. Ammonia Synthesis Using a Stable Electride as an Electron Donor and Reversible Hydrogen Store. *Nat. Chem.* **2012**, *4*, 934−940.

(25) Kitano, M.; Kanbara, S.; Inoue, Y.; Kuganathan, N.; Sushko, P. V.; Yokoyama, T.; Hara, M.; Hosono, H. Electride Support Boosts Nitrogen Dissociation over Ruthenium Catalyst and Shifts the Bottleneck in Ammonia Synthesis. *Nat. Commun.* **2015**, *6*, 6731.

(26) Peters, J. W.; Szilagyi, R. K. Exploring New Frontiers of Nitrogenase Structure and Mechanism. *Curr. Opin. Chem. Biol.* **2006**, *10*, 101−108 Bioinorganic chemistry/Biocatalysis and biotransformation.

(27) Burgess, B. K.; Lowe, D. J. Mechanism of Molybdenum Nitrogenase. *Chem. Rev.* **1996**, *96*, 2983−3012.

(28) Mortenson, L. E.; Thorneley, R. N. F. Structure and Function of Nitrogenase. *Annu. Rev. Biochem.* **1979**, *48*, 387−418.

(29) Hwang, D.-Y.; Mebel, A. M. Reaction Mechanism of N2/H2 Conversion to NH3: A Theoretical Study. *J. Phys. Chem. A* **2003**, *107*, 2865−2874.

(30) Kresse, G.; Hafner, J. Ab initiomolecular dynamics for liquid metals. *Phys. Rev. B* **1993**, *47*, 558−561.

(31) Kresse, G.; Furthmüller, J. Efficiency of Ab-initio Total Energy Calculations for Metals and Semiconductors Using a Plane-wave Basis Set. *Comput. Mater. Sci.* **1996**, *6*, 15−50.

(32) Kresse, G.; Furthmüller, J. Efficient iterative schemes forab initiototal-energy calculations using a plane-wave basis set. *Phys. Rev. B* **1996**, *54*, 11169−11186.

(33) Neese, F. The ORCA Program System. *Wiley Interdiscip. Rev.: Comput. Mol. Sci.* **2012**, *2*, 73−78.

(34) Neese, F. Software Update: the ORCA Program System, Version 4.0. *Wiley Interdiscip. Rev.: Comput. Mol. Sci.* **2018**, *8*, No. e1327.

(35) Valeev, E. F. Libint: A Library for the Evaluation of Molecular Integrals of Many-body Operators over Gaussian Functions. http://libint.valeyev.net/, 2020; version 2.7.0-beta.6, (accessed Aug 4, 2021).

(36) Lehtola, S.; Steigemann, C.; Oliveira, M. J. T.; Marques, M. A. L. Recent developments in libxc - A comprehensive library of functionals for density functional theory. *SoftwareX* **2018**, *7*, 1−5.

(37) Rappoport, D.; Furche, F. Property-optimized Gaussian Basis Sets for Molecular Response Calculations. *J. Chem. Phys.* **2010**, *133*, 134105.

(38) Kresse, G.; Joubert, D. From Ultrasoft Pseudopotentials to the Projector Augmented-wave Method. *Phys. Rev. B* **1999**, *59*, 1758−1775.

(39) Perdew, J. P.; Burke, K.; Ernzerhof, M. Generalized Gradient Approximation Made Simple. *Phys. Rev. Lett.* **1996**, *77*, 3865−3868.

(40) Grimme, S.; Ehrlich, S.; Goerigk, L. Effect of the Damping Function in Dispersion Corrected Density Functional Theory. *J. Comput. Chem.* **2011**, *32*, 1456−1465.

(41) Grimme, S.; Antony, J.; Ehrlich, S.; Krieg, H. A Consistent and Accurate ab Initio Parametrization of Density Functional Dispersion Correction (DFT-D) for the 94 Elements H-Pu. *J. Chem. Phys.* **2010**, *132*, 154104.

(42) Häfner, M.; Bredow, T.; Centers, M. FandMcenters in alkali halides: A theoretical study applying self-consistent dielectric-dependent hybrid density functional theory. *Phys. Rev. B* **2020**, *102*, 184108.

(43) Häfner, M.; Bredow, T. Mobility of F Centers in Alkali Halides. *J. Phys. Chem. C* **2021**, *125*, 9085−9095.

(44) Sheppard, D.; Xiao, P.; Chemelewski, W.; Johnson, D. D.; Henkelman, G. A Generalized Solid-state Nudged Elastic Band Method. *J. Chem. Phys.* **2012**, *136*, 074103.

(45) Sheppard, D.; Henkelman, G. Paths to Which the Nudged Elastic Band Converges. *J. Comput. Chem.* **2011**, *32*, 1769−1771.

(46) Sheppard, D.; Terrell, R.; Henkelman, G. Optimization Methods for Finding Minimum Energy Paths. *J. Chem. Phys.* **2008**, *128*, 134106.

(47) Henkelman, G.; Uberuaga, B. P.; Jónsson, H. A Climbing Image Nudged Elastic Band Method for Finding Saddle Points and Minimum Energy Paths. *J. Chem. Phys.* **2000**, *113*, 9901−9904.

(48) Henkelman, G.; Jónsson, H. Improved Tangent Estimate in the Nudged Elastic Band Method for Finding Minimum Energy Paths and Saddle Points. *J. Chem. Phys.* **2000**, *113*, 9978−9985.

(49) Jónsson, H.; Mills, G.; Jacobsen, K. W. *Classical and Quantum Dynamics in Condensed Phase Simulations*; Berne, B. J., Ciccotti, G., Coker, D. F., Eds.; World Scientific: Singapore, 1998; Chapter 16; pp 385−404.

(50) Ásgeirsson, V.; Birgisson, B. O.; Bjornsson, R.; Becker, U.; Neese, F.; Riplinger, C.; Jónsson, H. Nudged Elastic Band Method for Molecular Reactions Using Energy-Weighted Springs Combined with Eigenvector Following. *J. Chem. Theory Comput.* **2021**, *17*, 4929−4945.

(51) Skone, J. H.; Govoni, M.; Galli, G. Self-consistent Hybrid Functional for Condensed Systems. *Phys. Rev. B* **2014**, *89*, 195112.

(52) Hochheim, M.; Bredow, T. Band-edge Levels of the NaCl(100) Surface: Self-consistent Hybrid Density Functional Theory Compared to Many-body Perturbation Theory. *Phys. Rev. B* **2018**, *97*, 235447.

(53) Manz, T. A.; Limas, N. G. Chargemol Program for Performing DDEC Analysis, Version 3.5. https://sourceforge.net/projects/ddec/, 2017; (accessed Aug 4, 2021).

(54) Manz, T. A.; Limas, N. G. Introducing DDEC6 Atomic Population Analysis: Part 1. Charge Partitioning Theory and Methodology. *RSC Adv.* **2016**, *6*, 47771−47801.

(55) Limas, N. G.; Manz, T. A. Introducing DDEC6 Atomic Population Analysis: Part 2. Computed Results for a Wide Range of Periodic and Nonperiodic Materials. *RSC Adv.* **2016**, *6*, 45727−45747.

(56) Manz, T. A. Introducing DDEC6 Atomic Population Analysis: Part 3. Comprehensive Method to Compute Bond Orders. *RSC Adv.* **2017**, *7*, 45552−45581.

(57) Mostofi, A. A.; Yates, J. R.; Pizzi, G.; Lee, Y.-S.; Souza, I.; Vanderbilt, D.; Marzari, N. An Updated Version of Wannier90: A Tool for Obtaining Maximally-localised Wannier Functions. *Comput. Phys. Commun.* **2014**, *185*, 2309−2310.

(58) Momma, K.; Izumi, F. VESTA 3for three-dimensional visualization of crystal, volumetric and morphology data. *J. Appl. Crystallogr.* **2011**, *44*, 1272−1276.

(59) Ribeiro, R. F.; Marenich, A. V.; Cramer, C. J.; Truhlar, D. G. Use of Solution-Phase Vibrational Frequencies in Continuum Models for the Free Energy of Solvation. *J. Phys. Chem. B* **2011**, *115*, 14556−14562.

(60) Kuczynski, G. C.; Byun, J. J. Diffusion of F-centers in Potassium Chloride Crystals. *Phys. Status Solidi B* **1972**, *50*, 367−377.

(61) Kuklja, M. M.; Kotomin, E. A.; Popov, A. I. Semi-empirical Simulations of F-center Diffusion in KCl Crystals. *J. Phys. Chem. Solids* **1997**, *58*, 103−106.

(62) Vogt, J.; Weiss, H. Physisorption of Small Molecules on Single Crystal Alkali Halide Surfaces: CO and N2 Adsorbed on KCl(100). *Z. Physiol. Chem.* **2004**, *218*, 973−995.

(63) Miller, C. E. Hydrogenation with diimide. *J. Chem. Educ.* **1965**, *42*, 254.

(64) Logadottir, A.; Nørskov, J. K. The Effect of Strain for N2 Dissociation on Fe Surfaces. *Surf. Sci.* **2001**, *489*, 135−143.

Hydrogenation of CO and CO$_2$ Catalyzed by Potassium Chloride F Centers

Michael Häfner[*] and Thomas Bredow[*]

[*] Mulliken Center for Theoretical Chemistry, Universität Bonn, Beringstr. 4, 53115 Bonn, Germany
[†] Any request for the permisson to reuse material from this chapter should be directed to the American Chemical Society.

Article

Hydrogenation of CO and CO$_2$ Catalyzed by Potassium Chloride *F* Centers

Michael Häfner and Thomas Bredow*

ACCESS | Metrics & More | Article Recommendations | Supporting Information

ABSTRACT: The role of *F* centers on the KCl (100) surface in the hydrogenation of carbon monoxide and carbon dioxide was investigated theoretically at density-functional theory level. The surface defect was found to reduce all carbon-containing species involved in the reactions. In all cases, the defect electron occupies the lowest antibonding orbital of the molecules which weakens at least one of the C−O bonds. All reaction barriers of the hydrogenation on the defect are significantly reduced in comparison with the gas-phase reactions. The thermodynamic and kinetic parameters of the reaction pathways were computed, allowing for a comparison with the industrially established Cu/ZnO catalyst for methanol synthesis. It was found that methanol synthesis from CO$_2$ is thermodynamically and kinetically hindered, yielding formate as a product that blocks the *F* center. The reaction rate for the rate limiting step of the methanol synthesis from CO on the *F* center is about 10 times higher than that for the conventional catalyst. However, the end product methanol further dissociates into methanolate and free radical hydrogen with only a small activation barrier. Furthermore, it was found that water dissociates into OH$^-$ and H$^\bullet$ on the defective surface, so that even trace amounts can deactivate the *F* center.
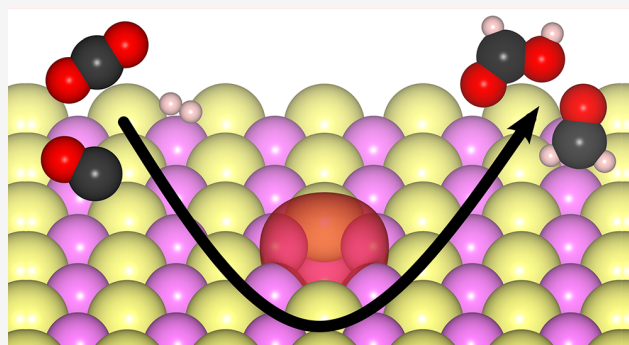
INTRODUCTION

Some of the technologically most relevant chemical reactions, e.g. the Haber−Bosch process for ammonia synthesis, and the production of methanol from carbon monoxide rely on catalysts to become thermodynamically feasible.[1,2] As these chemicals are produced in amounts far above 50 million tons per year, it is of utmost importance to reduce the energy consumption of their formation processes as much as possible.[3,4] The search for catalysts that are more efficient, cheaper, and less problematic for human health and the environment is, therefore, an ubiquitous topic in chemistry since the reactions were established. In the case of methanol synthesis, the mixture of copper and zinc oxide established in 1966 is still the standard catalyst material.[5] But the search for new catalysts for these reactions has gathered pace, also due to recent developments in theoretical modeling, allowing substances that are usually assumed unsuitable for catalysis to be investigated. One example of such a substance group are the alkali halides. They are abundant and environmentally benign, but highly unreactive because of their large band gap. However, if defects are introduced into the pristine lattice, their reactivity toward adsorbed molecules is strongly enhanced and activation barriers of surface reactions are reduced.

It was shown that *F* centers, anion vacancies with trapped electrons, created e.g. by heating,[6] by adding alkaline metal vapor,[7,8] electrochemically,[9,10] or by irradiation,[11,12] are capable of reducing molecules adsorbed on the NaCl (100) surface[13,14] and to split water molecules.[15,16]

Several theoretical studies corroborate these findings and expand the list of molecules that are reduced by alkali halide *F* centers.[17−21] In all investigated cases, the defect electron is transferred into the lowest unoccupied orbital of the adsorbed molecule, with immediate consequences for its reactivity. Even for highly unreactive molecules with large electronic gaps such as N$_2$, reduction was observed.[21] In this work, we investigate the catalytic effect of the *F* center on the hydrogenation of carbon monoxide and carbon dioxide to acetic acid, formaldehyde, methanol, and side products.

For our investigation, we propose a reaction mechanism involving hydrogen molecules from the gas phase reacting with the target molecule after its activation on a KCl (100) *F* center. Previous theoretical descriptions of the alkali halide *F* center with density functional theory (DFT) correctly reproduced the electronic band gap[22] and the migration enthalpy.[23] It was found that computationally efficient GGA methods describe the charge
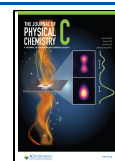
transfer from the *F* center to the molecules, the adsorption thermodynamics, and the stability and mobility of the defects with similar quality as more sophisticated self-consistent hybrid functionals. These methods are therefore applied in the present study.

The reaction pathways between the intermediates are calculated with the nudged elastic band (NEB) method.[24] Furthermore, the Gibbs free energies of the intermediates and transition structures are calculated in order to obtain reaction rate constants and equilibrium constants. As a general reference temperature, we chose 500 K which is typical for the hydrogenation of CO and CO_2 on standard industrial copper catalysts for methanol production.[25−30]

Computational Details. All surface calculations were performed with the plane-wave program package VASP,[31−33] employing standard PAW pseudopotentials[34] and a cutoff energy of 500 eV. Optimizations were performed with PBE[35] augmented by the dispersion correction D3(BJ)[36,37] as in our previous studies of defective alkali halides.[20−23] This method yields a lattice parameter of KCl of 6.26 Å, which is 1.3% larger than the experimental 0 K value of 6.18 Å.[38] Convergence of the structure optimizations was defined if the forces on the atoms were smaller than 0.01 eV/Å. The KCl(100) surface was modeled by a 4×4 supercell of a five-layer slab model with a 15 Å vacuum distance between the slabs. A Γ-point Monkhorst−Pack grid was found sufficient. The *F* center was mirrored at the central symmetry plane of the slab to avoid a spurious dipole moment.

In order to evaluate the catalytic effect of the KCl (100) surface, we calculated the reaction steps of CO_2 and CO with H_2 also in the gas phase. These calculations were performed with the program package ORCA,[39,40] the libraries libint,[41] libxc,[42] the Ahlrichs-type basis set def2-QZVPPD, and the associated auxiliary basis.[43,44]

The reaction pathways were simulated with the nudged elastic band (NEB) approach as implemented in ORCA[45] and VASP,[24,46−50] applying the climbing image (CI) algorithm to obtain the approximate transition state (TS). At least five intermediate images were used in the CI-NEB runs. In the gas-phase calculations, the standard accuracy parameters of ORCA were employed. For VASP CI-NEB calculations, the force convergence requirement for the optimizations was increased to 0.05 eV/Å.

Frequency calculations were performed for every stationary point to classify the obtained structure either as a local minimum with no negative eigenvalue or as a transition state with exactly one negative eigenvalue of the mass-weighted Hessian. The calculated vibrational frequencies were used to compute the thermal contributions to the Gibbs free energy at temperatures between 0 and 1000 K. For the surface calculations, only molecular vibrations were taken into account in order to reduce computational cost. The influence of the surface vibrations was found to be negligible (<0.02 eV). For the gas phase molecules, the rotational and translational contributions were calculated with the methodology implemented in ORCA, which is based on the quasi-RRHO model by Grimme.[51] In the surface calculations, this was considered by shifting frequencies smaller than 100 cm^{-1}, which can be considered as hindered rotations, to 100 cm^{-1}, similar to the suggestion of Ribeiro et al.[52] The thermal vibrational energy and entropy were obtained with eq 1 and eq 2, respectively.

$$E_{vib}(T) = h\nu_i \sum_{i=1}^{N} \left(\frac{1}{2} + \frac{1}{e^{h\nu_i/k_B T} - 1} \right)$$
(1)

$$S_{vib}(T) = k_B \sum_{i=1}^{N} \left(\frac{h\nu_i}{k_B T e^{h\nu_i/k_B T} - 1} - \ln(1 - e^{h\nu_i/k_B T}) \right)$$
(2)

The contribution of the molecular partial pressure to the free energy was considered with eq 3. The reference pressure p^0 was set to 1 bar.

$$E_{press}(p, T) = k_B T \ln\left(\frac{p}{p^0} \right)$$
(3)

The Gibbs free energy was calculated from the electronic energy E_{elec} and the corrections from eqs 1, 2, and 3 according to eq 4.

$$G(p, T) = E_{elec} + E_{vib}(T) - T S_{vib}(T) + E_{press}(p, T)$$
(4)

pV contributions from the slab models were negligible. With the Gibbs free energy of the ground and transition states, the reaction rate k and the equilibrium constant K_{eq} were calculated according to eqs 5 and 6, respectively.

$$k = \frac{k_B T}{h} e^{-\Delta G/k_B T}$$
(5)

$$K_{eq} = e^{-\Delta G/k_B T}$$
(6)

The relative coverage of surface defects θ was calculated with the Langmuir adsorption eq 7 based on the partial pressure p and the equilibrium constant K_{eq} obtained from the adsorption Gibbs free energy.
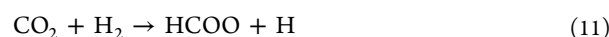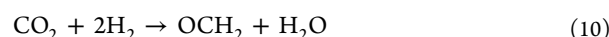
$$\theta = \frac{K_{eq}p}{1 + K_{eq}p}$$
(7)

The mass production rate r in g/m^2 h was calculated according to eq 8 from the molecular mass M, the reaction rate k, the relative F center concentration c, and the lattice constant of the crystal d.

$$r = \frac{2Mkc}{N_A d^2}$$
(8)

Bader charge analysis was performed with the grid based bader analysis by Arnaldsson et al. (version 1.04).[53] Orbital projections were calculated with Wannier90 (version 2.1.0),[54] and all structures were visualized with VESTA (version 3.4.7).[55]

■ RESULTS AND DISCUSSION

We investigated the following reactions on the defective KCl (100) surface:

$$CO + H_2 \rightarrow OCH_2$$
(9)

$$CO_2 + 2H_2 \rightarrow OCH_2 + H_2O$$
(10)

$$CO_2 + H_2 \rightarrow HCOO + H$$
(11)

$$OCH_2 + H_2 \rightarrow HOCH_3$$
(12)

$$HOCH_3 \rightarrow OH + CH_3$$
(13)

$$H_2O \rightarrow OH + H$$
(14)

All intermediates and transition structures were calculated as described above, and as discussed in the text, they are reduced by the defect with the surrounding cations balancing the negative charge.

Adsorption of CO, CO$_2$, and H$_2$. We begin with the investigation of the adsorption of the reactants carbon monoxide, carbon dioxide, and hydrogen on the F center. In the optimized structures of CO and CO$_2$, the C atom is located in the Cl vacancy site (Figures 1 and 2).
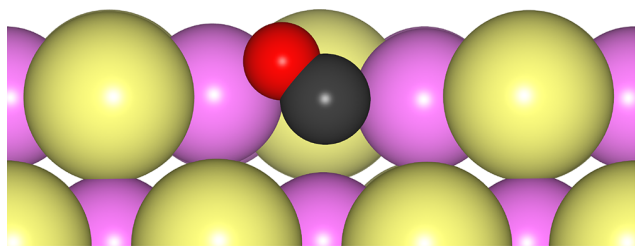

Figure 1. Minimum geometry of carbon monoxide in the KCl (100) defect cavity.
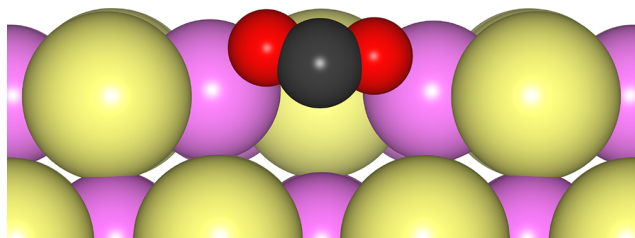
Figure 2. Minimum geometry of carbon dioxide in the KCl (100) defect cavity.

CO and CO$_2$ are both reduced by the F center. A Bader charge analysis[56−58] provides net charges of −0.81 e and −0.88 e for CO and CO$_2$, respectively. It furthermore indicates that the electron is mainly transferred to the carbon atom. For both molecules, the lowest unoccupied molecular orbital (LUMO) is occupied by the defect electron (see Figures S1 and S2 in the SI).

In accordance with the charge transfer, the calculated vibrational frequencies and bond lengths of both molecules change significantly. The calculated C−O stretching mode of carbon monoxide is lowered from 2127 to 1670 cm^{-1}, which matches the expected weakening of the bond due to occupation of an antibonding orbital. The C−O bond length increases from 1.14 Å in the gas phase to 1.22 Å on the F center. For CO$_2$, only the asymmetric stretching mode is affected by charge transfer. It is lowered from 2368 to 1734 cm^{-1}. The C−O bond lengths are increased from 1.18 to 1.24 Å. Additionally, the molecule becomes bent, as the OCO-angle is decreased to 136°.

It is observed that CO$_2$ is more strongly attracted by the F center than CO. The Gibbs free adsorption energies $\Delta G_{ads}^{0\,K}$ of CO and CO$_2$ are −0.88 eV and −1.52 eV, respectively. With increasing temperature, entropy reduces these binding energies. At 500 K, ΔG_{ads} is only −0.13 eV for CO and −0.73 eV for CO$_2$ (Tables 2 and 4). Subsequently the coverage decreases with increasing T if it is not counteracted by an increased partial pressure. This relationship is shown for the CO adsorption in Figure 3.

For CO partial pressures of 1 bar and more, more than 90% of the F centers are covered at 500 K. For the more strongly bound CO$_2$, this even holds for temperatures up to 1000 K (see Figure
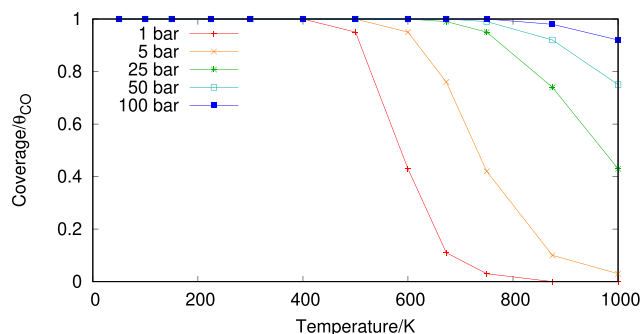

Figure 3. Coverage of KCl surface F centers depending on temperature and CO partial pressure.

S3 in the SI). Both CO and CO$_2$ have much smaller Gibbs free adsorption energies on the pristine surface, −0.13 eV and −0.24 eV, respectively (at 0 K). The latter value agrees well with the isosteric heat of adsorption of −0.27 eV as measured by Traeger et al.[59] for a saturated monolayer. It therefore becomes evident that an F center has a highly stabilizing effect on the molecules due to the charge transfer and the electrostatic stabilization. In conclusion, the analysis of geometry and vibrational frequencies indicates that both carbon oxides are reduced by the F center on the defective (100) KCl surface.

The hydrogen molecule, on the other hand, is neither reduced by the F center nor adsorbed at the defect site. With the same computational setup, we obtained $\Delta G_{ads}^{0\,K}$ = +0.16 eV for H$_2$, which mostly stems from the change of the zero point vibration energy. We also tested the possibility of homolytic H$_2$ dissociation by adsorbing one H atom in the F center and the other on a nearby Cl atom. However, this process is endothermic by +1.20 eV. Based on these results, it is expected that all reactions take place via the initial adsorption of a carbon oxide instead of a hydrogen molecule.

Adsorption of H$_2$O and Splitting into OH and H$_2$. The adsorption of H$_2$O and the OH$^\bullet$ radical on the F center was investigated to take potential side reactions originating from water traces and possible reaction side products (as in reaction 10) into account. The H$_2$O molecule is partially reduced by the F center, but during optimization no spontaneous dissociation takes place. According to the Bader analysis the water net charge is −0.63 e. Due to the occupation of an antibonding orbital, the O−H bonds are weakened. Consequently the antisymmetric O−H stretching mode decreases by ∼750 cm^{-1}. The calculated Gibbs free adsorption energy is $\Delta G_{ads}^{0\,K}$ = −0.65 eV, which is considerably less than calculated for CO and CO$_2$ (see above). Consequently, water is not expected to significantly replace CO and CO$_2$ on the defect site in equilibrium.

The hydrogen radical H$^\bullet$ does not interact with the pristine KCl surface $\left(\Delta G_{ads}^{0\,K} = 0.00 \text{ eV}\right)$ but shows strong interaction with a free F center ($\Delta G_{ads}^{0\,K}$ads = −2.91 eV). OH$^\bullet$ is even more strongly bound to the defect ($\Delta G_{ads}^{0\,K}$ = −5.12 e; see Figure 4) and is reduced to OH$^-$, as seen by the Bader net charge of −0.83 e. Similar to the case for water, the O−H stretching mode is decreased (by ∼300 cm^{-1}).

The Gibbs reaction energy of water dissociation according to H$_2$O$^-$(g) → OH$_{ads}^-$ + H$^\bullet$(g) (14) is $G_{diss}^{500\,K}$ = +0.42 eV without any additional activation barrier. At standard pressure, water molecules occupy 10% of the surface defects, yielding a turnover frequency f of 5.33×10^8 s^{-1} with the turnover frequency defined as overall reaction rate at the active center. The resulting gas-phase hydrogen radicals are expected to either occupy other
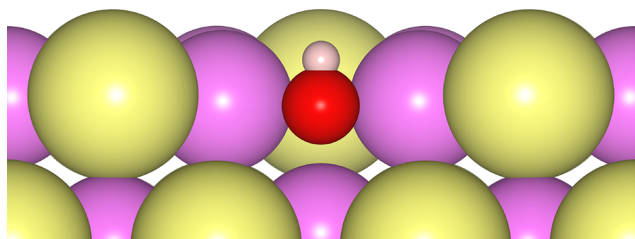
Figure 4. Minimum geometry of the hydroxy radical in the KCl (100) defect cavity.

available F centers or react to molecular hydrogen according to 2 $H^\bullet(g) \rightarrow H_2(g)$ with a highly exergonic Gibbs reaction energy of $\Delta G_R^{500\ K} = -2.00$ eV per radical.

In conclusion, the dissociation of water occurs readily at 500 K. While the thermodynamic equilibrium of the dissociation by itself strongly favors the reagent, the expulsion of free radical hydrogen atoms is expected to shift the equilibrium as they occupy other available F centers or form molecular hydrogen with an overall negative Gibbs energy. This is in qualitative accordance with the observations from experiments.[15,16] Therefore, even trace amounts of water gas are expected to act as a potent catalyst poison that quickly inhibits the catalyst.

Formaldehyde Formation from CO. The hydrogenation of carbon monoxide to formaldehyde (reaction 9) is expected to proceed in one step $CO + H_2 \rightarrow OCH_2$.

The Gibbs free energy diagram for this reaction is shown in Figure 5. Associated Gibbs free energies and kinetic parameters
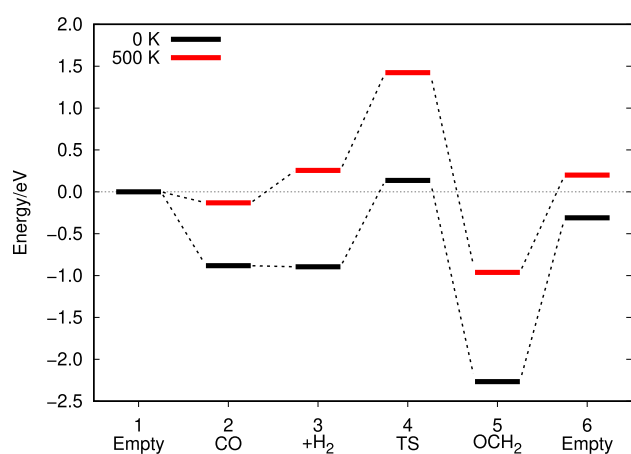

Figure 5. Calculated Gibbs free energy diagram for reaction 9 on the defective KCl (100) surface at 0 and 500 K and 1 bar p_{CO} and 1 bar p_{H_2}.

are collected in Table 1 and Table 2, respectively. In the following, all intermediate structures are labeled as 1−6, reactions from one intermediate n to another m are denoted with $n \rightarrow m$, and kinetic parameters linked to these reactions are denoted as $k_{n,m}$ and $\Delta G_{n,m}$. Unless noted otherwise, all calculations were carried out at standard pressure, i.e., at a partial pressure of 1 bar carbon monoxide and 1 bar hydrogen.

For the reaction of the adsorbed carbon monoxide with hydrogen, two mechanisms are possible. The hydrogen molecule reacts either according to a Langmuir−Hinshelwood (LH) mechanism by first adsorbing to the defect site (Figure 6a, $2 \rightarrow 3$) before reacting with CO (Figure 6b, $3 \rightarrow 5$) or according to an Eley−Rideal (ER) mechanism by reacting directly from the gas phase ($2 \rightarrow 5$).

Table 1. Calculated Gibbs Free Energies $\Delta G(0\ K)$ and $\Delta G(500\ K)$ of the Minima and Transition States (TS) of Reaction 9 on the Defective KCl (100) Surface at 0 and 500 K and 1 bar p_{CO} and 1 bar p_{H_2}[a]

	System	$\Delta G(0\ K)$ (eV)	$\Delta G(500\ K)$ (eV)
1	empty defect, CO(g)	0.00	0.00
2	CO(ads)	−0.88	−0.13
3	CO(ads), H_2(ads)	−0.90	0.23
4	CO + H_2 TS	0.14	1.42
5	OCH_2(ads)	−2.27	−0.96
6	empty defect, OCH_2(g)	−0.31	0.20

[a]G of the empty defective surface and the gas-phase molecules are taken as reference.

Table 2. Activation Energies ΔG_A, Reaction Energies ΔG_{reac}, and Reaction Rate Constants k for Reaction 9 on the Defective KCl (100) Surface at 500 K and 1 bar p_{CO} and 1 bar p_{H_2}

Reaction Step		ΔG_A (eV)	ΔG_{reac} (eV)	k (s^{-1})
$1 \rightarrow 2$	adsorption CO	0.00	−0.13	2.17×10^{14}
$2 \rightarrow 3$	adsorption $H_2(g)$	0.36	0.36	2.65×10^9
$3 \rightarrow 5$	$CO + H_2 \rightarrow OCH_2$	1.20	−1.22	9.00
$5 \rightarrow 6$	desorption OCH_2	1.16	1.16	2.24×10^1

In either case, one atom of the hydrogen molecule is immediately transferred to the adsorbed CO while the other atom is partially reduced ($q = -0.33e$) and stabilized by two adjacent cations (Figure 6b) before forming formaldehyde (Figure 6c), which is reduced by the defect with a Bader charge of $q = -0.85e$. The corresponding transition state is similar to the one calculated for the hydrogenation of N_2 on the defect.[21]

Only at 0 K, preadsorption of hydrogen (which is relevant for a LH mechanism) ($2 \rightarrow 3$) is slightly exergonic $\Delta G_{2,3}^{0\ K} = -0.02$ eV. With increasing temperature, entropy disfavors the adsorption process, increasing $\Delta G_{2,3}^{500\ K}$ to +0.36 eV at 500 K. This reduces the equilibrium H_2 coverage on sites occupied by CO $\theta_{H_2,CO}$ to only 0.025% at 1 bar partial pressure, which represents one of the LH reaction's two major bottlenecks. The other bottleneck is the activation barrier for the hydrogenation of CO ($3 \rightarrow 5$), which is calculated as $\Delta G_{3,4}^{500\ K} = 1.20$ eV. This corresponds to a reaction rate constant $k_{3,5}$ of 9.00 s^{-1} (Table 1). In contrast, the ER mechanism is only dependent on the activation barrier for the reaction of CO and H_2 from the gas phase ($2 \rightarrow 5$), which is however larger, 1.55 eV at 500 K. This corresponds to a reaction rate constant $k_{2,5}$ of only 2.29×10^{-3} s^{-1}. Under the assumption that the ER mechanism cannot take place if hydrogen is adsorbed on the active center, both mechanisms yield the same turnover frequency f according to eqs 15 and 16 for the reaction toward formaldehyde at 1 bar hydrogen partial pressure.

$$f_{LH,CO} = \theta_{CO}\theta_{H_2,CO}k_{3,5} \qquad (15)$$

$$f_{ER,CO} = \theta_{CO}(1 - \theta_{H_2,CO})k_{2,5} \qquad (16)$$

As such, the turnover frequencies are $f_{LH,CO}^{500\ K} = f_{ER,CO}^{500\ K} = 2.18 \times 10^{-3}$ s^{-1} with a combined turnover frequency of $f_{tot,CO}^{500\ K} = 4.36 \times 10^{-3}$ s^{-1}.

The LH mechanism is more sensitive to hydrogen pressures and, consequently, outpaces the ER mechanism at higher pressures.

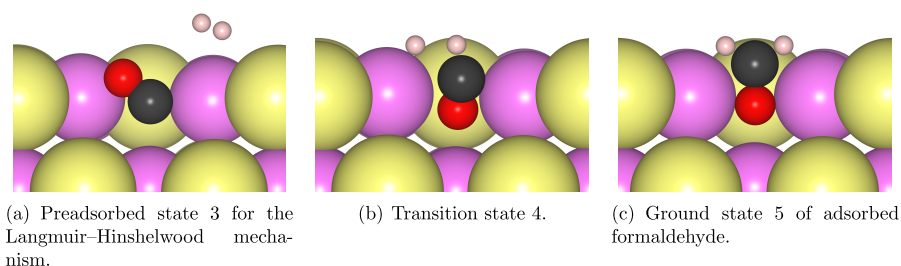(a) Preadsorbed state 3 for the Langmuir–Hinshelwood mechanism.

(b) Transition state 4.

(c) Ground state 5 of adsorbed formaldehyde.

Figure 6. Geometries of the hydrogenation of carbon monoxide on the defective KCl (100) surface.

The overall reaction $CO + H_2 \rightarrow OCH_2$ ($2 \rightarrow 5$) is exergonic with a $\Delta G_{2,5}^{500\ K} = -0.83$ eV. The back reaction of formaldehyde to the reactants is therefore extremely slow with a barrier of $\Delta G_{5,3}^{500\ K} = +2.38$ eV, and the corresponding rate constant is negligible ($k_{5,3}^{500\ K} = 1 \times 10^{-11}$ s^{-1}). The desorption energy of formaldehyde is $\Delta G_{5,6}^{500\ K} = +1.16$ eV, which is significantly higher than the desorption energy of carbon monoxide. From these results we conclude that the CO conversion to OCH_2 is irreversible, and is most efficient with a high ratio of hydrogen to carbon monoxide to overcome the reaction's unfavorable entropic balance.

Formaldehyde Formation from CO_2. The hydrogenation of carbon dioxide to formaldehyde (reaction 10) $CO_2 + 2H_2 \rightarrow OCH_2 + H_2O$ takes place in two steps. First, the formation of the intermediate formic acid $CO_2 + H_2 \rightarrow HCOOH$, and second the formation of formaldehyde $HCOOH + H_2 \rightarrow OCH_2 + H_2O$. The Gibbs free energy diagram for the overall reaction is shown in Figure 7 with the associated free energies and kinetic
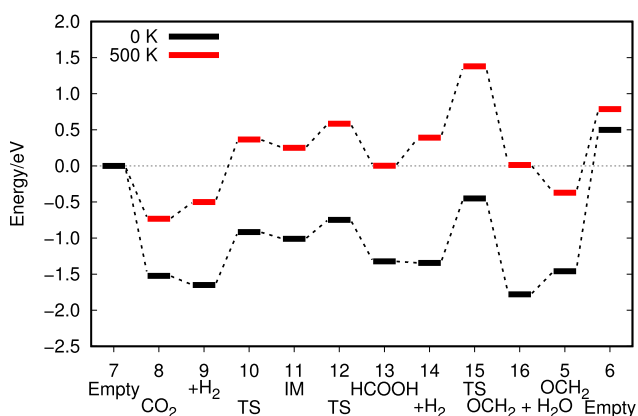

Figure 7. Calculated Gibbs free energy diagram for reaction 10 on the defective KCl (100) surface at 0 and 500 K and 1 bar p_{CO_2} and 1 bar p_{H_2}.

parameters in Table 3 and Table 4, respectively. Unless noted otherwise, all calculations were carried out at standard pressure, i.e., at a partial pressure of 1 bar carbon dioxide and 1 bar hydrogen.

Initially, we assumed that the hydrogenation of adsorbed carbon dioxide has a similar mechanism as the hydrogenation of carbon monoxide: H_2 can react either from an adsorbed state (Figure 8a, $8 \rightarrow 9$) according to an LH mechanism or from the gas phase according to an ER mechanism.

However, according to the PBE-D3(BJ) results, hydrogenation takes place via a homolytic split of the hydrogen molecule (Figure 8b) that yields the intermediate geometry

Table 3. Calculated Gibbs Free Energies $\Delta G(0\ K)$ and $\Delta G(500\ K)$ of the Minima, Intermediates (IM) and Transition States (TS) of Reaction 10 on the Defective KCl (100) Surface at 0 and 500 K and 1 bar p_{CO_2} and 1 bar p_{H_2}[a]

	System	$\Delta G(0\ K)$ (eV)	$\Delta G(500\ K)$ (eV)
7	empty defect, CO_2(g)	0.00	0.00
8	CO_2(ads)	−1.52	−0.73
9	CO_2(ads), H_2(ads)	−1.65	−0.50
10	$CO_2 + H_2$ TS1	−0.92	0.37
11	$CO_2 + H_2$ IM	−1.01	0.25
12	$CO_2 + H_2$ TS2	−0.75	0.59
13	HCOOH(ads)	−1.32	0.00
14	HCOOH(ads), H_2(ads)	−1.34	0.39
15	HCOOH + H_2 TS	−0.45	1.38
16	OCH_2(ads), H_2O (ads)	−1.78	0.01
5	OCH_2(ads)	−1.46	−0.37
6	OCH_2(g)	0.50	0.79
17	$CHOO^-$(ads), $H^\bullet$(g)	−1.00	−0.05

[a]G of the empty defective surface and the gas-phase molecules are taken as reference.

Table 4. Activation Energies ΔG_A, Reaction Energies ΔG_{reac}, and Reaction Rate Constants k for Reaction 10 on the Defective KCl (100) Surface at 500 K and 1 bar p_{CO_2} and 1 bar p_{H_2}

	Reaction Step	ΔG_A (eV)	ΔG_{reac} (eV)	k (s^{-1})
$7 \rightarrow 8$	adsorption CO_2	0.00	−0.73	2.49×10^{20}
$8 \rightarrow 9$	adsorption H_2(g)	0.23	0.23	4.92×10^{10}
$9 \rightarrow 11$	$CO_2 + H_2 \rightarrow$ IM	0.87	0.75	1.93×10^{4}
$11 \rightarrow 13$	IM $\rightarrow$ HCOOH	0.34	−0.37	4.40×10^{9}
	desorption HCOOH	0.67	0.67	1.73×10^{6}
$13 \rightarrow 14$	adsorption H_2(g)	0.39	0.39	1.26×10^{9}
$14 \rightarrow 16$	HCOOH + $H_2 \rightarrow$ $OCH_2 + H_2O$	0.99	−0.38	1.15×10^{3}
$16 \rightarrow 5$	desorption H_2O	0.00	−0.10	9.38×10^{13}
$5 \rightarrow 6$	desorption OCH_2	1.16	1.16	2.24×10^{1}

(IM) (Figure 8c) of a formate anion ($q = -0.88e$) and a hydrogen radical $H^\bullet$ ($q = -0.01e$). In the IM state, $H^\bullet$ is essentially unbound and entropy favors its desorption ($11 \rightarrow 17$) with $\Delta G_{11,17}^{500\ K} = -0.30$ eV and $k_{11,17}^{500\ K} = 1.17 \times 10^{16}$ s^{-1}. The next reaction step $11 \rightarrow 13$ to formic acid (Figure 8e) via transition state 12 (Figure 8d) has a barrier of $\Delta G_{11,13}^{500\ K} = +0.34$ eV. Since there is essentially no barrier for diffusion of $H^\bullet$ on the surface, IM is more likely to dissociate than to react to 13 (Figure 9), yielding an F center that is occupied by the stable formate

(a) Preadsorbed state 9 for the Langmuir–Hinshelwood mechanism.

(b) First transition state 10.

(c) Intermediate state 11.

(d) Second transition state 12.
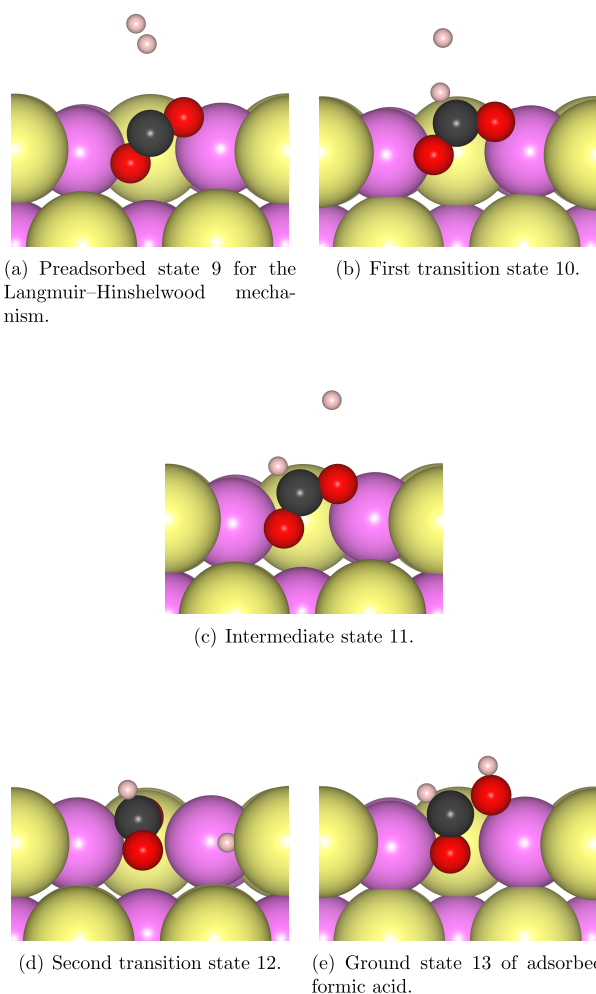
(e) Ground state 13 of adsorbed formic acid.

Figure 8. Geometries of the hydrogenation of carbon dioxide on the defective KCl (100) surface.

anion 17 ($\Delta G_{\text{ads}}^{500\text{ K}} = -4.40$ eV) and a hydrogen radical according to reaction eq 11, similar to the dissociation of water discussed above. In addition, the desorption of HCOOH is endergonic ($\Delta G^{500\text{ K}} = +0.66$ eV) since it is still being reduced ($q = -0.86e$) and stabilized by the F center. That makes it less likely to take place than both dissociation or back reaction.

The turnover frequency f of exclusively the reaction from carbon dioxide to formic acid is calculated according to eqs 17

and 18 with $k_{\text{n,m}}$ and $k_{\text{m,n}}$ being the reaction rates for reaction and back reaction.

$$f_{\text{LH,formic}} = \theta_{\text{H}_2,\text{CO}_2} \frac{k_{9,11}k_{11,13}}{k_{11,9}k_{13,11}} \tag{17}$$

$$f_{\text{ER,formic}} = (1 - \theta_{\text{H}_2,\text{CO}_2}) \frac{k_{8,11}k_{11,13}}{k_{11,8}k_{13,11}} \tag{18}$$

At 1 bar hydrogen and 1 bar carbon dioxide partial pressures, both turnover frequencies for the reaction to formic acid are equal and amount to $f_{\text{LH,formic}}^{500\text{ K}} = f_{\text{ER,formic}}^{500\text{ K}} = 4.00 \times 10^{-8}$ s^{-1} giving a total turnover frequency of $f_{\text{tot,fromic}}^{500\text{ K}} = 8.00 \times 10^{-8}$ s^{-1}. However, the turnover frequency for the reaction and subsequent dissociation into formate, $f_{\text{LH,diss}}^{500\text{ K}} = 1.58 \times 10^{-4}$ s^{-1}, is ~4000 times larger than the reaction toward formic acid.

The overall reaction $CO_2 + H_2 \rightarrow HCOOH$ ($8 \rightarrow 13$) is endergonic with $\Delta G_{8,13}^{500\text{ K}} = +0.73$ eV. The alternative dissociation $CO_2 + H_2 \rightarrow HCOO^- + H^\bullet$ ($8 \rightarrow 17$) is also endergonic with a slightly smaller $\Delta G_{8,17}^{500\text{ K}} = +0.68$ eV.

According to these results, the equilibrium of CO_2 and H_2 with both formic acid and the dissociation products at 500 K is strongly shifted toward the educts. However, the generation of unbound hydrogen radicals and the lower activation barriers allow the dissociation to gradually and irreversibly shift the reaction toward the nonreactive formate anion, which effectively deactivates the F center.

In conclusion, the first step of carbon dioxide hydrogenation is thermodynamically and kinetically hindered, making the synthesis of formic acid, methanol, or any other derivatives from carbon dioxide and hydrogen on the F center unfeasible.

A hypothetical further hydrogenation of the adsorbed formic acid with hydrogen (Figure 10) is expected to take place in the same pattern as the hydrogenation of carbon monoxide. The same formulas apply with slightly altered energies. Once again, the adsorption of hydrogen ($13 \rightarrow 14$) is extremely weak at 0 K with $\Delta G_{13,14}^{0\text{ K}} = -0.02$ eV and is furthermore entropically disfavored at 500 K with $\Delta G_{13,14}^{500\text{ K}} = +0.39$ eV. The corresponding equilibrium H_2 coverage on sites occupied by HCOOH $\theta_{\text{H}_2,\text{HCOOH}}$ amounts to only 0.01% at 1 bar partial pressure.

The transfer mechanism parallels the hydrogenation of carbon monoxide, but the intermediate hydrogen radical ($q = 0.00e$) in the transition state (Figure 10b) is not stabilized by the surface. The activation barrier for the reaction of HCOOH and H_2 to formaldehyde and water ($14 \rightarrow 16$) is the highest in this reaction $\Delta G_{14,16}^{500\text{ K}} = 0.99$ eV, larger than the barrier for desorption. The corresponding rate constant is $k_{14,16} = 1.15 \times 10^3$ s^{-1} (Table 4).
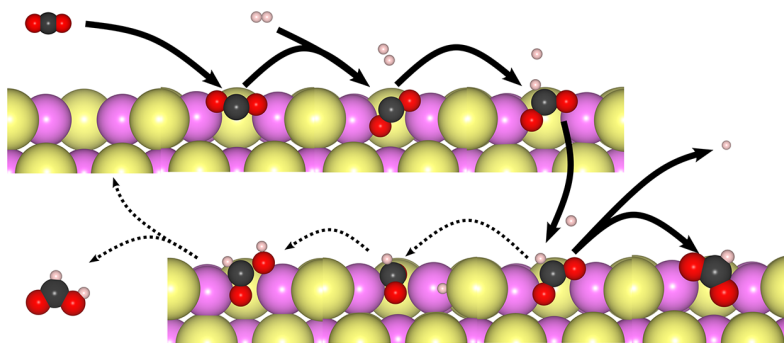

Figure 9. Reaction diagram for the hydrogenation of carbon dioxide on the defective KCl (100) surface.

(a) Preadsorbed state 14 for the Langmuir–Hinshelwood mechanism.

(b) Transition state 15.
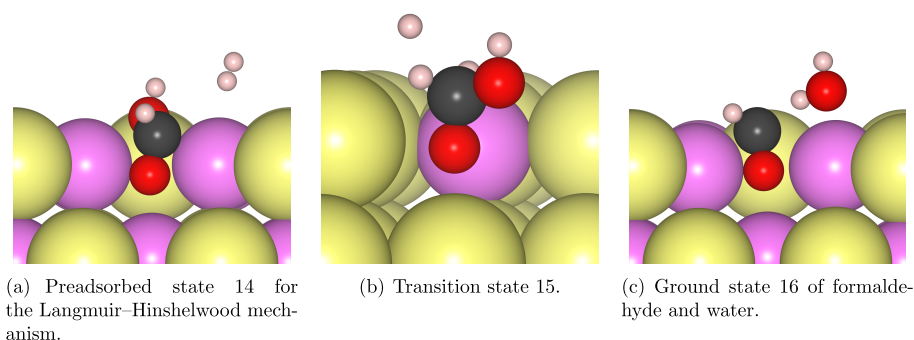
(c) Ground state 16 of formaldehyde and water.

Figure 10. Geometries of the hydrogenation of formic acid on the defective KCl (100) surface.

In conclusion, the hydrogenation of formic acid is significantly faster than the hydrogenation of any of the carbon oxides, and the reaction products are thermodynamically favorable. However, the reaction is not only hindered by low equilibrium concentrations of formic acid, but it also yields stoichiometric amounts of water, which acts as a strong catalyst poison. This renders the second step of reaction 10 unfeasible as well.

Methanol Formation from OCH$_2$. The hydrogenation of formaldehyde OCH$_2$ + H$_2$ → HOCH$_3$ (12), which is common for both CO and CO$_2$ reactions, yields methanol in a single step. The Gibbs free energy diagram for this reaction is shown in Figure 11. The corresponding Gibbs free energies and kinetic parameters are collected in Table 5 and Table 6, respectively.
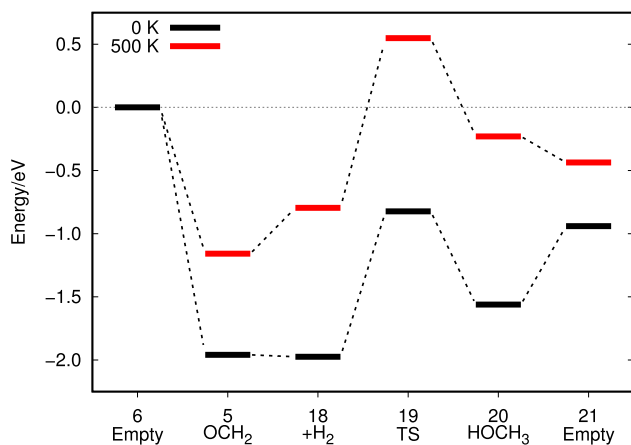

Figure 11. Calculated Gibbs free energy diagram for the methanol synthesis from OCH$_2$ and H$_2$ on the defective KCl (100) surface at 0 and 500 K and 1 bar p_{OCH_2} and 1 bar p_{H_2}.

In all qualitative aspects, the hydrogenation of formaldehyde (Figure 12) matches the hydrogenation of carbon monoxide or formic acid. The adsorption of H$_2$ (5 → 18), the first step of a LH mechanism, is endergonic ($\Delta G_{5,18}^{500\text{ K}}$ = +0.36 eV), corresponding to an equilibrium surface coverage θ_{H_2,OCH_2} of only 0.022% at 1 bar partial pressure. During the main reaction step (18 → 20), the hydrogen molecule is dissociated homolytically. The hydrogen atom which is unbound in the transition state carries a partial charge of $q = -0.11$ e and is stabilized by the surface cations (Figure 12b) before reacting with the rest to methanol, which is less reduced ($q = -0.60e$) and stabilized than all other carbon-containing molecules inves-

Table 5. Calculated Gibbs Free Energies ΔG(0 K) and ΔG(500 K) of the Intermediates and Transition States (TS) of Reaction 12 on the Defective KCl (100) Surface at 0 and 500 K and 1 bar p_{OCH_2} and 1 bar p_{H_2}^{a}

	System	ΔG(0 K) (eV)	ΔG(500 K) (eV)
6	empty defect, OCH$_2$(g)	0.00	0.00
5	OCH$_2$(ads)	−1.96	−1.16
18	OCH$_2$(ads), H$_2$(ads)	−1.97	−0.80
19	OCH$_2$ + H$_2$ TS	−0.82	0.55
20	HOCH$_3$(ads)	−1.56	−0.23
21	empty defect, HOCH$_3$(g)	−0.94	−0.44

^{a}G of the empty defective surface and the gas-phase molecules are taken as reference.

Table 6. Activation Energies ΔG_A, Reaction Energies ΔG_{reac}, and Reaction Rate Constants k for Reaction 12 on the Defective KCl (100) Surface at 500 K and 1 bar p_{OCH_2} and 1 bar p_{H_2}

	Reaction Step	ΔG_A (eV)	ΔG_{reac} (eV)	k (s^{-1})
6 → 5	adsorption OCH$_2$	0.00	−1.16	4.86 × 10^{24}
5 → 18	adsorption H$_2$(g)	0.36	0.36	2.33 × 10^9
18 → 20	OCH$_2$ + H$_2$ → HOCH$_3$	1.34	0.57	3.00 × 10^{-1}
20 → 21	desorption HOCH$_3$	0.21	0.21	1.26 × 10^{15}

tigated. The activation barrier of this hydrogenation is 1.36 eV, which is the highest calculated in this study. Accordingly, the reaction rate of methanol formation is 30 times smaller than that of formic acid from carbon monoxide, 3.00 × 10^{-1} s^{-1}. The turnover frequencies f are obtained with eqs 19 and 20.

$$f_{LH} = \theta_{H_2,OCH2}k_{18,20} \tag{19}$$

$$f_{ER} = (1 - \theta_{H_2,OCH2})k_{5,20} \tag{20}$$

At 1 bar hydrogen, both turnover frequencies for the reaction to methanol are equal and amount to $f_{LH,OCH_2}^{500\text{ K}} = f_{ER,OCH_2}^{500\text{ K}} = 6.71 \times 10^{-5}$ s^{-1} so that the total turnover frequency is $f_{tot,OCH_2}^{500\text{ K}} = 1.34 \times 10^{-4}$ s^{-1}.

The overall hydrogenation OCH$_2$ + H$_2$ → HOCH$_3$ reaction is endergonic with $\Delta G_{5,20}^{500\text{ K}}$ = +0.93 eV. However, at 500 K the back reaction ($k_{20,5}^{500\text{ K}}$ = 1.5 × 10^5 s^{-1}) is unfavorable because the desorption of methanol is fast with a reaction rate constant $k_{20,21}^{500\text{ K}}$ = 1.26 × 10^{15}, due to its small Gibbs free adsorption energy of

(a) Ground state 18 for the Langmuir–Hinshelwood mechanism.

(b) Transition state 19.
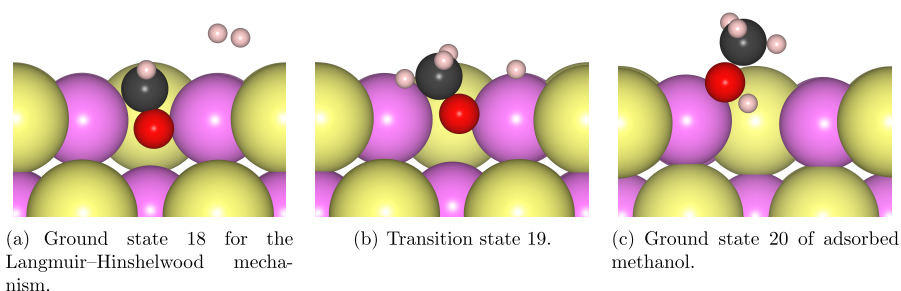
(c) Ground state 20 of adsorbed methanol.

Figure 12. Geometries of the hydrogenation of formaldehyde on the defective KCl (100) surface.

0.21 eV. Moreover, the readsorption of methanol is challenged by the adsorption of the much more stable carbon oxides, which is expected to drive the unfavorable reaction toward the product.

Dissociation of HOCH₃. The dissociation of methanol on the F center according to reaction 13 was investigated as a possible side reaction. The Gibbs free energy diagram for the reaction is shown in Figure 13. The corresponding Gibbs free energies and kinetic parameters are shown in Table 7 and Table 8, respectively.
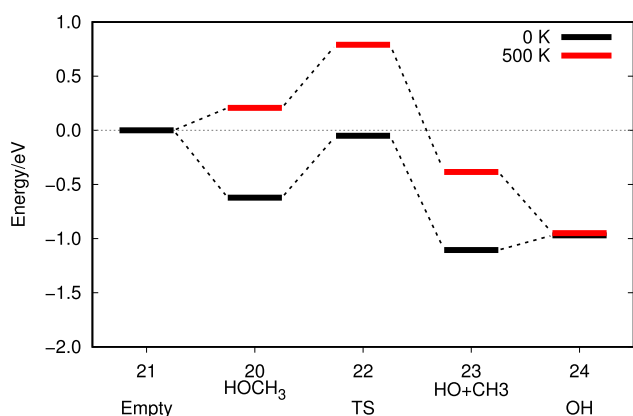

Figure 13. Calculated Gibbs free energy diagram for the dissociation of methanol on the defective KCl (100) surface at 0 and 500 K and 1 bar p_{HOCH_3}.

Table 7. Calculated Gibbs Free Energies $\Delta G(0\ K)$ and $\Delta G(500\ K)$ of the Intermediates and Transition States (TS) of Reaction 13 on the Defective KCl (100) Surface at 0 and 500 K and 1 bar p_{HOCH_3}[a]

	System	$\Delta G(0\ K)$ (eV)	$\Delta G(500\ K)$ (eV)
21	empty defect, HOCH₃(g)	0.00	0.00
20	HOCH₃(ads)	−0.62	0.21
22	HOCH₃ TS	−0.05	0.79
23	CH₃(ads), OH(ads)	−1.11	−0.39
24	OH(ads), CH₃(g)	−0.97	−0.95

[a]G of the empty defective surface and the gas-phase molecules are taken as reference.

Methanol adsorbed on the F center can dissociate into a hydroxy anion and a methyl radical (Figure 14, 2 → 4).

The reaction barrier of the dissociation is $\Delta G^{500\ K}_{21,23}$ = +0.58 eV which is significantly lower than all previous hydrogenation barriers, yielding a large reaction rate $k^{500\ K}_{21,23}$ = 1.35 × 10⁷ s⁻¹. At

Table 8. Activation Energies ΔG_A, Reaction Energies ΔG_{reac}, and Reaction Rate Constants k for Reaction 13 on the Defective KCl (100) Surface at 500 K and 1 bar p_{HOCH_3}

	Reaction Step	ΔG_A (eV)	ΔG_{reac} (eV)	k (s⁻¹)
21 → 20	adsorption HOCH₃	0.00	0.21	8.59 × 10¹⁰
20 → 23	HOCH₃ → CH₃• + OH•	0.58	−0.60	1.35 × 10⁷
23 → 24	desorption CH₃•	0.00	−0.56	2.13 × 10⁷

(a) Transition state of the dissociation 22.
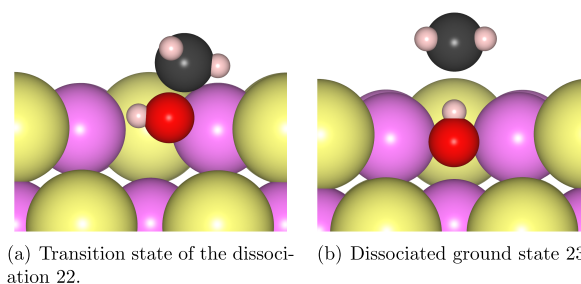
(b) Dissociated ground state 23.

Figure 14. Geometries of the dissociation of methanol on the defective KCl (100) surface.

500 K, the product $(CH_3^• + OH^{•-})$ is thermodynamically stable, compared to not only methanol adsorbed to the F center (by −0.60 eV) but also the gas-phase molecule (by −0.39 eV).

The abstraction of the methyl radical was investigated as well (23 → 24). It occurs without any additional barrier. While the reaction is slightly unfavorable at 0 K ($\Delta G^{0\ K}_{4,5}$ = +0.14 eV), it is exergonic due to entropic effects at higher temperatures ($\Delta G^{500\ K}_{4,5}$ = −0.56 eV). Consequently, methanol molecules adsorbed in F centers are expected to dissociate, similar to water as shown before, yielding a hydroxy radical that deactivates the F center and an unbound, highly reactive methyl radical.

Final Analysis. The theoretical results indicate that only the hydrogenation of carbon monoxide to formaldehyde (Reaction 9) is feasible on the defective KCl surface. At 2 bar pressure and a 1:1 ratio for H₂ and CO, the equilibrium constant K = 0.18 yields an equilibrium pressure of p_{OCH_2} = 0.135 bar for OCH₂. An increased hydrogen pressure increases the reaction rate and shifts the equilibrium toward total conversion of CO to OCH₂. This reaction also does not feature dissociative side reactions that deactivate the defect. It is only hindered by the high adsorption energy of formaldehyde. In equilibrium, the ratio of F centers occupied by CO and OCH₂ is $\frac{p_{CO}}{p_{OCH_2}}$ = 4.5 × 10⁻¹¹.

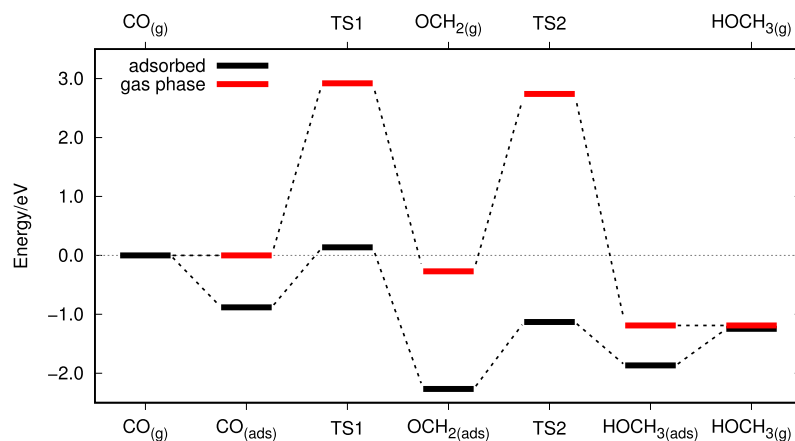Formaldehyde is therefore expected to readily react further to

Figure 15. Calculated Gibbs free energy diagrams for the methanol synthesis from CO and H_2 on the defective KCl (100) surface and in the gas phase at 0 K.

Table 9. Comparison of the Turnover Frequencies (tof) of the Common Copper-Based Catalysts and the F Center

Reference	System	Temp (K)	Pressure (bar)	tof/area (g/m^{2}h × 10^{-4})	tof/center (s^{-1} × 10^{-3})
Friedrich (1983)[26]	Raney Cu/ZnO	513	34.5	160	–
	Industrial	493	34.5	104	–
Bridgewater (1983)[27]	Industrial	513	32	94.7	–
Pan (1988)[28]	Cu/ZnO	523	50.66	300	–
Burch (1990)[29]	Cu/ZnO	513	50	–	10
	Cu	513	50	–	1
Robbins (1991)[30]	Cu/SiO$_2$	523	42	–	4.2
This study	KCl (100), 0.0092%	500	30	0.045	47.9
		500	40	0.070	75.2
		500	50	0.096	106
	KCl (100), 1%	500	50	10.5	102

methanol, as it effectively occupies most defects during the reaction that are not deactivated by a hydroxy anion.

Comparison with the Gas-Phase Reactions. Besides the various side reactions mentioned above, the F center has a significant catalytic effect on the reactivity of adsorbed CO and CO_2. This is shown for CO by comparison of the Gibbs free energy diagrams of the surface catalyzed hydrogenation and the gas-phase hydrogenation (Figure 15).

At 0 K, the activation barrier of the CO hydrogenation is reduced from 2.92 eV in the gas phase to 1.02 eV on the F center. The activation barrier for the hydrogenation of formaldehyde is reduced from 3.01 to 1.55 eV. At 500 K and 1 bar partial pressure per reagent, the activation barrier of the CO hydrogenation is reduced from 3.38 eV in the gas phase to 1.20 eV on the F center. The calculated reaction rate is increased from $k_{gas} = 9 \times 10^{-22}$ s^{-1} to $k_{surf} = 4 \times 10^{-3}$ s^{-1}. At 500 K, the activation barrier for the hydrogenation of formaldehyde is reduced from 3.51 to 1.71 eV, and the reaction rate is increased from $k_{gas} = 4 \times 10^{-23}$ s^{-1} to $k_{surf} = 1 \times 10^{-4}$ s^{-1}. At both temperatures, the F center accelerates the reaction by a factor of 10^{18} due to the activation of CO.

For the hydrogenation of carbon dioxide and formic acid, the barriers are reduced by similar amounts. At 0 K, the activation barrier of the CO_2 hydrogenation is lowered from 2.72 eV in the gas phase to 0.78 eV on the F center, and at 500 K from 3.16 eV in the gas phase to 1.32 eV between adsorbed CO_2 and gaseous hydrogen as the ground state and the second transition state. The barrier for the formic acid hydrogenation is lowered from 2.46 eV in the gas phase to 0.87 eV on the F center at 0 K, and from 3.00 eV in the gas phase to 1.38 eV at 500 K.

The F center is expected to retain the defect electron after desorption of the neutral molecules, as their reduced state is only stabilized by the Madelung potential of the surface. Therefore it fulfills all basic requirements of a catalyst.[60]

Comparison with the Industrial Catalyst. The industrial synthesis of methanol was used as a reference point because its kinetic parameters have been investigated in detail.[25−30] These studies were carried out at temperatures between 493 and 523 K and hydrogen partial pressures between 32 and 50 bar. In order to compare our results to the literature values, we calculated the kinetic parameters based on the previous free energies at 30, 40, and 50 bar hydrogen partial pressure. Only the results for the carbon monoxide reactant were considered in the comparison in Table 9, and the further reaction to methane was omitted. The pressure ratio $p(CO)/p(H_2)$ was adjusted to 3:97 to yield the highest reaction rate. This ratio also reflects the significance of the hydrogen adsorption for the reaction.

Per active center, the calculated turnover frequency on the F center is 1.0×10^{-1} s^{-1} at 50 bar, which exceeds the turnover frequency of the Cu/ZnO catalyst[29] by a factor of 10. However, the extremely low density of F centers yields a small turnover frequency per area which makes it a few thousand times slower than the copper based industrial catalysts, assuming similar accessible surface areas. For this estimate, the F center concentration was taken from a conservative estimation of 1.5×10^{18} F centers/cm^3 by Kuczynski and Byun[61] at temperatures up to 833 K, which leads to an effective concentration of 0.0092%. At this concentration, the turnover frequency is 1×10^{-5} g/m^2 h × 10^{-4} at 50 bar which is about 3000 times smaller than the turnover frequency found for the Cu/ZnO catalyst.[28] It

is estimated that at F center surface concentrations higher than 1%, the turnover frequency per area becomes comparable to the industrial catalysts. At lower temperatures, higher concentrations are experimentally proven to be possible. Przibram obtained a concentration of 2.85×10^{19} F centers/cm^3 (0.18%) via irradiation,[62] and Kaiser obtained a concentration of 1.1% by additive coloring at 90 K.[63] However, to the best of our knowledge, the stability of such high concentrations at temperatures of around 500 K has not been investigated.

In summary, the catalytic effect of the F center on the hydrogenation of carbon monoxide is superior to the copper catalysts on a per-center basis, but the overall effectiveness is highly dependent on the F center density, which is usually in the subper-mill range.

CONCLUSIONS

Periodic DFT calculations at the PBE-D3(BJ) level showed that the F center on the KCl (100) surface significantly reduces the reaction barriers associated with the hydrogenation of carbon monoxide and carbon dioxide compared to the gas phase. The F center also reduces water molecules, which leads to formation of free hydrogen radicals and hydroxy anions as experimentally observed, the latter effectively deactivating the F center.

The hydrogenation of methanol from CO_2 was found to be nonfeasible. The thermodynamic instability of the intermediate formic acid with respect to dissociation into strongly adsorbed formate and unbound hydrogen radicals blocks the reactive center and prevents further reaction.

The rate-limiting step of the successive hydrogenation of CO to methanol has a turnover frequency $f = 0.1$ s^{-1} per active center at 500 K and 50 bar, about ten times higher than the turnover frequencies found for the industrial catalysts used for methanol synthesis. However, the low defect concentration leads to very small turnover frequencies per surface area, which is 2000−3000 times smaller than reported for industrial catalysts. Moreover, the calculated thermodynamic and kinetic parameters favor dissociation of methanol to free methyl radicals and hydroxy anions, similar to the dissociation of water. In conclusion, the F center exhibits strong catalytic capabilities, but reactions are hampered by dissociative side reactions that affect all investigated reaction paths and effectively block the active sites.

Having identified and quantified this issue, the next step is to modify the defective halide surface in order to suppress the formation of formate and hydroxy anions as well as H and CH$_3$ radicals, while maintaining its activity toward CO and CO$_2$. One possibility is single-atom adsorption of transition metals at the F center sites. This will be the subject of a forthcoming study.

ASSOCIATED CONTENT

Ⓢ Supporting Information

The Supporting Information is available free of charge at https://pubs.acs.org/doi/10.1021/acs.jpcc.2c02067.

> Depictions of the relevant defect and gas phase orbitals of carbon monoxide and carbon dioxide. Analysis of the carbon dioxide coverage of the KCl (100) F centers. (PDF)

AUTHOR INFORMATION

Corresponding Author

Thomas Bredow − *Mulliken Center for Theoretical Chemistry, Institut für Physikalische und Theoretische Chemie, Universität Bonn, 53115 Bonn, Germany*; Phone: +49 (0)228 733839; Email: bredow@thch.uni-bonn.de; Fax: +49 (0)228 739064

Author

Michael Häfner − *Mulliken Center for Theoretical Chemistry, Institut für Physikalische und Theoretische Chemie, Universität Bonn, 53115 Bonn, Germany;* ⓘ orcid.org/ 0000-0002-2765-6689

Complete contact information is available at: https://pubs.acs.org/10.1021/acs.jpcc.2c02067

Notes

The authors declare no competing financial interest.

REFERENCES

(1) Jencks, W. P. *Catalysis in Chemistry and Enzymology*; Dover Publications, Inc., 1987.

(2) Jencks, G. C. *Heterogeneous Catalysis: Principles and Applications*; Oxford University Press, 1974.

(3) Apodaca, L. E. *Nitrogen (fixed)—Ammonia*. https://pubs.usgs. gov/periodicals/mcs2021/mcs2021-nitrogen.pdf, 2018; accessed March 17, 2022.

(4) (IRENA), I. R. E. A. *Innovation Outlook: Renewable Methanol*; International Renewable Energy Agency (IRENA), 2021.

(5) Klier, K. In *Methanol Synthesis*; Eley, D., Pines, H., Weisz, P. B., Eds.; Advances in Catalysis; Academic Press: 1982; Vol. *31*; pp 243−313.

(6) Scott, A. B.; Smith, W. A. The Thermal Stability of *F*-centers in Alkali Halides. *Phys. Rev.* **1951**, *83*, 982−986.

(7) Mizuno, H.; Inoue, M. Diffusion of *F* Centers into Potassium Chloride Single Crystals. *Phys. Rev.* **1960**, *120*, 1226−1229.

(8) Wolf, E. L. Diffusion Effects in the Inhomogeneously Broadened Case: High Temperature Saturation of the *F*-Center Electron Spin Resonance. *Phys. Rev.* **1966**, *142*, 555−569.

(9) Gravitt, J. C.; Gross, G. E.; Benson, D. K.; Scott, A. B. Motion of F Centers in KCl and KI. *J. Chem. Phys.* **1962**, *37*, 2783−2784.

(10) Tyagi, R. C.; Singh, R.; Gupta, A. K. Kinetics of Electrolytic Coloration in Alkali. *J. Phys.: Condens. Matter* **1970**, *3*, 769−772.

(11) Howard, C. L. H.; Kerr, P. F. Blue Halite. *Science* **1960**, *132*, 1886−1887.

(12) Zielasek, V.; Hildebrandt, T.; Henzler, M. Surface Color Centers on Epitaxial NaCl Films. *Phys. Rev. B* **2000**, *62*, 2912−2919.

(13) Tegenkamp, C.; Pfnür, H. Adsorbate Induced Contact Charging: Pure and OHsubstituted Benzoic Acids Adsorbed on Wide Band Gap Insulators. *Phys. Chem. Chem. Phys.* **2002**, *4*, 2653−2659.

(14) Malaske, U.; Tegenkamp, C.; Henzler, M.; Pfnür, H. Defect-induced Band Gap States and the Contact Charging Effect in Wide Band Gap Insulators. *Surf. Sci.* **1998**, *408*, 237−251.

(15) Fölsch, S.; Henzler, M. Water Adsorption on the NaCl Surface. *Surf. Sci.* **1991**, *247*, 269−273.

(16) Malaske, U.; Pfnür, H.; Bässler, M.; Weiss, M.; Umbach, E. Adsorption Geometry of OH Adsorbed at F Centers on a NaCl(100) Surface. *Phys. Rev. B* **1996**, *53*, 13115−13120.

(17) Chen, W.; Tegenkamp, C.; Pfnür, H.; Bredow, T. Tailoring Band Gaps of Insulators by Adsorption at Surface Defects: Benzoic Acids on NaCl Surfaces. *Phys. Rev. B* **2009**, *79*, 235419.

(18) Chen, W.; Tegenkamp, C.; Pfnür, H.; Bredow, T. Color Centers in NaCl by Hybrid Functionals. *Phys. Rev. B* **2010**, *82*, 104106.

(19) Hochheim, M.; Bredow, T. Adsorption of PTCDA on NaCl Surfaces with Color Centers: Charge Transfer and Formation of Radical Ions. *J. Phys. Chem. C* **2018**, *122*, 29426−29434.

(20) Häfner, M.; Hochheim, M.; Bredow, T. Chemistry with F Centers: Reduction of Organic Molecules on the Defective Potassium Chloride(100) Surface. *J. Phys. Chem. C* **2020**, *124*, 12606–12616.

(21) Häfner, M.; Bredow, T. Nitrogen Activation on Defective Potassium Chloride and Sodium Chloride. *J. Phys. Chem. C* **2021**, *125*, 23764–23772.

(22) Häfner, M.; Bredow, T. F. *F* and *M* in Alkali Halides: A Theoretical Study Applying Self-consistent Dielectric-dependent Hybrid Density Functional Theory. *Phys. Rev. B* **2020**, *102*, 184108.

(23) Häfner, M.; Bredow, T. Mobility of F Centers in Alkali Halides. *J. Phys. Chem. C* **2021**, *125*, 9085–9095.

(24) Jónsson, H.; Mills, G.; Jacobsen, K. W. In *Classical and Quantum Dynamics in Condensed Phase Simulations*; Berne, B. J., Ciccotti, G., Coker, D. F., Eds.; World Scientific: 1998; Chapter 16; pp 385–404.

(25) Yoshihara, J.; Campbell, C. T. Methanol Synthesis and ReverseWater-Gas Shift Kinetics over Cu(110) Model Catalysts: Structural Sensitivity. *J. Catal.* **1996**, *161*, 776–782.

(26) Friedrich, J.; Young, D.; Wainwright, M. Methanol Synthesis over Raney copper-zinc Catalysts: II. Activities and Surface Properties of a Partially Leached Alloy. *J. Catal.* **1983**, *80*, 14–24.

(27) Bridgewater, A.; Wainwright, M.; Young, D.; Orchard, J. Methanol Synthesis over Raney Copper-zinc Catalysts. III. Optimization of Alloy Composition and Catalyst Preparation. *Appl. Catal.* **1983**, *7*, 369–382.

(28) Pan, W.; Cao, R.; Roberts, D.; Griffin, G. Methanol Synthesis Activity of CuZnO Catalysts. *J. Catal.* **1988**, *114*, 440–446.

(29) Burch, R.; Golunski, S.; Spencer, M. The Role of Hydrogen in Methanol Synthesis over Copper Catalysts. *Catal. Lett.* **1990**, *5*, 55–60.

(30) Robbins, J. L.; Iglesia, E.; Kelkar, C.; DeRites, B. Methanol Synthesis over Cu/SiO 2 Catalysts. *Catal. Lett.* **1991**, *10*, 1–10.

(31) Kresse, G.; Hafner, J. Ab Initio Molecular Dynamics for Liquid Metals. *Phys. Rev. B* **1993**, *47*, 558–561.

(32) Kresse, G.; Furthmüller, J. Efficiency of Ab-initio Total Energy Calculations for Metals and Semiconductors Using a Plane-wave Basis Set. *Comput. Mater. Sci.* **1996**, *6*, 15–50.

(33) Kresse, G.; Furthmüller, J. Efficient Iterative Schemes for Ab Initio Total-energy Calculations Using a Plane-wave Basis Set. *Phys. Rev. B* **1996**, *54*, 11169–11186.

(34) Kresse, G.; Joubert, D. From Ultrasoft Pseudopotentials to the Projector Augmentedwave Method. *Phys. Rev. B* **1999**, *59*, 1758–1775.

(35) Perdew, J. P.; Burke, K.; Ernzerhof, M. Generalized Gradient Approximation Made Simple. *Phys. Rev. Lett.* **1996**, *77*, 3865–3868.

(36) Grimme, S.; Ehrlich, S.; Goerigk, L. Effect of the Damping Function in Dispersion Corrected Density Functional Theory. *J. Comput. Chem.* **2011**, *32*, 1456–1465.

(37) Grimme, S.; Antony, J.; Ehrlich, S.; Krieg, H. A Consistent and Accurate ab Initio Parametrization of Density Functional Dispersion Correction (DFT-D) for the 94 Elements H-Pu. *J. Chem. Phys.* **2010**, *132*, 154104.

(38) Rodriguez, R.; Barboza-Flores, M.; Perez, R.; Clark, A. A Laboratory Project to Obtain the Low-temperature Lattice Constants of Ionic Crystals. *Eur. J. Phys.* **1992**, *13*, 189–192.

(39) Neese, F. The ORCA Program System. *Wiley Interdiscip. Rev. Comput. Mol. Sci.* **2012**, *2*, 73–78.

(40) Neese, F. Software Update: the ORCA Program System, Version 4.0. *Wiley Interdiscip. Rev. Comput. Mol. Sci.* **2018**, *8*, e1327.

(41) Valeev, E. F. *Libint: A Library for the Evaluation of Molecular Integrals of Many-body Operators over Gaussian Functions*. http://libint.valeyev.net/, 2020; version 2.7.0 beta.6 (accessed March 17, 2022).

(42) Lehtola, S.; Steigemann, C.; Oliveira, M. J.; Marques, M. A. Recent Developments in Libxc — A Comprehensive Library of Functionals for Density Functional Theory. *SoftwareX* **2018**, *7*, 1–5.

(43) Rappoport, D.; Furche, F. Property-optimized Gaussian Basis Sets for Molecular Response Calculations. *J. Chem. Phys.* **2010**, *133*, 134105.

(44) Weigend, F. Accurate Coulomb-fitting Basis Sets for H to Rn. *Phys. Chem. Chem. Phys.* **2006**, *8*, 1057–1065.

(45) Ásgeirsson, V.; Birgisson, B. O.; Bjornsson, R.; Becker, U.; Neese, F.; Riplinger, C.; Jónsson, H. Nudged Elastic Band Method for Molecular Reactions Using Energy- Weighted Springs Combined with Eigenvector Following. *J. Chem. Theory Comput.* **2021**, *17*, 4929–4945.

(46) Sheppard, D.; Xiao, P.; Chemelewski, W.; Johnson, D. D.; Henkelman, G. A Generalized Solid-state Nudged Elastic Band Method. *J. Chem. Phys.* **2012**, *136* (074103), 074103.

(47) Sheppard, D.; Henkelman, G. Paths to Which the Nudged Elastic Band Converges. *J. Comput. Chem.* **2011**, *32*, 1769–1771.

(48) Sheppard, D.; Terrell, R.; Henkelman, G. Optimization Methods for Finding Minimum Energy Paths. *J. Chem. Phys.* **2008**, *128* (13), 134106.

(49) Henkelman, G.; Uberuaga, B. P.; Jónsson, H. A Climbing Image Nudged Elastic Band Method for Finding Saddle Points and Minimum Energy Paths. *J. Chem. Phys.* **2000**, *113*, 9901–9904.

(50) Henkelman, G.; Jónsson, H. Improved Tangent Estimate in the Nudged Elastic Band Method for Finding Minimum Energy Paths and Saddle Points. *J. Chem. Phys.* **2000**, *113*, 9978–9985.

(51) Grimme, S. Supramolecular Binding Thermodynamics by Dispersion-Corrected Density Functional Theory. *Chem.—Eur. J.* **2012**, *18*, 9955–9964.

(52) Ribeiro, R. F.; Marenich, A. V.; Cramer, C. J.; Truhlar, D. G. Use of Solution-Phase Vibrational Frequencies in Continuum Models for the Free Energy of Solvation. *J. Phys. Chem. B* **2011**, *115*, 14556–14562.

(53) Arnaldsson, A.; Tang, W.; Chill, S.; Chai, W.; Henkelman, G. *Code: Bader Charge Analysis*. http://theory.cm.utexas.edu/henkelman/code/bader/, 2020; version 1.04 (accessed March 17, 2022).

(54) Mostofi, A. A.; Yates, J. R.; Pizzi, G.; Lee, Y.-S.; Souza, I.; Vanderbilt, D.; Marzari, N. An Updated Version of Wannier90: A Tool for Obtaining Maximally-localised Wannier Functions. *Comput. Phys. Commun.* **2014**, *185*, 2309–2310.

(55) Momma, K.; Izumi, F. VESTA3 for Three-dimensional Visualization of Crystal, Volumetric and Morphology Data. *J. Appl. Crystallogr.* **2011**, *44*, 1272–1276.

(56) Henkelman, G.; Arnaldsson, A.; Jónsson, H. A Fast and Robust Algorithm for Bader Decomposition of Charge Density. *Computat. Mater. Sci.* **2006**, *36*, 354–360.

(57) Sanville, E.; Kenny, S. D.; Smith, R.; Henkelman, G. Improved Grid-based Algorithm for Bader Charge Allocation. *J. Comput. Chem.* **2007**, *28*, 899–908.

(58) Tang, W.; Sanville, E.; Henkelman, G. A Grid-based Bader Analysis Algorithm without Lattice Bias. *J. Phys.: Condens. Matter* **2009**, *21*, No. 084204.

(59) Traeger, F.; Hadnadjev, M.; Vogt, J.; Weiss, H. Structure of CO2 Adsorbed on the KCl(100) Surface. *J. Phys. Chem. A* **2011**, *115*, 6986–6996.

(60) McNaught, A. D.; Wilkinson, A. *IUPAC Compendium of Chemical Terminology*, 2nd ed.; Blackwell Scientific Publications: 1997.

(61) Kuczynski, G.; Byun, J. Diffusion of F-centers in Potassium Chloride Crystals. *Phys. Status Solidi B* **1972**, *50*, 367–377.

(62) Przibram, K. Verfärbung und Lumineszenz durch Becquerelstrahlen V nebst Verwandten Erscheinungen. *Z. Phys.* **1951**, *130*, 269–292.

(63) Kaiser, R. Störstellen Hoher Konzentration in Alkalihalogeniden. *Z. Phys.* **1952**, *132*, 482–496.

Methanol Synthesis on Copper-doped F Centers

Michael Häfner[*] and Thomas Bredow[*]

[*] Mulliken Center for Theoretical Chemistry, Universität Bonn, Beringstr. 4, 53115 Bonn, Germany
[†] Any request for the permisson to reuse material from this chapter should be directed to the American Chemical Society.

Methanol Synthesis on Copper-Doped *F* Centers

Michael Häfner and Thomas Bredow*

ACCESS | Metrics & More | Article Recommendations | Supporting Information

ABSTRACT: We investigate the influence of single copper atoms adsorbed at *F* centers on the KCl (100) surface on the reaction of adsorbed hydrogen and carbon monoxide with density functional theory methods. Adsorption at an *F* center strongly stabilizes and reduces the copper atom, as its 4s electron pairs with the defect electron to form a closed-shell state. The Cu-doped *F* center readily reduces adsorbed formaldehyde and strongly interacts with carbon monoxide and methanol, weakening and activating intramolecular bonds, but unlike the empty *F* center, it does not dissociate methanol. During hydrogenation of adsorbed CO and CH₃OH, hydrogen reacts with the adsorbed copper atom to form a stable linear HCuH complex. The hydrogen affinity of the copper atom facilitates the reaction of adsorbed molecules with hydrogen molecules as well as the attachment and removal of hydrogen atoms, enabling a fast synthesis route from carbon monoxide to methanol. The rate-limiting step of the reaction is the final hydrogenation, which recovers the active center and liberates methanol. Computing the thermodynamic and kinetic parameters of the intermediates and transition states and simulating the reaction pathway with a kinetic Monte Carlo approach, we obtained a turnover frequency of 230 s^{-1} per active site at 500 K and 50 bar with a 1:9 ratio of CO/H₂, exceeding the rate on the empty defect by 3 orders of magnitude and the conventional catalyst by 4 orders of magnitude. The present results indicate that the addition of a metal atom to the alkali halide *F* center can enhance, stabilize, and control its reactivity. In the case of copper, they point toward the existence of a synthesis route for methanol with an overall activity comparable to the conventional copper-based catalysts but with much smaller metal loading.
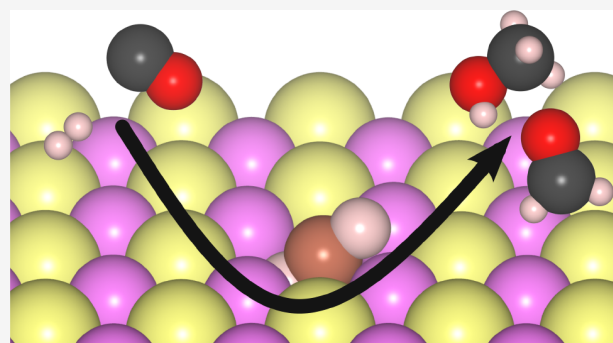
INTRODUCTION

The synthesis of methanol is one of the most important chemical processes, as methanol is the starting point for the production of formaldehyde and other chemicals, resulting in an annual demand in the range of 100 million tons.[1] The demand is expected to rise even further in the near future, also because methanol may be employed as a green fuel alternative to diesel and gasoline when produced from CO₂.

On industrial scales, methanol is currently produced from synthesis gas, a mixture of hydrogen, carbon monoxide, and carbon dioxide, via a hydrogenation on a copper and zinc oxide catalyst first developed in 1966,[2] and the fundamental concept has not changed since then. Other oxides like Al₂O₃, SiO₂, and MgO have been added to the mixture to stabilize and enhance the catalyst,[3−7] but the overall reactivity has only slightly improved compared to the original Cu/ZnO mixtures and pure copper.[8,9] Because the synthesis has to be performed at temperatures of >500 K and high pressures, there is ample research on more efficient alternatives to this catalyst. Among the studied systems are various metals, oxygen-deficient materials, and other catalytic systems with diverse kinds of mechanisms.[10]

One potential candidate for the methanol synthesis are the alkali halides, like NaCl and KCl. While unreactive in their pristine state, the introduction of *F* centers via various well-explored means activates the surface of the alkali halide crystal and allows it to interact and reduce various adsorbates.[11−17] This is documented in experiments for the reduction of salicylic acid[18,19] and the dissociation of water[20,21] and was calculated for various other molecules and systems.[22−24]

In our previous theoretical investigations, we found that the *F* center on the KCl (100) surface exhibits a strong catalytic effect on the hydrogenation of nitrogen,[25] carbon monoxide, and carbon dioxide.[26] Unfortunately, the electronic properties of the defect also favor homolytic dissociation of molecules like formic acid or the target molecule methanol. To address this kind of side reaction, we added a copper atom to our model of the *F* center and investigated how the doping affects the reaction energies and activation barriers of the hydrogenation of carbon monoxide and the dissociative side reactions.
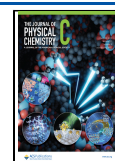
In the first step, we examine the adsorption of copper on the *F* center and the hydrogenation analogous to the reaction pathways calculated in our previous investigation[26] to compare the reactivity of doped and undoped surfaces. Next, we explore the hydrogenation of the adsorbed copper atom and its ramifications on the reaction diagram.

The methodology applied in this work is based on our previous theoretical investigations.[25–27] We used the PBE functional[28] to calculate the energetic properties of our models, which as a computationally efficient GGA functional provides a comparable charge transfer behavior as self-consistent hybrid functionals for various defective alkali halide surfaces.[22,23,27] For calculating kinetic properties such as reaction paths and activation barriers, we used the nudged elastic band method.[29]

Electronic energies are augmented with thermal corrections from local frequency calculations to obtain the Gibbs free energy in order to account for rate and equilibrium constants. Because most experiments on the hydrogenation of CO and CO_2 on the industrial copper catalyst are performed at ≈ 500 K,[3–9,30–32] we took this temperature as the reference for our thermodynamic and kinetic calculations.

COMPUTATIONAL DETAILS

All surface calculations were performed with the plane-wave program package VASP,[33–35] standard PAW pseudopotentials,[36] and a cutoff energy of 500 eV. ORCA[37,38] was employed with the libraries libint[39] and libxc[40] and the Ahlrichs-type basis set def2-QZVPPD[41,42] to compute the vibrations of gas-phase molecules. PBE[28] with D3(BJ) dispersion correction[43,44] was employed for all calculations, in accordance with our previous investigations of the vacant *F* center.[25,26]

The defective KCl (100) surface was modeled as a 4 × 4 supercell of a five-layer slab with 15 Å vacuum between the repeating slabs and a central mirror plane to prevent artificial dipole moments. For this model, a Γ-point Monkhorst−Pack grid was sufficient. Structure optimizations were considered as converged if the highest atomic force was below 0.01 eV/Å. A reference calculation for fcc bulk copper was performed with a Monkhorst−Pack grid of 12 × 12 × 12, yielding a lattice constant of 3.68 Å, which is in reasonable agreement with the experimental value 3.61 Å.[45]

Reaction barriers and transition states (TS) were obtained with the nudged elastic band (NEB) approach and the climbing image (CI) convention as implemented in VASP by Henkelman et al.[29,46–50] All reaction steps were modeled with at least five images, and the convergence criterion was set at a maximum force of 0.05 eV/Å per atom.

Each stationary point was checked with a frequency calculation and classified as local minimum or transition state if the mass-weighted Hessian had no or one negative eigenvalue within the numerical accuracy, respectively. Thermal corrections for the gas phase molecules were computed with ORCA, employing the quasi-RRHO model by Grimme.[51] For the surface models, only the copper atoms and the adsorbed molecules were taken into account for the frequency calculations because the influence of the surface was found to be negligible (<0.02 eV) compared to the cost and accuracy of the method. The obtained frequencies ν_i were used to calculate the vibrational correction (eq 1) the vibrational entropy (eq 2) and the Gibbs free energy of all systems at a temperature T.

$$E_{\text{vib}}(T) = h \sum_{i=1}^{N} \nu_i \left(\frac{1}{2} + \frac{1}{e^{h\nu_i/k_{\text{B}}T} - 1} \right) \tag{1}$$

$$S_{\text{vib}}(T) = k_{\text{B}} \sum_{i=1}^{N} \left(\frac{h\nu_i}{k_{\text{B}}T e^{h\nu_i/k_{\text{B}}T} - 1} - \ln\left(1 - e^{h\nu_i/k_{\text{B}}T}\right) \right) \tag{2}$$

Based on the findings of Ribeiro et al.,[52] frequencies below 100 cm^{-1} were shifted to 100 cm^{-1} for the computation of the entropy because the model of the harmonic oscillator breaks down at low frequencies and does not correctly describe the translational entropy. However, this only poses an issue for low adsorbate migration barriers,[53] which are not expected due to the localized nature of the defect. The error of this approximation was estimated by varying the value of the frequency cutoff, and it was found to lie within 0.05 eV for reaction barriers and energies (the vibrational frequencies of all ground and transition states can be found in the Supporting Information).

The influence of partial pressure of gas-phase molecules was accounted for with eq 3 with a reference pressure p^0 of 1 bar.

$$E_{\text{press}}(p, T) = k_{\text{B}} T \ln\left(\frac{p}{p^0} \right) \tag{3}$$

Neglecting pV for the condensed-phase systems, the Gibbs free energy G is obtained from the results of eqs 1−3 and the electronic energy of the state E_{elec} according to eq 4.

$$G(p, T) = E_{\text{elec}} + E_{\text{vib}}(T) - TS_{\text{vib}}(T) + E_{\text{press}}(p, T) \tag{4}$$

The temperature T and the difference of the Gibbs energies $\Delta G^{\ddagger}$ between intermediates and transition states constitute the essential components for the reaction rate k (eq 5) and the equilibrium constant K_{eq} (eq 6), which is derived from the reaction rates.

$$k = \frac{k_{\text{B}}T}{h} e^{-\Delta G^{\ddagger}/k_{\text{B}}T} \tag{5}$$

$$K_{\text{eq}} = e^{-\Delta G^{\ddagger}/k_{\text{B}}T} \tag{6}$$

From the partial pressure p of selected gas-phase molecules, the coverage of surface defect sites θ is obtained by the Langmuir adsorption (eq 7).

$$\theta = \frac{K_{\text{eq}}p}{1 + K_{\text{eq}}p} \tag{7}$$

The kinetic Monte Carlo simulation was performed with a program written for this work (see the Supporting Information for details). All structure images were generated with VESTA (ver. 3.4.7),[54] the orbital projections were generated with Wannier90 (ver. 2.1.0),[55] and the Bader charge analysis[56–58] was performed with a grid-based Bader analysis.[59]

RESULTS AND DISCUSSION

Copper Atoms Adsorbed on *F* Centers. In the first step, the adsorption of copper on the *F* center was investigated. After geometry optimization, the Cu atom is situated in the Cl vacancy site (Figure 1). According to a Bader charge analysis, the copper atom is reduced with a net charge of −0.71 *e*, effectively yielding Cu⁻ replacing Cl⁻ in the lattice. The
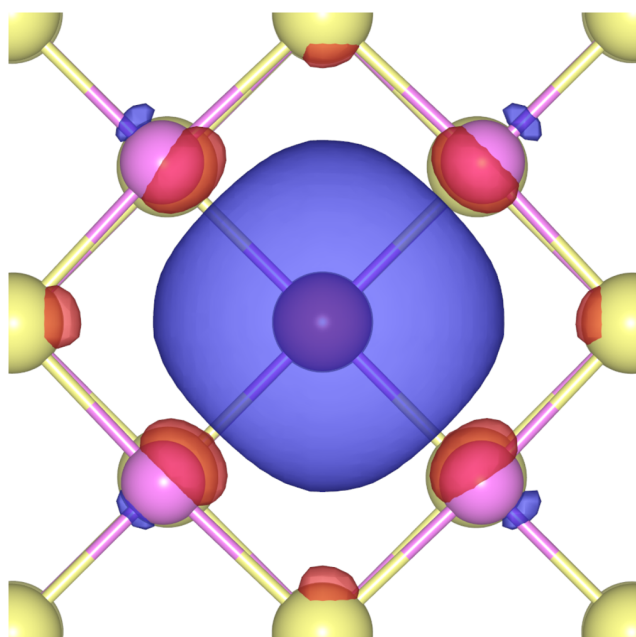
Figure 1. Highest occupied crystal orbital of the Cu-doped F center on the KCl (100) surface. Yellow spheres represent chlorine ions, violet spheres represent potassium ions, and the orange sphere at the center represents the copper atom. Isosurface cutoff = 2.5 $Å^{-3/2}$.

into a closed-shell system while maintaining the s-character and strong localization of the defect orbital (Figure 1).

In order for the doping to be feasible, the atom also has to be sufficiently stabilized by the defect cavity to enable further adsorption and subsequent reactions. The calculated adsorption energy for copper in the F center is −2.99 eV with respect to the gas phase atom, The adsorption energy on the pristine KCl (100) surface is much smaller, −0.79 eV, indicating a strong contribution of the defect to the adsorption. The cohesive energy of the fcc Cu bulk is −2.62 eV, which is slightly lower than the adsorption energy in the surface defect. This relationship still holds for the Gibbs free energies at 500 K, where entropy reduces the copper adsorption on the F center to −2.35 eV and the cohesive energy of bulk copper to −1.86 eV. Accordingly, desorption from the defect to the gas phase occurs at a rate of k_{desorp} = 2.3 × 10^{-11} s^{-1}, and desorption onto the adjacent (100) surface occurs at a rate of k_{desorp} = 1.2 × 10^{-10} s^{-1}, assuming an optimal, barrierless transition. Thus, the F center binds tightly enough to the copper atom to prevent any kind of desorption and inhibits agglomeration under reaction conditions.

Cu-Doped Defect. Figure 2 provides an overview of all minimum structures and reaction barriers investigated in this work. To be comparable to experimental data, all reaction barriers, energies, and rate constants are given at a temperature of 500 K unless stated otherwise, and for the sake of readability, the adsorption of hydrogen was omitted. In the diagram, only the barriers for an Eley−Rideal (ER) mechanism are discussed, which assumes reaction of the adsorbed molecule with H_2 from the gas phase. All energies and the Langmuir−Hinshelwood (LH) barriers, which assume reaction with preadsorbed H_2, can be found in the Supporting Information.

CO adsorbed on the Cu-doped defect (2) was set as the reference for the minimum energies because the energies for the free Cu-doped and HCuH-doped defect can be defined
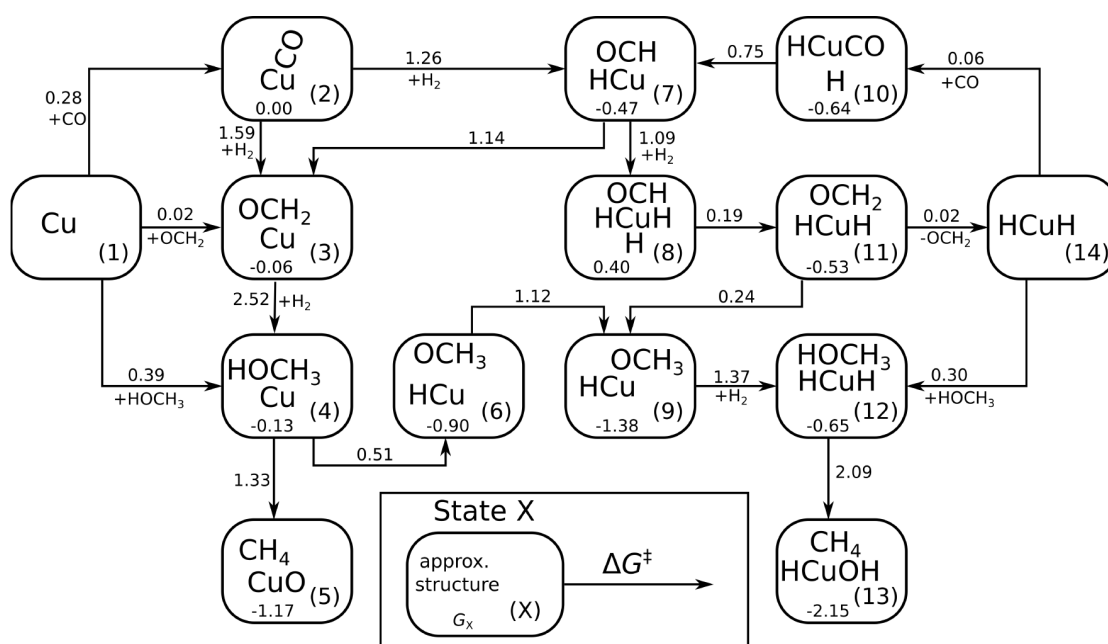
reduction is also apparent in the positioning of the copper atom, as it is centered in the defect cavity, 0.3 Å above the surface plane, indicating that its radius is similar to Cl^-. From the distance to the neighboring potassium ions (for which an ionic radius of 1.52 Å was assumed[60]), a formal radius of 1.75 Å is obtained for the reduced copper atom, which is significantly larger than its covalent radius of 1.35 Å.[61]

The defect electron forms an electron pair with the 4s electron of the copper atom, turning the open-shell F center

Figure 2. Reaction diagram for the hydrogenation of CO on the Cu-doped KCl F center at 500 K and 1 bar partial pressure for H_2 and CO. All energies are in eV.
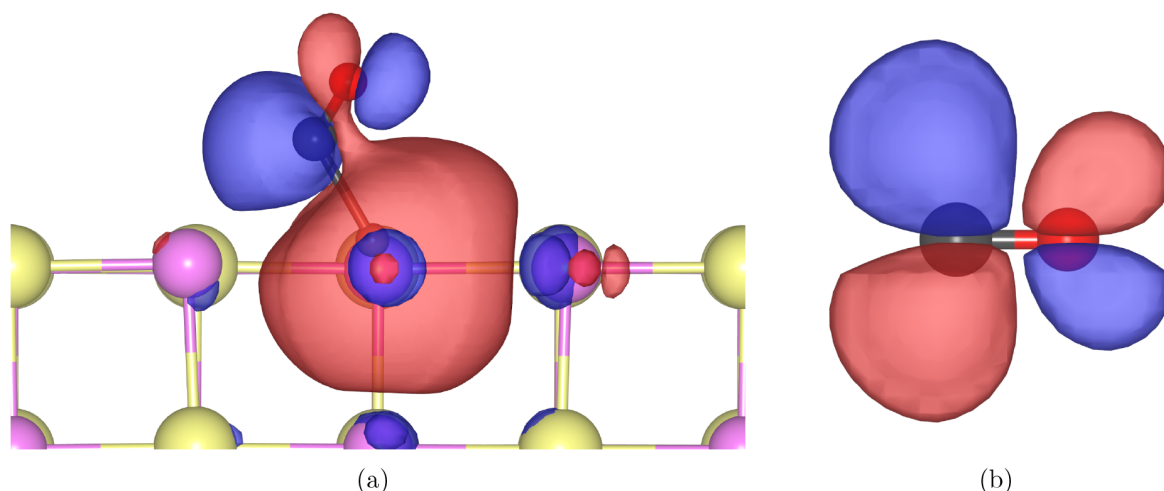
Figure 3. Highest occupied crystal orbital of CO on the Cu-doped F center on the KCl (100) surface (a) and π^*-antibonding LUMO of CO in the gas phase (b). The gray sphere represents carbon and the red sphere oxygen. Isosurface cutoff = 2.5 Å$^{-3/2}$.

with respect to CO, H_2CO, and CH_3OH. Reactions from one state n to another state m are written as $n \rightarrow m$, and they are reflected in the kinetic and thermodynamic parameters as a subscript n, m.

Adsorption of CO, H_2CO, and CH_3OH on Cu. In the following, the adsorption of the molecules involved in the hydrogenation reaction of carbon monoxide on the Cu-doped defect is explored. CO binds to the Cu atom via the carbon atom (Figure 3a, $1 \rightarrow 2$). CO is less stabilized on Cu ($E_{ads} = -0.48$ eV) than in the empty defect ($E_{ads} = -0.88$ eV, see Table 1) but still exhibits a much larger interaction with

Table 1. Properties of CO in the Gas Phase, on the Pristine, on the Defective, and on the Doped KCl (100) Surface

			defective	
	gas phase	pristine	empty	Cu-doped
frequency/cm^{-1}	2127	2108	1670	1869
bond length/Å	1.14	1.15	1.22	1.18
Bader charge CO/e	0.00	−0.02	−0.81	−0.33
E_{ads}/eV		−0.13	−0.88	−0.48

copper than with the pristine KCl (100) surface ($E_{ads} = -0.13$ eV). This trend is also observed from the C–O frequency shifts: -457 cm^{-1} on the empty F center, -258 cm^{-1} on Cu, and only -19 cm^{-1} on KCl (100). Contrary to the strong reduction on the empty F center ($q_{CO} = -0.81$), CO is only slightly reduced on the Cu atom ($q_{CO} = -0.33e$) with the remaining charge of $q_{Cu} = -0.41e$ remaining at the copper atom, according to the Bader charges. This matches the expectation based on the electron affinities of Cu and CO which are comparable (1.24 eV[62] and 1.33 eV,[63] respectively), as the copper atom shares the defect electron with CO. Nevertheless, the defect electron remains strongly localized to the defect. Inspection of the highest occupied crystal orbital (HOCO, Figure 3a) shows that the Cu/defect electrons contribute to the π^*-antibonding orbital of CO (Figure 3b), weakening and activating the bond.

Entropic effects lower the adsorption energy of CO at higher temperatures ($\Delta G_{1,2}(500$ K$) = 0.28$ eV), which reduces the Cu/defect coverage to $\theta_2(500$ K,1 bar$) = 0.16\%$ compared to >90% on the empty defect.
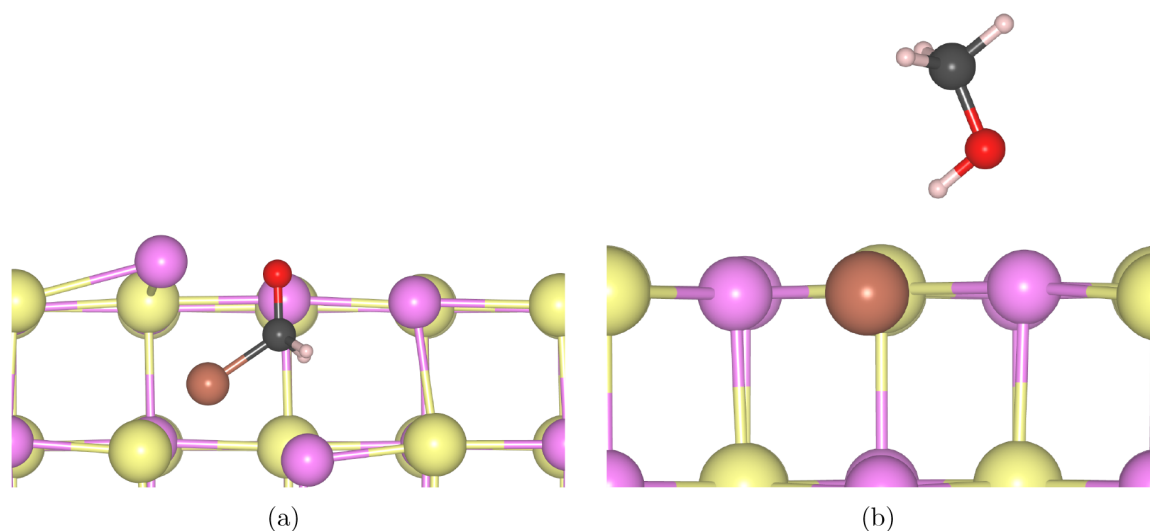

Figure 4. Minimum geometries of formaldehyde (a) and methanol (b) on the KCl F center occupied by Cu. White spheres denote hydrogen.

In the next step, formaldehyde (Figure 4a, 1 → 3) and methanol (Figure 4b, 1 → 4) are investigated regarding their adsorption on the Cu-doped F center as they are products of the hydrogenation process. Table 2 lists their adsorption energies and Bader charges.

Table 2. Calculated Adsorption Energies E_{ads} (eV) and Bader Charges (e) of H$_2$CO and CH$_3$OH on the Defective and on the Cu-Doped Defective KCl (100) Surface

| | E_{ads}/eV | | Bader charge/e | |
	empty	Cu-doped	empty	Cu-doped
H$_2$CO	−1.96	−0.91	−0.85	−1.18
CH$_3$OH	−0.85	−0.44	−0.60	−0.13

Overall, the adsorption energy of these molecules is reduced on the Cu-doped defect compared to the empty F center, similar as found for CO. In contrast to what was observed for CO, the reduction of formaldehyde is even stronger on Cu than on the empty F center ($q_{H_2CO} = -1.18e$ compared to $q_{H_2CO} = -0.85e$), owing to an additional partial reduction through the copper atom, which obtains a slightly positive partial charge of $q_{Cu} = +0.27e$. From the optimized geometry (Figure 4a) it can be seen that the copper atom is pushed by H$_2$CO into an interstitial site, creating a cavity for the molecule and stabilizing it by 0.2 eV compared to a reference calculation with the Cu atom in the chlorine position and H$_2$CO above the defect. However, H$_2$CO is essentially unbound at 500 K with $\Delta G_{1,3} = 0.02$ eV, desorbing at a rate of $k_{3,1} = 1.6 \times 10^{13}$ s^{-1}.

On the other hand, methanol is essentially not reduced by the defect ($q_{CH_3OH} = -0.13e$), and it interacts with the surface mainly by a hydrogen bond with the negatively charged copper atom ($q = -0.61e$). This leads to fast desorption at a rate of $k_{4,1} = 9.5 \times 10^{16}$ s^{-1} at 500 K and a free energy gain of $\Delta G_{4,1} = -0.39$ eV.

To summarize this part of the study, all molecules involved in the CO hydrogenation have a weaker interaction with the Cu-doped defect than with the empty defect, but their relative stability is maintained. In addition, the copper doping makes the reduction process more dynamic, allowing for a gradual reduction and a greater degree of reduction of adsorbates than was observed for the empty defect.

Formaldehyde Formation on Cu. In this section, we study the hydrogenation reactions of CO as in our previous work,[26] but on the Cu-doped defect. The reaction toward methanol and other intermediates and products proceeds along the vertical axis of the reaction diagram 2. The first hydrogenation 2 → 3 takes place as a 1,2-addition at the carbon atom via the transition state shown in Figure 5, analogous to the hydrogenation on the undoped defect or in the uncatalyzed gas phase.[64] Furthermore, it is similar to the hydrogenation of nitrogen in the gas phase,[65] but to the best of the authors' knowledge, this mechanism has not been described in any catalytic investigations of the hydrogenation of carbon monoxide so far.

The negative charge of the Cu/defect is distributed among carbon monoxide and the hydrogen atoms, facilitating dissociation of the molecule and stabilizing the transition state. At the same time, the reaction displaces the neighboring cation as the copper atom is moving into the surface. At 500 K,
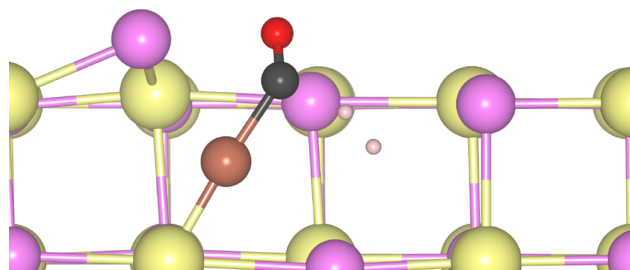

Figure 5. Transition state for the 1,2-hydrogenation of CO on the Cu-doped defect.

the free activation energy for the LH hydrogenation is $\Delta G^{\ddagger}_{doped,LH} = 1.19$ eV, which matches the barrier for the same reaction on the empty defect ($\Delta G^{\ddagger}_{empty,LH} = 1.20$ eV[26]). Likewise, the adsorption of hydrogen on the Cu-doped defect, $\Delta G^{doped}_{ads,H_2} = 0.40$ eV, matches the adsorption on the empty defect ($\Delta G^{empty}_{ads,H_2} = 0.36$ eV[26]). Entropy reduces the Gibbs free reaction energy of the hydrogenation from $\Delta G(0\ K)_{doped} = -0.74$ eV to $\Delta G(500\ K)_{doped} = -0.06$ eV. The Cu-doped defect has a similar reactivity with respect to hydrogenation as the undoped defect, as is apparent from the calculated rate constants for the ER mechanism, which are $k_{doped} = 1.0 \times 10^{-3}$ s^{-1} and $k_{empty} = 2.3 \times 10^{-3}$ s^{-1} at 500 K. This indicates that the copper atom does neither diminish nor enhance the reactivity of the defect electron.

There exists an alternate path for the hydrogenation of carbon monoxide that takes place via a mediation of the copper atom as shown in Figure 6. In this case, the hydrogen affinity of copper stabilizes the transition state, reducing the reaction barrier of the direct hydrogenation 2 → 3 at 500 K from 1.59 eV (empty F center) to 1.26 eV for 2 → 7. In the second step, 7 → 3, the hydrogen atom at the copper atom is inserted into the formyl group, yielding formaldehyde (3) with a barrier of 1.14 eV. Because it is an intramolecular step, it is not affected by hydrogen pressure and entropy, making it the fastest step of the alternative hydrogenation. This type of copper-mediated hydrogen exchange is similar to theoretical and experimental observations for [HCuH]$^{-}$ in the gas phase[66] and copper hydride complexes in solution[67−73] for the hydrogenation and hydrosilylation of carbon dioxide.

Unfortunately, the hydrogen affinity of copper also stabilizes the intermediate (7) with respect to (2) and (3) by ~0.4 eV at 500 K, effectively hindering the hydrogenation of CO on the pure copper atom.

Methanol Formation on Cu. As reaction 2 → 3, the hydrogenation of H$_2$CO 3 → 4 takes place as a 1,2-addition at the C and O atom. The reaction Gibbs free energy of the hydrogenation at 500 K is $\Delta G_{3,4} = -0.06$ eV, slightly favoring the product methanol. But the activation barrier is high, $\Delta G^{\ddagger}_{3,4} = 2.52$ eV, which corresponds to a negligible rate constant of $k_{3,4} = 3.8 \times 10^{-13}$ s^{-1}. This makes the reaction about 2×10^8 times slower than the corresponding reaction on the empty defect. The main reason behind the low efficiency of this reaction on Cu/defect is most likely its steric situation, as the transition from formaldehyde (Figure 4a) to methanol (Figure 4b) requires the adsorbate to turn by 180° and move from the defect vacancy to a position above it.

In summary, the Cu-doped defect exhibits significant reactivity regarding the hydrogenation of CO, as the hydrogen
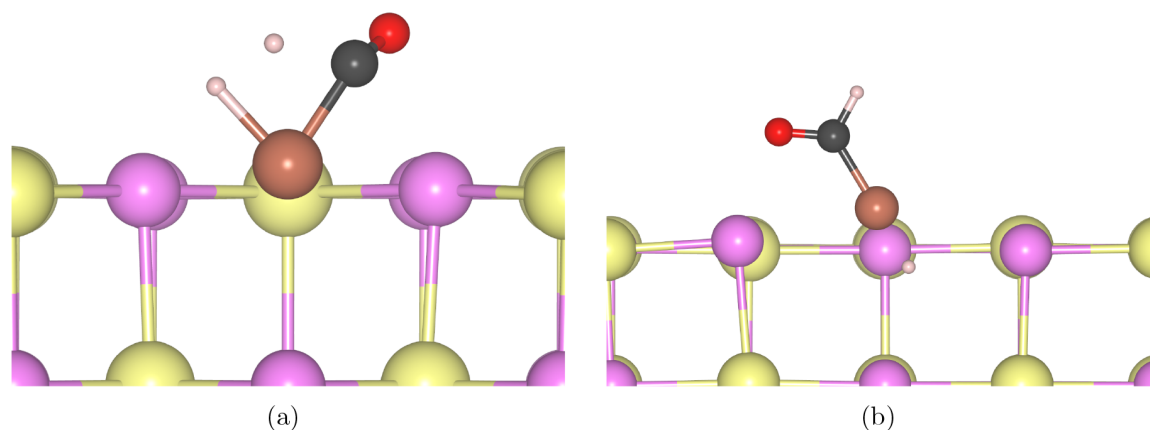
Figure 6. Transition state (a) and resulting intermediate (b) of the hydrogenation $2 \rightarrow 7$ of CO on the Cu-doped defect and insertion of copper.
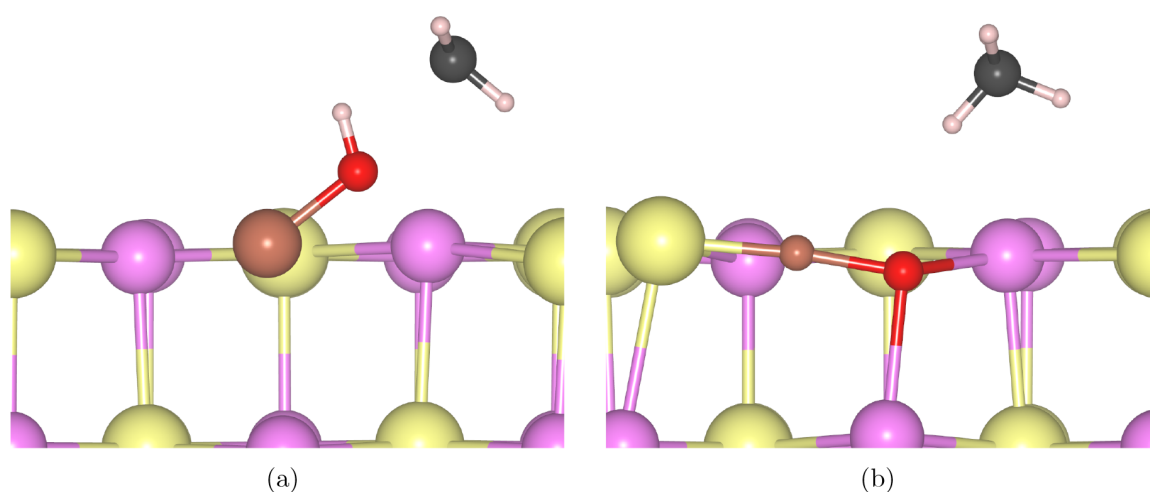

Figure 7. Transition state (a) and product (b) of the dissociation $4 \rightarrow 5$ of CH_3OH on the Cu-doped F center.

affinity of the reduced Cu atom facilitates the dissociation of H_2 and stabilizes the transition states for the reactions $2 \rightarrow 7$ and $7 \rightarrow 3$, but the second step in methanol formation is sterically hindered.

Dissociation of CH_3OH on Cu. One focus of this work is the dissociation of methanol on the doped defect because this was an important side reaction on the undoped F center.[26] First, we modeled the dissociation to methane and CuO $4 \rightarrow 5$ on the Cu-doped defect (Figure 7). While the free reaction energy $\Delta G_{4,5} = -1.05$ eV for the formation of CuO and CH_4 (Figure 7b) is strongly negative at 500 K, the free activation energy $\Delta G_{4,5}^{\ddagger}$ is quite high, 1.33 eV. This is 0.75 eV higher than on the empty defect, reducing the dissociation rate of methanol from $k_{empty} = 1.4 \times 10^7$ s^{-1} to $k_{4,5} = 4.4 \times 10^{-1}$ s^{-1} at 500 K. The main reason for this difference is the different electronic structure of the defect with and without copper. In the case of the empty defect, the dissociation takes place homolytically via the liberation of a methyl radical and is thermodynamically driven by the formation of a stable hydroxy anion in the cavity. The Cu-doped defect, however, is a closed-shell system, and methanol dissociation takes place via a methyl radical in the transition state (Figure 7a), which is poorly stabilized. The thermodynamic driving force behind this dissociation is the oxidation of the adsorbed copper atom under formation of methane. In combination with the low adsorption energy of methanol on the Cu-doped defect, this dissociation becomes a

negligible side reaction. This relationship also holds for higher temperatures, as entropy disfavors adsorption.

Methanol can also react with the doped defect via the reduction of the hydrogen atom in the hydroxy group to intermediate (9) (Figure 8) in two steps via intermediate (6) (Figures S6−S8). With an free activation energy of $\Delta G_{4,6}^{\ddagger} = 0.51$ eV at 500 K, the initial reaction toward the intermediate (6) is much faster than the dissociation with a
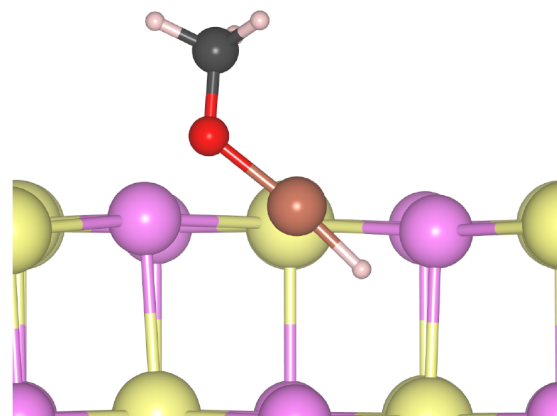

Figure 8. Methoxy intermediate 9.

reaction rate of $k_{4,6} = 7.2 \times 10^7$ s^{-1}. The first reaction $4 \rightarrow 6$ is exergonic, $\Delta G_{4,6} = -0.78$ eV. The second reaction $6 \rightarrow 9$ has a free activation energy $\Delta G_{6,9}^{\ddagger} = 1.12$ eV, which is lower than the barrier of the back-reaction and is also exergonic ($\Delta G_{6,9} = -0.47$ eV). The overall stabilization compared to methanol on the Cu-doped defect is therefore -1.25 eV. The hydrogen affinity of copper makes this side reaction kinetically and thermodynamically favorable compared to the dissociation to CuO and methane.

Copper Hydride Formation in the F Center. Bihydrogenated copper doping of the F center was observed during optimization of the intermediates of the previous reactions (Figure 9, state 14), in the following denoted as HCuH or
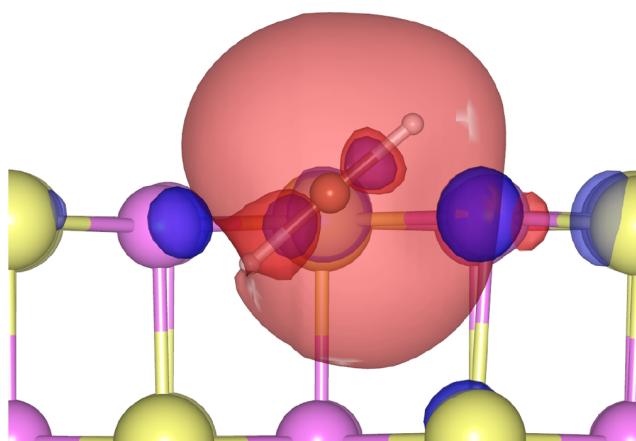

Figure 9. Highest occupied crystal orbital of the hydrogenated copper on the F center on the KCl (100) surface. Isosurface cutoff = 2.5 Å$^{-3/2}$.

HCuH-doped defect. In this case, the defect electron is delocalized over the hydrogen atoms, yielding the same charge $q_H = -0.47e$ for each, while the metal atom becomes slightly positively charged, $q_{Cu} = +0.14e$. Conceptually, this structure resembles the first stable complex copper hydride LiCuH$_2$ synthesized by Ashby et al.[74] with the defective surface acting as countercation, and the linear geometry of HCuH matches the measurements and calculations for the gas-phase anion by Zavras et al.[66]

The defect orbital (Figure 9) maintains its diffuse s-type character while featuring a σ^*-contribution to the bond between the hydrogen atoms and the central Cu atom. Despite the occupation of the antibonding orbital, the system is thermodynamically more stable than the single Cu atom. The main stabilization originates from the reduction, as the hydrogenation of the Cu-doped defect (eq 8) is exothermic, $\Delta E_{1,14} = -0.89$ eV, which matches ΔE of the HCuH$^-$ formation in the gas phase, -0.90 eV. In contrast, the neutral reaction of hydrogen and copper in the gas phase is endothermic, $\Delta E = 0.09$ eV.

$$Cu(ads) + H_2(g) \rightarrow HCuH(ads) \qquad (8)$$
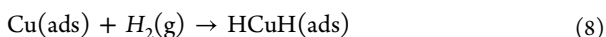
At standard pressure and 500 K, the hydrogenation is exergonic ($\Delta G_{1,14} = -0.43$ eV), whereas the hydrogen molecule is not stabilized by either the vacant F center[26] or the doped F center. However, the reaction according to eq 8 is kinetically hindered by a large barrier of $\Delta G_{1,14}^{\ddagger} = 2.60$ eV, which yields a negligible reaction rate ($k_{1,14} = 6.6 \times 10^{-14}$ s^{-1}).

Therefore, we exclude direct formation of HCuH due to the presence of H$_2$.

However, while reaction $1 \rightarrow 14$ is kinetically hindered, the addition of CO or CH$_3$OH facilitates this reaction from the left side of the diagram in Figure 2 to the right side. The turnover frequency from Cu to HCuH was evaluated with a kinetic Monte Carlo simulation for both cases, including all states featured in the diagram in Figure 2. In the presence of CO, the hydrogenation of copper occurs according to $1 \rightarrow 2 \rightarrow 7 \rightarrow 10 \rightarrow 14$ at a rate of $k_{1,14,CO} = 4.5 \times 10^{-4}$ s^{-1}, and in the presence of methanol, the same reaction occurs according to $1 \rightarrow 4 \rightarrow 6 \rightarrow 9 \rightarrow 12 \rightarrow 14$ at a rate of $k_{1,14,CH_3OH} = 3.6 \times 10^{-1}$ s^{-1}, exceeding the performance of the direct hydrogenation by several orders of magnitude.

Once formed, HCuH does not dissociate, as the most thermodynamically favorable decomposition to H$_2$ and solid copper is still endergonic with a Gibbs free reaction energy of 0.92 eV. Furthermore, the desorption of HCuH from the F center into the gas phase is strongly endergonic by +3.14 eV at 500 K, corresponding to a reaction rate of $k_{desorb} = 2.4 \times 10^{-19}$ s^{-1}, and the desorption onto the KCl (100) surface via an optimal, barrierless transition is similarly endergonic by +3.44 eV, corresponding to a rate reaction of $k_{desorb} = 2.3 \times 10^{-22}$ s^{-1}. Consequently, the HCuH molecule remains firmly adsorbed to the defect under reaction conditions, presenting a more stable active center for adsorbates than Cu.

Adsorption of CO, H$_2$CO, and CH$_3$OH on HCuH. On the HCuH-doped defect, CO binds to Cu via the C atom (Figure 10, state 10), similar to the Cu-doped defect. Carbon
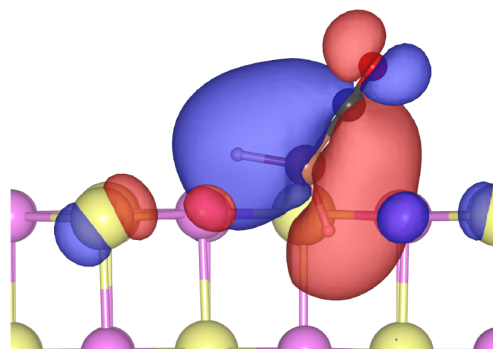

Figure 10. HOCO of CO on the HCuH-doped F center on the KCl (100) surface. Isosurface cutoff = 2.5 Å$^{-3/2}$.

monoxide is stronger adsorbed on the HCuH-doped defect than on the Cu-doped F center (see Table 3). It interacts with the σ-bonding orbital of HCuH via a π^*-antibonding orbital,

Table 3. Stretching Frequency (cm^{-1}), Bond Length (Å), Bader Charge (e), and Adsorption Energy E_{ads} (eV) of CO in the Gas Phase and on the Pristine, Defective, and Doped KCl (100) Surface

			defective surface		
	gas phase	pristine surface	empty	Cu-doped	HCuH-doped
frequency/cm^{-1}	2127	2108	1670	1869	2011
bond length/Å	1.14	1.15	1.22	1.18	1.16
Bader charge CO/e	0.00	−0.02	−0.81	−0.33	−0.29
E_{ads}/eV		−0.13	−0.88	−0.48	−0.73

slightly weakening the C—O bond (Figure 10). At 500 K, the increasing entropy lowers the CO adsorption energy to $G_{14,10}$ = 0.06 eV, but the CO defect coverage is still relatively high, $\theta_{10}(500\ K, 1\ bar)$ = 20%, compared to only 0.2% on the Cu-doped defect.

In Table 4, the adsorption of formaldehyde and methanol (Figure 11) on HCuH is compared to the empty defect and

Table 4. Calculated Adsorption Energies E_{ads} (eV) and Bader Charges (e) of H_2CO and CH_3OH on the Empty and the Doped F Center

	E_{ads}/eV			Bader charge/e		
	empty	Cu-doped	HCuH-doped	empty	Cu-doped	HCuH-doped
H_2CO	−1.96	−0.91	−0.88	−0.85	−1.18	−0.55
CH_3OH	−0.85	−0.44	−0.53	−0.60	−0.13	−0.07

the Cu-doped defect. The adsorption energy of both molecules is similar on the two doped defects. The Bader charge of the molecules adsorbed on HCuH is less negative than on empty or Cu-doped F centers because the hydrogen atoms carry part of the defect charge. This indicates that the molecules do not primarily interact with the defect via electrostatic attraction through a transferred charge, as observed for the empty defect, but predominantly via bonding to the copper atom in the case of formaldehyde and a hydrogen bond in the case of methanol. Accordingly, H_2CO and CH_3OH are effectively unbound at 500 K with an adsorption free energy of $G_{14,11}$ = −0.02 eV and $G_{14,12}$ = 0.30 eV, respectively, which makes methanol in particular a favorable reaction product.

Dissociation of CH_3OH on HCuH. The dissociation of methanol on the HCuH-doped defect, 12 → 13, is similar as on the Cu-doped defect. On HCuH, the reaction free energy $\Delta G_{12,13}$ = −1.50 eV toward the product 13 (Figure 12) is more negative than obtained for Cu, but the free activation energy $\Delta G^{\ddagger}_{12,13}$ is larger, 2.09 eV. This is 0.76 eV higher than on the Cu-doped defect, reducing the dissociation rate to $k_{12,13}$ = 8.1 × 10$^{−9}$ s$^{−1}$. Consequently, the dissociation is kinetically blocked at 500 K and has no relevance in the overall reaction.
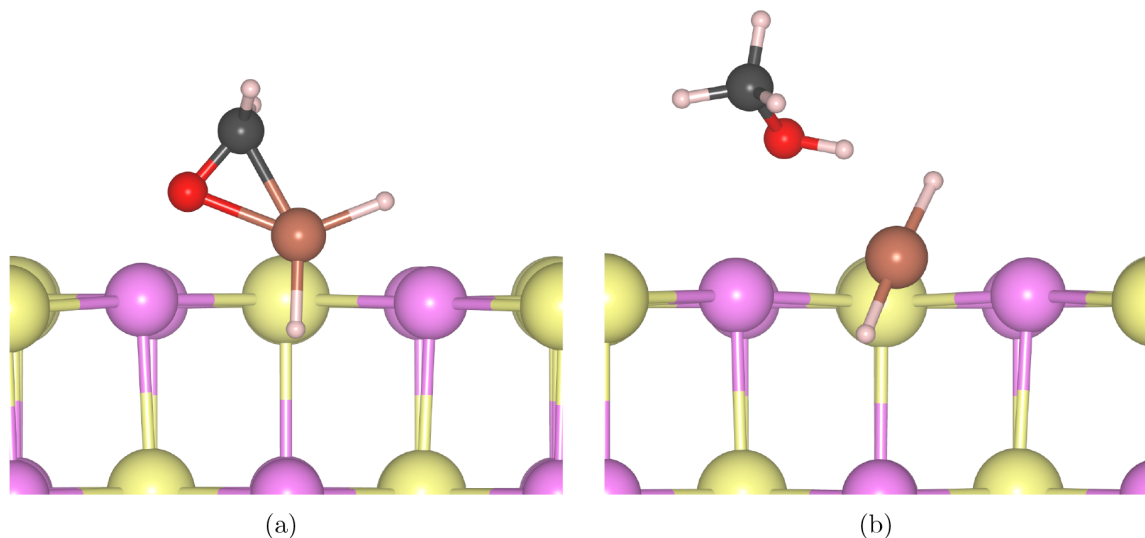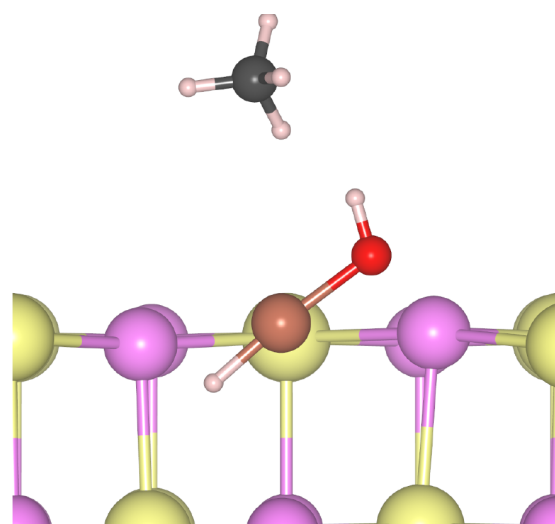

Figure 12. Minimum geometry of CuO and CH_4 on the HCuH-doped defect (13).

Apart from this reaction and the restructuring to intermediate (9) (Figure 8), no other reaction of methanol was found.

Hydrogenation of CO on HCuH. On the HCuH-doped defect, the direct hydrogenation of CO to H_2CO 10 → 11 could not be identified. Instead, it rearranges to the formyl intermediate (7). At 500 K, the attachment of an hydrogen atom to CO has an activation barrier of $\Delta G^{\ddagger}_{10,7}$ = 0.74 eV, which corresponds to a reaction rate of $k_{10,7}$ = 3.9 × 10^5. However, the aforementioned stability of HCuH$^-$ makes this reaction slightly endergonic with $\Delta G^{\ddagger}_{10,7}$ = 0.18 eV, shifting the reaction toward the starting state 10.

Hydrogenating the formyl intermediate (7) on HCuH further yields a new intermediate with three hydrogen atoms and the formyl group arranged around the copper in a square-planar configuration (Figure 13b, state (8)).

The transition state in Figure 13a shows that the hydrogen atoms bound to the Cu atom is very mobile, which is further corroborated by the transition states for the reactions 8 → 11

Figure 11. Minimum geometry of formaldehyde (a) and methanol (b) on the KCl F center occupied by HCuH.
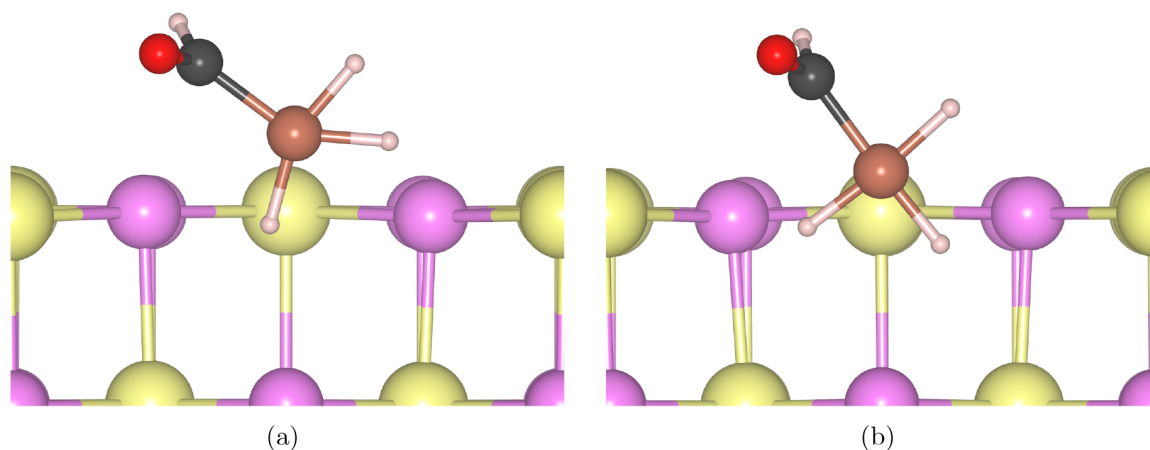
Figure 13. Transition state (a) and product (b) of the hydrogenation $7 \rightarrow 8$ of the formyl intermediate on HCuH.

and $11 \rightarrow 9$ (shown in the Supporting Information). All of these reactions are facilitated by the proximity of the reagents, requiring only a small shift from the initial minimum geometry to transfer the hydrogen atom. The first barrier is calculated as $\Delta G_{7,8}^{\ddagger} = 1.09$ eV at 500 K, which corresponds to a reaction rate of $k_{7,8} = 1.0 \times 10^2$ s^{-1}. The second barrier is much smaller, $\Delta G_{8,11}^{\ddagger} = 0.19$ eV, so the intermediate rearranges toward formaldehyde with $k_{8,11} = 1.3 \times 10^{11}$ s^{-1}. Formaldehyde then reacts rapidly with the hydrogenated copper, abstracting one more hydrogen atom to form a methoxy group. This is connected with a free activation energy of $\Delta G_{11,9}^{\ddagger} = 0.24$ eV to create intermediate (9) (Figure 8) with a reaction free energy of $\Delta G_{11,9} = -1.09$ eV. These reactions demonstrate that the hydrogenated copper on the defective KCl (100) surface is still flexible and reactive enough to donate hydrogen atoms to an adsorbed molecule.

In the final reaction step, methanol is formed by hydrogenating the Cu-bound methoxy group ($9 \rightarrow 12$), and similar to the hydrogenation of CO on the copper-doped defect, $2 \rightarrow 7$, the reaction is mediated by the Cu atom (TS in the Supporting Information). The direct hydrogenation of H$_2$CO to CH$_3$OH $11 \rightarrow 12$ could not be found. The activation free energy is $\Delta G_{9,12}^{\ddagger} = 1.37$ eV, and the reaction free energy is $\Delta G_{9,12} = 0.73$ eV, classifying the reaction as endergonic at 500 K. This corresponds to a reaction rate of $k_{9,12} = 1.8 \times 10^{-1}$ s^{-1} and a back-reaction rate of $k_{12,9} = 4.2 \times 10^6$ s^{-1}. Consequently, the equilibrium of the reaction is shifted toward the intermediate (9), which also represents the thermodynamic minimum of the overall hydrogenation process. At the same time, the back-reaction $12 \rightarrow 9$ is contested by the favorable desorption of methanol from the HCuH-doped defect $12 \rightarrow 14$, making the overall equilibrium dependent on the methanol and hydrogen partial pressures, as will be discussed in the next section.

Methanol Formation on HCuH. Taking all preceding reaction steps into account, we summarized the methanol synthesis from CO and H$_2$ on the HCuH-doped defect. In Figure 14, all steps and intermediates for this synthesis are shown. The corresponding Gibbs free energy diagram is shown in Figure 15 for 500 K and 50 bar pressure, which are typical values for industrial methanol synthesis, with a 1:9 ratio of CO:H$_2$. The adsorption energies for methanol and formaldehyde are given for standard pressure of 1 bar.
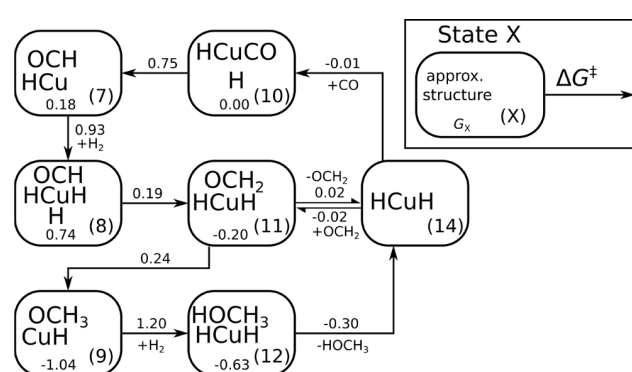

Figure 14. Reaction diagram for the hydrogenation of CO on the HCuH KCl F center at 500 K and 50 bar pressure with a 1:9 ratio of CO:H$_2$.
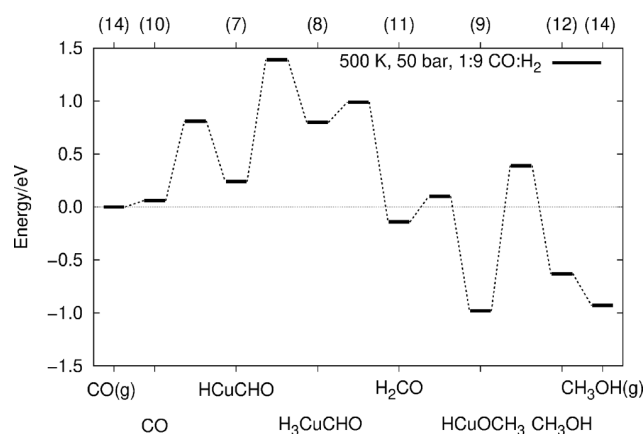

Figure 15. Calculated free energy diagram for the hydrogenation of CO on the HCuH-doped KCl F center at 500 K and 50 bar pressure with a 1:9 ratio of CO:H$_2$. All energies are in eV.

In the following, the turnover frequency (tof) of the entire reaction was investigated with a kinetic Monte Carlo simulation, including all states shown in diagram 2 with their energies adjusted according to the total pressure. The rate-limiting reaction steps of this synthesis are the hydrogenation of the formyl intermediate (7) and the hydrogenation of the methoxy intermediate (9), as it has the highest overall barrier. The most prevalent states are CO in the gas phase (14) and on the HCuH-doped defect (10), which exist during a combined

Table 5. Comparison of the Specific Activity and the Turnover Frequencies (tof) for the Conventional Catalysts and the HCuH-Doped Defect at 40, 50, and 70 bar Syngas Pressure of Various Compositions (CO, CO_2, H_2)

reference	catalyst	temp (K)	press. (bar)	specific activity (g/m^2 h × 10^{-4})	tof/center (s^{-1})
Höppener (1986)[5]	Cu/ZnO/Al$_2$O$_3$	513	70	600	
Pan (1988)[8]	Cu/ZnO	523	50.66	300	
	Cu	523	50.66	30	
Burch (1990)[9]	Cu/ZnO	513	50		0.010
Robbins (1991)[7]	Cu/SiO$_2$	523	42		0.0042
Studt (2015)[6]	Cu/MgO	503	30		0.018
	Cu/ZnO/Al$_2$O$_3$	503	30		0.019
Van Den Berg (2016)[4]	Cu	533	40		0.0025
	Cu/ZnO	533	40		0.025
	CuZn/HSAG	533	40		0.03
Dalebout (2022)[3]	CuZn-25/C	533	40		0.011
	Cu/ZnO/Al$_2$O$_3$/MgO	533	40		0.04
vacant F center[26]	*/KCl, 0.0092%	500	50	0.096	0.02
this study	HCuH/KCl, 0.0092%	500	40	150	160
		500	50	210	230
		500	70	340	370

15% of the total reaction time at 50 bar, and the methoxy intermediate (9), which exists during 84% of the total reaction time. The hindrance for the first hydrogenation is the thermodynamic instability of the formyl intermediate (7) compared to CO because it only exists for about 0.2% of the total reaction time. Changing the overall pressure does not significantly affect the state distribution over time.

In addition, a sensitivity analysis was carried out, and the degree of rate control was determined according to the definition by Campbell[75] to be 0.11 for the hydrogenation of the formyl intermediate (7) and 0.84 for the hydrogenation of the methoxy intermediate (9), confirming that step 9 → 12 is the rate-determining step, while the remaining steps are of negligible influence.

Once the second formyl intermediate (8) is formed, it rapidly reacts toward intermediate (9) via adsorbed formaldehyde (11) with barriers smaller than 0.3 eV. Alternatively, formaldehyde can rapidly desorb from the defect with a barrier of 0.02 eV at 500 K and 1 bar. The desorption predominates at reaction start and low pressures, with a reaction rate similar to 11 → 9, and reaches equilibrium at a pressure of ∼2 mbar.

In Table 5, the tof and specific activity obtained for the doped defect are compared to kinetic measurements of various conventional copper-based catalysts. The specific activity denotes the amount of methanol obtained over a period of time on a given catalyst surface.

The overall tof obtained by the simulation exceeds our previous findings for the empty F center by 3 orders of magnitude[26] and the experimental findings for the conventional copper-based catalysts by 4 orders of magnitude. Of course, the low loading of KCl surface with F centers must be taken into account.[26] In our previous investigations, we reported the lack of experimental research on the possible F center concentration at temperatures relevant for this reaction, i.e., around 500 K. We applied the value found by Kuczynski and Byun[76] at 833 K of 1.5×10^{18} F centers/cm^3 or 0.0092%. Employing the same conservative estimation for the concentration, assuming all F centers are occupied with copper atoms, yields a specific activity which is in the same order as the specific activity found by researchers for the conventional copper catalysts.

Because the methoxy intermediate (9) is the thermodynamic minimum of the energy diagram, it might block the reactive centers of the catalyst. On the other side, methanol has a low defect coverage at 500 K, and states 9 and 12 are in thermal equilibrium. Effectively, the relation between θ_9 and θ_{12} can be approximated with eq 9 with $K_{x,y}$ being the equilibrium constant for states x and y and θ_9 being the relative abundance of intermediate (9).

$$\theta_9 = \theta_{12} \frac{K_{9,12}}{K_{9,12} - 1} \tag{9}$$

With this formula, the amount of available surface defects was computed as shown in Figure 16.
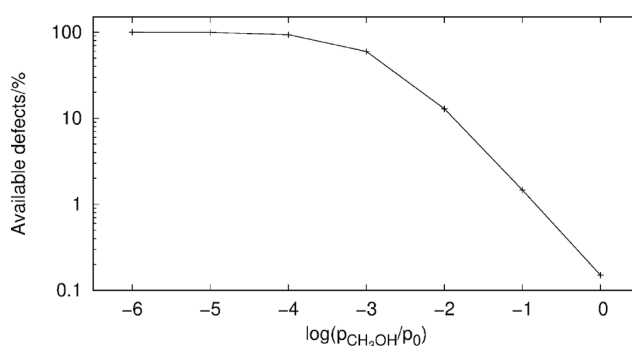
Figure 16. Calculated amount of available defects on the KCl (100) surface at 500 K and varying amounts of methanol pressure.

Accordingly, the reactivity of the defective surface is roughly reduced by 50% at a methanol pressure of 1 mbar, as half of the copper atoms are in state (9). This should not pose an issue at high carbon monoxide concentrations, however, as the adsorption of CO outweighs and hinders this side reaction under the assumption that methanol cannot react on the already occupied defect.

In conclusion, the reactivity of the HCuH-doped F center exceeds the reactivity of the industrial copper catalyst and of the empty F center by several orders of magnitude. Thus, even assuming low concentrations of HCuH-doped F centers on the KCl (100) surface, the defective KCl system is calculated to

yield similar productivity as the industrial copper catalyst. However, the reactivity decreases with increasing methanol pressure, as the defect sites are occupied by the methoxy intermediate (9).

CONCLUSIONS

The effect of Cu doping of the F center on the KCl (100) surface was investigated with periodic DFT. The doping process itself is exergonic, and copper atoms are expected to preferably occupy F centers and not defect-free terraces. The defect electron remains strongly localized at the doped defect, and the reactant CO and products (H_2CO, CH_3OH) are strongly bound to the copper atom. Only formaldehyde is fully reduced by the defect, at variance with the empty F center where all molecules were reduced, whereas CO and CH_3OH share the defect electron with the copper atom. Most activation barriers for the CO hydrogenation are as low or even lower than on the empty F center. The reductive environment created in the defect cavity is still the major driving force behind the reactivity of the defect, but it is amplified by the hydrogen affinity of copper, which facilitates the dissociation of hydrogen molecules and attachment of hydrogen atoms to adsorbates similar as observed for copper hydride complexes in solution. The main issue of the CO hydrogenation on the empty F center, the deactivation of the active site via the homolytic dissociation of the product methanol, was remedied by Cu doping, and the relevant barriers for alternative dissociation routes are not significantly reduced under typical reaction conditions. Unfortunately, the first hydrogenation of CO to formaldehyde on the Cu-doped defect is hindered by the hydrogen affinity of copper and the second hydrogenation to methanol by steric hindrance. HCuH was identified as a thermodynamically more stable dopant in comparison to Cu on the F center. Its direct formation from H_2 and Cu/defect is kinetically hindered. However, its formation is facilitated by adsorption and hydrogenation of CO or CH_3OH. On the HCuH-doped defect, the synthesis of methanol from CO through a successive hydrogenation has a turnover frequency of 230 s^{-1} at 500 K and 50 bar, which exceeds that calculated for the empty defect by 3 orders of magnitude and the measured value of conventional catalysts by 4 orders of magnitude. Consequently, even at a low F center concentration of 0.01%, the HCuH/F center catalyst is expected to yield turnover frequencies per surface area in the range of conventional catalysts, but with far lower Cu loading.

In summary, the addition of copper to the KCl F center is expected to enhance its reactivity toward hydrogenation of CO and diminishes its tendency of dissociating adsorbates, addressing the most crucial issues of the empty F center. Having demonstrated the capabilities of the doped defective KCl surface, its effect on other adsorbates than CO, H_2CO, and CH_3OH is a focus of future research as the effect of other metal atoms as dopants and its general applicability as a hydrogenation catalyst.

ASSOCIATED CONTENT

ⓈI **Supporting Information**

The Supporting Information is available free of charge at https://pubs.acs.org/doi/10.1021/acs.jpcc.2c08809.

Theory and specifications of the kinetic Monte Carlo simulation and the degree of rate control calculation, additional transition and ground state structure images with visualizations of the transition state vibrational mode and energy splines of the NEB calculations, discussion of alternative C1 intermediate states, discussion of the dissociation of water on the Cu-doped and HCuH-doped defect (PDF)

A list of the vibrational frequencies of all ground and transition states (XLSX)

A list of the energies of all ground and transition states (XLSX)

AUTHOR INFORMATION

Corresponding Author

Thomas Bredow − *Mulliken Center for Theoretical Chemistry, Clausius-Institut für Physikalische und Theoretische Chemie, Universität Bonn, 53115 Bonn, Germany*; Phone: +49 (0) 228 733839; Email: bredow@thch.uni-bonn.de; Fax: +49 (0)228 739064

Author

Michael Häfner − *Mulliken Center for Theoretical Chemistry, Clausius-Institut für Physikalische und Theoretische Chemie, Universität Bonn, 53115 Bonn, Germany*; ⦿ orcid.org/0000-0002-2765-6689

Complete contact information is available at:
https://pubs.acs.org/10.1021/acs.jpcc.2c08809

Notes

The authors declare no competing financial interest.

REFERENCES

(1) (IRENA), I. R. E. A. *Innovation Outlook: Renewable Methanol*; International Renewable Energy Agency (IRENA): 2021.

(2) Klier, K. In *Methanol Synthesis*; Eley, D., Pines, H., Weisz, P. B., Eds.; Advances in Catalysis; Academic Press: 1982; Vol. 31, pp 243−313.

(3) Dalebout, R.; Barberis, L.; Totarella, G.; Turner, S. J.; La Fontaine, C.; de Groot, F. M. F.; Carrier, X.; van der Eerden, A. M. J.; Meirer, F.; de Jongh, P. E. Insight into the Nature of the ZnOx Promoter during Methanol Synthesis. *ACS Catal.* **2022**, *12*, 6628−6639.

(4) Van Den Berg, R.; Prieto, G.; Korpershoek, G.; Van Der Wal, L. I.; Van Bunningen, A. J.; Lægsgaard-Jørgensen, S.; De Jongh, P. E.; De Jong, K. P. Structure Sensitivity of Cu and CuZn Catalysts Relevant to Industrial Methanol Synthesis. *Nat. Commun.* **2016**, *7*, 1−7.

(5) Höppener, R.; Doesburg, E.; Scholten, J. Preparation and Characterization of Stable Copper/zinc oxide/alumina Catalysts for Methanol Systhesis. *Appl. Catal.* **1986**, *25*, 109−119.

(6) Studt, F.; Behrens, M.; Kunkes, E. L.; Thomas, N.; Zander, S.; Tarasov, A.; Schumann, J.; Frei, E.; Varley, J. B.; Abild-Pedersen, F.; et al. The Mechanism of CO and CO_2 Hydrogenation to Methanol over Cu-Based Catalysts. *ChemCatChem* **2015**, *7*, 1105−1111.

(7) Robbins, J. L.; Iglesia, E.; Kelkar, C.; DeRites, B. Methanol Synthesis over Cu/SiO 2 Catalysts. *Catal. Lett.* **1991**, *10*, 1−10.

(8) Pan, W.; Cao, R.; Roberts, D.; Griffin, G. Methanol Synthesis Activity of CuZnO Catalysts. *J. Catal.* **1988**, *114*, 440−446.

(9) Burch, R.; Golunski, S.; Spencer, M. The Role of Hydrogen in Methanol Synthesis over Copper Catalysts. *Catal. Lett.* **1990**, *5*, 55−60.

(10) Dang, S.; Yang, H.; Gao, P.; Wang, H.; Li, X.; Wei, W.; Sun, Y. A Review of Research Progress on Heterogeneous Catalysts for

Methanol Synthesis from Carbon Dioxide Hydrogenation. *Catal. Today* **2019**, *330*, 61−75.

(11) Scott, A. B.; Smith, W. A. The Thermal Stability of *F*-centers in Alkali Halides. *Phys. Rev.* **1951**, *83*, 982−986.

(12) Mizuno, H.; Inoue, M. Diffusion of *F* Centers into Potassium Chloride Single Crystals. *Phys. Rev.* **1960**, *120*, 1226−1229.

(13) Wolf, E. L. Diffusion Effects in the Inhomogeneously Broadened Case: High-Temperature Saturation of the *F*-Center Electron Spin Resonance. *Phys. Rev.* **1966**, *142*, 555−569.

(14) Gravitt, J. C.; Gross, G. E.; Benson, D. K.; Scott, A. B. Motion of F Centers in KCl and KI. *J. Chem. Phys.* **1962**, *37*, 2783−2784.

(15) Tyagi, R. C.; Singh, R.; Gupta, A. K. Kinetics of Electrolytic Coloration in Alkali Halide Crystals. *J. Phys.: Condens. Matter* **1970**, *3*, 769−772.

(16) Zielasek, V.; Hildebrandt, T.; Henzler, M. Surface Color Centers on Epitaxial NaCl Films. *Phys. Rev. B* **2000**, *62*, 2912−2919.

(17) Howard, C. L. H.; Kerr, P. F. Blue Halite. *Science* **1960**, *132*, 1886−1887.

(18) Tegenkamp, C.; Pfnür, H. Adsorbate Induced Contact Charging: Pure and OH-substituted Benzoic Acids Adsorbed on Wide Band Gap Insulators. *Phys. Chem. Chem. Phys.* **2002**, *4*, 2653−2659.

(19) Malaske, U.; Tegenkamp, C.; Henzler, M.; Pfnür, H. Defect-induced Band Gap States and the Contact Charging Effect in Wide Band Gap Insulators. *Surf. Sci.* **1998**, *408*, 237−251.

(20) Fölsch, S.; Henzler, M. Water Adsorption on the NaCl Surface. *Surf. Sci.* **1991**, *247*, 269−273.

(21) Malaske, U.; Pfnür, H.; Bässler, M.; Weiss, M.; Umbach, E. Adsorption Geometry of OH Adsorbed at F Centers on a NaCl(100) Surface. *Phys. Rev. B* **1996**, *53*, 13115−13120.

(22) Häfner, M.; Hochheim, M.; Bredow, T. Chemistry with F Centers: Reduction of Organic Molecules on the Defective Potassium Chloride(100) Surface. *J. Phys. Chem. C* **2020**, *124*, 12606−12616.

(23) Hochheim, M.; Bredow, T. Adsorption of PTCDA on NaCl Surfaces with Color Centers: Charge Transfer and Formation of Radical Ions. *J. Phys. Chem. C* **2018**, *122*, 29426−29434.

(24) Chen, W.; Tegenkamp, C.; Pfnür, H.; Bredow, T. Tailoring Band Gaps of Insulators by Adsorption at Surface Defects: Benzoic Acids on NaCl Surfaces. *Phys. Rev. B* **2009**, *79*, 235419.

(25) Häfner, M.; Bredow, T. Nitrogen Activation on Defective Potassium Chloride and Sodium Chloride. *J. Phys. Chem. C* **2021**, *125*, 23764−23772.

(26) Häfner, M.; Bredow, T. Hydrogenation of CO and CO_2 Catalyzed by Potassium Chloride F Centers. *J. Phys. Chem. C* **2022**, *126*, 9713−9723.

(27) Häfner, M.; Bredow, T. F and M Centers in Alkali Halides: A Theoretical Study Applying Self-consistent Dielectric-dependent Hybrid Density Functional Theory. *Phys. Rev. B* **2020**, *102*, 184108.

(28) Perdew, J. P.; Burke, K.; Ernzerhof, M. Generalized Gradient Approximation Made Simple. *Phys. Rev. Lett.* **1996**, *77*, 3865−3868.

(29) Jónsson, H.; Mills, G.; Jacobsen, K. W. In *Classical and Quantum Dynamics in Condensed Phase Simulations*; Berne, B. J., Ciccotti, G., Coker, D. F., Eds.; World Scientific: 1998; Chapter 16, pp 385−404.

(30) Yoshihara, J.; Campbell, C. T. Methanol Synthesis and Reverse Water−Gas Shift Kinetics over Cu(110) Model Catalysts: Structural Sensitivity. *J. Catal.* **1996**, *161*, 776−782.

(31) Friedrich, J.; Young, D.; Wainwright, M. Methanol Synthesis over Raney copper-zinc Catalysts: II. Activities and Surface Properties of a Partially Leached Alloy. *J. Catal.* **1983**, *80*, 14−24.

(32) Bridgewater, A.; Wainwright, M.; Young, D.; Orchard, J. Methanol Synthesis over Raney Copper-zinc Catalysts. III. Optimization of Alloy Composition and Catalyst Preparation. *Appl. Catal.* **1983**, *7*, 369−382.

(33) Kresse, G.; Hafner, J. Ab Initio Molecular Dynamics for Liquid Metals. *Phys. Rev. B* **1993**, *47*, 558−561.

(34) Kresse, G.; Furthmüller, J. Efficiency of Ab-initio Total Energy Calculations for Metals and Semiconductors Using a Plane-wave Basis Set. *Comput. Mater. Sci.* **1996**, *6*, 15−50.

(35) Kresse, G.; Furthmüller, J. Efficient Iterative Schemes for Ab Initio Total-energy Calculations Using a Plane-wave Basis Set. *Phys. Rev. B* **1996**, *54*, 11169−11186.

(36) Kresse, G.; Joubert, D. From Ultrasoft Pseudopotentials to the Projector Augmented-wave Method. *Phys. Rev. B* **1999**, *59*, 1758−1775.

(37) Neese, F. The ORCA Program System. *Wiley Interdiscip. Rev. Comput. Mol. Sci.* **2012**, *2*, 73−78.

(38) Neese, F. Software Update: the ORCA Program System, Version 4.0. *Wiley Interdiscip. Rev. Comput. Mol. Sci.* **2018**, *8*, No. e1327.

(39) Valeev, E. F. Libint: A Library for the Evaluation of Molecular Integrals of Many-body Operators over Gaussian Functions. http://libint.valeyev.net/, 2020; ver. 2.7.0-beta.6 (accessed 2022-03-17).

(40) Lehtola, S.; Steigemann, C.; Oliveira, M. J.; Marques, M. A. Recent Developments in Libxc — A Comprehensive Library of Functionals for Density Functional Theory. *SoftwareX* **2018**, *7*, 1−5.

(41) Rappoport, D.; Furche, F. Property-optimized Gaussian Basis Sets for Molecular Response Calculations. *J. Chem. Phys.* **2010**, *133*, 134105.

(42) Weigend, F. Accurate Coulomb-fitting Basis Sets for H to Rn. *Phys. Chem. Chem. Phys.* **2006**, *8*, 1057−1065.

(43) Grimme, S.; Ehrlich, S.; Goerigk, L. Effect of the Damping Function in Dispersion Corrected Density Functional Theory. *J. Comput. Chem.* **2011**, *32*, 1456−1465.

(44) Grimme, S.; Antony, J.; Ehrlich, S.; Krieg, H. A Consistent and Accurate ab Initio Parametrization of Density Functional Dispersion Correction (DFT-D) for the 94 Elements H-Pu. *J. Chem. Phys.* **2010**, *132*, 154104.

(45) Suh, I.-K.; Ohta, H.; Waseda, Y. High-temperature Thermal Expansion of Six Metallic Elements Measured by Dilatation Method and X-ray Diffraction. *J. Mater. Sci.* **1988**, *23*, 757−760.

(46) Sheppard, D.; Xiao, P.; Chemelewski, W.; Johnson, D. D.; Henkelman, G. A Generalized Solid-state Nudged Elastic Band Method. *J. Chem. Phys.* **2012**, *136*, 074103.

(47) Sheppard, D.; Henkelman, G. Paths to Which the Nudged Elastic Band Converges. *J. Comput. Chem.* **2011**, *32*, 1769−1771.

(48) Sheppard, D.; Terrell, R.; Henkelman, G. Optimization Methods for Finding Minimum Energy Paths. *J. Chem. Phys.* **2008**, *128*, 134106.

(49) Henkelman, G.; Uberuaga, B. P.; Jónsson, H. A Climbing Image Nudged Elastic Band Method for Finding Saddle Points and Minimum Energy Paths. *J. Chem. Phys.* **2000**, *113*, 9901−9904.

(50) Henkelman, G.; Jónsson, H. Improved Tangent Estimate in the Nudged Elastic Band Method for Finding Minimum Energy Paths and Saddle Points. *J. Chem. Phys.* **2000**, *113*, 9978−9985.

(51) Grimme, S. Supramolecular Binding Thermodynamics by Dispersion-Corrected Density Functional Theory. *Chem.—Eur. J.* **2012**, *18*, 9955−9964.

(52) Ribeiro, R. F.; Marenich, A. V.; Cramer, C. J.; Truhlar, D. G. Use of Solution-Phase Vibrational Frequencies in Continuum Models for the Free Energy of Solvation. *J. Phys. Chem. B* **2011**, *115*, 14556−14562.

(53) Bajpai, A.; Mehta, P.; Frey, K.; Lehmer, A. M.; Schneider, W. F. Benchmark First-Principles Calculations of Adsorbate Free Energies. *ACS Catal.* **2018**, *8*, 1945−1954.

(54) Momma, K.; Izumi, F. VESTA3 for Three-dimensional Visualization of Crystal, Volumetric and Morphology Data. *J. Appl. Crystallogr.* **2011**, *44*, 1272−1276.

(55) Mostofi, A. A.; Yates, J. R.; Pizzi, G.; Lee, Y.-S.; Souza, I.; Vanderbilt, D.; Marzari, N. An Updated Version of Wannier90: A Tool for Obtaining Maximally-localised Wannier Functions. *Comput. Phys. Commun.* **2014**, *185*, 2309−2310.

(56) Henkelman, G.; Arnaldsson, A.; Jónsson, H. A Fast and Robust Algorithm for Bader Decomposition of Charge Density. *Computat. Mater. Sci.* **2006**, *36*, 354−360.

(57) Sanville, E.; Kenny, S. D.; Smith, R.; Henkelman, G. Improved Grid-based Algorithm for Bader Charge Allocation. *J. Comput. Chem.* **2007**, *28*, 899−908.

(58) Tang, W.; Sanville, E.; Henkelman, G. A Grid-based Bader Analysis Algorithm without Lattice Bias. *J. Phys.: Condens. Matter* **2009**, *21*, 084204.

(59) Arnaldsson, A.; Tang, W.; Chill, S.; Chai, W.; Henkelman, G. Code: Bader Charge Analysis. http://theory.cm.utexas.edu/henkelman/code/bader/, 2020; ver. 1.04, (accessed 2022-03-17).

(60) Shannon, R. D. Revised Effective Ionic Radii and Systematic Studies of Interatomic Distances in Halides and Chalcogenides. *Acta Cryst. A* **1976**, *32*, 751−767.

(61) Cordero, B.; Gómez, V.; Platero-Prats, A. E.; Revés, M.; Echeverría, J.; Cremades, E.; Barragán, F.; Alvarez, S. Covalent Radii Revisited. *Dalton Trans* **2008**, 2832−2838.

(62) Wu, X.; Qin, Z.; Xie, H.; Cong, R.; Wu, X.; Tang, Z.; Fan, H. Photoelectron Imaging and Theoretical Studies of Group 11 Cyanides MCN (M = Cu, Ag, Au). *J. Phys. Chem. A* **2010**, *114*, 12839−12844.

(63) Endoergic Ion−molecule-collision Processes of Negative Ions. III. Collisions of I− on O2, CO, and CO2. *Int. J. Mass Spectrom. Ion Phys.* **1976**, *20*, 19−32.

(64) Fan, L.; Ziegler, T. Nonlocal density functional theory as a practical tool in calculations on transition states and activation energies. Applications to elementary reaction steps in organic chemistry. *J. Am. Chem. Soc.* **1992**, *114*, 10890−10897.

(65) Hwang, D.-Y.; Mebel, A. M. Reaction Mechanism of N2/H2 Conversion to NH3: A Theoretical Study. *J. Phys. Chem. A* **2003**, *107*, 2865−2874.

(66) Zavras, A.; Ghari, H.; Ariafard, A.; Canty, A. J.; O'Hair, R. A. J. Gas-Phase Ion−Molecule Reactions of Copper Hydride Anions [CuH2]− and [Cu2H3]. *Inorg. Chem.* **2017**, *56*, 2387−2399.

(67) Zall, C. M.; Linehan, J. C.; Appel, A. M. A Molecular Copper Catalyst for Hydrogenation of CO2 to Formate. *ACS Catal.* **2015**, *5*, 5301−5305.

(68) Thiel, N. O.; Pape, F.; Teichert, J. F. In *Homogeneous Hydrogenation with Non-Precious Catalysts*; Teichert, J. F., Ed.; John Wiley & Sons, Ltd: 2019; Chapter 4, pp 87−109.

(69) Zall, C. M.; Linehan, J. C.; Appel, A. M. Triphosphine-Ligated Copper Hydrides for CO2 Hydrogenation: Structure, Reactivity, and Thermodynamic Studies. *J. Am. Chem. Soc.* **2016**, *138*, 9968−9977.

(70) Zhang, L.; Cheng, J.; Hou, Z. Highly Efficient Catalytic Hydrosilylation of Carbon Dioxide by an N-heterocyclic Carbene Copper Catalyst. *Chem. Commun.* **2013**, *49*, 4782−4784.

(71) Nakamae, K.; Kure, B.; Nakajima, T.; Ura, Y.; Tanase, T. Facile Insertion of Carbon Dioxide into Cu2(μ-H) Dinuclear Units Supported by Tetraphosphine Ligands. *Chem.—Asian J.* **2014**, *9*, 3106−3110.

(72) Motokura, K.; Kashiwame, D.; Takahashi, N.; Miyaji, A.; Baba, T. Highly Active and Selective Catalysis of Copper Diphosphine Complexes for the Transformation of Carbon Dioxide into Silyl Formate. *Chem.—Eur. J.* **2013**, *19*, 10030−10037.

(73) Watari, R.; Kayaki, Y.; Hirano, S.-i.; Matsumoto, N.; Ikariya, T. Hydrogenation of Carbon Dioxide to Formate Catalyzed by a Copper/1,8-Diazabicyclo[5.4.0]undec-7-ene System. *Adv. Synth. Catal.* **2015**, *357*, 1369−1373.

(74) Ashby, E. C.; Korenowski, T. F.; Schwartz, R. D. Preparation of the First Stable Complex Metal Hydride of Copper, LiCuH2. *J. Chem. Soc. Chem. Commun.* **1974**, 157−158.

(75) Campbell, C. T. The Degree of Rate Control: A Powerful Tool for Catalysis Research. *ACS Catal.* **2017**, *7*, 2770−2779.

(76) Kuczynski, G.; Byun, J. Diffusion of F-centers in Potassium Chloride Crystals. *Phys. Status Solidi B* **1972**, *50*, 367−377.